THE UNIVERSITY OF
SYDNEY

Ruthenium Arene Complexes as Anticancer Agents: An XAS Study

Zhi Jun Lim

A thesis submitted in fulfillment of the requirements

for the degree of Doctor of Philosophy

School of Chemistry

University of Sydney

2014

The work presented in this thesis is my own, unless otherwise stated.

Zhi Jun Lim

Acknowledgements

First of all I would like to thank my supervisor Prof. Peter A. Lay for his guidance, patience and support throughout these years which have really helped to make the completion of this thesis possible. I am also extremely grateful to my co-supervisor Dr. Aviva Levina for offering lots of assistance and advice whenever I encountered any problems in my experimental work.

I would like to express my gratitude to the following people who have helped me throughout this project. Dr. Michael Cheah for synchrotron work at the ANBF, Dr. Jade Aitken for synchrotron studies, obtaining and processing the XAS and XFM data, Dr. Ian Luck for help with NMR spectroscopy, Dr. Keith Fisher and Dr. Nick Proschogo for ESI studies.

Past and present colleagues and friends from the Lay group; Nguyen, Michelle, Hannah, Joon, Annie, Anna, Ravinder, Lauren, Sylvia who played such a huge role in my mental health and wellbeing, showered me with lots of care and are the best colleagues one can ever wish to have. Special thanks to Ravinder and Michelle for helping to proofread my introduction. Also to all my friends for always being there when I need them, in particular Jane, Erica, Emily and Ee Lin.

Finally, my dear parents back in Malaysia for always providing lots of encouragement and support for whatever I wished to pursue.

Zhi Jun LIM

List of Presentations and Publications

"Ruthenium Complexes as Potential Anti-cancer Agents" Zhi Jun Lim, Aviva Levina, Jade B. Aitken, Peter A. Lay. Poster presented at the BSR and MASR 2010 Conference, Melbourne, Australia, **2010**.

"Ruthenium Complexes as Potential Anti-cancer Agents" Zhi Jun Lim, Aviva Levina, Peter A. Lay. Poster presented at the Inaugural One-Day RACI Inorganic Student Symposium, **2011**.

"Ruthenium Complexes as Potential Anti-cancer Agents" Zhi Jun Lim, Aviva Levina, Peter A. Lay. Orally presented at the IC11 Inorganic Chemistry 2011 Conference, Perth, Australia, **2011**.

"Characterization of a Ruthenium(III)/NAMI-A adduct with bovine serum albumin that exhibits a high anti-metastatic activity." M. Liu, Z.-J Lim, Y.-Y Gwee, A. Levina, P.A. Lay, *Angew. Chem., Int. Ed.* **2010,** *49*, 1661-1664.

"Biotransformations of Anticancer Ruthenium(III) Complexes: An X-Ray Absorption Spectroscopic Study". Levina, A.; Aitken, J. B.; Gwee, Y. Y.; Lim, Z. J.; Liu, M.; Singharay, A. M.; Wong, P. F.; Lay, P. A., *Chem. Eur. J.* **2013,** *19*, 3609-3619.

Table of Contents

List of Abbreviations

ε	extinction coefficient
δ	Chemical shift
acac	acetylacetonate
ANBF	Australian National Beamline Facility
AS	Australian Synchrotron
BN	Boron nitride
BSA	Bovine serum albumin
Cat B	Cathepsin B
Cys	cysteine
DCM	dichloromethane
DFT	Density Functional Theory
DMEM	Dulbecco's Minimal Essential Medium
DMF	*N*,*N*-dimethylformamide
DMSO	dimethylsulfoxide
DNA	deoxyribonucleic acid
en	Ethylenediamine=1,2-ethanediamine
EtOH	Ethanol
ESI-MS	Electrospray ionisation mass spectroscopy
EXAFS	extended X-ray absorption fine structure
FT	Fourier transform
FTIR	Fourier transform infrared
HBS	HEPES-buffered saline
hr	hour
HEPES	4-(2-hydroxyethyl)-1-piperazine-ethanesulfonic acid
HEPG2	Liver carcinoma cells
IR	Infra-red spectroscopy
KP1019	indazolium (*trans*-tetrachloridoruthenate(III))
MeOH	Methanol
MES	2-[N-morpholino]ethanesulfonic acid

Mimid	*N*-methylimidazole
MS	Multiple scattering
MW	Molecular weight
N	Determinacy
NAMI-A	imidazolium *trans*-tetrachlorido(dimethylsulfoxide)imidazoleruthenate(III)
NaSPh	sodium thiolphenolate
NMR	Nuclear Magnetic Resonance
NO	Nitric oxide
PAGE	polyacrylamide gel electrophoresis
PBS	Phosphate buffered saline
PDT	Photodynamic therapy
PTA	1,3,5-triaza-7-phosphatricyclo-[3.3.1.1]decane
PVDF	polyvinylidene difluoride
R	Residual factor
RAPTA	Ruthenium Arene 1,3,5-triaza-7-phosphaadamantane
RBC	Red blood cell
Ru	Ruthenium
Tf	Transferrin
TMS	tetramethylsilane
Tsal	Thiosalicylic acid
UV-Vis	Ultraviolet-Visible
XANES	X-ray absoption near edge structure
XAS	X-ray absorption spectroscopy
XFM	X-ray fluorescence mapping

Abstract

Two Ru(III) complexes that have already entered clinical trials, [ImH]*trans*-[$RuCl_4$(dmso)(Im)] (NAMI-A, Im = imidazole) and [InH]*trans*-[$RuCl_4(Ind)_2$] (KP1019, Ind = indazole), are potential alternatives to Pt chemotherapeutic drugs since they are effective against cancers untreatable by cisplatin. These compounds have been proposed to operate by an "activation by reduction" process, with a reduction of Ru(III) to the more active Ru(II) species *in vivo,* which has thus generated an interest towards organometallic Ru(II) arene complexes.

The leading complexes of this field would be the RAPTA-C pioneered by Dyson and co-workers which showed anti-metastatic activity akin to NAMI-A and the [Ru(*p*-cymene)(en)]Cl pioneered by Sadler and co-workers which displayed cytotoxicity *in vitro*. These compounds show great promise due to the versatility in systematically modifying them in order to exhibit desirable physical, chemical and biological properties, mainly by changing the nature of the arene ligand and introducing different chelating ligands that may enhance selectivity towards tumour cells. Traditional anticancer drugs were designed to target DNA but in recent years, serum proteins have been found to be more relevant for the field of Ru anticancer drugs. In order to improve drug efficacy, an understanding of the mechanisms and speciation of these complexes in biological medium is needed.

X-ray absorption spectroscopy (EXAFS, XANES) and X-ray fluorescence mapping (XFM) have been used according to previous methods to study the speciation in biological fluids, extracellular matrix and cells to provide insights into the biological activities of various Ru arene complexes. The compounds were first analysed using UV-Vis for their kinetics but this technique was not sensitive enough to differentiate the speciation products. A library of

Ru(II) arene model complexes containing biologically relevant ligands (*N/O* and *S*-donors) were synthesized and their structures confirmed using multiple scattering (MS). The Ru compounds reacted under various biological conditions were then analysed using multiple linear regression, and the speciation products formed either by aquation or ligand-exchange were able to be identified. In particular, the results of RAPTA-C in rat blood cells were interesting where large changes in the XAS spectra was observed when red blood cells were present in the samples, which indicates extensive metabolism of Ru in whole blood. XFM was useful in analysing the speciation of the Ru-bound proteins in electrophoresis gels and the preliminary results of NAMI-A, KP1019 and RAPTA-C provided good insights on the different serum protein binding affinity of these complexes, and how it might affect their anticancer properties.

Chapter One

Introduction to Anticancer Drugs

1.1 Introduction

1.1.1 An overview of cancer

Cancer is still a major cause of death worldwide and arises due to factors such as the effects of carcinogens, pathogens or genetic mutation that have damaged the DNA thereby causing normal cells to proliferate and spread out of control. For solid tumours, uncontrolled cell multiplication will eventually form a neoplasm, which can be benign (non-cancerous), or in situ cancers, malignant (cancerous).[1]

Malignant tumours spread rapidly to other parts of the body in a process known as metastasis. The tumour cells will push and break through the surrounding cells and structures, with the aid of matrix metalloproteinases, which degrade the extracellular matrix. This enables the bloodstream and the lymphatic system to carry and lodge metastasising cells some distance away from the primary tumour, resulting in a secondary tumour or metastases. These tumours will interfere with the organs where they lodge, and are the main cause of cancer-related deaths.[1]

In 2012, more than 120,700 Australians were estimated to be diagnosed with cancer, with more than half being Australian males, the most common being prostate cancer (28% of the total diagnosed). For females, a total of 14,560 cases were diagnosed with breast cancer, accounting for 27% of the total diagnosed.[1] Cancer accounted for 7.6 million deaths worldwide in 2008 and is estimated to increase to over 13.1 million in 2030, without improved medical interventions.[2]

1.1.2 Current treatments

Over the years, a variety of ways and means of treating cancer have been used. Treatment is undertaken in stages, such as surgery, followed by radiotherapy, often combined with chemotherapy, which is aimed primarily to remove as many cancer cells as possible and also to ensure the minimal possibility of recurrence.[1]

The main concern is the distant metastasis that may occur from primary tumours and are the major cause of death.[3] Surgery and radiotherapy are more successful methods in removing the primary tumour but not metastatic ones due to their scattered locations.[3, 4] Since it is easy to overlook cancer symptoms in the early stages, metastases may have already occurred during the more advanced stages of the disease in which the use of chemotherapy treatments might be a more appropriate approach to reduce cancer progression and symptoms.[3] However, different types of cancers at different sites in the body exhibit different biochemical properties; and the available treatments and drugs are not effective for some forms of metastases, which is why the discovery of novel active chemotherapeutic agents is important.[4, 5]

Chemotherapeutic drugs can also be designed to target selectively certain tumour cells. Thus, they are more suitable for treatments of tumours that have spread since they may be able to reach any location in the body.[3] Most anti-cancer drugs are cytotoxic and induce cell death by interfering with vital mechanisms. Hence, they are required to be selective towards the tumour cells in order to minimise side-effects.[4, 6]

1.1.3 Platinum anti-cancer drugs and their development

The pharmaceutical industry was traditionally dominated by organic chemistry. As such, it overlooked metal-based drugs, which have served important roles in the treatments of various diseases dating back many centuries.[7] These include arsenic and gold complexes for arthritis, bismuth for ulcer-treatment, magnesium and aluminium oxides for gastrointestinal problems and lithium for bipolar diseases.[7-10]

The serendipitous discovery of the platinum drug cisplatin **(Figure 1.1)**, a square-planar Pt(II) complex by Rosenberg in the 1960s opened the doors to the use of metal-based drugs for cancer treatment.[4, 7] The proposed mechanism of action of cisplatin is that it binds to DNA and hinders replication by cross-linking with the adjacent guanine bases. This is because the changed shape of DNA is not recognized by enzymes that repair DNA and this induces cancer cell apoptosis.[7] However, cisplatin has its limitations. It exhibits a high general toxicity, which causes severe side-effects. In addition, some patients develop tumour resistance to the drugs.[7, 11]

Cisplatin displays great efficacy against ovarian, bladder and, in particular testicular cancers, but has limited activity against breast and colon cancers, as well as being inactive against metastasis (secondary) tumours.[3] However**,** the effective activity range has increased enormously by its use in combination therapy.[7]

These limitations have stimulated research for its less toxic Pt drugs; carboplatin and oxaliplatin; the only two other Pt drugs that have entered world-wide clinical use.[4] As toxicity is associated with the rapid aquation rate of the chlorido ligands, preliminary studies

of the second-generation platinum drug, carboplatin displayed less side-effects and thus is more easily used in combination therapy.[12] Carboplatin is used mainly for ovarian cancer treatment and oxaliplatin is now one of the most successful drugs for treating colon cancer in the market.[13-15]

These success stories have led to platinum drugs being regarded as one of the most effective classes of anti-cancer drugs which have so far played a major role in stimulating interest towards developing and designing other metal-based anti-cancer drugs.

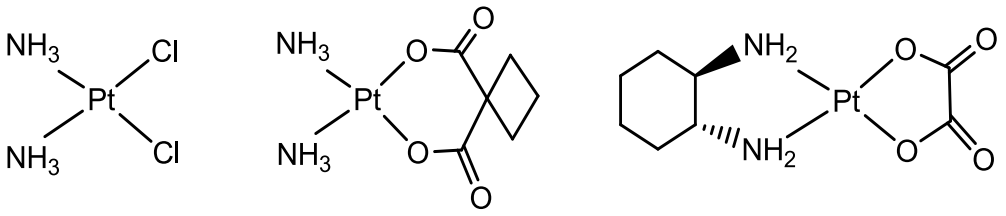

Cisplatin Carboplatin Oxaliplatin

Figure 1.1: Platinum complexes currently used for anti-cancer chemotherapy.

1.2 Ruthenium as anti-cancer alternatives

1.2.1 Overview

Following the clinical success of platinum complexes, alternative anti-cancer complexes that satisfy the following criteria: (a) effective against Pt-resistant tumours, (b) void of cross resistance to cisplatin and (c) low side-effects; are constantly being sought.[5, 6, 16]

Ruthenium complexes are considered attractive due to several factors:

a) the easily accessible oxidation states (from II to IV) via redox reactions in biological media, enabling them to be good redox-active agents;[17]

b) the kinetic stabilities in various oxidation states for various ligand types, as well as the reversible nature of some redox couples;[6] and

c) the ease in preparing mixed-ligand complexes by controllable stepwise methods, which is crucial for drug design.[3]

Based on these traits, a wide range of complexes have been synthesized and tested. In general, they exhibit lower cytotoxicity at an active dose as compared to cisplatin, which resulted in the need for a higher therapeutic dose *in vivo*.[18] Interactions with serum proteins are important in controlling both the activities and the bio-distribution of drugs within the body.[19-21] Ruthenium-based anti-cancer drugs display a higher binding affinity to transferrin and albumin compared to platinum compounds under physiological conditions.[19] This may allow Ru(III) complexes to be targeted to tumours since they have higher transferrin receptor densities than normal cells.[3] The difference in ligand geometry leads to favourable Ru binding to DNA via inter-strand crosslinking, which is different to cisplatin where intra-strand crosslinking is favoured.[22, 23]

Many ruthenium complexes are scavengers for nitric oxide (NO) molecules in cells.[24] NO is crucial for the growth and progression of tumour cells by regulating the blood flow for

tumour cells, as well as being active mediators for tumour angiogenesis.[7, 24] As scavengers, Ru compounds undergo rapid reactions with NO to inhibit cell metastasis.[24]

1.2.2 Development of ruthenium(III) complexes

Ru complexes were first tested successfully for anti-cancer activity by Dwyer and co-workers in the 1950s.[25, 26] In 1976, chloro-ammine Ru(III) complexes; e.g., *fac*-$[Ru(NH_3)_3Cl_3]$ were found to induce filamentous growth of *Escherichia coli* cells, with comparable activity to cisplatin.[27] Subsequently, *cis*-$[Ru(NH_3)_4Cl_2]$ was observed by Clarke in 1980 to show anticancer properties.[28] Unfortunately, these complexes turned out to be too insoluble for pharmaceutical use.[29]

Later on, the Keppler group introduced Ru(III) complexes that displayed activity against several screening tumour lines, especially significant results against Pt-resistant colorectal tumours in mice.[30-33] Sava focused on complexes bearing the DMSO-ligand, which were effective against solid metastasizing tumours in mice.[34]

After much extensive research, two ruthenium complexes, imidazolium *trans*-tetrachlorido(dimethylsulfoxide)imidazoleruthenate(III) (NAMI-A) (developed by Sava *et al.*)[35] and indazolium (*trans*-tetrachloridoruthenate(III)) (KP1019) (developed by Keppler *et al.*)[36] **(Figure 1.2)** were found to display the highest potential as anti-cancer agents. Although they look similar, the properties displayed were found to be very different. Both of these compounds have successfully completed Phase I clinical trials.[37] However, further progress with KP1019 was hindered due to its poor aqueous solubility and the fact that the

maximum tolerated dose and optimal dose could not be determined.[38] This issue was solved by replacing the indazolium counter ion with sodium,[38] and the new complex (called KP1339) is still undergoing clinical trials.[39]

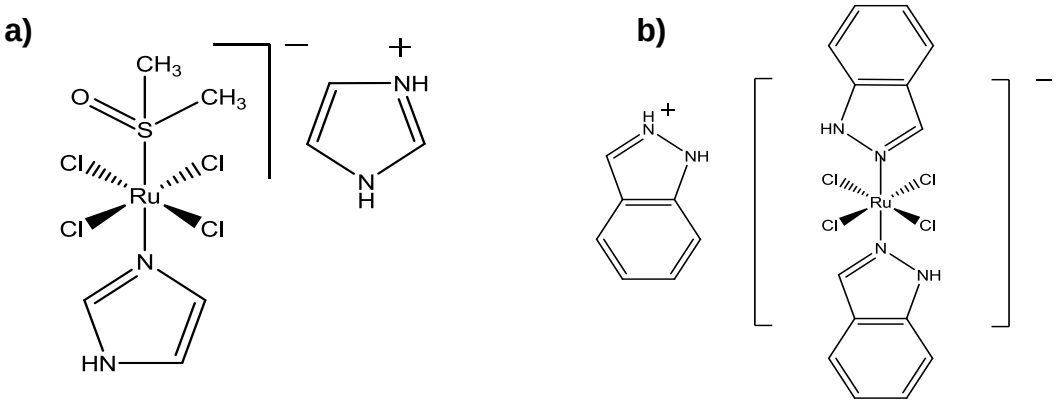

Figure 1.2 : Structures of **a)** NAMI-A and **b)** KP1019

The discovery of NAMI-A has been one of the most promising developments in metal-based anti-cancer drugs since cisplatin due to its strong anti-cancer properties and low toxicity.[7] So far, it has shown encouraging results in Phase II clinical trials especially in liver, colon, head and neck and endometrial cancers.[40] NAMI-A is known to be effective in reducing metastasis formation,[41] but has a negligible effect on the primary tumour itself due to being mildly cytotoxic *in vitro.*[42] It increased the life expectancy of the host (tumour bearing mice) regardless of the tumour types (tested against several tumour models Lewis lung carcinoma, TS/A mammary adeno-carcinoma, MCa mammary carcinoma and B16 melanoma).[43-45] Many of the properties of NAMI-A are postulated to be related to the dimethyl sulfoxide (DMSO) ligand[3] which aids in the solubility of the complex, thus allowing it to diffuse through biological membranes readily. This is thought to improve the ease of

drug administration, which is also associated with the increased solubility of complexes in aqueous solutions.[34]

In aqueous media, the chlorido ligands of the Ru complexes can exchange with water in an aqueous environment to form aqua complexes.[46] An example is shown for the aquation of NAMI-A **(Figure 1.3)**, in which the Cl^- ligand dissociates stepwise under physiological conditions (pH 7.4), while the dissociation is inhibited by decreases in pH.[47] The pH value was then thought to affect the overall treatment process of NAMI-A as at lower pH levels (e.g. pH < 6), only partial Cl^- hydrolysis was detected which may lead to selective activity in solid tumours.[47, 48] This effect was observed in a study with tumour-bearing mice in which 25% decrease in inhibiting metastasis formation resulted.[46, 49- 51]

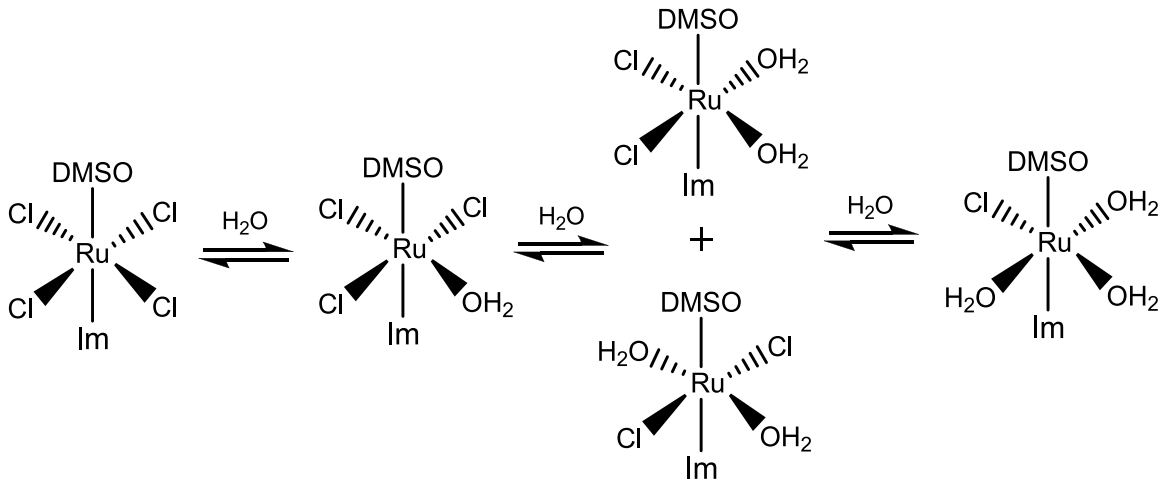

Figure 1.3: Proposed pathways of the aquation of NAMI-A in water at pH 7.4.[47]

Because of this hypothesis regarding aquation and hydrolysis processes, Alessio *et al.*[52] developed new NAMI-A type complexes, which had less basic ligands compared to imidazole, such as thiazole, pyrazole and pyrazine. These new complexes proved to be more stable in slightly acidic solutions due to a slower loss of DMSO.

KP1019 was the second Ru drug to pass Phase I clinical trials. Although its chemical properties largely resembled NAMI-A, it has the additional advantage of having the ability to induce cell apoptosis (programmed cell death). This is attributed to the different protein binding interactions of the two complexes.[51, 53]

Ru(III) complexes may be expected to remain in the same oxidation state until they reach the tumour site although partial reduction in biological media is still possible as revealed by XAS studies.[51] The "activation-by-reduction" process , with the reduction of Ru(III) to the more reactive and labile Ru(II)-chlorido species *in vivo* is also expected to take place due to the lower oxygen content found in tumour cells. Thus Ru(III) complexes are considered as pro-drugs.[54] Normally, Ru(III) complexes are relatively inert to ligand substitution. Consequently, the fairly rapid ligand exchange that is observed under biological conditions may depend on *in vivo* reduction to Ru(II) intermediates, the biologically active species which are reactive to chlorido loss.[55] This is because the reduction of Ru(III) to Ru(II) fills the d_{π} orbitals, which causes the π-donor ligands like Cl^{-} to dissociate since they do not bind strongly to Ru(II). As mentioned previously, selective reduction to Ru(II) is expected to take place in tumours where it is more hypoxic (low in O_2) and acidic due to insufficient formation of new blood vessels.[56] The lowering of the pH value is

because these cells tend to be more dependent on glycolysis for energy and produce an excess of lactic acid, thus affecting the pH value.[57] Glutathione, a sulfur-containing tripeptide may act as a reducing agent for the pro-drugs and the formed adducts were shown to prevent Ru binding to DNA.[58] As described in the previous section, activation by ligand substitution in Ru(III) are thought to be important for both NAMI-A and KP1019 which has thus generated an interest towards compounds that have a stable Ru(II) oxidation state, such as the organometallic Ru(II) arene complexes.[55, 59-61]

1.3 Ruthenium(II) arene complexes

1.3.1 General structure

Ruthenium arene complexes were first tested for anti-cancer activity when the anti-cancer agent metronidazole was coordinated to a Ru(II)-benzene complex to form [Ru(η^6-C_6H_6)Cl_2(metronidazole)], and cytotoxic effects of the resulting compound were observed.[62, 63] The amphiphilic behaviour of the metal-arene unit serves as a very useful and attractive scaffold for targeted drug design.[64] The arene ligand provides a hydrophobic face with increasing hydrophobicity depending on the size of the arene ring system, which may assist in passive transport across cell membranes, as well as improving biomolecular recognition processes.[46, 65] It also stabilizes ruthenium in its Ru(II) oxidation state, which is important in preventing the compound from oxidizing to Ru(III).[66]

Ru(II) arene compounds that are currently being actively investigated were originally developed by the Dyson and Sadler groups, and have the general formula

[Ru(η^6-arene)(X)(Y)(Z)], which resemble a half-sandwich "piano-stool" in structure **(Figure 1.4)**. The remaining three coordinating sites can be occupied in three different ways, tridentate (X-Y-Z), bidentate (X-Y) with monodentate (Z), or three monodentate ligands (X)(Y)(Z). "Z" is the "leaving group" ligand (usually a chlorido ligand) that is crucial for timing the activation process when undergoing hydrolysis. How these ligands are manipulated can give rise to reactive or labile complexes.[16, 67]

Overall these compounds show great promise due to the versatility in systematic modification of the ligands in order to exhibit desirable physical, chemical and biological properties. This is done mainly by changing the nature of the arene ligand and introducing different chelating ligands, which will enhance selectivity towards tumour cells.[4, 60, 68, 69]

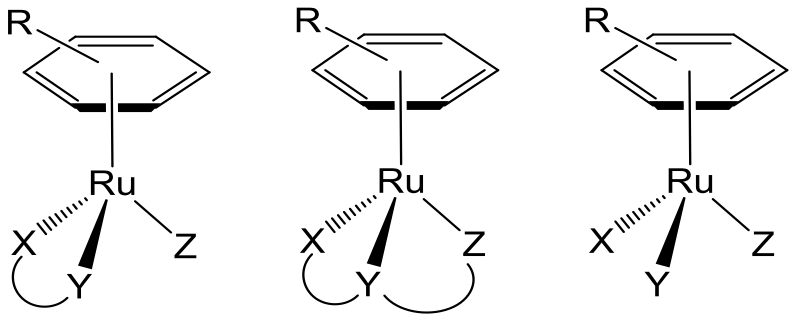

Figure 1.4: General structures of Ru(II) "piano-stool" arene complexes

1.3.2 Ruthenium(II) arene complexes

The RAPTA series (*R*uthenium *A*rene 1,3,5-triaza-7-phosphaadamantane) **(Figure 1.5)** pioneered by the Dyson group were found to exhibit similar properties to NAMI-A, being devoid of *in vitro* cytotoxicity, but capable of *in vivo* metastasis inhibition.[61] These complexes exhibit pH-dependent damage towards DNA, and it was proposed that for the pH of hypoxic tumour cells, DNA was damaged; whereas little or none were detected at the pH of healthy cells.[4, 68] This hypothesis, however, might not be valid since intracellular pH values are the same in tumour cells and normal cells, and only the extracellular pH values change.[70, 71]

The toluene derivative, RAPTA-T inhibits lung metastases *in vivo*, and also cell detachment from the primary tumour *in vitro*.[68] The *p*-cymene analogue RAPTA-C also exhibits anti-metastatic activity, as observed in the increase of the survival rates of mice bearing Ehrlich ascites carcinoma (EAC).[61, 72] These results were expected due to the similarity and relatively simple overall structures that might allow easier binding to many biomolecular targets.

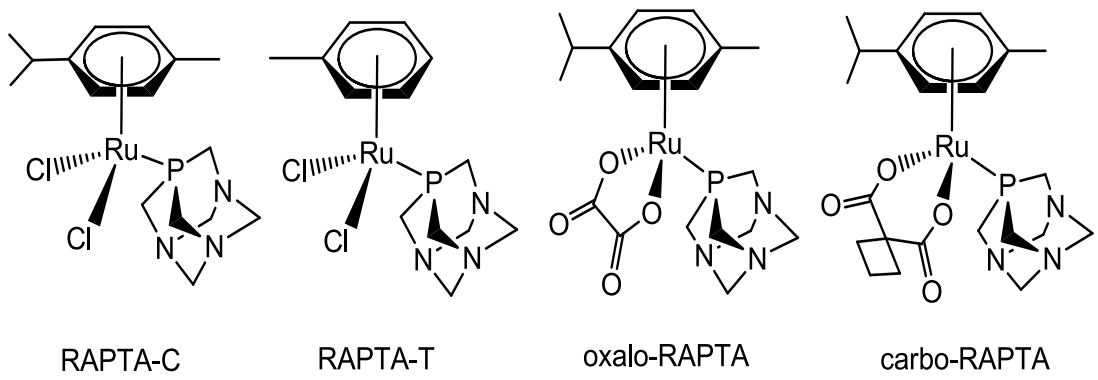

Figure 1.5: Examples of RAPTA complexes.[73]

The RAPTA-C complex undergoes rapid aquation in pure water (over 20 minutes),[61] and would have to be administered together with saline (~100 mM) in order to suppress the rate of chloride substitution as this would greatly affect any further pharmocokinetic studies. Therefore, bidentate ligands were introduced to replace the labile chlorido ligands in order to stabilize the compound. These ligands also helped to increase solubility in aqueous environments and were more resistant to aquation and hydrolysis, as already shown from the development of cisplatin derivatives: carboplatin and oxaliplatin.[17, 74]

The next group of arene compounds pioneered by the Sadler groups are of the Ru(II) piano-stool chelating ligand structure, (X-Y)(Z) **(Figure 1.6)**. The linking of X and Y to form a chelating ligand helped to provide stability towards aquation by controlling the ligand-exchange kinetics.[75] It also has a major influence on the pK_a of the products and selectivity of binding to the nucleobases. An example is [Ru(η^6-arene)(en)(Cl]PF_6 (en = 1,2-ethanediamine) in which the replacement of 'en' with acetylacetonate (acac), resulted in an increase in the aquation and hydrolysis rate, which then changed the specificity of the nucleobase.[75] A possible reason is thought to be the stronger electron-donating ability of the acac ligand.[76]

These compounds, unlike the RAPTA complexes, displayed high cytotoxic activity *in vitro* and *in vivo*.[77] They bind strongly to G (guanosine bases) through N7 coordination together with arene-purine base stacking, to enable DNA intercalation, forming monofunctional adducts.[69] Several derivatives of this complex were synthesized and tested against A2780 human ovarian cancer cells and the results showed an increase in activity

with the size of the coordinated arene: benzene < *p*-cymene < biphenyl < dihydroanthracene (DHA) < tetrahydroanthracene (THA).[69, 77] In light of this information, further development by incorporating a biphenyl ligand allowed the arene ligands to have more flexibility through rotation around the arene-Ru π bonds, which enabled simultaneous arene-base stacking and N7 covalent binding in order to increase the DNA recognition behaviour of the compound.[78]

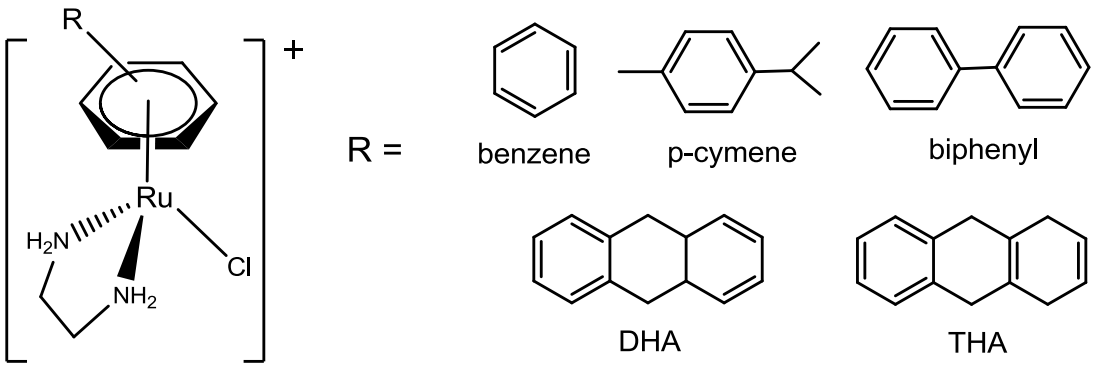

Figure 1.6: Examples of Ru[(η^6-arene)(en)(Cl]PF_6 complexes.[67]

1.3.3 Speciation in blood and cells

Traditional anti-cancer drugs were mainly designed to target DNA due to the success of Pt drugs which formed the "DNA-paradigm".[7] However, it became increasingly obvious that other enzymes and serum proteins played a role in the anti-cancer activity.[79] Therefore, drugs were later designed to target cellular signalling pathways that were specific to the

cancer cells instead. An emerging and fascinating new idea is to use proteomics and genomics as a base for designing novel agents and they have much potential.[54]

Many studies have focused on reactions within cells and not in the extracellular matrix or in the blood.[5] Blood plasma is typically made up of around 90% water and other components including albumin (~4.5%), globulins (~2.5%), fibrinogen (~0.3%), sodium chloride, amino acids and many more.[8] Blood serum can be differentiated from plasma by not containing fibrinogen and proteins that help with clotting.[8] It is important to understand the interactions of ruthenium with plasma proteins and their speciation in biological media to optimize drug design.[5]

Albumin is the most abundant plasma protein comprising about 52% of the protein content in an average healthy individual.[19, 80] It has been proven to have the ability to bind and transport a large variety of compounds; e.g. fatty acids, vitamins and metallodrugs.[81, 82] The binding affinity to albumin determines the amount of free drug concentrations in plasma, thus affecting the transfer to tissues. On average, pharmaceutical drugs are effective at a concentration way below the albumin drug site concentrations, so the protein itself is not yet saturated.[83]

Albumin has also been observed to accumulate in malignant and inflamed tissues, and hence it can be used as a delivery vehicle as its clearance from tumour tissues is less efficient due to the defective lymphatic drainage system.[83] With this in mind, passive tumour targeting by coordinating a complex with albumin has been proposed as an

alternative way to improve selectivity of therapeutic drugs,[83, 84] In the case of NAMI-A, it was shown that the Ru-albumin complex was the active form of the drug.[21]

Human serum transferrin (hTf) is found in the blood plasma with a concentration of ~2.5 g/L. It is the main protein that acts as an iron transporter through the body and is capable of binding two iron ions in the Fe(III) oxidation state.[85] Ruthenium and iron were hypothesized to have similarities in the biochemistry, which would then result in the transport of ruthenium in the body via transferrin. Therefore, due to tumour cells having a higher demand for iron and increased number of transferrin receptors, the Ru(III) complexes were postulated to bind to transferrin, which can then serve as a natural route to deliver the Ru(III) complexes to the tumour cells to be released as active Ru(II) complexes.[85,86, 87] Further investigations with XAS however, suggested passive diffusion into cells which is another possible route for cellular Ru uptake.[51] Transferrin is only 30% saturated with iron. Therefore, it has potential binding sites for other metal ions at both the Fe binding site and surface protein residues.[69, 88, 89]

The hydrolysis process as mentioned before, might be important for serum protein binding and thus determine the overall properties *in* vivo. Ruthenium compounds bind to both albumin and transferrin when incubated with each protein separately in buffers but there is a preference to albumin binding (~80-90%) in serum.[85] Studies have also shown that the selectivity exhibited by some Ru complexes towards cancer cells have to do with their binding ability to hTf.[90] The binding strengths of NAMI-A and KP1019 to these proteins have been extensively explored using a wide range of techniques.[21, 85, 90-92]

When the Ru[(η^6-arene)(en)(Cl]PF_6 complex was incubated with albumin, binding to Cys34 was kinetically favoured and His128 binding was thermodynamically favoured.[93] The nature of the arene ligand does, however, affect the binding process as the biphenyl complex was not observed to bind to Cys34 under similar conditions.[93] RAPTA-T demonstrated binding to albumin with results comparable to cisplatin, which might mean that binding is possible under blood plasma conditions due to the abundance of this protein.[20] This complex also exhibited more extensive binding to apo-transferrin compared to cisplatin, which indicated a greater selectivity in blood protein targeting.[20]

A general summary of possible speciation pathways of Ru is shown in **Figure 1.7**.[5] In the extracellular matrix (ECM), Ru complexes can form adducts with collagen or other ECM proteins[40] or with cell surface proteins like actins, which might be the reason for anti-metastatic properties.[44] The complex can also diffuse into the cell cytoplasm, bind to enzymes[5, 94] or be targeted to concentrate in this section after being coordinated to porphyrins, forming conjugates that are activated by photodynamic therapy (PDT).[95, 96] In order to reach the nucleus, apart from the transferrin delivery pathway mentioned earlier, Ru complexes can passively diffuse and bind covalently or intercalate with DNA to form adducts.[5] The reason for the cytotoxic nature of KP1019 was suggested to be due to the complex being readily taken up by cells because of its more aquation-resistant properties compared to NAMI-A.[5]

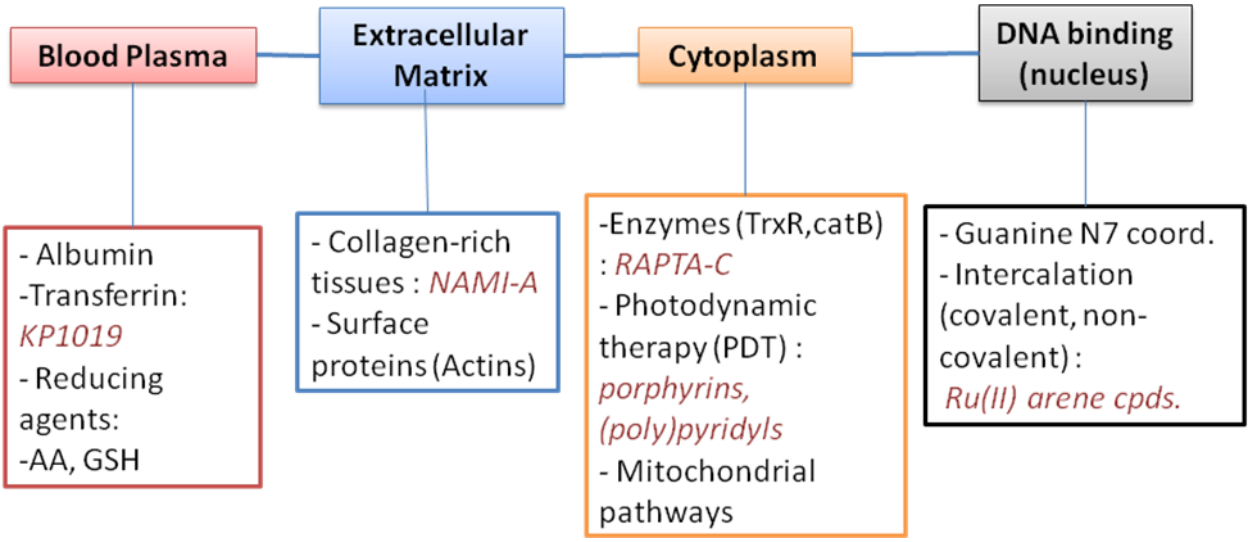

Figure 1.7 : Proposed metabolism pathways of Ru anti-cancer complexes.[5]

Electron paramagnetic resonance (EPR) spectroscopy is a technique frequently used for the characterization of metal binding to serum components. It is sensitive to changes in the coordination sphere and also selective to the particular metal. However, relatively high concentrations needed for this technique to observe speciation is a problem since biologically relevant concentrations are not used. Recently, KP1019 and KP418 have been characterized using EPR spectroscopy for their speciation in blood serum and shown to bind preferentially to albumin.[97] Other useful methods for studying Ru speciation involve synchrotron-based techniques, such as XAS and XFM which can specifically detect the changes in the metal coordination environment in complex biological systems.[21, 51, 98-102]

1.4 Further developments in Ru anti-cancer drugs

A study was done in which NAMI-A and cisplatin were co-administered on MCa mammary carcinoma cells, and the results showed superior activity compared to those observed for either drug individually.[103] This further proved that the two drugs have their individual modes of action. Further development in combination therapy include the multitargeted Ru(II) arene complexes which incorporate flavonoids to the arene moiety.[104] These complexes inhibited topoisomerase IIα and binded covalently to DNA, demonstrating possibility for a double-strike approach in tumour therapy.[105]

Multinuclear compounds are another advance in chemotherapy, displaying a different mechanism of action and selectivity towards tumour cells.[106-108] Dinuclear complexes coupled with pyridone linkers exhibited high activity comparable to cisplatin and oxaliplatin in A2780 and human colon cancer cell lines with the level of cytotoxicity dependant on the spacer length.[109] A combination of multinuclear ruthenium arene complexes and dendritic polypyridyl scaffolds were developed based on the theory of targeting tumour cells with 'enhanced permeability and retention' effect.[110] In this case, macromolecules accumulate at the tumour site due to increased blood vessel permeability within diseased tissues compared to healthy ones. They were then retained in the diseased tissues due to the absence of lymphatic drainage system.[111] The compounds studied showed a correlation between size and cytotoxicity against human ovarian cancer cell lines, with the octanuclear systems being the most reactive.[106] Encapsulating a RAPTA-pyrenyl compound in a water-soluble metalla-cage served as a good molecular carrier for targeted

drug delivery exploiting the EPR effect, thus producing ~10 times more cytotoxicity than RAPTA-C in several human cancer cell lines.[112]

1.5 Aims

This thesis is centered on investigating the interactions of ruthenium arene anti-cancer complexes with biological media, cells and extracellular proteins. In order to predict the possible changes in the environment of the complex and gain further insights, an XAS library of model ruthenium(II) arene complexes containing mainly N-O, O-O, S ligands were synthesized and characterized when their structures were unknown.

X-ray absorption spectroscopy (XAFS, XANES) has been employed as the main technique to study the biotransformation of various Ru arene complexes in biological media and with biomolecules in order to obtain a better understanding of the active forms of these drugs.[5, 21, 113] The aim was to understand the biotransformation, speciation and biodistributions of Ru drugs in biological fluids and cells. This could be used to understand the important pathways of the activity of Ru drugs and the information might be useful for improved design of new drugs or improved methods of delivery.

1.6 References

1. AIHW&AACR, Cancer in Australia: an overview, 2012. In *Cancer Series no. 74*, AIHW: Canberra, 2012.

2. American Cancer Society, Cancer Facts & Figures 2012. Atlanta: American Chemical Society, 2012.

3. Kostova, I., *Curr. Med Chem* **2006,** *13*, 1085-1107.

4. Dyson, P. J.; Sava, G., *Dalton Trans.* **2006**, 1929-1933.

5. Levina, A.; Mitra, A.; Lay, P. A., *Metallomics* **2009,** *1*, 458-470.

6. Allardyce, C. S.; Dorcier, A.; Scolaro, C.; Dyson, P. J., *Appl. Organomet. Chem.* **2005,** *19*, 1-10.

7. Fricker, S. P., *Dalton Trans.* **2007**, 4903-4917.

8. Pessoa, J. C.; Tomaz, I., *Curr. Med. Chem.* **2010,** *17*, 3701-3738.

9. Jungwirth, U.; Kowol Christian, R.; Keppler Bernhard, K.; Hartinger Christian, G.; Berger, W.; Heffeter, P., *Antioxidants Redox Signal.* **2011,** *15*, 1085-1127.

10. Ott, I.; Gust, R., *Arch. Pharm. (Weinheim, Ger.)* **2007,** *340*, 117-126.

11. Borst, P.; Rottenberg, S.; Jonkers, J., *Cell Cycle* **2008,** *7*, 1353-1359.

12. Harrap, K. R., *Cancer Treat. Rev.* **1985,** *12*, 21-33.

13. Fuertes, M. A.; Alonso, C.; Perez, J. M., *Chem. Rev.* **2003,** *103*, 645-662.

14. Kelland, L. R.; Sharp, S. Y.; O'Neill, C. F.; Raynaud, F. I.; Beale, P. J.; Judson, I. R., *J. Inorg. Biochem.* **1999,** *77*, 111-115.

15. Wong, E.; Giandomenico, C. M., *Chem. Rev.* **1999,** *99*, 2451-2466.

16. Suess-Fink, G., *Dalton Trans.* **2010,** *39*, 1673-1688.

17. Ang , W. H.; Daldini, E.; Scolaro, C.; Scopelliti, R.; Juillerat-Jeannerat, L.; Dyson , P. J., *Inorg. Chem.* **2006,** *45*, 9006-9013.

18. Alessio, E.; Mestroni, G.; Bergamo, A.; Sava, G., *Curr. Top. Med. Chem.* **2004,** *4*, 1525-1535.

19. Timerbaev, A. R.; Hartinger, C. G.; Aleksenko, S. S.; Keppler, B. K., *Chem. Rev.* **2006,** *106*, 2224-2248.

20. Groessl, M.; Terenghi, M.; Casini, A.; Elviri, L.; Lobinski, R.; Dyson, P. J., *J. Anal. At. Spectrom.* **2010,** *25*, 305-313.

21. Liu, M.; Lim, Z. J.; Gwee, Y. Y.; Levina, A.; Lay, P. A., *Angew. Chem., Int. Ed.* **2010,** *49*, 1661-1664.

22. Fruehauf, S.; Zeller, W. J., *Cancer Res.* **1991,** *51*, 2943-2948.

23. Gallori, E.; Vettori, C.; Alessio, E.; Vilchez, F. G.; Vilaplana, R.; Orioli, P.; Casini, A.; Messori, L., *Arch. Biochem. Biophys.* **2000,** *376*, 156-162.

24. Morbidelli, L.; Donnini, S.; Filippi, S.; Messori, L.; Piccioli, F.; Orioli, P.; Sava, G.; Ziche, M., *Br. J. Cancer* **2003,** *88*, 1484-1491.

25. Dwyer, F. P.; Gyarfas, E. C.; Rogers, W. P.; Koch, J. H., *Nature* **1952,** *170*, 190-191.

26. Dwyer, F. P.; Mayhew, E.; Roe, E. M. F.; Shulman, A., *Br. J. Cancer* **1965,** *19*, 195-199.

27. Durig, J. R.; Danneman, J.; Behnke, W. D.; Mercer, E. E., *Chem.-Biol. Interact.* **1976,** *13*, 287-294.

28. Clarke, M. J., *Met. Ions Biol. Syst.* **1980,** *11*, 231-283.

29. Clarke, M. J.; Zhu, F.; Frasca, D. R., *Chem. Rev.* **1999,** *99*, 2511-2533.

30. Keppler, B. K.; Wehe, D.; Endres, H.; Rupp, W., *Inorg. Chem.* **1987,** *26*, 844-846.

31. Keppler, B. K.; Rupp, W.; Juhl, U. M.; Endres, H.; Niebl, R.; Balzer, W., *Inorg. Chem.* **1987,** *26*, 4366-4370.

32. Keppler, B. K.; Rupp, W., *J. Cancer Res. Clin. Oncol.* **1986,** *111*, 166-168.

33. Garzon, F. T.; Berger, M. R.; Keppler, B. K.; Schmaehl, D., *Cancer Chemother. Pharmacol.* **1987,** *19*, 347-349.

34. Mestroni, G.; Alessio, E.; Sava, G.; Pacor, S.; Coluccia, M.; Boccarelli, A., *Met.-Based Drugs* **1994,** *1*, 41-63.

35. Sava, G.; Capozzi, I.; Clerici, K.; Gagliardi, G.; Alessio, E.; Mestroni, G., *Clin. Exp. Metastasis* **1998,** *16*, 371-379.

36. Keppler, B. K.; Henn, M.; Juhl, U. M.; Berger, M. R.; Niebl, R.; Wagner, F. E., *Prog. Clin. Biochem. Med.* **1989,** *10*, 41-69.

37. Brouwers, E. E. M.; Tibben, M. M.; Rosing, H.; Schellens, J. H. M.; Beijnen, J. H., *Rapid Commun. Mass Spectrom.* **2007,** *21*, 1521-1530.

38. Heffeter, P.; Boeck, K.; Atil, B.; Hoda, M. A. R.; Koerner, W.; Bartel, C.; Jungwirth, U.; Keppler, B. K.; Micksche, M.; Berger, W.; Koellensperger, G., *J. Biol. Inorg. Chem.* **2010,** *15*, 737-748.

39. Doemoetoer, O.; Hartinger, C. G.; Bytzek, A. K.; Kiss, T.; Keppler, B. K.; Enyedy, E. A., *J. Biol. Inorg. Chem.* **2013,** *18*, 9-17.

40. Bergamo, A.; Gaiddon, C.; Schellens, J. H. M.; Beijnen, J. H.; Sava, G., *J. Inorg. Biochem.* **2012,** *106*, 90-99.

41. Bergamo, A.; Gava, B.; Alessio, E.; Mestroni, G.; Serli, B.; Cocchietto, M.; Zorzet, S.; Sava, G., *Int. J. Oncol.* **2002,** *21*, 1331-1338.

42. Pluim, D.; van Waardenburg, R. C. A. M.; Beijnen, J. H.; Schellens, J. H. M., *Cancer Chemother. Pharmacol.* **2004,** *54*, 71-78.

43. Bergamo, A.; Gagliardi, R.; Scarcia, V.; Furlani, A.; Alessio, E.; Mestroni, G.; Sava, G., *J. Pharmacol. Exp. Ther.* **1999,** *289*, 559-564.

44. Sava, G.; Zorzet, S.; Turrin, C.; Vita, F.; Soranzo, M.; Zabucchi, G.; Cocchietto, M.; Bergamo, A.; DiGiovine, S.; Pezzoni, G.; Sartor, L.; Garbisa, S., *Clin. Cancer Res.* **2003,** *9*, 1898-1905.

45. Gava, B.; Zorzet, S.; Spessotto, P.; Cocchietto, M.; Sava, G., *J. Pharmacol. Exp. Ther.* **2006,** *317*, 284-291.

46. Yan, Y. K.; Melchart, M.; Habtemariam, A.; Sadler, P. J., *Chem. Commun.* **2005**, 4764-4776.

47. Vargiu, A. V.; Robertazzi, A.; Magistrato, A.; Ruggerone, P.; Carloni, P., *J. Phys. Chem. B* **2008,** *112*, 4401-4409.

48. Sava, G. A., E.; Bergamo, A.; Mestroni, G., Sulfoxide ruthenium complexes: non-toxic tools for the selective treatment of solid tumour metastases. In *Metallopharmaceuticals*. Clarke, M.J.; Sadler, P.J. (Eds.), **1999**, Vol. 1, pp 143-169

49. Sava, G.; Bergamo, A.; Zorzet, S.; Gava, B.; Casarsa, C.; Cocchietto, M.; Furlani, A.; Scarcia, V.; Serli, B.; Iengo, E.; Alessio, E.; Mestroni, G., *Eur. J. Cancer* **2002,** *38*, 427-435.

50. Ravera, M.; Baracco, S.; Cassino, C.; Zanello, P.; Osella, D., *Dalton Trans.* **2004**, 2347-2351.

51. Levina, A.; Aitken, J. B.; Gwee, Y. Y.; Lim, Z. J.; Liu, M.; Singharay, A. M.; Wong, P. F.; Lay, P. A., *Chem. Eur. J.* **2013,** *19*, 3609-3619.

52. Alessio, E.; Balducci, G.; Lutman, A.; Mestroni, G.; Calligaris, M.; Attia, W. M., *Inorg. Chim. Acta* **1993,** *203*, 205-217.

53. Bergamo, A.; Masi, A.; Jakupec, M. A.; Keppler, B. K.; Sava, G., *Met. Based Drugs* **2009,** *2009*, 681270.

54. Bruijnincx, P. C. A.; Sadler, P. J., *Curr. Opin. Chem. Biol.* **2008,** *12*, 197-206.

55. Clarke, M. J.; Bitler, S.; Rennert, D.; Buchbinder, M.; Kelman, A. D., *J. Inorg. Biochem.* **1980,** *12*, 79-87.

56. Sava, G.; Pacor, S.; Bregant, F.; Ceschia, V.; Mestroni, G., *Anticancer Drugs* **1990,** *1*, 99-108.

57. Hartinger, C. G.; Zorbas-Seifried, S.; Jakupec, M. A.; Kynast, B.; Zorbas, H.; Keppler, B. K., *J. Inorg. Biochem.* **2006,** *100*, 891-904.

58. Frasca, D. R.; Clarke, M. J., *J. Am. Chem. Soc.* **1999,** *121*, 8523-8532.

59. Dougan, S. J.; Sadler, P. J., *Chimia* **2007,** *61*, 704-715.

60. Peacock, A. F. A.; Sadler, P. J., *Chemistry-An Asian Journal* **2008,** *3*, 1890-1899.

61. Scolaro, C.; Bergamo, A.; Brescacin, L.; Delfino, R.; Cocchietto, M.; Laurenczy, G.; Geldbach, T. J.; Sava, G.; Dyson, P. J., *J. Med. Chem.* **2005,** *48*, 4161-4171.

62. Dale, L. D.; Dyson, T. M.; Tocher, D. A.; Tocher, J. H.; Edwards, D. I., *Anti-Cancer Drug Des.* **1989,** *4*, 295-302.

63. Dale, L. D.; Tocher, J. H.; Dyson, T. M.; Edwards, D. I.; Tocher, D. A., *Anti-Cancer Drug Des.* **1992,** *7*, 3-14.

64. Dyson, P. J., *Chimia* **2007,** *61*, 698-703.

65. Grguric-Sipka, S.; Ivanovic, I.; Rakic, G.; Todorovic, N.; Gligorijevic, N.; Radulovic, S.; Arion, V. B.; Keppler, B. K.; Tesic, Z. L., *Eur. J. Med. Chem.* **2010,** *45*, 1051-1058.

66. Bennett, M. A.; Byrnes, M. J.; Kovacik, I., *J. Organomet. Chem.* **2004,** *689*, 4463-4474.

67. Noffke, A. L.; Habtemariam, A.; Pizarro, A. M.; Sadler, P. J., *Chem. Commun.* **2012,** *48*, 5219-5246.

68. Bergamo, A.; Masi, A.; Dyson, P. J.; Sava, G., *Int. J. Oncol.* **2008,** *33*, 1281-1289.

69. Morris, R. E.; Aird, R. E.; Murdoch, P. d. S.; Chen, H.; Cummings, J.; Hughes, N. D.; Parsons, S.; Parkin, A.; Boyd, G.; Jodrell, D. I.; Sadler, P. J., *J. Med. Chem.* **2001,** *44*, 3616-3621.

70. Webb, S. D.; Sherratt, J. A.; Fish, R. G., *J Theor Biol* **1999,** *196*, 237-250.

71. Song, C., Influence of Tumour pH on Therapeutic Response. In *Cancer Drug Discovery and Development: Cancer Drug Resistance.*, Teicher, B., Ed. Humana Press Inc.: Totowa, NJ, 2006; pp 21-42.

72. Chatterjee, S.; Kundu, S.; Bhattacharyya, A.; Hartinger, C. G.; Dyson, P. J., *J. Biol. Inorg. Chem.* **2008,** *13*, 1149-1155.

73. Ang, W.-H.; Casini, A.; Sava, G.; Dyson, P. J., *J. Organomet. Chem.* **2011,** *696*, 989-998.

74. Pasini, A. Z., F., *Angew. Chem., Int. Ed. Engl.* **1987,** *26*, 615-624.

75. Fernandez, R.; Melchart, M.; Habtemariam, A.; Parsons, S.; Sadler, P. J., *Chem. Eur. J.* **2004,** *10*, 5173-5179.

76. Hasegawa, T.; Lau, T. C.; Taube, H.; Schaefer, W. P., *Inorg. Chem.* **1991,** *30*, 2921-2928.

77. Aird, R. E.; Cummings, J.; Ritchie, A. A.; Muir, M.; Morris, R. E.; Chen, H.; Sadler, P. J.; Jodrell, D. I., *Br. J. Cancer* **2002,** *86*, 1652-1657.

78. Chen, H.; Parkinson, J. A.; Parsons, S.; Coxall, R. A.; Gould, R. O.; Sadler, P. J., *J. Am. Chem. Soc.* **2002,** *124*, 3064-3082.

79. Casini, A.; Gabbiani, C.; Sorrentino, F.; Rigobello, M. P.; Bindoli, A.; Geldbach, T. J.; Marrone, A.; Re, N.; Hartinger, C. G.; Dyson, P. J.; Messori, L., *J. Med. Chem.* **2008,** *51*, 6773-6781.

80. Kratz, F., In *Metal Complexes in Cancer Chemotherapy*, Keppler Bernhard, K., Ed. VCH: Weinheim, Germany, 1993; p 391.

81. Esposito, B. P.; Najjar, R., *Coord. Chem. Rev.* **2002,** *232*, 137-149.

82. Carter, D. C.; Ho, J. X., *Adv. Protein Chem.* **1994,** *45*, 153-203.

83. Kratz, F., *J. Controlled Release* **2008,** *132*, 171-183.

84. Ang, W. H.; Daldini, E.; Juillerat-Jeanneret, L.; Dyson, P. J., *Inorg. Chem.* **2007,** *46*, 9048-9050.

85. Kratz, F.; Hartmann, M.; Keppler, B.; Messori, L., *J. Biol. Chem.* **1994,** *269*, 2581-2588.

86. Groessl, M.; Reisner, E.; Hartinger, C. G.; Eichinger, R.; Semenova, O.; Timerbaev, A. R.; Jakupec, M. A.; Arion, V. B.; Keppler, B. K., *J. Med. Chem.* **2007,** *50*, 2185-2193.

87. Musgrove, E.; Rugg, C.; Taylor, I.; Hedley, D., *J. Cell. Physiol.* **1984,** *118*, 6-12.

88. Gorzsas, A.; Andersson, I.; Pettersson, L., *Eur. J. Inorg. Chem.* **2006**, 3559-3565.

89. Li, H.; Qian, Z. M., *Med. Res. Rev.* **2002,** *22*, 225-250.

90. Clarke, M. J., *Coord. Chem. Rev.* **2002,** *232*, 69-93.

91. Hartinger Christian, G.; Jakupec Michael, A.; Zorbas-Seifried, S.; Groessl, M.; Egger, A.; Berger, W.; Zorbas, H.; Dyson Paul, J.; Keppler Bernhard, K., *Chem. Biodiversity* **2008,** *5*, 2140-2155.

92. Bergamo, A.; Stocco, G.; Gava, B.; Cocchietto, M.; Alessio, E.; Serli, B.; Iengo, E.; Sava, G., *J. Pharmacol. Exp. Ther.* **2003,** *305*, 725-732.

93. Hu, W.; Luo, Q.; Ma, X.; Wu, K.; Liu, J.; Chen, Y.; Xiong, S.; Wang, J.; Sadler, P. J.; Wang, F., *Chem. Eur. J.* **2009,** *15*, 6586-6594.

94. Chatterjee, D.; Mitra, A.; Levina, A.; Lay, P. A., *Chem. Commun.* **2008,** *25*, 2864-2866.

95. Gianferrara, T.; Bergamo, A.; Bratsos, I.; Milani, B.; Spagnul, C.; Sava, G.; Alessio, E., *J. Med. Chem.* **2010,** *53*, 4678-4690.

96. Betanzos-Lara, S.; Salassa, L.; Habtemariam, A.; Novakova, O.; Pizarro, A. M.; Clarkson, G. J.; Liskova, B.; Brabec, V.; Sadler, P. J., *Organometallics* **2012,** *31*, 3466-3479.

97. Cetinbas, N.; Webb, M. I.; Dubland, J. A.; Walsby, C. J., *J. Biol. Inorg. Chem.* **2010,** *15*, 131-145.

98. Levina, A.; Harris, H. H.; Lay, P. A., *J. Am. Chem. Soc.* **2007,** *129*, 1065-1075.

99. Nguyen, A.; Mulyani, I.; Levina, A.; Lay, P. A., *Inorg. Chem.* **2008,** *47*, 4299-4309.

100. Aitken, J. B.; Antony, S.; Weekley, C. M.; Lai, B.; Spiccia, L.; Harris, H. H., *Metallomics* **2012,** *4*, 1051-1056.

101. Weekley, C. M.; Aitken, J. B.; Vogt, S.; Finney, L. A.; Paterson, D. J.; de Jonge, M. D.; Howard, D. L.; Witting, P. K.; Musgrave, I. F.; Harris, H. H., *J. Am. Chem. Soc.* **2011,** *133*, 18272-18279.

102. Hummer, A. A.; Heffeter, P.; Berger, W.; Filipits, M.; Batchelor, D.; Buechel, G. E.; Jakupec, M. A.; Keppler, B. K.; Rompel, A., *J. Med. Chem.* **2013,** *56*, 1182-1196.

103. Khalaila, I.; Bergamo, A.; Bussy, F.; Sava, G.; Dyson, P. J., *Int. J. Oncol.* **2006,** *29*, 261-268.

104. Kurzwernhart, A.; Kandioller, W.; Bartel, C.; Baechler, S.; Trondl, R.; Muehlgassner, G.; Jakupec, M. A.; Arion, V. B.; Marko, D.; Keppler, B. K.; Hartinger, C. G., *Chem. Commun.* **2012,** *48*, 4839-4841.

105. Kurzwernhart, A.; Kandioller, W.; Baechler, S.; Bartel, C.; Martic, S.; Buczkowska, M.; Muehlgassner, G.; Jakupec, M. A.; Kraatz, H.-B.; Bednarski, P. J.; Arion, V. B.; Marko, D.; Keppler, B. K.; Hartinger, C. G., *J. Med. Chem.* **2012,** *55*, 10512-10522.

106. Govender, P.; Antonels, N. C.; Mattsson, J.; Renfrew, A. K.; Dyson, P. J.; Moss, J. R.; Therrien, B.; Smith, G. S., *J. Organomet. Chem.* **2009,** *694*, 3470-3476.

107. Ang, W. H.; Grote, Z.; Scopelliti, R.; Juillerat-Jeanneret, L.; Severin, K.; Dyson, P. J., *J. Organomet. Chem.* **2009,** *694*, 968-972.

108. Giannini, F.; Suss-Fink, G.; Furrer, J., *Inorg. Chem.* **2011,** *50*, 10552-10554.

109. Mendoza-Ferri, M.-G.; Hartinger, C. G.; Eichinger, R. E.; Stolyarova, N.; Severin, K.; Jakupec, M. A.; Nazarov, A. A.; Keppler, B. K., *Organometallics* **2008,** *27*, 2405-2407.

110. Govender, P.; Renfrew, A. K.; Clavel, C. M.; Dyson, P. J.; Therrien, B.; Smith, G. S., *Dalton Trans.* **2011,** *40*, 1158-1167.

111. Baban, D. F.; Seymour, L. W., *Adv. Drug Delivery Rev.* **1998,** *34*, 109-119.

112. Furrer, M. A.; Schmitt, F.; Wiederkehr, M.; Juillerat-Jeanneret, L.; Therrien, B., *Dalton Trans.* **2012,** *41*, 7201-7211.

113. Aitken, J. B.; Carter, E. A.; Eastgate, H.; Hackett, M. J.; Harris, H. H.; Levina, A.; Lee, Y.-C.; Chen, C.-I.; Lai, B.; Vogt, S.; Lay, P. A., *Radiat. Phys. Chem.* **2009,** *79*, 176-184.

Chapter Two

Synthesis and Characterization

2.1 Materials and Reagents

The following analytical and high purity grade reagents were used as received: diethyl ether, *N*,*N*-dimethylformamide (DMF), HPLC-grade methanol from Merck, dimethysulfoxide (DMSO) from Aldrich, dichloromethane (DCM) and toluene from Ajax, acetonitrile (CH_3CN) from Lab-Scan, methanol (MeOH) (99.9% v/v), ethanol (EtOH) (99.7% v/v), acetone and hexane from Redox Chemicals.

The following starting materials were purchased and used without further purification $[Ru(\eta^6\text{-}p\text{-cymene})Cl_2]_2$, 1,3,5-triaza-7-phosphatricyclo-[3.3.1.1]decane (pta), 1,2-ethanediamine (en), 2,4-pentanedione (acac), *N*-methylimidazole (mimid), sodium thiolphenolate (NaSPh), sodium methoxide ($NaCH_3O$), Celite® S filtration aid from Sigma-Aldrich; tetrabutylammonium hexafluorophosphate (NH_4PF_6), sodium tetraphenylborate ($NaBPh_4$), potassium hexafluorophosphate (KPF_6) from Merck; sodium hydroxide (NaOH) and thiosalicylic acid from Fluka; sodium oxalate $Na_2(COO)_2$ from BDH chemicals, silver nitrate ($AgNO_3$) from AGR Matthey; and triethylamine (Et_3N) and magnesium sulfate ($MgSO_4$) from Ajax. All solvents, methanol, ethanol and acetone were distilled over dry magnesium sulfate under argon prior to use. For NMR spectroscopy, the following deuterated solvents were used: $CDCl_3$, D_2O, MeOD-d_4 and DMSO-d_6 from Cambridge Isotope Laboratories Inc.

The following biochemicals were used as received: bovine serum albumin (BSA) fraction V (purity~99% Cat. No. A3059), bovine apo-transferrin (BTf, ≥98 %, Cat. No. T4382) and bovine type I collagen (≥98 %, Cat. No. C3511) from Sigma-Aldrich and

deoxyribonucleic acid sodium salt (DNA) from salmon testes from ICN Biomedicals. Cell culture materials were used as received: Dulbecco's Modified Eagle's Medium (DMEM with 2% v/v fetal calf serum), newborn calf serum, pre-sterilized solutions from Invitrogen and sterile disposable plasticware from Becton Dickinson. The HEPG2 human hepatoma cell line was received from the American Type Culture Collection (ATCC).[1] Stock solutions used for buffer preparation were HEPES-buffered saline (HBS: 20 mM HEPES and 140 mM NaCl, pH = 7.4) were stored at 4°C. Water was purified by the Milli-Q technique.

Blood samples were obtained from healthy male Sprague-Dawley rats handled in accordance with the policy of The University of Sydney (Animal Ethics Approval L07/1-2004/3/3846).

2.2 Analysis and Instrumentation

2.2.1 NMR Spectroscopy

^{1}H, ^{13}C and ^{31}P NMR spectroscopy were recorded on a Bruker AVANCE DRX-300 MHz spectrometer equipped with an auto-switching quad-nucleus 5 mm QNP(HCPF) *z*-gradient probe at 300 K. Chemical shifts (δ) are quoted at parts per million (ppm). δ_H and δ_C are referenced internally to tetramethylsilane (TMS) at 0 ppm, δ_P referenced externally to 85% H_3PO_4. The ruthenium complexes were dissolved in deuterated solvents just before analysis. Spectra was collected with Bruker TopSpin (ver. 3.0) software,[2] and processed using Spinworks (ver. 3.13).[3]

2.2.2 Electrospray mass spectrometry (ESMS)

ESMS data were collected using a Finnigan LCQ ESI-APCI Triple Quadrupole Mass Spectrometer. Experimental settings were set as: capillary temperature = 200 °C; pressure of sheath gas (N_2) = 50 psi; cap voltage = 15-45 V; spray voltage = 4.5 kV, tube lens offset = 25 V; *m/z* range = 150-1000 (positive- and negative-ion modes). Samples (1.0 mM) were dissolved in methanol or acetonitrile and injected with a flow rate of 0.3 mL/min.

2.2.3 UV-Vis spectroscopy

UV-Vis spectra were recorded on a Hewlett-Packard 8452A diode-array spectrophotometer fitted with a HP89090A Peltier temperature control, using a 1-cm path-length quartz cell. The stock solutions were prepared by dissolving the complexes in DMF or H_2O/DMF and the spectra were monitored at 37 °C for the following spectra changes. Data were processed using the Origin 6.1 software[4] and kinetics using the Pro-Kineticist software.[5]

2.2.4 Elemental analysis

Elemental analysis (C,H,N) were carried out by the Microanalytical Unit, Research School of Chemistry, Australian National University using a Carlo Erba 1106 automatic analyser.

2.2.5 Infrared (IR) Spectroscopy

Solid-state Fourier transform infrared (FTIR) spectra were recorded on a Varian FTS-800 Scimitar series spectrometer in a potassium bromide (KBr) matrix over the range 4000-400 cm^{-1} at a wavenumber resolution of 4 cm^{-1}. Samples were diluted ~1:10 with KBr and finely ground before use. A KBr background was collected and subtracted prior to the sample scan.

2.2.6 X-Ray Absorption Spectroscopy (XAS)

Ru K-edge XAS data were recorded in the Australian National Beamline Facility (ANBF) at the Photon Factory, Tsukuba, Japan, or at the Australian Synchrotron (AS). The electron beam energy was 2.5 GeV (ANBF), or 3.0 GeV (AS), the electron beam current was 300-400 mA (ANBF), or 200 mA (AS). Measurements were carried out in the fluorescence mode, using a 36-pixel Ge detector (Canberra-Eurisys) at ANBF, or a 100-element Ge detector (Canberra-Eurisys) at AS; and a water-cooled channel-cut double-crystal Si(311) monochromator (ANBF), or a cryogenic double-crystal Si(311) monochromator (AS). Ionisation chambers contained an atmosphere of N_2 (I_0) or Ar (I_1/I_2). Data were recorded over the energy range of 21900-22900 eV (step size: 9 eV for pre-edge, 21900-22080 eV; 0.25 eV for 22080-22180 eV XANES region; 0.05 $Å^{-1}$ steps in *k* for 22180-22900 eV EXAFS region). A Ru foil was used as the internal standard to calibrate the energy scale, the calibration energy = 22124 eV corresponded to y = 0 of the first

peak after the edge,[6] instead of 22117 eV which corresponded to first peak of the first derivative of Ru(0) edge.[7] Samples for the model Ru(II) complexes were mixed with boron nitride (1:10), ground to a fine powder and were used undiluted for the rest of the samples. These samples were pressed into four-slit 0.5 mm pellets supported within an Al spacer and secured on each side with 63.5-µm-thick Kapton tape. The temperature was maintained below 15 K, using a closed-cycle He CryoIndustries REF-1577-D22 cryostat.

Data analysis of the results including averaging, background subtraction, modeling and calculations were carried out using the XFIT software package.[8] Multiple scattering (MS) analysis of the EXAFS data was performed as reported previously[9] using XFIT, which calculates *ab-initio* FEFF 6.01 algorithms for the fittings.[10, 11] Multiple linear regression analysis was performed using the Origin software.[4] For multiple scattering (MS) analysis, the scale factor S_0^2 was constrained to be ~0.9, bond lengths and angles were restrained to within 0.02-0.05 Å and 2-10°, respectively, for model complexes. All arene rings were restrained to be planar, all C atoms in the ring restrained to ~1.41 Å from each other and constrained to be within a plane. The Debye-Waller factors were restrained between 0.0005 and 0.02 $Å^2$ and equivalent atoms were constrained to be equal. Counter ions were not included in MS modeling.

Details of all constraints and restraints are presented in **Appendix A2-A25**. Conservative errors were estimated using a combination of systematic errors and Monte-Carlo analysis as reported in previous work.[12] More information was extracted from the EXAFS spectra by examining Fourier transforms (FT), which decomposed the *k*-space

signal into its constituent frequencies.[13] This resulted in a series of peaks that corresponded to the shells of the atoms contributing to EXAFS, some which were caused by background noise.[14] The FT spectra were useful to understand the shells present and the principal interatomic distances within the structures.[14] However, peaks may overlap due to the spectrum consisting of both real and imaginary components thus causing destructive interference and loss of phase information.[15] XFIT calculated this value by first filtering it to remove the noisy unwanted sections, producing equation **2.1**:[10]

$$\chi_{\text{filtered}} = \Im^{-1}\left[\Lambda_R\left(\Im\Lambda_k k^n \chi_{\text{original}}\right)\right] \qquad \textbf{(2.1)}$$

where $\Im$ is the FT, $\Im^{-1}$ is the inverse FT, Λ_k is the EXAFS window, Λ_R is the FT window and n is the k-weighting.

Ru XFM experiments were performed at beamline 8-BM-B, Sector 8, Advanced Photon Source (APS), Lemont, IL, USA. The X-ray beam (12.8 keV) was monochromatized and passed through a pinhole (spot size on sample = 0.5 mm). Full X-ray spectra were collected in fluorescence mode and collected by a four-element silicon drift detector (Vortex EX, SII Nanotechnology) every 0.5 mm step over a 2 s dwell time. The spectra were fitted against NIST standards NBS1832 and NBS1833 using the MAPS software.[16] The experiments at the APS were carried out by Dr. Aviva Levina and Ms Hannah O'Riley. Maps and Ru content were processed and calculated by Dr. Jade Aitken. Some XFM measurements on Ru-protein complexes (separated by gel electrophoresis) were also

performed at the X-ray absorption spectroscopy (XAS) beamline, Australian Synchrotron (AS). The following beamline parameters were used: electron beam energy, 3.0 GeV; maximal electron beam current, 200 mA; monochromator, channel cut Si[111]; fluorescence detection mode (100-element Ge planar detector) and a Ru foil used for calibration. Settings for XANES spectra collection at Ru hotspots were as follows: (i) pre-edge, 21917.0-22097.0 eV (step size, 10 eV); (ii) edge, 22097.0-22167.0 eV (step size, 0.25 eV); and (iii) post-edge, linear range to k_{max} = 9 $Å^{-1}$ (step size, 0.05 $Å^{-1}$). The dwell time per point was 2.0 s for the steps (i)-(iii).

2.3 Synthesis and Characterisation of Ruthenium Arene Compounds

Unless otherwise stated, these synthetic procedures were carried out under Ar using Schlenk methods to ensure an air and moisture-free atmosphere, despite most being reported to be air stable in literature.[17,19,21] All solvents were freshly distilled prior to use and all reactions were conducted in a fume hood with the temperature constantly monitored. Literature characterization results are included if available. Numbers in brackets are the designated numbers for the compounds and will be referred to in later chapters.

2.3.1 Synthesis of Ru (η^6-*p*-cymene)(pta)Cl_2 (RAPTA-C) (2)

This synthetic procedure was modified from that in the literature.[17]

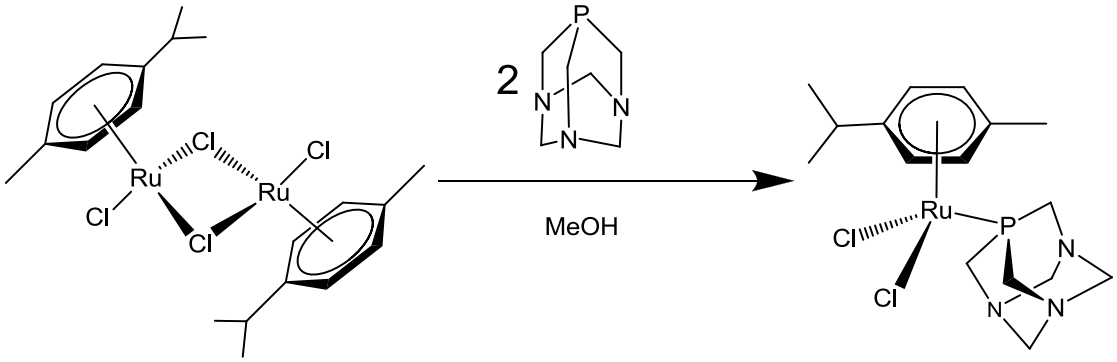

A solution of $[Ru(\eta^6\text{-}p\text{-cymene})Cl_2]_2$ (55.1 mg, 0.09 mmol) and pta (28.3 mg, 0.18 mmol) were suspended in freshly distilled MeOH (~22 mL) and the mixture was heated to reflux at 80 °C for 3 hr using an open-reflux system. The dark orange-red solution was then left to cool to room temperature, the small amount of black precipitate observed was filtered off and then the solution was rotary-evaporated (337 mBar, 60 °C) to remove the solvent. The product was then put under a vacuum pump for 2 hr to reveal an air-stable dark orange-red precipitate, which was then recrystallised from hot MeOH (yield: 52.5 mg, 63 %). 300-MHz ^{1}H NMR ($CDCl_3$): δ 5.43-5.51 (doublet of doublets, C_6H_4, J = 6 Hz), 4.54 (s, 6H), 4.34 (s, 6H), 2.80 (septet, $CHCH_3$), 2.10 (s, 3H), 1.27 (d, 6H, J = 7 Hz). Literature ^{1}H NMR ($CDCl_3$): δ 5.46 (doublet of doublets), 4.53 (s), 4.32 (s), 2.78 (septet), 2.08 (s), 1.22 (d). ^{31}P-NMR ($CDCl_3$): δ 36.51 (s). Literature ^{31}P NMR ($CDCl_3$): δ 36.63 (s).[17] ESI-MS (MeOH): *m/z* = 461 (M), 428 $[Ru(\eta^6\text{-}p\text{-cymene})(pta)Cl]^+$ Literature ESI-MS (H_2O): *m/z* = 464 ($M+H^+$), 428 $[Ru(\eta^6\text{-}p\text{-cymene})(pta)Cl]^+$.[17] Anal. found (calculated) for $C_{16}H_{26}Cl_2N_3PRu$: C, 41.14 (41.47); H, 5.64 (5.66). UV in MeOH λ_{max}, nm (ε, M^{-1} cm^{-1}): 343 (1.4×10^3). Literature UV in H_2O λ_{max}, nm: 342.[18]

2.3.2 Synthesis of [Ru(η^6-*p*-cymene)(en)Cl]PF_6 (3)

This synthetic procedure was modified from that in the literature.[19] The ligand, 1,2-ethanediamine is hygroscopic and the reaction system needs to be degassed before adding it to the solution.

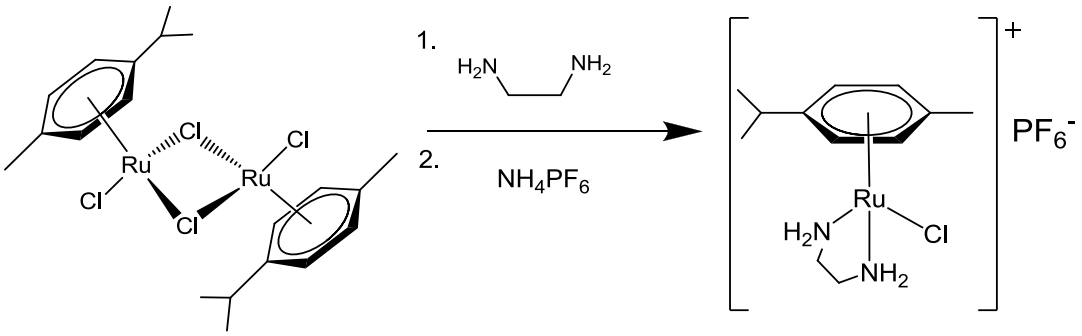

A solution of [Ru(η^6-*p*-cymene)Cl_2]$_2$ (0.39 g, 0.64 mmol) was suspended in freshly distilled MeOH (150 mL) and an excess of 1,2-ethanediamine (0.12 g, 2.0 mmol) was added, which caused the solution to turn an intense yellow immediately. The solution was stirred at room temperature for 3 hr under Ar. The yellow solution was filtered to remove black precipitates, then a small amount was taken out for ESMS analysis. An excess of tetra-1-butylammonium hexaflourophosphate (0.52 g, 3.2 mmol) was added to the yellow filtrate, which was stirred for another hour then concentrated to 15 mL on a rotary evaporator (337 mBar, 60 °C). The flask was left standing in the refrigerator (~4 °C) to enable precipitation. The next day, the yellow precipitate was filtered and re-crystallized with dry MeOH, concentrated again and left at 4°C until yellow-orange crystals formed. These crystals were washed with diethyl ether (4 x 2.5 mL) and dried under vacuum (yield: 0.26 g, 62 %). 300-MHz ^{1}H-NMR (DMSO-d_6): δ 6.10 (b, 2H), 5.50 (d,

2H, *J* = 6 Hz), 5.35 (d, 2H, *J* = 6 Hz), 4.17 (b, 2H), 2.73 (septet, $CHCH_3$), 2.41 (m, 2H), 2.11 (s, 3H), 1.22 (d, 6H, *J* = 7 Hz). Literature ^{1}H-NMR (DMSO-d_6): δ 6.13 (b), 5.48 (d), 5.32 (d), 4.22 (b), 2.71 (septet), 2.43 (m), 2.11 (s), 1.25 (d).[19] ESI-MS (MeOH): *m/z* = 295 (M), 331 [Ru(η^6-*p*-cymene)(en)Cl]$^+$. Literature ESI-MS (H_2O): *m/z* = 295 (M), 331 [Ru(η^6-*p*-cymene)(en)Cl]$^+$.[19] UV in MeOH λ_{max}, nm (ε, M^{-1} cm^{-1}): 313 (2.6 x 10^3). Literature UV in $NaClO_4$ λ_{max}, nm: 319.[20] Anal. Found (calculated) for $C_{12}H_{22}ClN_2PF_6Ru$: C, 30.50(30.29); H, 4.75(4.66); N, 5.95(5.88).

2.3.3 Synthesis of [Ru(η^6-*p*-cymene)(acac)Cl] (4)

This synthetic procedure was modified from literature.[21]

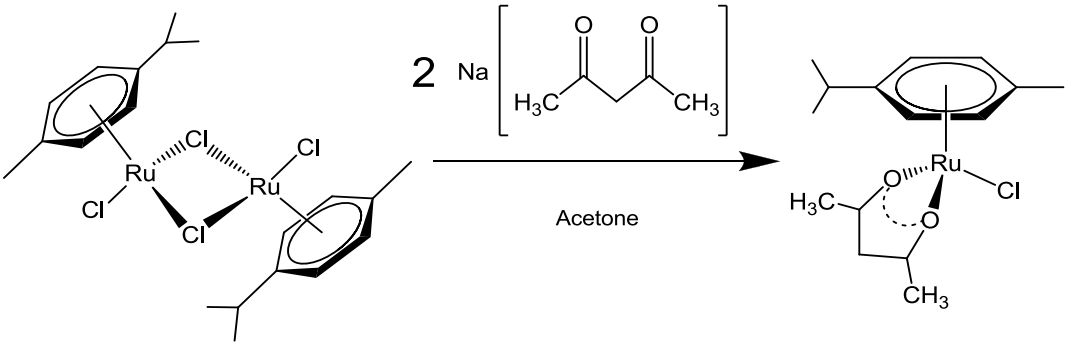

Preparation of ligand Na(acac):

Bulk Na(acac) was prepared by first dissolving sodium hydroxide (4 g, 0.1 mol) in deionized water (5 mL), then the solution was added to freshly distilled MeOH (20 mL). The combined solution was then added to acetylacetone (10.26 mL, 0.1 mol) in a 100-mL conical flask. The mixture turned creamy light yellow with a white precipitate. The flask

was stoppered and left at 4°C for 7 hr. The salt was collected with vacuum filtration then washed with cold MeOH before use.

Synthesis:

$[Ru(\eta^6\text{-}p\text{-cymene})Cl_2]_2$ (0.24 g, 0.40 mmol) and Na(acac) monohydrate (0.12 g, 0.85 mmol) were stirred in acetone (27.3 mL) for 1 hr. The resulting orange liquid was concentrated on a rotary evaporator (337 mBar, 60 °C); the dark orange residue was then extracted with dichloromethane and filtered. The solvent was removed again and the residue was dissolved in acetone, then concentrated down and diluted with diethyl ether (5 mL). This was left to stand at 4°C until dark red crystals formed (yield: 0.09 g, 31 %). 300 MHz ^{1}H NMR ($CDCl_3$): δ 5.45 (d, 2H, J = 6 Hz), 5.20 (d, 2H, J = 6 Hz), 5.14 (s, 1H), 2.86 (septet, $CHCH_3$), 2.26 (s, 3H), 1.98 (s, 6H), 1.32 (d, 6H, J = 7 Hz). Literature ^{1}H NMR ($CDCl_3$): δ 5.46 (d), 5.21 (d), 5.16 (s), 2.88 (septet), 2.27 (s), 2.00 (s), 1.32 (d).[21] ESI-MS (MeOH): m/z = 335 $[Ru(\eta^6\text{-}p\text{-cymene})(acac)]^+$. UV in MeOH λ_{max}, nm (ε, M^{-1} cm^{-1}): 312 (2.8 x 10^3) 447 (3.7 x 10^2). Anal. Found (calculated) for $C_{15}H_{22}ClO_2Ru$: C, 48.43 (48.57); H, 4.70 (4.66).

2.3.4 Synthesis of $[Ru(\eta^6\text{-}p\text{-cymene})(pta)(C_2O_4)]$ (OxaloRAPTA-C) (5)

This synthetic procedure was modified from that in the literature.[22]

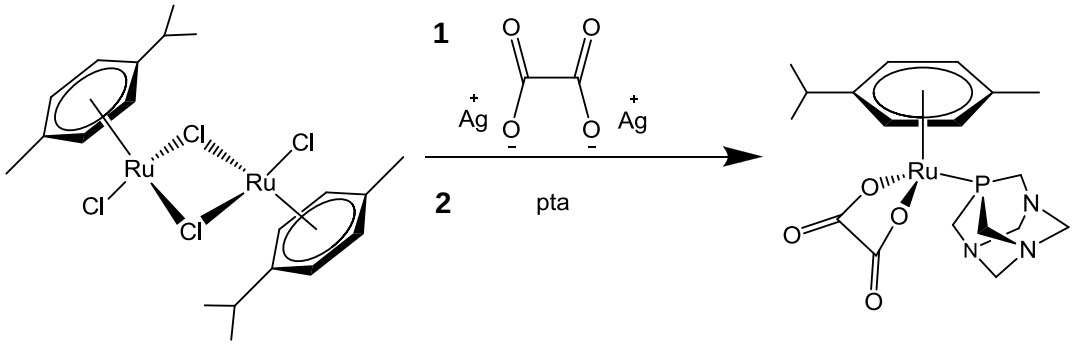

Preparation of ligand silver oxalate:

Silver oxalate was prepared by dissolving silver nitrate (1.86 g, 11 mmol) in deionised water, then the solution was added dropwise to sodium oxalate (0.67 g, 5 mmol), in which a precipitate formed immediately. The solution was stirred for 10 min and the white precipitate was filtered, washed with water and dried over vacuum. *Note: Silver oxalate had to be freshly prepared before each synthesis because its colour turned darker within 1 month, indicating decomposition.*[23]

Synthesis:

$[Ru(\eta^6\text{-}p\text{-cymene})Cl_2]_2$ (0.19 g, 0.32 mmol) and silver oxalate (0.24 g, 0.79 mmol) were stirred in deionized water (60 mL) for 12 hr at room temperature. The orange mixture was filtered through Celite to remove the AgCl precipitate. Then the solvent was removed under vacuum (80 mBar, 60 °C). The yellow residue was redissolved in MeOH (25 mL), then pta (0.12 g, 0.76 mmol) was added and the solution was stirred for a further 2 hr. The solvent was rotary evaporated down to ~10 mL and diethyl ether (25 mL) was added. The slurry was left in a refrigerator (~4 °C) for 12 hr to complete the precipitation. This was then filtered and recrystallised from MeOH/diethyl ether (1:1) to give a dark yellow precipitate, which was dried under vacuum (yield: 0.14 g, 45 %).

300 MHz ^{1}H NMR (D_2O): δ 6.00, 5.93 (dd, 4H, J = 6 Hz), 4.60 (s, 6H), 4.19 (s, 6H), 2.65 (septet, $CHCH_3$), 2.09 (s, 3H), 1.27 (d, 6H, J = 7 Hz). ^{31}P NMR (D_2O): δ -33.28. Literature ^{1}H-NMR (D_2O): δ 5.98, 5.89 (dd), 4.57 (s), 4.15 (s), 2.61 (septet), 2.05 (s), 1.22 (d). ^{31}P NMR

(D_2O): δ -33.39.[22] ESI-MS (MeOH): *m/z* = 504 $[M+Na]^+$; 984 $[2M+Na]^+$. Literature ESI-MS (H_2O): *m/z* = 504 $[M+Na]^+$; 984 $[2M+Na]^+$.[22] UV in MeOH λ_{max}, nm (ε, M^{-1} cm^{-1}): 305 (2.7 x 10^3). Literature UV in NaCl λ_{max}, nm: 303.[22] Anal. Found (calculated) for $C_{18}H_{26}N_3O_4PRu$: C, 44.24 (44.17); H, 5.50 (5.45); N, 8.86 (8.75).

2.3.5 Synthesis of [$RuCl_2$(η^6-*p*-cymene)(mimid)] (6)

This compound was synthesized according to literature procedures.[24] *N*-methylimidazole is hygroscopic and has to be added into the air-free system with a syringe to prevent as much moisture as possible.

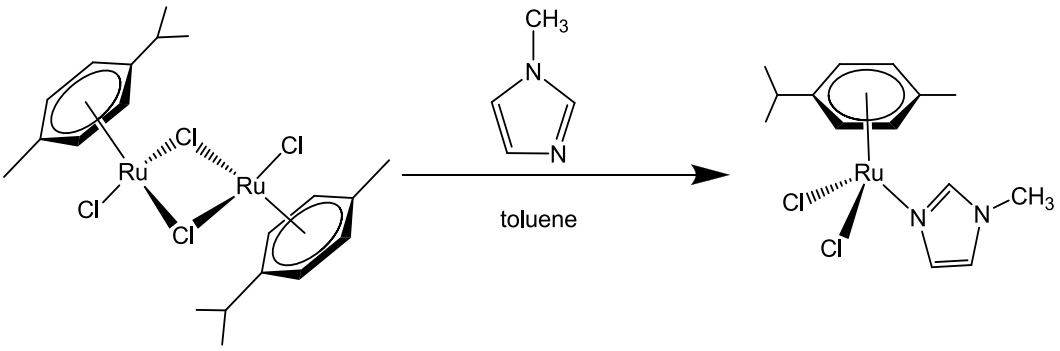

[Ru(η^6-*p*-cymene)Cl_2]$_2$ (0.20 g, 0.33 mmol) was suspended in freshly distilled toluene (30 mL). *N*-methylimidazole (52 µL, 0.66 mmol) was added at room temperature. The resulting mixture was heated to reflux for 3 hr and a precipitate formed within an hour of vigorous stirring. After cooling down, the reddish brown precipitate formed was filtered, washed with diethyl ether (4 x 10 mL) and dried under vacuo (yield: 0.17g, 67 %). 300 MHz ^{1}H NMR ($CDCl_3$): δ 7.87 (s, 1H), 7.30 (s, 1H), 5.45, 5.26 (dd, 4H, *J* = 6 Hz), 3.65 (s, 3H), 2.99 (septet, $CHCH_3$), 2.19 (s, 3H), 1.27 (d, 6H, *J* = 7 Hz). Literature ^{1}H NMR ($CDCl_3$): δ 7.87 (s), 7.30 (s), 5.44, 5.25 (dd), 3.65 (s), 2.99 (septet), 2.19 (s), 1.28 (d).[24] ESI-MS

(CH_3CN): *m/z* = 353 [Ru(cymene)Cl(mimid)]$^+$, 312 [Ru(cymene)Cl(CH_3CN)]$^+$, 271 [Ru(cymene)Cl]$^+$. Literature ESI-MS (CH_3CN): *m/z* = 353 [Ru(cymene)Cl(mimid)]$^+$, 311.9 [Ru(cymene)Cl(CH_3CN)]$^+$.[24] UV in MeOH λ_{max}, nm (ε, M^{-1} cm^{-1}): 327 (1.25 x 10^3), 409 (8.6 x 10^2). Literature UV in MeOH $\lambda_{max,}$ nm: 330, 407.[25] Anal. Found (calculated) for $C_{14}H_{20}Cl_2N_2Ru$: C, 43.35 (43.29); H, 5.17 (5.19); N, 7.50 (7.22).

2.3.6 Synthesis of $[Ru_2(\eta^6\text{-}p\text{-cymene})_2(OH)_3]BPh_4.3H_2O$ (7)

This synthetic procedure was modified from that in the literature.[26, 27]

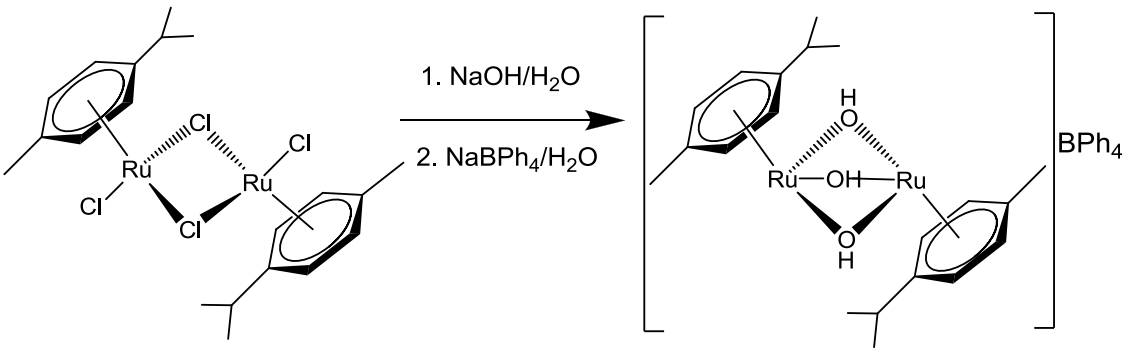

A solution of $[Ru(\eta^6\text{-}p\text{-cymene})Cl_2]_2$ (0.25 g, 0.4 mmol) was dissolved in deionised water (20 mL) with NaOH (0.15 g, 4.0 mmol). The solution was stirred and warmed up to 60°C for 2 hr. The pale yellow solution was filtered to remove black impurities formed at the bottom of the flask then the filtrate was concentrated to 10 mL. $NaBPh_4$ (0.20 g, 0.60 mmol) in water (5 mL) was added, which resulted in a gummy precipitate. The solution was stirred vigorously for another 6 hr at 56 °C to give a chunky powdery yellow precipitate, which was filtered, washed with water and hexane and then dried under vacuo. The compound was recrystallised with acetone to yield the tri-hydroxido species

(yield: 0.27 g, 79 %). Selected IR: *v*(OH) 3560 cm^{-1}. Literature: *v*(OH) 3550 cm^{-1}.[26] 300 MHz $^{13}C\{^1H\}$ NMR ($CDCl_3$): δ 122-136 (BPh_4^-), 96.7 (Ar), 93.3 (Ar), 77.4 (Ar), 74.9 (Ar), 31.1 (CH), 22.6 ($2CH_3$), 18.2 (CH_3). Literature $^{13}C\{^1H\}$ NMR ($CDCl_3$): δ 121-136 (BPh_4^-), 96.4 (Ar), 93.0 (Ar), 77.4 (Ar), 74.8 (Ar), 31.1 (CH), 22.4 ($2CH_3$), 17.9 (CH_3).[26] ESI-MS (MeOH): *m/z* = 564 $[M+CMe_2]^+$, 551 $[M+CMe]^+$ 520 $[M]^+$. UV in MeOH λ_{max}, nm (ε, M^{-1} cm^{-1}): 314 (8.3 x 10^2), 400 (4.4 x 10^2). Anal. Found (calculated) for $C_{47}H_{57}O_4BRu_2$: C, 62.60 (62.79); H, 6.30 (6.39).

2.3.7 Synthesis of $[Ru(\eta^6\text{-}p\text{-cymene})(tsal)]_2$ (8)

This compound was synthesized according to literature procedures.[28] Note that the thiosalicylic acid is extremely pungent and the reaction has to be conducted in a fume hood. All used glassware has to be rinsed well in a base bath.

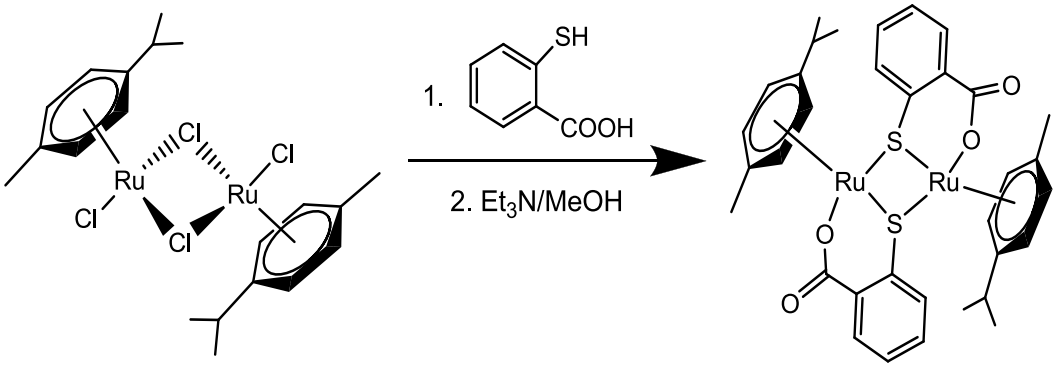

$[Ru(\eta^6\text{-}p\text{-cymene})Cl_2]_2$ (0.18 g, 0.20 mmol) and thiosalicylic acid (0.62 mg, 0.40 mmol) were suspended in freshly distilled MeOH (10 mL), then triethylamine (Et_3N) (0.11 mL, 0.80 mmol) was added and the mixture was refluxed for 30 min. Deionised water (50 mL) was added to the orange-red solution and the mixture was cooled to room temperature and an orange precipitate formed almost immediately. The flask was

purged with N_2, sealed, and placed in the refrigerator (~4 °C) for more crystals to form. The orange powder formed was washed with water and 1-hexane then dried under vacuum (0.07 g, 45 %). ^{1}H NMR ($CDCl_3$): δ 8.10 (d, 1H, *J* = 7 Hz), 7.64 (d, 1H, *J* = 7 Hz), 7.33 (t, 1H, *J* = 7 Hz), 7.25 (t, 1H, *J* = 7 Hz), 5.07 (d, 1H, *J* = 6 Hz), 4.75 (d, AB pattern, 1H, *J* = 6 Hz), 4.70 (d, 1H, *J* = 6 Hz), 2.54 (septet, $CHCH_3$), 1.80 (s, 3H), 1.12 (d, 3H, *J* = 7 Hz), 0.82 (d, 3H, *J* = 7 Hz). Literature ^{1}H NMR ($CDCl_3$): δ 8.08 (d), 7.62 (d), 7.31 (t), 7.23 (t), 5.04 (d), 4.73 (d), 4.71 (d), 2.51 (septet), 1.79 (s), 1.10 (d), 0.81 (d).[28] ESI-MS (MeOH): *m/z* = 777 $[2M+ H]^+$. Literature ESI-MS (MeCN): m/z 777 $[2M+H]^+$.[28] UV in MeOH λ_{max}, nm (ε, M^{-1} cm^{-1}): 277 (2.3 x 10^3), 362 (7.7 x 10^2). Anal. Found (calculated) for $C_{34}H_{36}O_4S_2Ru_2$: C, 52.40 (52.72); H, 4.65 (4.71).

2.3.8 Synthesis of [Ru(η^6-*p*-cymene)(en)(S-Ph)]PF_6 (9)

This new complex was synthesed by a procedure that was modified from a general method in literature.[29]

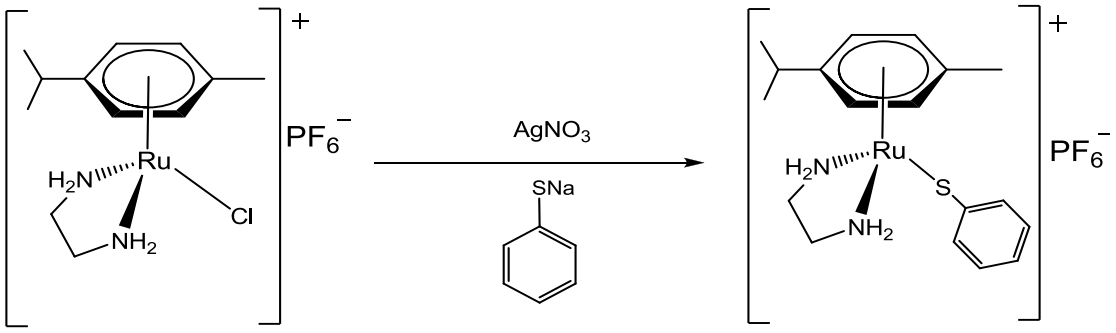

[Ru(η^6-p-cymene)(en)Cl]PF_6 (0.20 g, 0.43 mmol) was stirred with $AgNO_3$ (0.07 g 0.43 mmol) in 1:1 MeOH and H_2O (40 mL) for 20 hr. Then AgCl was filtered off with celite, the solution was rotary-evaporated to dryness, then the solid was redissolved in MeOH. The solution was filtered then sodium thiophenolate (0.06 g, 0.48 mmol) was added and the mixture was stirred for a further 15 hr. After that, an excess of KPF_6 (0.39 g, 2.14 mmol) was added, the orange solution was stirred for 1 hr, purged with N_2 then left in a refrigerator (~4 °C) for 8 hr. The first lot of pale yellow precipitate, which mainly consisted of KCl was discarded, then the solution was concentrated down to ~5 mL. It was cooled at 4 °C again to yield tiny yellow crystals (yield: 0.07 g, 21 %). 300 MHz ^{1}H NMR (MeOD-d_4): δ 7.49 (d, 2H, *J* = 7.5 Hz), 7.18 (t, 2H, *J* = 6.5 Hz), 7.13 (t, 1H, *J* = 6.7 Hz), 5.68 (b, 2H), 5.28 (d, 2H, *J* = 6 Hz), 5.19 (d, 2H, *J* = 6 Hz), 3.75 (b, 2H), 2.75 (septet, 1H), 2.51 (m, 2H), 2.19 (s, 3H), 1.22 (d, 6H, *J* = 6.9 Hz). ESI-MS (MeOH): *m/z* = 295 [(η^6-$C_{10}H_{14}$)Ru(en)]$^+$, 405 [(η^6-$C_{10}H_{14}$)Ru(en)(S-Ph)]$^+$. UV in MeOH λ_{max}, nm (ε, M^{-1} cm^{-1}): 269 (8.6 x 10^2), 314 (4.5 x 10^2). Anal. found for $C_{18}H_{27}N_2SPF_6Ru$: C, 39.23 (39.34); H, 4.45 (4.50); N, 5.27 (5.20).

2.3.8.1 Other synthetic procedures for the benzenethiolato complex

The benzenethiolato ligand was found to have a high affinity to Ru, and was more likely to form dimers and trimers; possibly replacing the en ligand either during the reaction or after recrystallization. Therefore, it had to be deprotonated and it was equally important to ensure complete removal of the Cl^- ligands in the starting

compound before continuing the reaction. Stirring **3** with $AgNO_3$ for > 20 h was found to be the optimum time for chloride removal. As the thiol is hygroscopic, all water and moisture had to be removed from the reaction vessel after removal of AgCl. The addition of NH_4PF_6 for the counter anion as mentioned in the literature,[29] did not result in a pure compound, probably because NH_4^+ reprotonated the thiophenolate. Thus, $NaPF_6$ or KPF_6 were more appropriate for this synthesis.

2.4 UV-Vis Kinetics Studies on Ru (II) complexes

UV-Vis electronic absorption spectroscopy was carried out for compounds **2-6** to investigate their aquation/decomposition rate in biological media (DMEM and HBS). Stock solutions (50 mM) were prepared by dissolving these complexes in a small amount of DMF or DMF/H_2O before pipetting the solutions into the respective biological solutions (final concentration of 1.0 mM) prior to measurements. Measurements were performed in 1-cm path-length quartz cells. All reactions were performed at 37 °C. The background measurements were taken for solutions that contained all components accept Ru compounds. Global kinetic analysis of time-dependent UV-Vis spectra (range: 300-800 nm; resolution: 2 nm) was performed with Pro-Kineticist software,[5] as described previously.[30] Application of singular value decomposition (SVD) procedure to the absorbance-wavelength-time data matrices led to separation of significant spectral changes from the noise and allowed a prediction of the numbers of independent absorbing species in the reaction mixture.[30] On the basis of these observations, the

simplest kinetic models (typically one or two sequential pseudo-first reactions) were proposed.[30] These models were then fitted to the matrices of experimental data using the Marquart-Levenberg non-linear least-squares fitting algorithm.[5] This procedure provided the optimal values of rate constants, as well as the estimated spectra of the initial, intermediate and final absorbing species.[5] This information was used to predict the nature of chemical changes in Ru(II) complexes during the interactions with biological media.[30]

2.5 XAFS sample preparation

2.5.1 Incubation in biological media

Stock solutions (60 mM) of each compound were prepared immediately before use according to previous published methods;[31] 5.0 µL was pipetted into 0.5 mL of biological media (HBS, DMEM or serum). All reaction mixtures were incubated at 37°C. For reactions with bovine serum albumin (BSA), 1.0 mL of each of the samples were prepared in HBS, after incubating for the respective times, a 100 µL aliquot of the sample was filtered through Bio-Gel P-30 spin columns (molecular mass cut-off at 30 kDa) and centrifuged for 2 min to remove unbound Ru. The purified samples were then freeze-dried to stop the reaction, concentrate the Ru content, and to reduce photoreduction during XAS experiments.[32]

2.5.2 Reactions with HEPG2 cells

HEPG2 human liver carcinoma cells[1] were grown for 1 week prior to their incubation with test compounds. The Ru compounds (0.60 mM) were used to treat the cells for 4 hr, using an incubation temperature of 37°C. The medium was then removed and the cell monolayers were washed three times with 0.5 mL of phosphate-buffered saline (PBS). The cells were then scraped off into PBS (~ 0.5 mL) on ice and centrifuged for 2 min. The pellets formed were suspended in fresh PBS. The solution (cells + buffer) was collected then freeze-dried. The cell medium was also kept for analysis to observe possible changes in the spectra.

2.5.3 Reactions with DNA

These samples were prepared by Dr. Aviva Levina. DNA sodium salt from salmon sperm (DNA-Na) was prepared in HBS (~pH 7.1) then RAPTA-C (0.60 mM) was added to different concentrations of DNA-Na; 10.0, 5.0 and 2.5 mg/mL. The samples were kept at room temperature in the dark for ~15 hr then freeze-dried.

2.5.4 Reactions with Rat blood

These samples were prepared by Dr. Aviva Levina and Dr. Tony Bonin. RAPTA-C (0.50 mM) was added into rat blood, centrifuged then separated into the red blood cell (RBC) and plasma fraction. These fractions were incubated for 1 or 6 hr at 37°C then

freeze-dried. For isolated reactions, the plasma fraction was first separated from the blood before reacting with Ru.

2.5.5 Gel electrophoresis

The Ru samples and NuPAGE LDS sample buffer (4x) were loaded onto a NuPAGE 12% Bis-Tris gel (1.0 x 15 well). The chamber was filled with MES running buffer (10x) (80 mL) and deionized water (720 mL). Electrophoresis was then run at 200 V, 200 mA for 40 min until completion. The membrane transfer buffer was the Bicine transfer buffer (100 mL), MeOH (100 mL) and deionized water (800 mL), in which 600 mL of this buffer was used to soak blotting pads before use. The pads were properly squeezed and soaked to remove any air bubbles. The membrane, an Invitrolon PVDF Filter Paper Sandwich (0.45 µm pore size) was soaked in MeOH for 30 s, then water and buffer before use. Filter paper was soaked in buffer then placed carefully on the gel, using the body of a glass pipette to gently roll over the surface. After that, the membrane was removed, rinsed with water, stained with Ponceau S solution for ~10 min to determine the molecular weights of the proteins, and left to dry for ~2 hr before inserting in sample bags for XAS.

2.6 References

1. HepG2 human hepatocellular carcinoma cell line (ATCC Number: HB-8065).
2. *TopSpin ver. 3.0 for Windows 7*, Bruker BioSpin: Rheinstetten, Germany, 2007.
3. Marat, K. *Spinworks, 3.1.3*, University of Manitoba, Winnipeg, 2010.
4. *Origin*, 6.1; Origin Lab Corporation: Northhampton, MA, USA, 1991-1999.

5. King, P. J. M., M. *Pro-Kineticist*, 1; Applied Photophysics Ltd.: Leatherhead, U.K., 1996.

6. Levina, A.; Aitken, J. B.; Gwee, Y. Y.; Lim, Z. J.; Liu, M.; Singharay, A. M.; Wong, P. F.; Lay, P. A., *Chem.-Eur. J.* **2013,** *19*, 3609-3619.

7. Cetinbas, N.; Webb, M. I.; Dubland, J. A.; Walsby, C. J.*, J. Biol. Inorg. Chem.* **2010,** *15*, 131-145.

8. *XFIT for Windows, version 1.1*, Australian Synchrotron Research Program: Sydney, Australia, 1996.

9. Levina, A.; Harris, H. H.; Lay, P. A., *J. Am. Chem. Soc.* **2007,** *129*, 1065-1075.

10. Ellis, P. J.; Freeman, H. C., *J. Synchrotron Radiat.* **1995,** *2*, 190-195.

11. Mustre de Leon, J.; Rehr, J. J.; Zabinsky, S. I.; Albers, R. C., *Phys. Rev. B: Condens. Matter* **1991,** *44*, 4146-4156.

12. Levina, A.; Armstrong, R. S.; Lay, P. A., *Coord. Chem. Rev.* **2005,** *249*, 141-160.

13. Sayers, D. E.; Stern, E. A.; Lytle, F., *Phys. Rev. Lett.* **1971,** *27*, 1204-1207.

14. Gurman, S. J., *J. Synchrotron Radiat.* **1995,** *2*, 56-63.

15. Penner-Hahn, J. E., *Coord. Chem. Rev.* **1999,** *190-192*, 1101-1123.

16. Finney, L.; Chishti, Y.; Khare, T.; Giometti, C.; Levina, A.; Lay, P. A.; Vogt, S., *ACS Chem. Biol.* **2010,** *5*, 577-587.

17. Allardyce, C. S.; Dyson, P. J.; Ellis, D. J.; Heath, S. L., *Chem. Commun.* **2001**, 1396-1397.

18. Scolaro, C.; Bergamo, A.; Brescacin, L.; Delfino, R.; Cocchietto, M.; Laurenczy, G.; Geldbach, T. J.; Sava, G.; Dyson, P. J., *J. Med. Chem.* **2005,** *48*, 4161-4171.

19. Morris, R. E.; Aird, R. E.; Murdoch, P. d. S.; Chen, H.; Cummings, J.; Hughes, N. D.; Parsons, S.; Parkin, A.; Boyd, G.; Jodrell, D. I.; Sadler, P. J., *J. Med. Chem.* **2001,** *44*, 3616-3621.

20. Wang, F.; Chen, H.; Parsons, S.; Oswald, I. D. H.; Davidson, J. E.; Sadler, P. J., *Chem. Eur. J.* **2003,** *9*, 5810-5820.

21. Habtemariam, A.; Melchart, M.; Fernandez, R.; Parsons, S.; Oswald, I. D. H.; Parkin, A.; Fabbiani, F. P. A.; Davidson, J. E.; Dawson, A.; Aird, R. E.; Jodrell, D. I.; Sadler, P. J., *J. Med. Chem.* **2006,** *49*, 6858-6868.

22. Ang , W. H.; Daldini, E.; Scolaro, C.; Scopelliti, R.; Juillerat-Jeannerat, L.; Dyson , P. J., *Inorg. Chem.* **2006,** *45*, 9006-9013.

23. Leiga, A. G., *J. Phys. Chem.* **1966,** *70*, 3254-3259.

24. Vock, C. A.; Scolaro, C.; Phillips, A. D.; Scopelliti, R.; Sava, G.; Dyson, P. J., *J. Med. Chem.* **2006,** *49*, 5552-5561.

25. Singh, S. K.; Trivedi, M.; Chandra, M.; Sahay, A. N.; Pandey, D. S., *Inorg. Chem.* **2004,** *43*, 8600-8608.

26. Arthur, T.; Robertson, D. R.; Tocher, D. A.; Stephenson, T. A., *J. Organomet. Chem.* **1981,** *208*, 389-400.

27. Kang, J. W.; Maitlis, P. M., *J. Organomet. Chem.* **1971,** *30*, 127-133.

28. Henderson, W.; Nicholson, B. K.; Oliver, A. G.; Rickard, C. E. F., *J. Organomet. Chem.* **2001,** *625*, 40-46.

29. Wang, F.; Habtemariam, A.; van der Geer, E. P. L.; Fernandez, R.; Melchart, M.; Deeth, R. J.; Aird, R.; Guichard, S.; Fabbiani, F. P. A.; Lozano-Casal, P.; Oswald, I. D. H.; Jodrell, D. I.; Parsons, S.; Sadler, P. J., *Proc. Natl. Acad. Sci. U. S. A.* **2005,** *102*, 18269-18274.

30. Lay, P. A.; Levina, A., *Inorg. Chem.* **1996,** *35*, 7709-7717.

31. Liu, M.; Lim, Z. J.; Gwee, Y. Y.; Levina, A.; Lay, P. A., *Angew. Chem., Int. Ed.* **2010,** *49*, 1661-1664.

32. George, G. N.; Pickering, I. J.; Pushie, M. J.; Nienaber, K.; Hackett, M. J.; Ascone, I.; Hedman, B.; Hodgson, K. O.; Aitken, J. B.; Levina, A.; Glover, C.; Lay, P. A., *J. Synchrotron Radiat.* **2012,** *19*, 875-886.

Chapter Three

X-ray Absorption Spectroscopy (XAS)

3.1 Introduction and general theory

The XAS technique was used to characterise the structure of new complexes and to investigate the biological activities of ruthenium complexes. Conventional X-ray crystallography is still mainly used for structure determination, but there are limitations as it is not always easy to obtain diffraction quality crystals and is not appropriate if the metal of interest is in solution. Using XAS, the local atomic environment of the metal can be determined by analysing the extended X-ray absorption fine structure (EXAFS) oscillations.[1-4]

XAS occurs when incoming X-rays are absorbed by core electrons, causing photo-excitation thus ejecting the core electrons into a higher unoccupied orbital or the continuum **(Figure 3.1)**. The promotion of core electrons generates an intense absorption that is known as an "edge". Relaxation can then happen by Auger electron emission and/or X-ray fluorescence, but the latter dominates at high energies, such as the Ru K-edge.[5] The energy of this absorption edge is specific for a specific element.[6] The shape and position of the edge also gives information about the oxidation state, the geometry, the coordination number and the donor ligands.[7] XAS can be divided into X-ray absorption near-edge structure (XANES), which is in the vicinity, ~50 eV from the edge and X-ray absorption fine structure (EXAFS), ~ 40-1000 eV above the edge **(Figure 3.2).**[8] The oscillatory pattern observed in EXAFS is due to constructive and destructive interferences with outgoing electron waves originating and propagating away from its absorber, and the backscattered wave from neighbouring atoms (scatterers).[6]

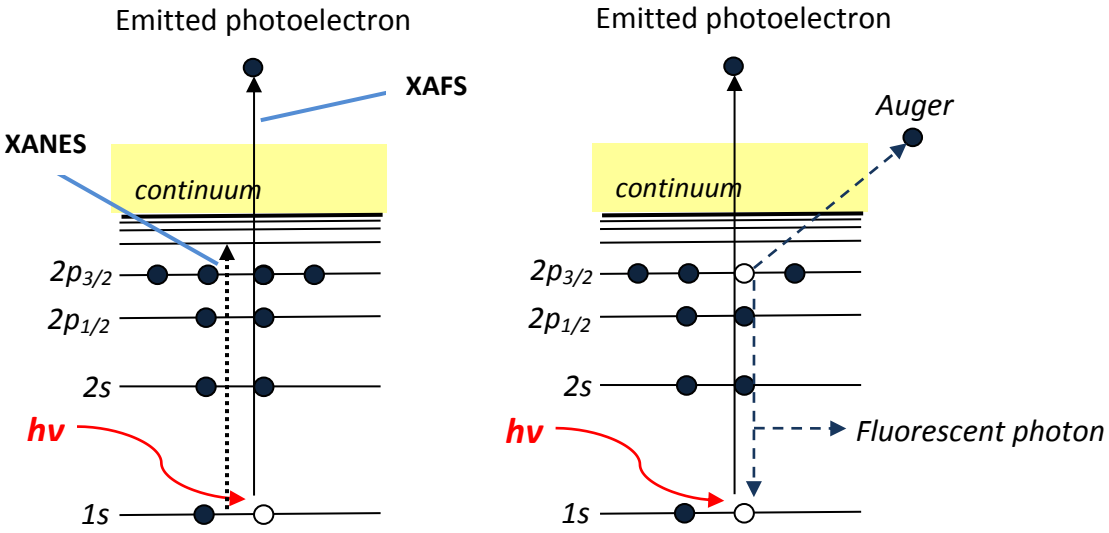

Figure 3.1: Schematic illustration of the XAS theory.[9]

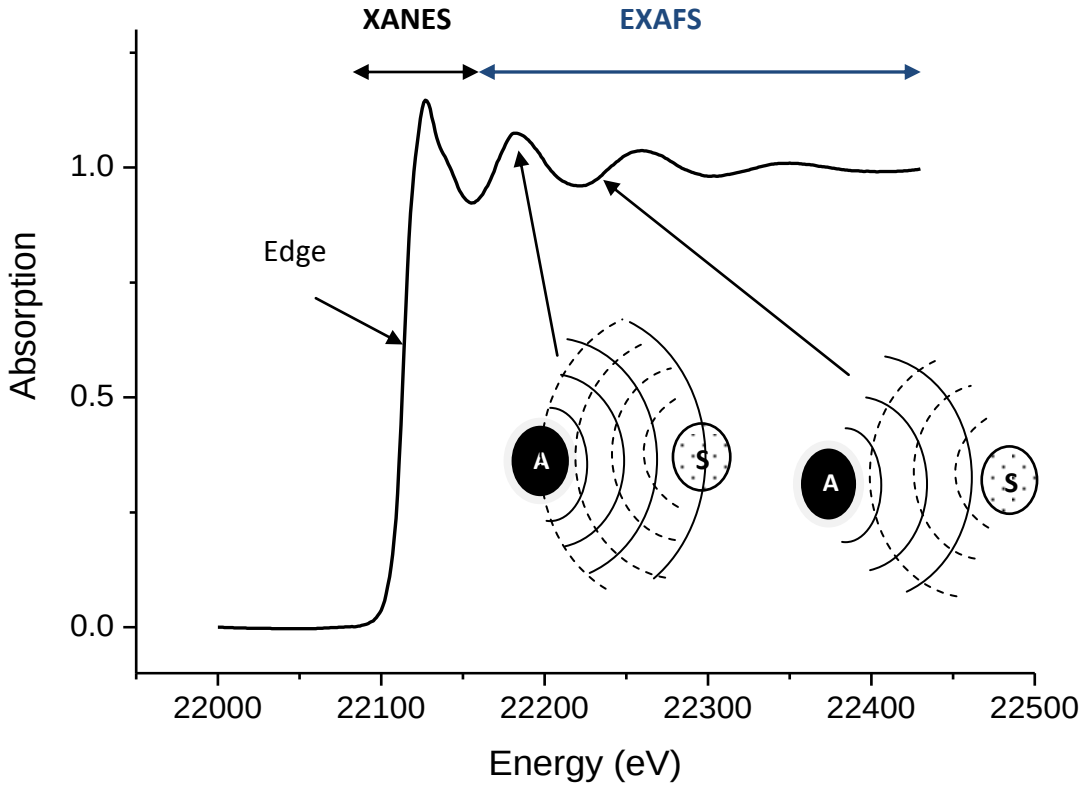

Figure 3.2: Normalized XANES and EXAFS absorption spectrum of the Ru K-edge (~0.5 % solid mixtures of Ru w/w with BN). Constructive and destructive interference of the photoelectron waves are depicted within the spectrum in which **A** and **S** refer to the absorber and scatterer respectively.[6, 10]

3.1.1 XANES

X-ray absorption near-edge structure (XANES) is a type of X-ray spectroscopy in which the promotion of a core electron to an unoccupied orbital forms a steep edge due to intense absorption by allowed electronic transitions. These electrons are usually from the K shell (principal quantum number, *n* = 1) to unoccupied p-orbitals, or from the L (n = 2) or M (n = 3) for heavier elements.[10] The low photoelectron energy region has a large electron-scattering factor due to the long elastic mean free path, thus multiple scattering becomes an important aspect to consider.[11]

3.1.2 EXAFS

Extended X-ray absorption fine structure (EXAFS) is the region after the edge in which the oscillations are extended for 1000 eV or more from the edge. It is used for quantitative analysis to determine the bond lengths and coordination environment of the absorbing atom and scatterers and the angular arrangement of ligands around the absorber when multiple- scattering is incorporated.[5, 6, 12]

EXAFS, $\chi(k)$ is defined as the fractional modulation of the absorption coefficient, which includes both the total amplitude function and total phase function, thus giving rise to a general equation**:** [6]

$$\chi(k) = \sum_s \frac{N_s A_s(k) S_0^2}{kR_{as}^2} \exp(-2k^2\sigma_{as}^2) \times \exp\left(-\frac{2R_{as}}{\lambda(k)}\right) \sin\left(2kR_{as} + \phi_{as}(k)\right) \quad \textbf{(1)}$$

where k is the photoelectron wavevector, R_{as} is the absorber-scatterer distance, N_s is the number of scattering atoms, A_s is the backscattering amplitude, S_0^2 is the amplitude reduction factor, $\lambda(k)$ is the mean free path of the photoelectron, σ^2 is the mean-square deviation in R_{as} which the Debye-Waller factor depends on and ϕ_{as} is the total phase shift that the photoelectron undergoes during the scattering process.[6, 8, 11]

The equation above **(1)** only assumes single scattering (the excited photoelectron travelling from the absorber to the scatterer and back) and breaks down at the low-k region (k < 3 Å^{-1}), which is the low energy range of the photoelectron.[6] This makes multiple-scattering theory important as shown, for instance, in **Figure 3.3**, which contributes to the observed EXAFS signal.[6]

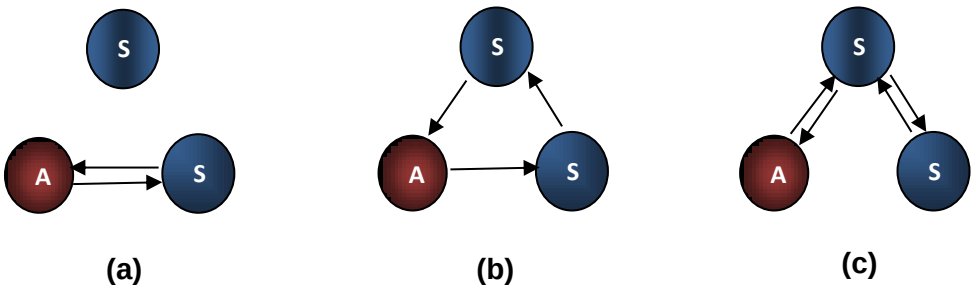

Figure 3.3: Illustration of possible scattering pathways for a three-body system with **A** being the absorber and **S** being the neighboring scatterers: **a)** Single-scattering, **b)** and **c)** being two of the possible multiple-scattering pathways.

Multiple-scattering is highly dependent on the scattering angle that determines the intensity. Angles less than 150° generally have weak MS effects but angles between

150° and 180° have more significant MS, which may make major contributions to the measured EXAFS.[12-14] For biological systems, linear arrangements such as in binding of C=O and rigid ligands such as porphyrins and imidazoles, have some of the most prominent MS effects.[12,15-17] In general, this aspect is useful for finding out the bond angles and lengths as some of the coordinating groups demonstrate unique signals due to amplitude enhancement.[6]

3.1.3 Sample preparation and experimentation

The field of XAS has blossomed ever since intense synchrotron radiation became readily accessible. For the research reported herein, electrons are accelerated by the bending magnets or wigglers in the storage ring producing broad energies of photons.[10] The experimental apparatus was set up as shown in **Figure 3.4**. The incident and transmitted beams are measured by ionization chambers (I_0, I_1, I_2) in which I_0 normalizes the output of the incident beam and I_1 and I_2 are used to measure the x-ray absorption spectrum of the standard in order to calibrate the incident beam, which varies over time due to change in the temperature of the monochromator and other factors.[10] The sample holder was placed at an angle ~45° to I_0 and a Ge fluorescence detector. This detector (that contained 34 live channels at ANBF) was moved as close as possible to the sample in order to capture the largest solid angle, which provided the highest signal-to-noise for the fluorescent x-rays coming from the sample.[10] However, care needed to be taken not to bring the detector too close to the sample as this would occlude detector

channels. A thin ruthenium foil with a known absorption edge (~22,100 eV) was placed between I_1 and I_2. The readings for each scan are then collected digitally.[5,10]

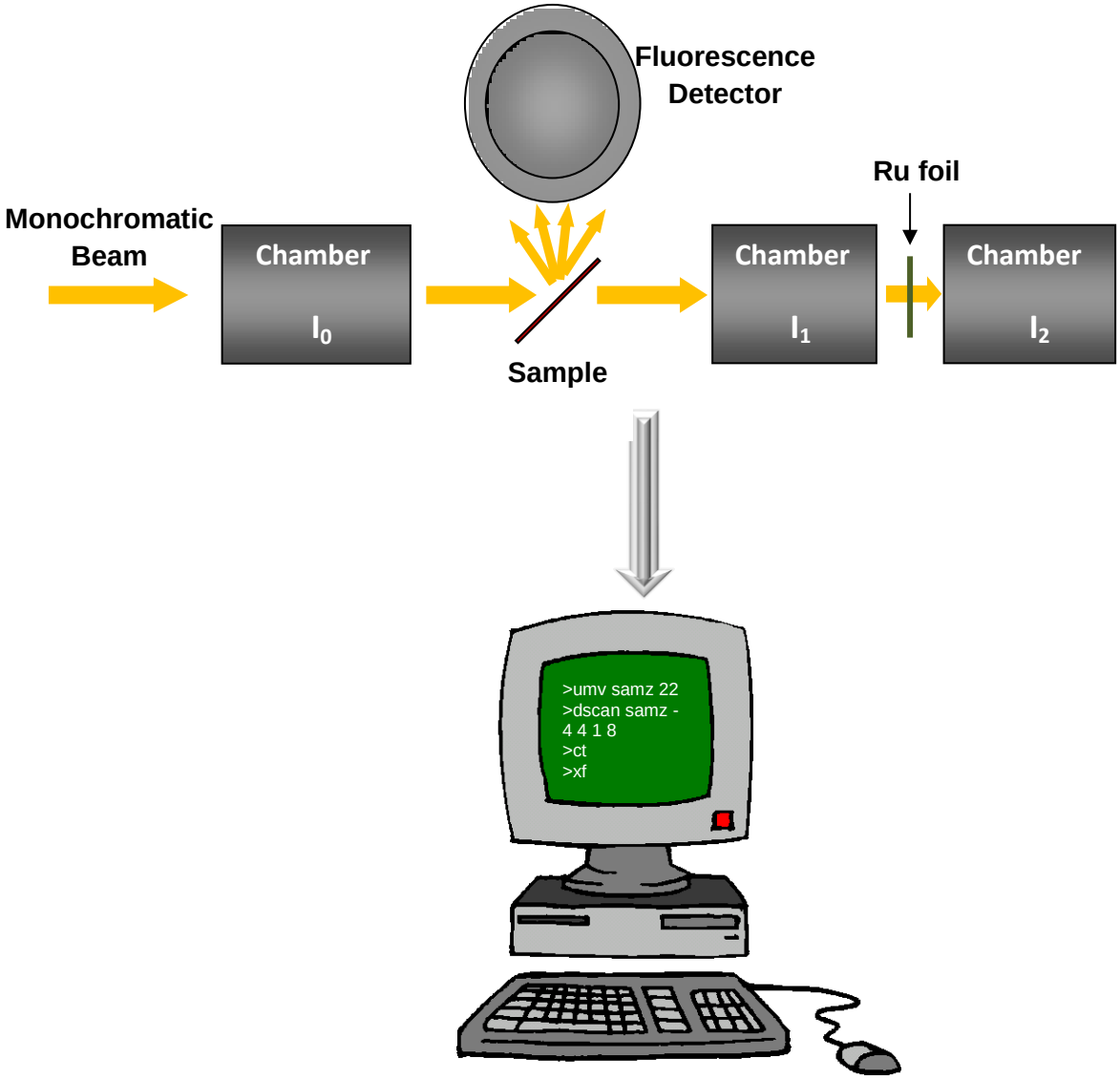

Figure 3.4: Illustration of the apparatus used for XAS experiments (not to scale). Arrows shows the direction of the X-ray beam.

The fluorescent detection mode is much more sensitive than the absorption mode, which is why x-ray fluorescence is preferred for biological samples.[12] Ruthenium samples were cooled in liquid nitrogen prior to experiments before moving the sample

into a cryostat, which was maintained at a temperature < 20 K by closed-cycle liquid He circulation for XAS measurements.[5] This helped retain sample stability, reduced beam heating effects, minimized photoreduction and increased EXAFS intensities by minimizing Debye-Waller factors.[10] Before running the experiments, traces of air were eliminated from the sample chamber with He/vacuum cycles and the sample was kept under vacuum in a He atmosphere to avoid water condensation problems.[10]

3.2 Building the XAS Library for Linear Regression XAS Analysis

As mentioned above, the XANES spectra of the element of interest within biological samples can serve as a fingerprint to identify the possible products formed in reactions. Using a representative library of XAS of known model complexes containing the biologically relevant donor groups, spectral comparisons can thus be made using multiple linear regressions.[5, 10, 18-20]

The ruthenium arene complexes used in this study are illustrated in **Figure 3.5**: $[Ru(\eta^6\text{-}p\text{-cymene})Cl_2]_2$ **(1)**, RAPTA-C **(2)**, $[Ru(\eta^6\text{-}p\text{-cymene})(en)Cl]PF_6$ **(3)**, $[Ru(\eta^6\text{-}p\text{-cymene})(acac)Cl]$ **(4)**, OxaloRAPTA-C **(5)**, $[Ru(\eta^6\text{-}p\text{-cymene})Cl_2(mimid)]$ **(6)**, $[Ru_2(\eta^6\text{-}p\text{-cymene})_2(\mu\text{-}OH)_3]BPh_4$ **(7)**, $[Ru(\eta^6\text{-}p\text{-cymene})(tsal)]_2$ **(8)**, $[Ru(\eta^6\text{-}p\text{-cymene})(en)(S\text{-}Ph)]PF_6$ **(9)**.

The choice of complexes, apart from the drugs being investigated, is dictated by the following. Imidazole is known to be a common binding site for serum proteins to Ru complexes,[21, 22] the presence of tris-hydroxo ligands are thought to be the end product for compounds undergoing aquation and hydrolysis in aqueous media.[23] Ru(II)

complexes also bind avidly and strongly to S-donor (thiol) ligands in biomolecules forming S-bound adducts which might then form S-bridged dimers.[24, 25] In addition, Ru(II) may also bind to other *N*/O-donor ligands in other ligand-exchange reactions with biomolecules, as was observed with Ru(III) complexes.[20, 26] A general comparison of the EXAFS and FT EXAFS spectra obtained for each compound is shown in **Figure 3.6**.

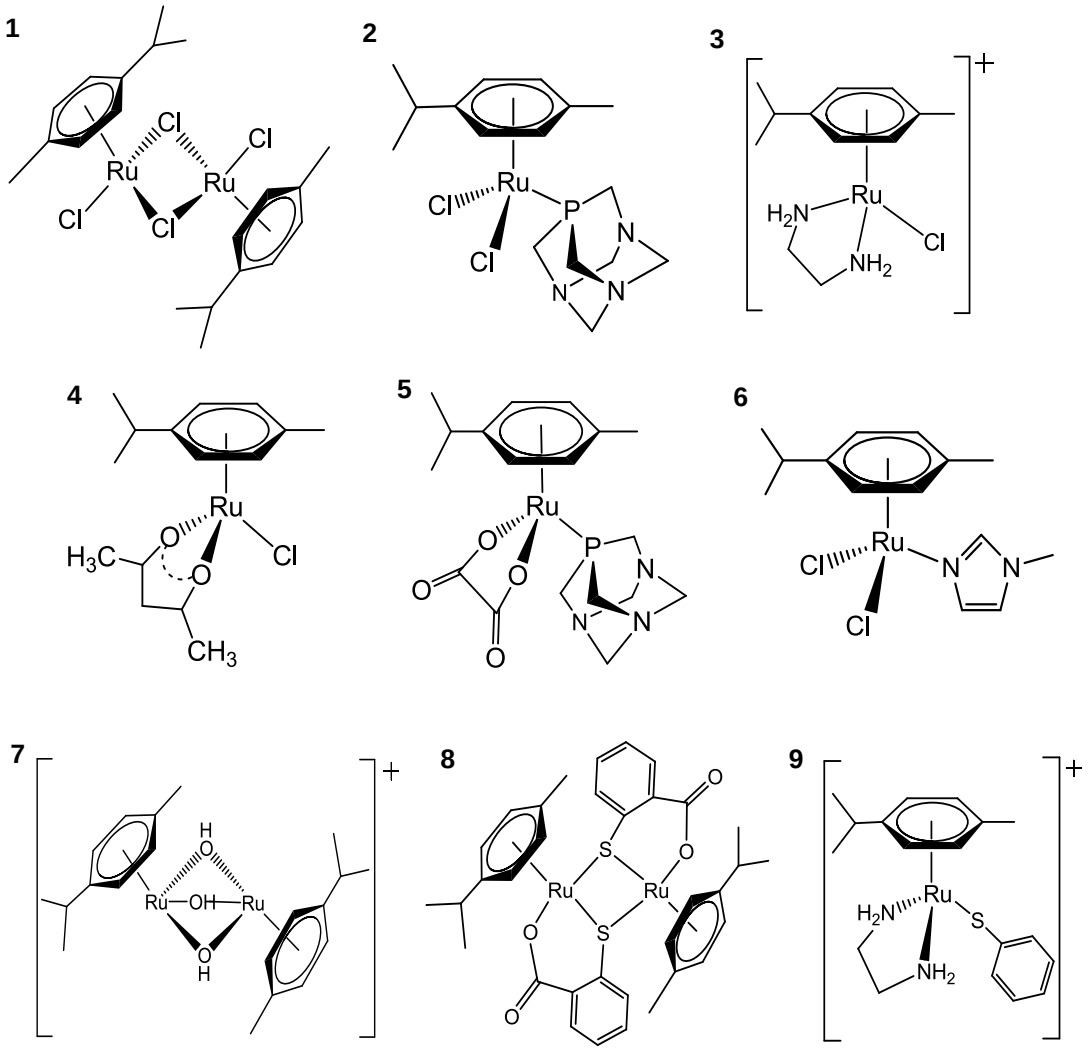

Figure 3.5: Library of Ru(II) arene model complexes that were used for multiple linear regression and their structures determined by multiple-scattering analysis of EXAFS data. Synthesis procedures are described in detail in Chapter 2.

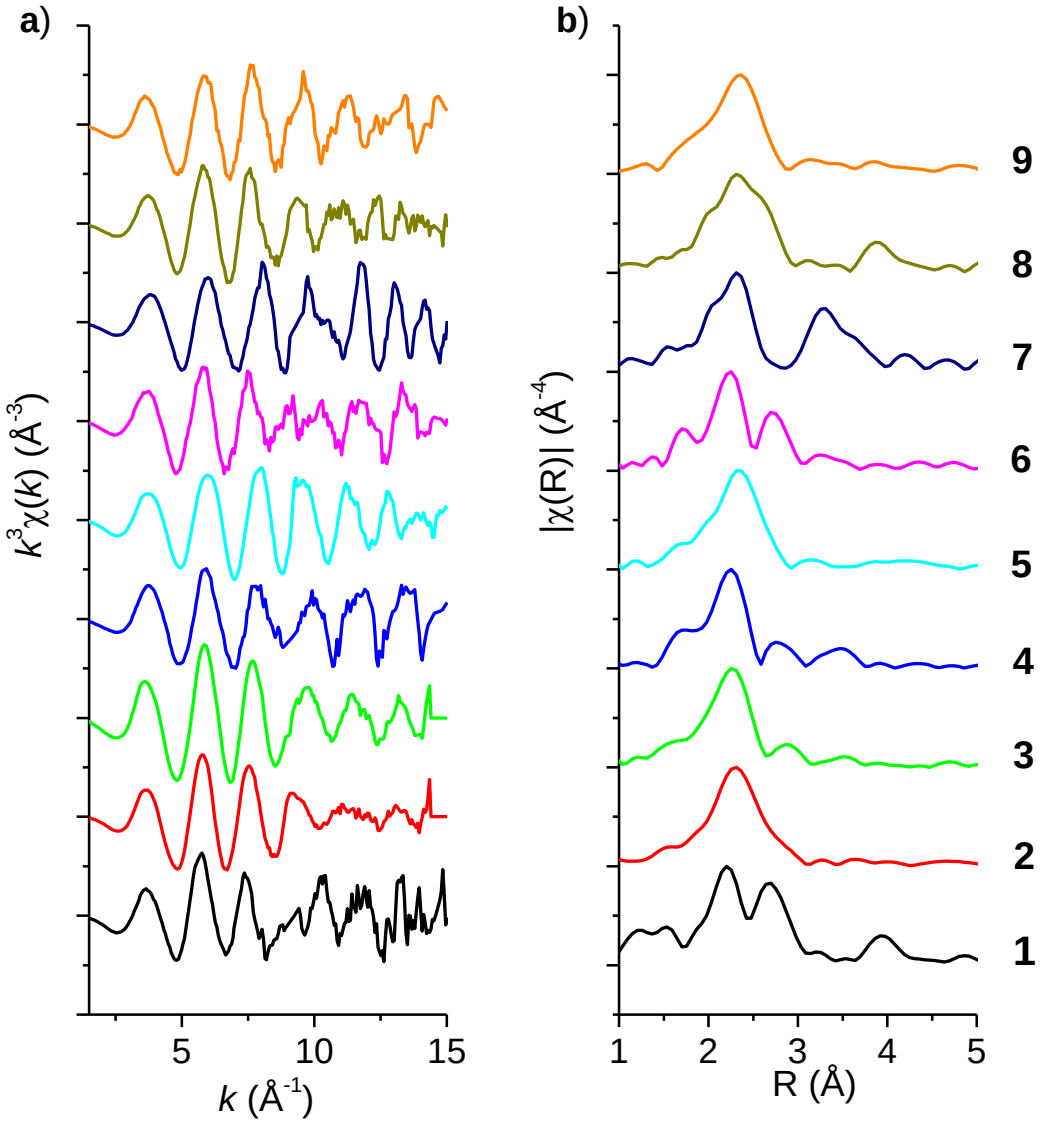

Figure 3.6: Comparison of: **a)** k^3-weighted EXAFS; and **b)** FT EXAFS spectra of the nine model Ru(II) arene compounds. All samples were prepared by mixing the solid compounds with BN (~1:10 ratio) and were ran at low temperature (10-15 K) in fluorescence detection mode to compare with biological samples. Spectra for models **2** and **3** were only taken up to the *k* range of 13 Å due to the high noise levels.

3.3 Multiple-Scattering EXAFS Analysis of the Structures of Model Ru(II) Complexes

First of all multiple-scattering analysis was performed on the EXAFS from crystallographically characterized complexes **2-8** to test the accuracy of the modeling to be applied to unknown structures. Complexes **7** and **9** were not characterized and other structurally similar complexes were used as references to build the models. The structures, atom-numberings, experimental and calculated EXAFS, FT spectra of the Ru(II) arene complexes are shown in **Figures 3.7-3.22**. Bond lengths are compared to published crystal structure data for previously characterized species and corresponded well; an *R*-factor of around or less than 20% are considered satisfactory.[27] Fitting parameters, which included the threshold energy, E_0, scale factor, S_0^2, and Debye-Waller factors, σ^2, are presented in **Appendix Table A2-A25.**

The degree of determinacy of the system is quantified by a ratio of the number of independent observations, N_i and the number of refined parameters, p.[27] Taking both constrained and restrained refinements into consideration, the value of N_i is given by:

$$N_i = \frac{2(\Delta r)(\Delta k)}{\pi} + \sum[D(N-2)+1] \quad \textbf{(2)}$$

where *r* and *k* are the ranges of the FT and EXAFS filtered spectra, *D* is the number of dimensions for refinement and *N* is the number of atoms in the unit.[27] For an N_i/p ratio less than one, the fit is underdetermined and a unique answer is not possible. Values above one are required for overdeterminacy of the refinement.[28] The ratio obtained for all models accessed were > 1.

3.4 Results

3.4.1 RAPTA-C (2)

The modeling conditions and fitting parameters for RAPTA-C are presented in Appendix **Table A.2-A.3**. The bond lengths and angles obtained from MS calculations (**Table 3.1**) were in good agreement and within error range with the literature crystal structure.[29] The model (**Figure 3.8**) took into account all the non-hydrogen atoms within 5 Å of the scattering atom that might contribute to the spectra;[12] a fit of R = 18% was obtained over the k range 0-13 Å^{-1}. Unfortunately, at k > 13 Å^{-1} the oscillations were weak and were mainly noise. As such a reduced k-range was used to collect the spectra.

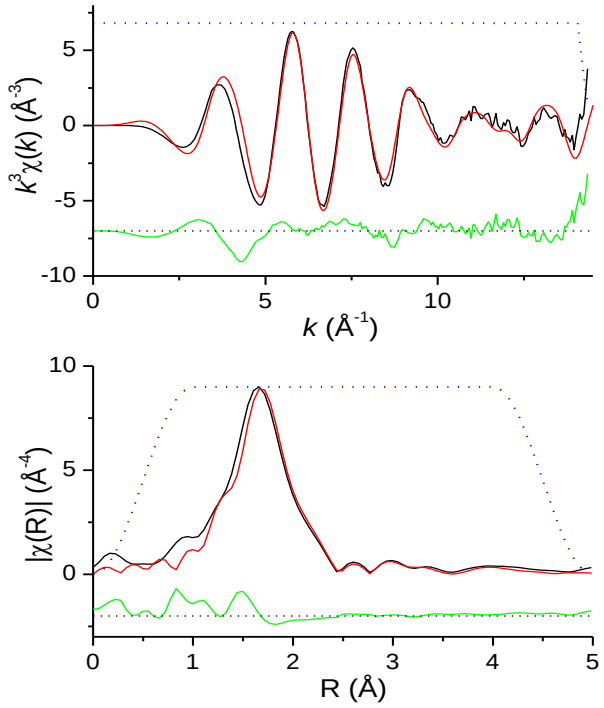

Figure 3.7: k^3-weighted EXAFS data and FT spectra for compound **2**: Observed (black), calculated (red), residual (green) spectra, window function (dashed blue line). EXAFS cut at k = 13 Å^{-1} due to the noise levels at a higher k range.

The fit was overdetermined with an N_i/p value of 1.1. The EXAFS data and the corresponding FT are shown in **Figure 3.7**, together with the calculated data from the fit (red line). Appendix **Table A.4** provides the significant paths for the calculated EXAFS spectra.

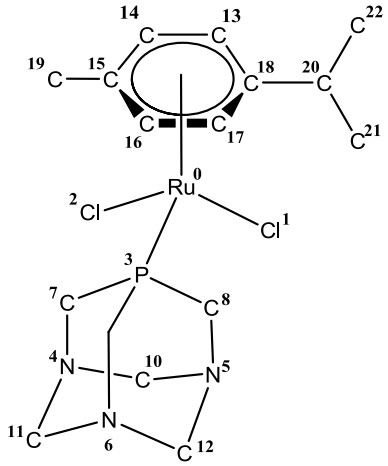

Figure 3.8: The model used for the MS EXAFS fits based on the crystal structure of compound **2**.[29] Atom numbers correspond to Table 3.1.

Table 3.1: Comparison of the bond lengths and angles of EXAFS analysis results to the published crystal structure of RAPTA-C.

Atom-atom	Crystal Structure[29]	EXAFS
Bond lengths (Å)		
Ru^0–Cl^1	2.412(3)	2.43(2)
Ru^0–Cl^2	2.429(2)	2.43(2)
Ru^0–P^3	2.296(2)	2.32(2)
Ru^0–$C^{13\text{-}18}$	2.194(10)	2.19(2)
Bond angles (°)		
P^3–Ru^0–Cl^2	83.42(8)	82(3)
P^3–Ru^0–Cl^1	89.80(3)	89(2)
Cl^2–Ru^0–Cl^1	87.25(8)	88(1)

3.4.2 [(η^6-*p*-cymene)Ru(en)Cl]PF_6 (3)

The model used for MS calculations was based on the published crystal structure,[30] with a fit of R = 19% and an N_i/p value of 1.1. Experimental and calculated EXAFS and FT spectra are shown in **Figure 3.9** and fitting parameters in **Appendix Table A.5**. A comparison is shown with the crystal structure bond angle and length data (**Table 3.2**); best fits include the Ru-Cl bond (2.41 Å), the shorter Ru-N chelating bonds (average of 2.11 Å) and the Ru-arene carbon bonds (average 2.19 Å). Although the bonding parameters were consistent with literature values, the small k range used (~11 Å^{-1}) would mean that some fitting parameters such as the Debye-Waller factors, are not optimal. MS analysis over a longer k range will be needed for more accurate results.

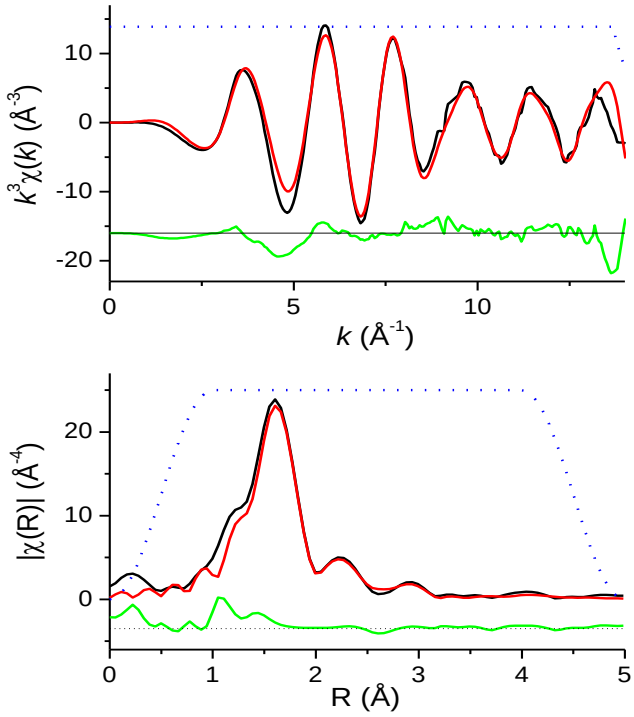

Figure 3.9: k^3-weighted EXAFS and FT spectra for compound **3**: Observed (black), calculated (red), residual (green) spectra, window function (dashed blue line). EXAFS cut at k = 13 Å^{-1} due to the noise levels at a higher k range.

Conditions applied for MS modelling are similar to RAPTA-C but slightly loosened with bond lengths and angles within 0.03 Å and 2-5° respectively, according to the error range published.[30] The model, based on the crystal structure, is given in **Figure 3.10**; further details of the significant path lengths, constraint and restraint parameters are presented in **Appendix A.5-A.7**.

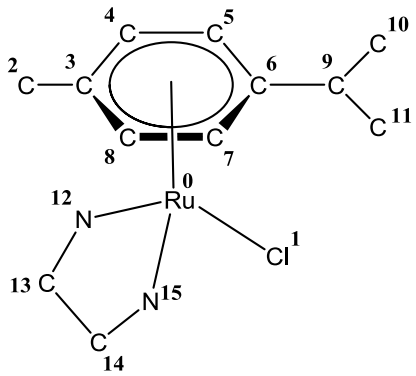

Figure 3.10: The model used in the MS EXAFS fits based on the crystal structure of compound **3**.[30] Atom numbers correspond to those in Table 3.2.

Table 3.2: Comparison of the bond lengths and angles of EXAFS analysis results to the published crystal structure of $[(\eta^6\text{-}p\text{-cymene})Ru(en)Cl]PF_6$.

Atom-atom	**Crystal Structure**[30]	**EXAFS**
Bond lengths (Å)		
$Ru^0–Cl^1$	2.442(5)	2.41(2)
$Ru^0–N^{12}$	2.130(2)	2.11(2)
$Ru^0–C^{3\text{-}8}$	2.195(3)	2.19(2)
Bond angles (°)		
$N^{12}–Ru^0–N^{15}$	78.97(5)	77(6)
$N^{12}–Ru^0–Cl^1$	84.53(8)	84(7)
$Ru^0–N^{15}–C^{14}$	123.34(5)	128(6)
$N^{15}–C^{14}–C^{13}$	110.80(3)	112(6)

3.4.3 [(η^6-*p*-cymene)Ru(acac)Cl]PF_6 (4)

The model used for MS EXAFS calculations was based on the published crystal structure,[31] with a fit of *R* = 17% **(Figure 3.11)**.

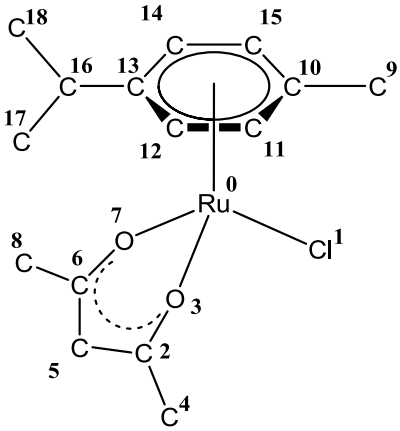

Figure 3.11: Model used for the MS EXAFS analysis based on the crystal structure of compound **4**.[31] Atom numbers correspond to those in Table 3.3.

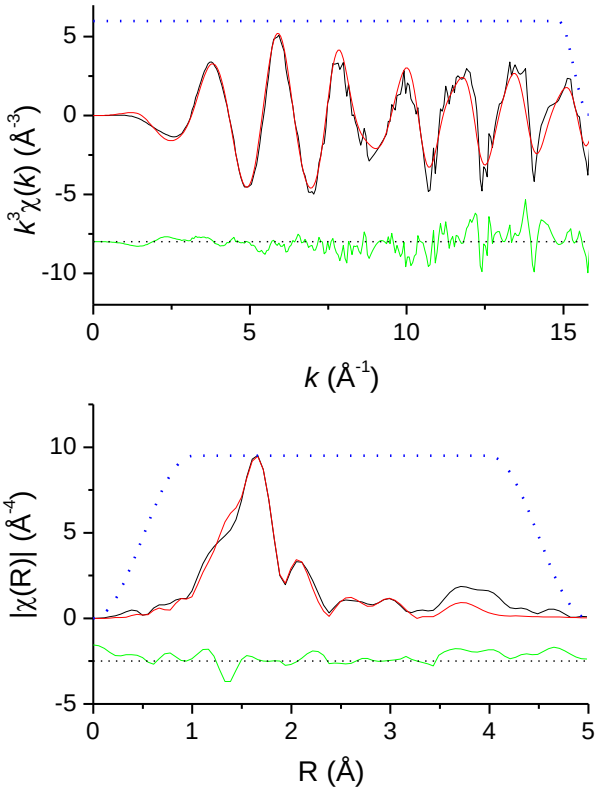

Figure 3.12: k^3-weighted EXAFS and FT spectra for compound **4**: Observed (black), calculated (red), residual (green) spectra, window function (dashed blue line).

Experimental and calculated EXAFS and FT spectra are shown in **Figure 3.12**; the resultant fitting parameters were within acceptable ranges (**Table A.9, Appendix)**. A comparison of bond length and angle data is shown with the crystal structure data (**Table 3.3**); best fits included the Ru-Cl bond (2.41 Å), the shorter Ru-O bond (2.05 Å) and the Ru-arene carbon bonds (average 2.16 Å). Restraints applied for MS modelling had bond lengths and angles within 0.03-0.05 Å and 2-5° respectively, according to the error range published.[31] Further details of the significant path lengths, constraint and restraint parameters, are presented in **A.8-A.11 Appendix**.

Table 3.3: Comparison of the bond lengths and angles of EXAFS analysis results to the published crystal structure of [(η^6-*p*-cymene)Ru(acac)Cl]PF_6.

Atom-atom	Crystal Structure[31]	EXAFS
Bond lengths (Å)		
Ru^0–Cl^1	2.406(2)	2.41(2)
Ru^0–O^3	2.061(4)	2.05(2)
Ru^0–$C^{10\text{-}15}$	2.169(2))	2.16(2)
Bond angles (°)		
O^3–Ru^0–Cl^1	87.26(7)	86(5)
O^7–Ru^0–Cl^1	83.34(7)	84(5)
O^7–Ru^0–O^3	85.24(8)	86(5)

3.4.4 OxaloRAPTA-C (5)

The model used for MS EXAFS calculations was based on the published crystal structure,[32] with an excellent fit of *R* = 11% **(Figure 3.13)**. Experimental and calculated EXAFS and FT spectra are shown in **Figure 3.14**; fitting parameters were within acceptable values (**Appendix Table A.12)**. A comparison is shown with the crystal

structure bond angle and length data (**Table 3.4**); best fits include the Ru-O bond (2.10 Å), O-C bonds (1.27 Å) and the Ru-arene carbon bonds (average 2.22 Å). Further details of the significant path lengths, constraint and restraint parameters are presented in **Appendix A.11-A.13.**

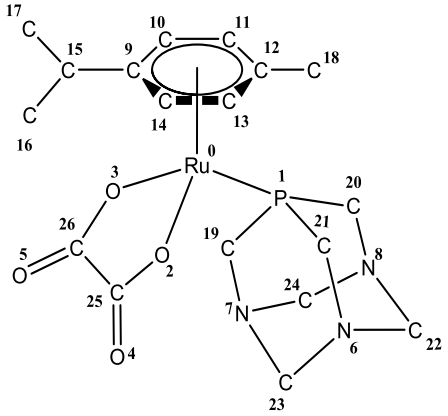

Figure 3.13: Model used for the MS EXAFS analysis based on the crystal structure of compound **5**.[32] Atom numbers correspond to Table 3.4.

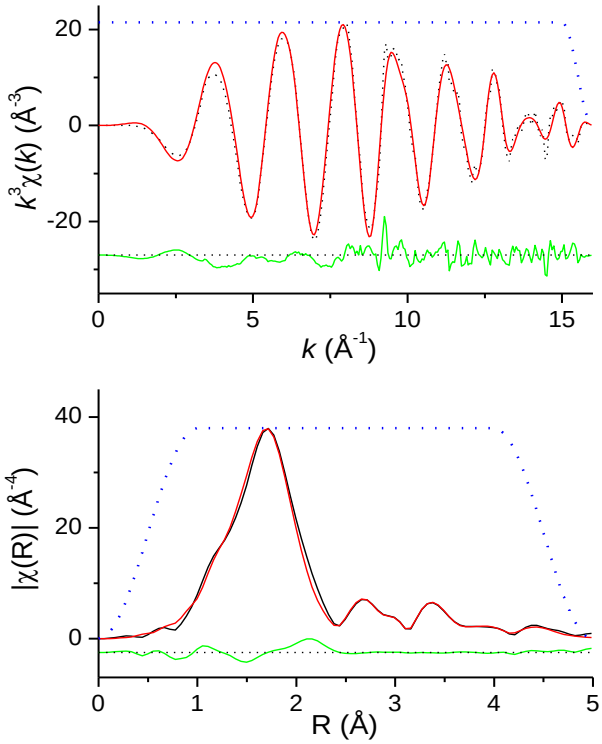

Figure 3.14: k^3-weighted EXAFS and FT spectra for compound **5**: Observed (black), calculated (red), residual (green) spectra, window function (dashed blue line).

Table 3.4: Comparison of the bond lengths and angles of EXAFS analysis results to the published crystal structure of OxaloRAPTA-C.

Atom-atom	Crystal Structure[32]	EXAFS
Bond lengths (Å)		
$Ru^0–P^1$	2.310(1)	2.33(2)
$Ru^0–O^3$	2.093(2)	2.10(2)
$Ru^0–C^{9-14}$	2.224(2)	2.22(2)
$O^3–C^{26}$	1.288(3)	1.27(2)
$O^5–C^{26}$	1.232(3)	1.23(2)
Bond angles (°)		
$O^3–Ru^0–O^2$	78.43(7)	74(5)
$P^1–Ru^0–O^3$	82.83(5)	82(5)
$P^1–Ru^0–O^2$	88.79(5)	86(5)

3.4.5 [Ru(η^6-*p*-cymene)Cl_2(mimid)] (6)

MS EXAFS calculations were based on the published crystal structure[33] with a fit of *R* = 20% obtained **(Figure 3.15)**. Experimental and calculated EXAFS and FT spectra are shown in **Figure 3.16**; fitting parameters were within acceptable ranges (**Appendix Table A.14)**. Comparisons with the bond length and angle data from the crystal structure are shown in **Table 3.5**; best fits include the Ru-Cl bond (2.44 Å), Ru-N, which was similar to compound **3** (2.12 Å) and the main N-C bonds in the imidazole ligand (average 1.37 Å). The results obtained were the same within experimental error.[33] Further details of the significant path lengths, constraint and restraint parameters are presented in **Appendix A.14-A.16**.

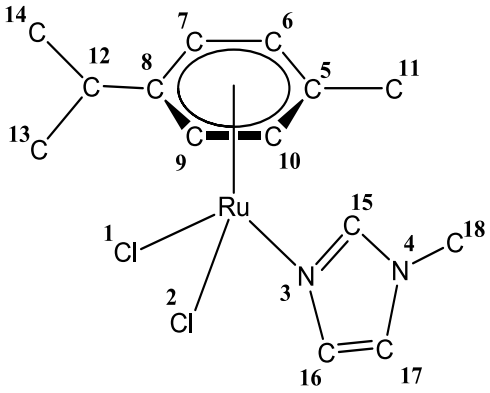

Figure 3.15: Model used for the MS EXAFS analysis based on the crystal structure of compound **6**.[33] Atom numbers correspond to those in Table 3.5.

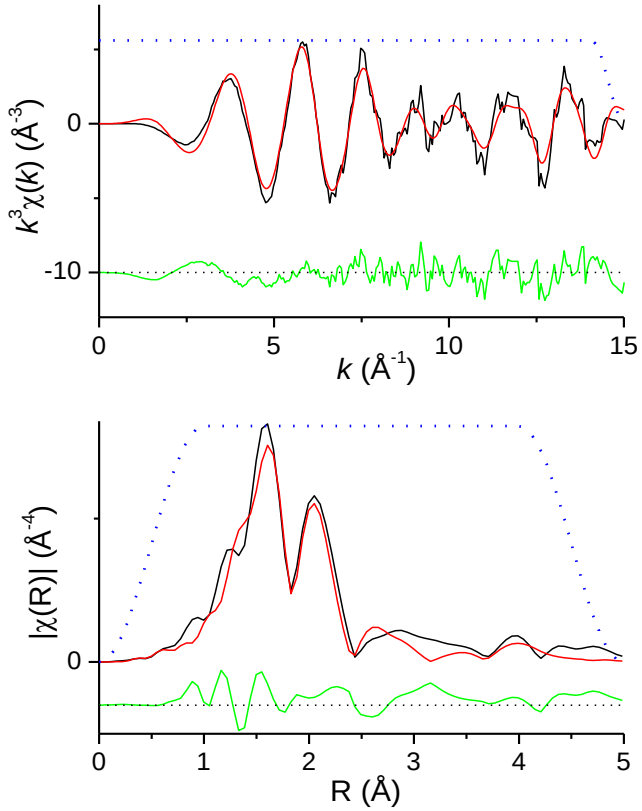

Figure 3.16: k^3-weighted EXAFS and FT spectra for compound **6**: Observed (black), calculated (red), residual (green) spectra, window function (dashed blue line).

Table 3.5: Comparison of the bond lengths and angles of EXAFS analysis results to the published crystal structure of [Ru(η^6-*p*-cymene)Cl_2(mimid)]PF_6.

Atom-atom	Crystal Structure[33]	EXAFS
Bond lengths (Å)		
Ru^0–Cl^1	2.422(1)	2.44(2)
Ru^0–N^3	2.122(2)	2.09(2)
Ru^0–$C^{5\text{-}10}$	2.181(2)	2.19(2)
N^3–C^{16}	1.352(15)	1.35(2)
N^3–C^{15}	1.380(4)	1.38(2)
N^4–C^{15}	1.355(3)	1.35(2)
N^4–C^{18}	1.374(7)	1.38(2)
Bond angles (°)		
Cl^1–N^3–Cl^2	88.79(14)	87(5)
Cl^2–Ru^0–N^3	84.5(5)	84(3)
N^3–Ru^0–Cl^1	85.14(6)	84(3)

3.4.6 $[Ru_2(\eta^6\text{-}p\text{-cymene})_2(\mu\text{-OH})_3]BPh_4$ (7)

There was no crystal structure published, so the model for this compound was built with XFIT with reference to another structurally similar Ru(II) tris-hydroxido compound for the bond lengths and angles.[34] A very good fit of *R* = 13% was obtained. Experimental and calculated EXAFS and FT spectra are shown in **Figure 3.18**; fitting parameters were within acceptable ranges and are given in **Appendix Table A.18**. Comparisons with bond lengths and angles from reported structures with similar bonding are shown in **Table 3.6**. The Ru-Ru distance (3.04 Å) fell within the range reported for the *tri*-hydroxido benzene complexes and the *di*-hydroxido *p*-cymene complex,[34] the bond angles for the bridging hydroxide groups compared with those in the structures of the

benzene complex.[34] The Ru-O[3] bond length did not agree with the crystal structure value within error. This might be due to the poor refinement results at $k > 10$ Å^{-1} which would also affect the Debye-Waller factors. Further details of the significant path lengths, constraint and restraint parameters are presented in **Appendix A.17-A.19**.

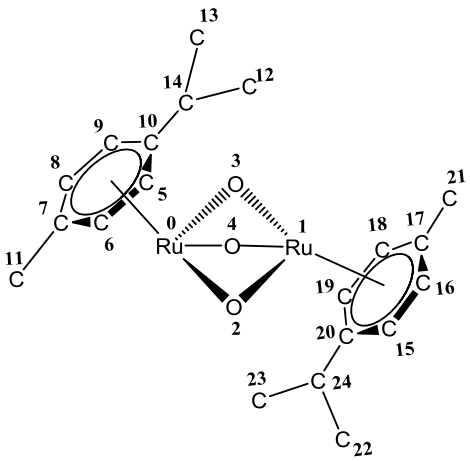

Figure 3.17: Model used for the MS EXAFS analysis based on a reference crystal structure for compound **7**.[34] Atom numbers correspond to those in Table 3.6.

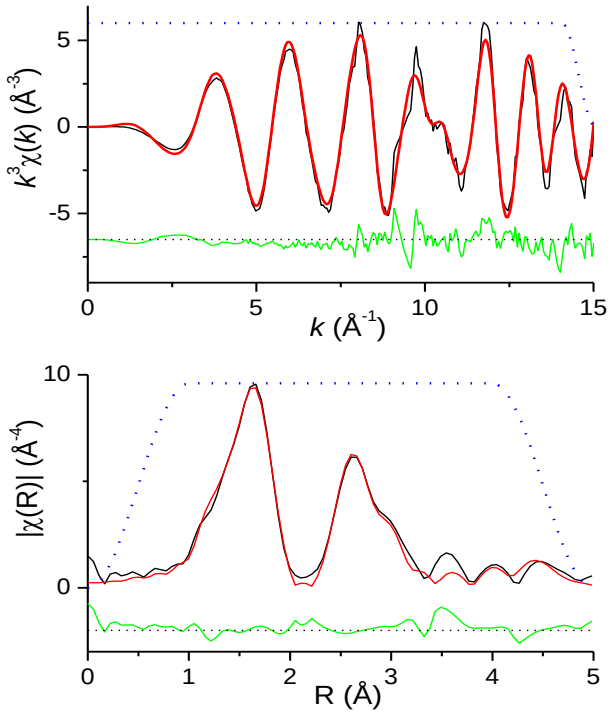

Figure 3.18: k^3-weighted EXAFS and FT spectra for compound **7**: Observed (black), calculated (red), residual (green) spectra, window function (dashed blue line).

Table 3.6: Comparison of the bond lengths and angles of the EXAFS analysis results to the reference crystal structure of $[Ru_2(\eta^6\text{-p-cymene})_2(\mu\text{-OH})_3]BPh_4$.

Atom-atom	EXAFS[a]	Reference Complex[34]
Bond lengths (Å)		
$Ru^0–Ru^1$	2.98(2)	2.989(3)
$Ru^0–O^2$	2.07(2)	2.090(3)
$Ru^0–O^3$	2.13(2)[b]	2.085(3)
$Ru^0–C^{10}$	2.18(2)	2.181(4)
$Ru^1–C^{20}$	2.18(2)	2.188(5)
Bond angles (°)		
$O^3–Ru^0–O^2$	77(5)	76.0(1)
$Ru^1–O^3–Ru^0$	88(5)	90.3(3)
$Ru^1–O^2–Ru^0$	91(5)	91.5(1)

[a]Model built and compared with structurally similar Ru(II) tris-hydroxido compound, $[Ru_2(\eta^6\text{-arene})_2(\mu\text{-OH})_3]BF_4$ for bond lengths and angles.[34] [b]Bond length did not correspond to crystal structure value due to data quality.

3.4.7 $[Ru(\eta^6\text{-}p\text{-cymene})(tsal)]_2$ (8)

MS EXAFS calculations used for the model in **Figure 3.19** were based on the published crystal structure[35] and resulted in an excellent fit of *R* = 12%. Experimental and calculated EXAFS and FT spectra are shown in **Figure 3.20**; fitting parameters were within acceptable value ranges (**Appendix Table A.20)**. Comparisons with the crystal structure are shown in **Table 3.7**; Ru-S (average 2.40 Å), Ru-O (average 2.09 Å) and all other bonds and angles obtained were in very good agreement. Details of the significant path lengths, constraint and restraint parameters are presented in **Appendix A.20-A.22**.

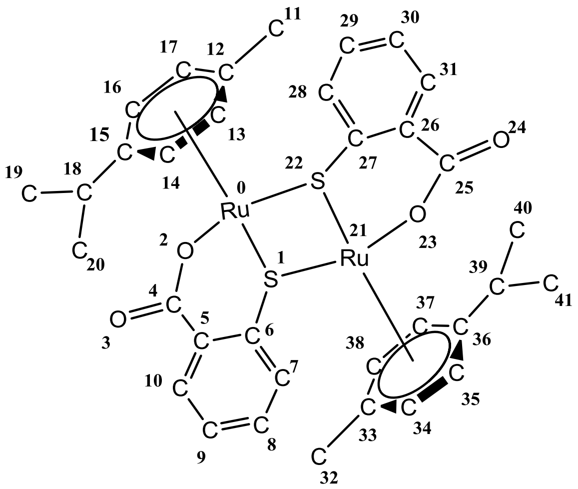

Figure 3.19: Model used for the MS EXAFS analysis based on the crystal structure of compound **8**.[35] Atom numbers correspond to Table 3.7.

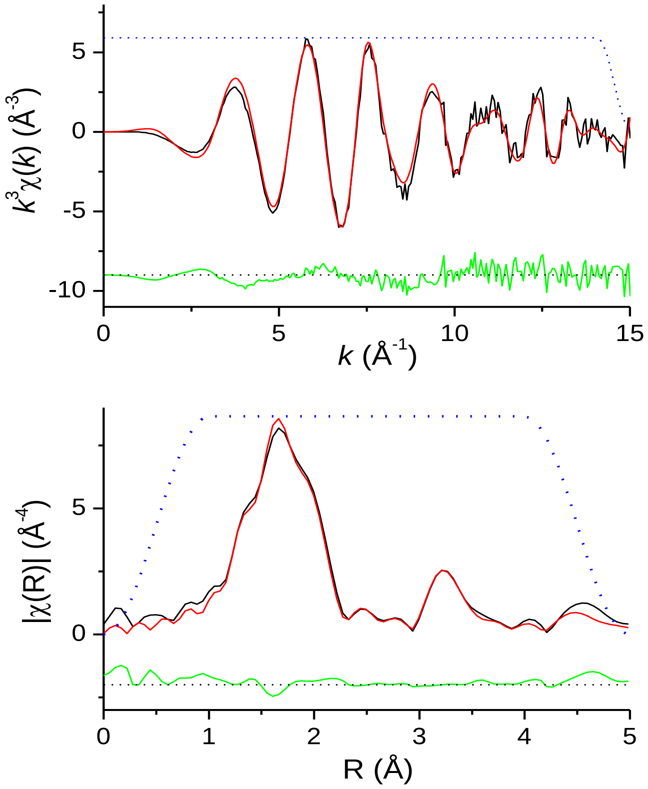

Figure 3.20: k^3-weighted EXAFS and FT spectra for compound **8**: Observed (black), calculated (red), residual (green) spectra, window function (dashed blue line).

Table 3.7: Comparison of the bond lengths and angles of the published crystal structure and EXAFS analysis results of [Ru(η^6-*p*-cymene)(tsal)]$_2$.

Atom-atom	Crystal Structure[35]	EXAFS
Bond lengths (Å)		
Ru^0–S^1	2.3848(4)	2.38(2)
Ru^0–O^2	2.0930(12)	2.09(2)
Ru^0–C^{13}	2.2274(17)	2.21(2)
Ru^0–S^{22}	2.4177(4)	2.41(2)
O^3–C^4	1.230(2)	1.25(2)
S^1–C^6	1.7831(18)	1.78(2)
O^2–C^4	1.288(2)	1.26(2)
Bond angles (°)		
O^2–Ru^0–S^1	87.80(4)	88(5)
O^2–Ru^0–S^{22}	77.80(4)	78(5)
S^1–Ru^0–S^{22}	80.714(15)	82(5)
Ru^0–S^1–Ru^{21}	99.286(15)	98(5)

3.4.8 [Ru(η^6-*p*-cymene)(en)(S-Ph)]PF_6 (9)

The crystal structure for this compound has not been reported. From the modelling of the structures for compounds **2-6, 8** a model for MS EXAFS analysis was built **(Figure 3.21)**. The Ru-arene bond lengths and angles were assigned the same starting values, as in all the previous compounds, en and S-Ph were referred to published data with similar ligands.[36, 37] A good fit of *R* = 19% was obtained. Experimental and calculated EXAFS and FT spectra are shown in **Figure 3.22**. Fitting parameters including acceptable ranges are given in **Appendix Table A.24**.

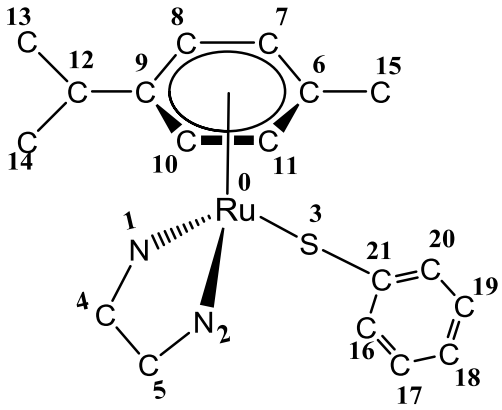

Figure 3.21: Model used for the MS EXAFS analysis based on a reference crystal structure for compound **9.**[36] Atom numbers correspond to those in **Table 3.8**.

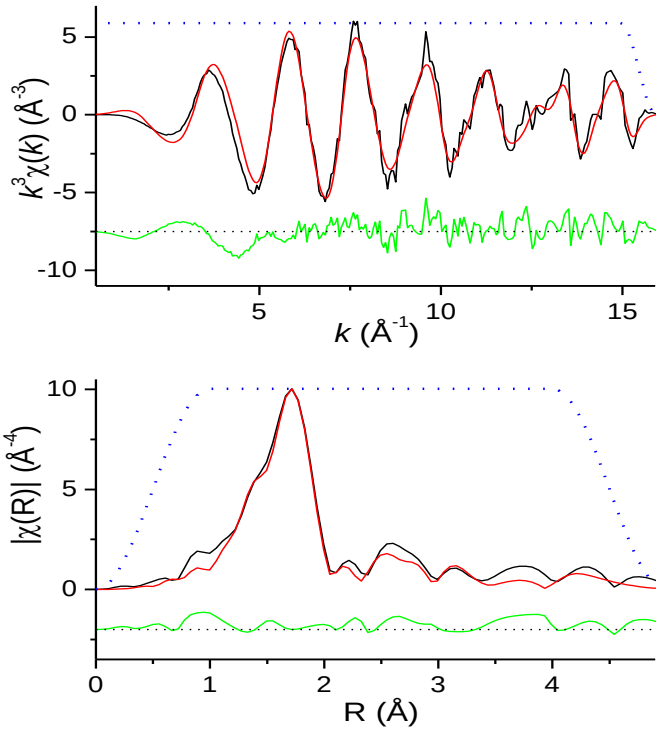

Figure 3.22: k^3-weighted EXAFS and FT spectra for compound **9**: Observed (black), calculated (red), residual (green) spectra, window function (dashed blue line).

Comparisons with the literature bond length and angle values on a structurally similar complex is shown in **Table 3.8**, notable fits were Ru-S (2.38 Å) and Ru-N (average 2.13 Å).

The Ru-en angle (73(5) Å) was not significantly different to the literature value (79 Å) for a similar complex,[37] and was the same value as that obtained for compound **3** (73 Å). Further details of the significant path lengths, constraint and restraint parameters are presented in **Appendix A.23-A.25**.

Table 3.8: Comparison of the bond lengths and angles of the EXAFS analysis results to the reference crystal structure of [Ru(η^6-*p*-cymene)(en)(S-Ph)]PF_6.

Atom-atom	EXAFS	Reference Complex[36]
Bond lengths (Å)		
Ru^0– S^3	2.38(2)	2.3936(6)
Ru^0–N^1	2.13(2)	2.134(2)
S^3–C^{21}	1.75(2)	1.768(2)
Ru^0–$C^{6\text{-}11}$	2.16(2)	2.175(2)
Bond angles (°)		
N^1–Ru^0–N^2	73(5)	79.16(8)
S^3–Ru^0–N^2	82(5)	82.76(6)
S^3–Ru^0–N^1	83(5)	83.75(6)

[a]Model built and compared with a structurally similar compound,[Ru(η^6-arene)(en)(S-Ph)]$^+$ for bond lengths and angles.[36]

3.5 References

1. Messori, L.; Balerna, A.; Ascone, I.; Castellano, C.; Gabbiani, C.; Casini, A.; Marchioni, C.; Jaouen, G.; Congiu Castellano, A., *JBIC, J. Biol. Inorg. Chem.* **2011,** *16*, 491-499.

2. Bertagnolli, H.; Weber, A.; Hoerner, W.; Ertel, T. S.; Reinoehl, U.; Hanack, M.; Hees, M.; Polley, R., *Inorg. Chem.* **1997,** *36*, 6397-6400.

3. Berry, F. J.; Xu, C.; Jobson, S.; Strange, R., *J. Chem. Soc., Faraday Trans. 1* **1989,** *85*, 3891-3898.

4. Aitken, J. B.; Carter, E. A.; Eastgate, H.; Hackett, M. J.; Harris, H. H.; Levina, A.; Lee, Y.-C.; Chen, C.-I.; Lai, B.; Vogt, S.; Lay, P. A., *Radiat. Phys. Chem.* **2009,** *79*, 176-184.

5. Penner-Hahn, J. E., X-ray Absorption Spectroscopy. In *Comprehensive Coordination Chemistry II, From Biology to Nanotechnology*, Elsevier Ltd.: Oxford, UK, 2003; Vol. 2, pp 159-186.

6. Zhang, H.; Hedman, B.; Hodgson, K. O., X-Ray Absorption Spectroscopy and EXAFS Analysis: The Multiple-Scattering Method and Applications in Inorganic and Bioinorganic Chemistry. In *Inorganic Electronic Structure and Spectroscopy* John Wiley & Sons, Inc.: New York, 1999; Vol. 1, pp 513-554.

7. Kau, L. S.; Spira-Solomon, D. J.; Penner-Hahn, J. E.; Hodgson, K. O.; Solomon, E. I., *J. Am. Chem. Soc.* **1987,** *109*, 6433-6442.

8. Penner-Hahn, J. E., *Coord. Chem. Rev.* **1999,** *190-192*, 1101-1123.

9. Mulyani, I. *In Vitro* Biological Activities and Chemistry of Cr(III) Dietary Supplements. PhD Thesis, University of Sydney, 2006.

10. Gunter, K. K.; Miller, L. M.; Aschner, M.; Eliseev, R.; Depuis, D.; Gavin, C. E.; Gunter, T. E., *Neurotoxicology* **2002,** *23*, 127-146.

11. Gurman, S. J., *J. Synchrotron Radiat.* **1995,** *2*, 56-63.

12. Levina, A.; Armstrong, R. S.; Lay, P. A., *Coord. Chem. Rev.* **2005,** *249*, 141-160.

13. Teo, B.-K., *J. Am. Chem. Soc.* **1981,** *103*, 3990-4001.

14. Westre, T. E.; Di Cicco, A.; Filipponi, A.; Natoli, C. R.; Hedman, B.; Solomon, E. I.; Hodgson, K. O., *J. Am. Chem. Soc.* **1995,** *117*, 1566-1583.

15. Filipponi, A.; Di Cicco, A.; Zanoni, R.; Bellatreccia, M.; Sessa, V.; Dossi, C.; Psaro, R., *Chem. Phys. Lett.* **1991,** *184*, 485-490.

16. Co, M. S.; Scott, R. A.; Hodgson, K. O., *J. Am. Chem. Soc.* **1981,** *103*, 986-988.

17. Cramer, S. P.; Hodgson, K. O.; Stiefel, E. I.; Newton, W. E., *J. Am. Chem. Soc.* **1978,** *100*, 2748-61.

18. Nguyen, A.; Mulyani, I.; Levina, A.; Lay, P. A., *Inorg. Chem.* **2008,** *47*, 4299-4309.

19. Levina, A.; Harris, H. H.; Lay, P. A., *J. Am. Chem. Soc.* **2007,** *129*, 1065-1075.

20. Liu, M.; Lim, Z. J.; Gwee, Y. Y.; Levina, A.; Lay, P. A., *Angew. Chem., Int. Ed.* **2010,** *49*, 1661-1664.

21. Trynda-Lemiesz, L.; Keppler, B. K.; Kozlowski, H., *J. Inorg. Biochem.* **1999,** *73*, 123-128.

22. Kratz, F.; Hartmann, M.; Keppler, B.; Messori, L., *J. Biol. Chem.* **1994,** *269*, 2581-2588.

23. Vargiu, A. V.; Robertazzi, A.; Magistrato, A.; Ruggerone, P.; Carloni, P., *J. Phys. Chem. B* **2008,** *112*, 4401-4409.

24. Wang, F.; Xu, J.; Habtemariam, A.; Bella, J.; Sadler, P. J., *J. Am. Chem. Soc.* **2005,** *127*, 17734-17743.

25. Wang, F.; Chen, H.; Parkinson, J. A.; Murdoch, P. d. S.; Sadler, P. J., *Inorg. Chem.* **2002,** *41*, 4509-4523.

26. Levina, A.; Mitra, A.; Lay, P. A., *Metallomics* **2009,** *1*, 458-470.

27. Binsted, N.; Strange, R. W.; Hasnain, S. S., *Biochemistry* **1992,** *31*, 12117-12125.

28. Aitken, J. B. Applications of Synchrotron Radiation to Investigate Bioinorganic Systems. PhD Thesis, University of Sydney, 2004.

29. Allardyce, C. S.; Dyson, P. J.; Ellis, D. J.; Heath, S. L., *Chem. Commun.* **2001**, 1396-1397.

30. Morris, R. E.; Aird, R. E.; Murdoch, P. d. S.; Chen, H.; Cummings, J.; Hughes, N. D.; Parsons, S.; Parkin, A.; Boyd, G.; Jodrell, D. I.; Sadler, P. J., *J. Med. Chem.* **2001,** *44*, 3616-3621.

31. Habtemariam, A.; Melchart, M.; Fernandez, R.; Parsons, S.; Oswald, I. D. H.; Parkin, A.; Fabbiani, F. P. A.; Davidson, J. E.; Dawson, A.; Aird, R. E.; Jodrell, D. I.; Sadler, P. J., *J. Med. Chem.* **2006,** *49*, 6858-6868.

32. Ang , W. H.; Daldini, E.; Scolaro, C.; Scopelliti, R.; Juillerat-Jeannerat, L.; Dyson , P. J., *Inorg. Chem.* **2006,** *45*, 9006-9013.

33. Vock, C. A.; Scolaro, C.; Phillips, A. D.; Scopelliti, R.; Sava, G.; Dyson, P. J., *J. Med. Chem.* **2006,** *49*, 5552-5561.

34. Carmona, D.; Mendoza, A.; Ferrer, J.; Lahoz, F. J.; Oro, L. A., *J. Organomet. Chem.* **1992,** *431*, 87-102.

35. Henderson, W.; Nicholson, B. K.; Oliver, A. G.; Rickard, C. E. F., *J. Organomet. Chem.* **2001,** *625*, 40-46.

36. Petzold, H.; Xu, J.; Sadler, P. J., *Angew. Chem., Int. Ed.* **2008,** *47*, 3008-3011.

37. Wang, F.; Habtemariam, A.; van der Geer, E. P. L.; Fernandez, R.; Melchart, M.; Deeth, R. J.; Aird, R.; Guichard, S.; Fabbiani, F. P. A.; Lozano-Casal, P.; Oswald, I. D. H.; Jodrell, D. I.; Parsons, S.; Sadler, P. J., *Proc. Natl. Acad. Sci. U. S. A.* **2005,** *102*, 18269-18274.

Chapter Four

Decomposition Studies in Biological Media

- UV-Vis

4.1 UV-Vis results in biological media

Many studies concerning the aquation and hydrolysis process of metallocomplexes in aqueous media have been conducted, which have been crucial for predicting the *in* vivo mode of action and interactions with biomolecular targets.[1-6] As discussed in Chapter 1 (Section 1.3.2), the nature of the coordinated ligands affect the aquation rate constants of the compound, as does the size of the arene ligand,[3] which has not been investigated in the current studies. A general understanding of the kinetics of reactions of these compounds under different biologically relevant conditions is a precursor for the subsequent XANES studies.

UV-Vis kinetic experiments were undertaken to investigate the stability of compounds **2-6** in cell culture medium (DMEM), with proteins in buffer solutions at physiological pH values. Studies in calf serum could not be conducted due to the cloudiness of the solutions. Sample preparation procedures and experimental conditions are described in Chapter 2.

4.1.1 RAPTA-C (2)

4.1.1.1 Reaction of complex 2 in HBS (pH 7.4)

As already noted in the literature,[3, 7] due to the presence of the two chlorido-ligands, which can potentially undergo ligand-exchange reactions in solution, RAPTA-C (compound **2**) undergoes rapid substitution chemistry that goes to completion within

1 hr (**Figure 4.1a**). The substitution reactivity of compound **2** in HEPES-buffered saline (HBS: 20 mM HEPES, 140 mM NaCl, pH 7.4) and pure HEPES (a weakly coordinating buffer, 20 mM, pH 7.4)[8] are shown in **Figure 4.1 a,c**. In HBS, the strong absorption band at 343 nm, corresponding to the parent complex,[3] decreased with time to produce another species that absorbed at 297 nm and this peak continued to grow up to 24 hr incubation. This process was characterized with three isosbestic points at 322, 375 and 440 nm. Similar reactivity was observed in an NMR spectroscopic study carried out in aqueous solutions (pH 7)[3] and a UV-Vis spectral study in phosphate buffer (pH 7).[7] The results were compared to previous DFT calculations performed for the aquation of RAPTA-B.[9] These observations indicated that the newly formed species might be a mixture of aquation and hydrolysis products ([Ru(η^6-*p*-cymene)Cl(OH_2)(PTA)]$^+$) and hydroxido-aqua ([Ru(η^6-*p*-cymene)(OH)(OH_2)(PTA)]$^+$) complexes **(Scheme 4.1)**.[3]

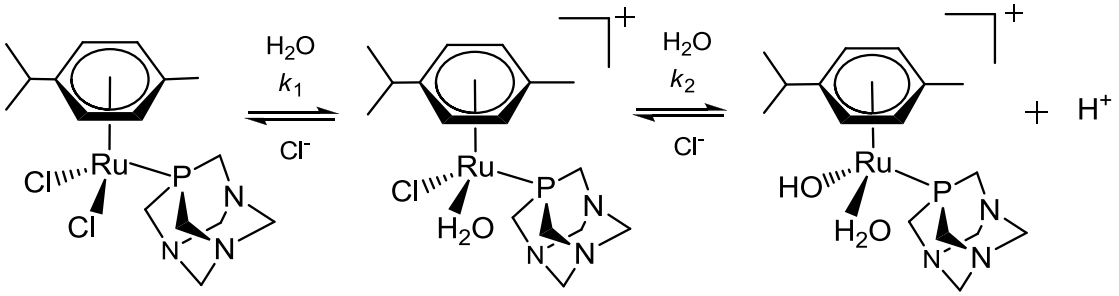

Scheme 4.1: Aquation and hydrolysis of RAPTA-C in aqueous media.[3]

The presence of sodium chloride in the HBS (~140 mM Cl^- ions) suppressed the rate of aquation as compared to that in HEPES (no Cl^-), where the rapid substitution chemistry went to completion within 5 min **(Figure 4.1a,b)**[3]. However, the Cl^-

concentration of 140 mM was not enough to inhibit aquation entirely, which was in contrast to reports in the literature that 100 mM NaCl was enough to prevent any aquation.[3] Therefore, compound **2** would undergo partial ligand exchange in the bloodstream, which has the Cl^- concentration of ~150 mM before entering the cells.[3]

Previous studies of the hydrolysis of RAPTA-B showed that the side product; dihydroxido complex, was unlikely to form at biologically relevant pH values (~pH 6.5-7.4) for tumours whereas hydroxido-aqua complexes (Scheme 4.1), which were stable over a wide pH range might be the dominant species.[9] This is a more desirable outcome as the tendency to form inert dihydroxido-species might lower the compound's reactivity towards biological targets as was observed with the Os(II) arene complexes.[1] Therefore, the aquation product at 60 min was compared to the spectra for the tris-hydroxido-compound **7 (Figure 4.1c)**, but was found to be very different. This may be partly due to significant binding of the chlorido ligands at equilibrium.

The pseudo-first order rate constant *k* and concentration profiles were determined using global kinetic analysis (refer to Chapter 2, **Section 2.4**), in which the kinetic data were fitted with the model reactions with initial concentrations fixed as: A (initial compound) 0.001 M; B(intermediate) 0.0 M; C (final product) 0.0 M. Results are listed in **Table 4.1**. Not all values could be determined due to the lack in spectral changes for some of the compounds within the analyzed timeframe and the reversible reactions were not modelled.

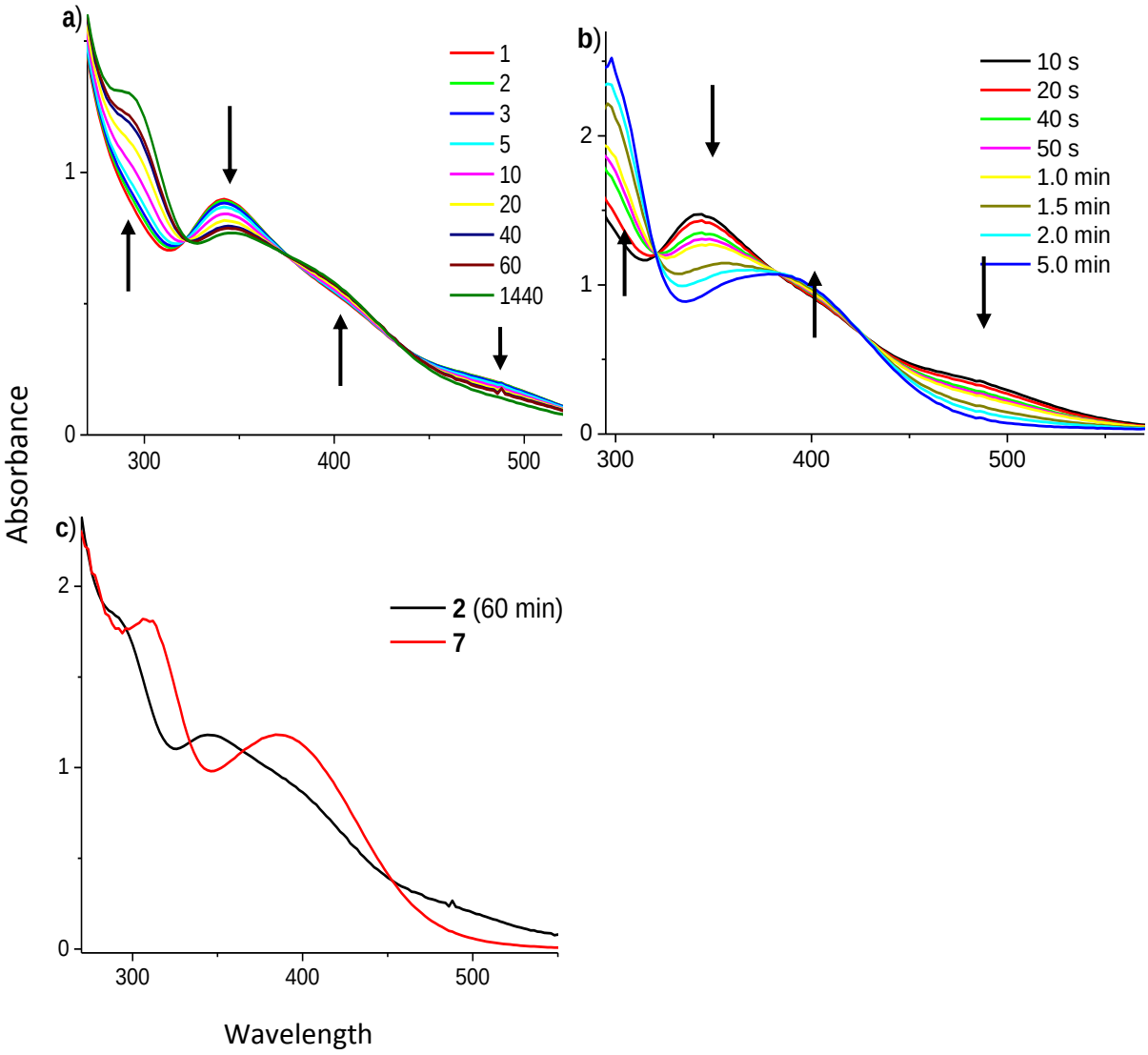

Figure 4.1: UV-Vis electronic absorption spectra for compound **2** (1.0 mM): **(a)** time evolution in HBS (1 h, 20 mM HEPES, 140 mM NaCl, pH 7.4); **(b)** time evolution in HEPES (5 min, 20 mM, pH 7.4) at 37 °C; and **(c)** comparison with the spectrum of compound **7** at 60 min. The arrows indicate the direction of changes within the spectra.

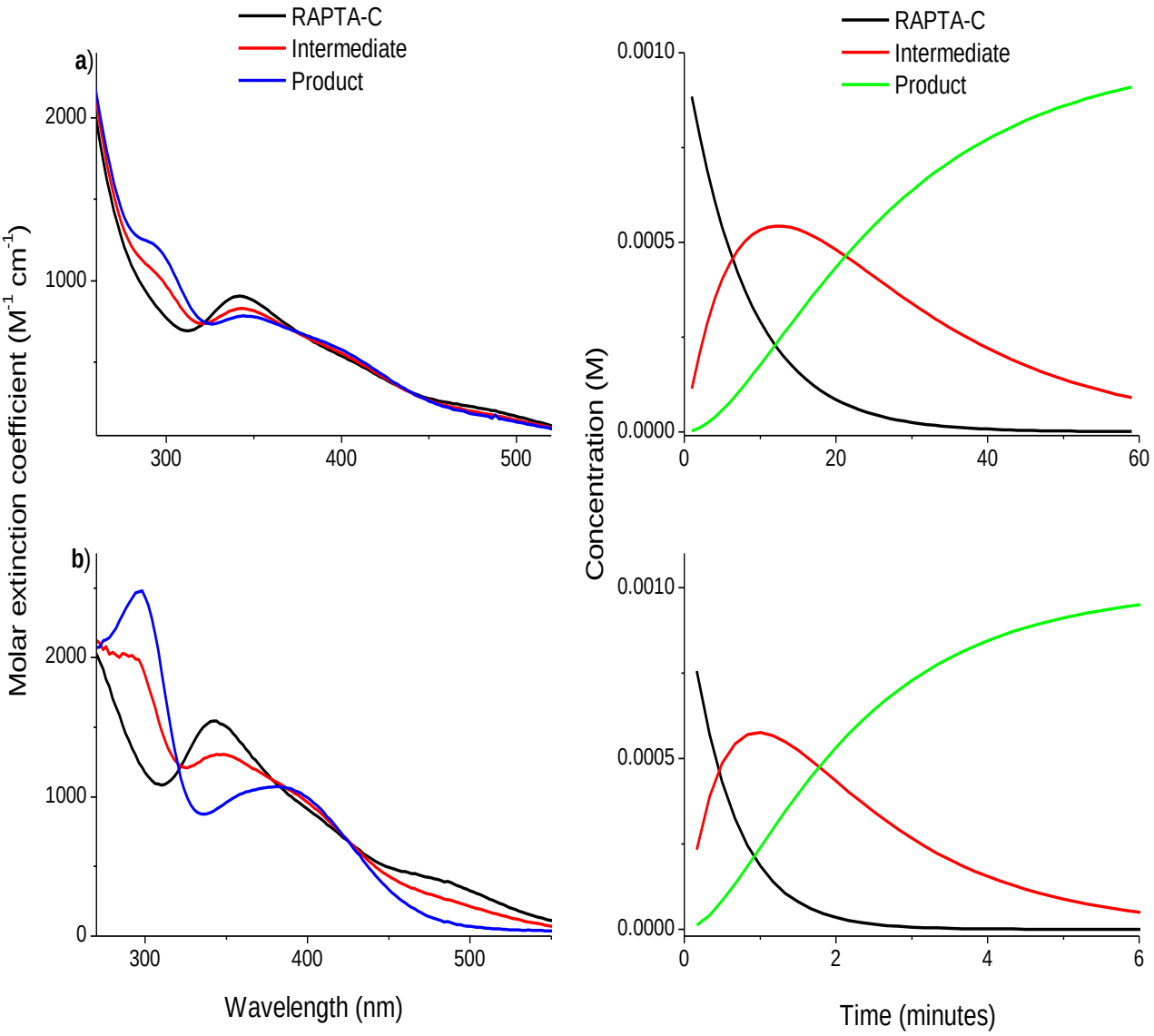

Figure 4.2: Global kinetic analysis results for the extinction coefficients and time dependent concentration profiles upon aquation of 1.0 mM compound **2** in **a)** HBS (20 mM HEPES, 140 mM NaCl, pH 7.4) and **b)** HEPES (20 mM, pH 7.4) at 37 °C. Product refers to the final state of the reaction after the specified reaction time.

Table 4.1: Selected first order rate constants obtained from global analysis kinetic data for Ru compounds (1.0 mM) in aqueous buffers and DMEM at pH 7.4, 37 °C. Literature values provided if available.

	Experimental Results	
Conditions	**2 (x10^{-2}) (s^{-1})**	**3 (x10^{-2}) (s^{-1})**
HBS (140 mM NaCl, pH = 7.4)	k_1 = 0.21 ± 0.01 k_2 = 0.08 ± 0.01	k_1 = 0.12 ± 0.01
HEPES (20 mM, pH = 7.4)	k_1 = 2.81 ± 0.02 k_2 = 0.94 ± 0.01	NA
HEPES (20 mM, 4.0 mM NaCl, pH = 7.4)	k_1 = 4.03 ± 0.02 k_2 = 1.98 ± 0.01	k_1 = 1.47 ± 0.05
DMEM (pH = 7.4)	k_1 = 0.44 ± 0.01 k_2 = 1.28 ± 0.02	k_1 = 0.13 ± 0.01
	Literature Values	
Aqueous	0.33 ± 0.01[a]	0.12 ± 0.01[b]

Conditions described in literature which might contribute to the difference in experimental values: [a]1 mM Ru in 150 mM $NaClO_4$ at 25 °C, pH 7.0; [b]100 mM NaCl at 25 °C, pH 6.27. The missing data is due to minimal changes in the spectrum.

4.1.1.2 Reaction of complex 2 in HEPES buffer

In the HEPES solution (20 mM, pH 7.4) under the same conditions, the initial peak at 343 nm shifted rapidly to 392 nm with two peaks arising at 297 and 390 nm characterized with three isosbestic points at 321, 383 and 425 nm; displaying a similar behaviour to the reactivity in HBS **(Figure 4.1b)**. This reaction had to be monitored every 10 s due to the rapid aquation rate. The same absorption maximum indicated the same

decomposition product forming as was the case in HBS. Concentration profiles revealed that equilibrium was reached after 60 min in HBS and 6 min in HEPES, which confirmed that aquation in HEPES occurred at a rate that was an order of a magnitude faster than in HBS **(Table 4.1 and Figure 4.2).**

4.1.1.3 Reaction of complex 2 in DMEM

The initial absorption band at 348 nm, which corresponded to compound **2** shifted to 385 nm and decreased with time, whereas another species that absorbed at 300 nm gradually formed (**Figure 4.3a**). This reactivity was characterized by three isosbestic points at 320, 384 and 421 nm in the spectrum, which were slightly different from those observed in HBS and showed some differences in products. The rate constants differed from the values observed in HBS, with the reaction rate of the second chlorido exchange faster than the first one, indicating other ligand-exchange processes occurred in the medium. Only detailed UV-Vis studies in aqueous buffer have been reported and the more complex spectrum in DMEM is to be explored further in Chapter 5.

The spectrum at 60 min was compared to the spectrum of the tris-hydroxido compound **7** (**Figure 4.3b**) and was, surprisingly, found to have a similar absorption peak at 385 nm but deviated in λ_{max} value for the new peak by ~4 nm. This observation suggested that compound **2** might have undergone aquation in DMEM to form hydroxido-bridges before interacting with other components.

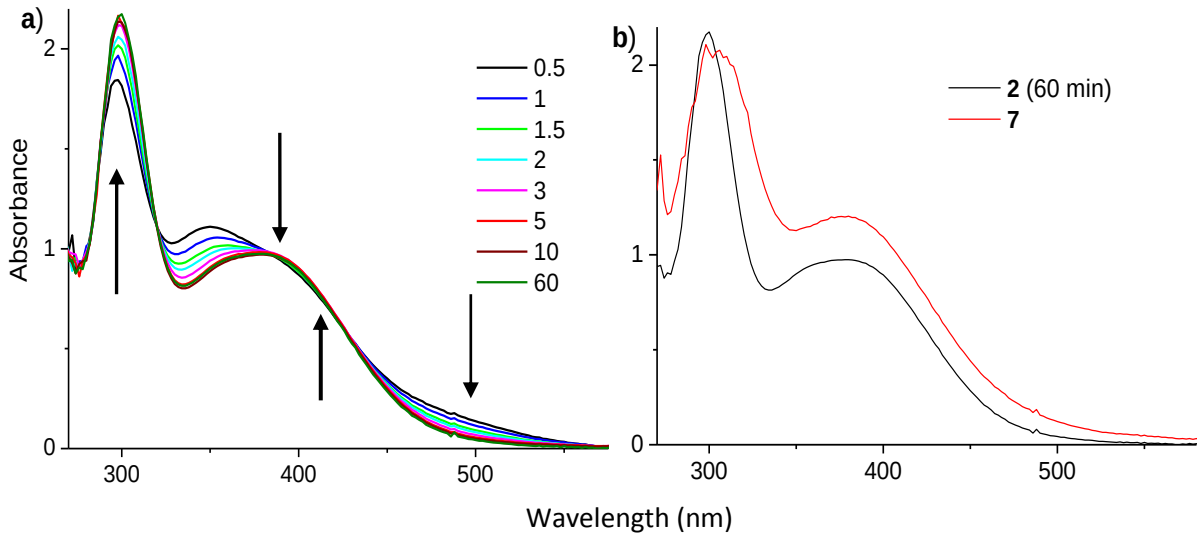

Figure 4.3: UV-Vis electronic absorption spectra for compound **2** (1.0 mM) in DMEM (pH 7.4) at 37 °C: **(a)** time evolution taken within a timeframe of 60 min, recorded at 30 s intervals; and **(b)** comparison with compound **7** at 60 min. The arrows indicate the direction of changes within the spectra.

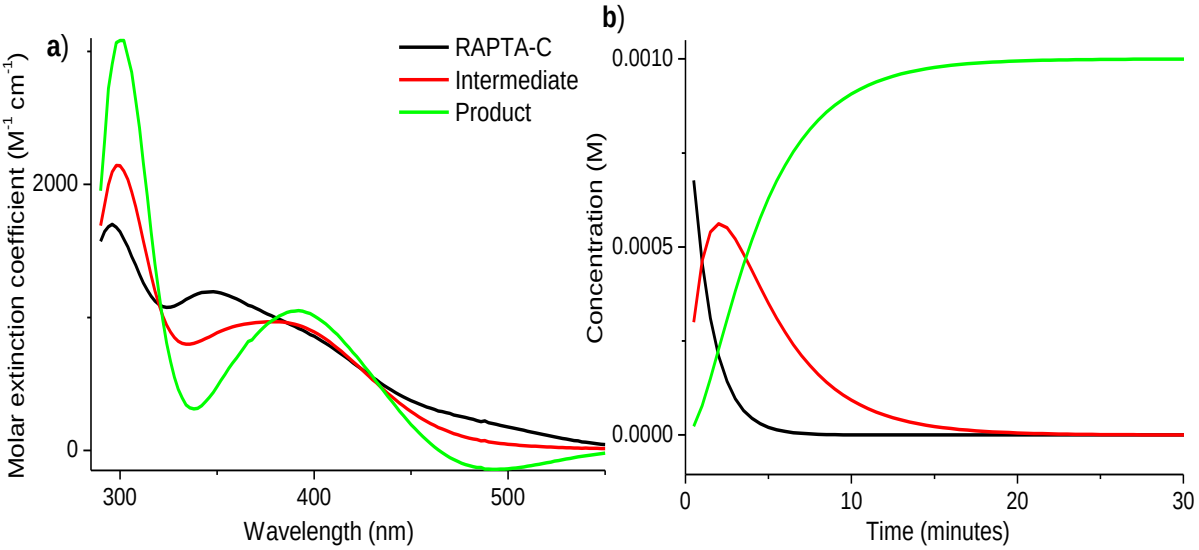

Figure 4.4: Global kinetic analysis results for the **(a)** molar extinction coefficients and **(b)** time dependent concentration profiles upon the aquation of compound **2** (1.0 mM) in DMEM (pH 7.4) at 37 °C. Product refers to the state of the solution after the reaction time.

The rate constants were then determined using global kinetic analysis **(Table 4.1)** and the concentration profiles revealed that an equilibrium was reached in ~15 min, which is at a slightly faster rate compared to the reactivity in HBS and the literature value in aqueous media.[3] Since those buffer solutions have a similar chloride concentration to that in DMEM, which is representative of the blood concentration (~150 mM Cl^-), the hydrolysis of **2** should be suppressed. The results indicated that there was competition for Cl^- rebinding and biomolecule binding, such that less Cl^- is bound in the final product mixture.

4.1.1.4 Reactions of complex 2 with BSA

To observe reactivity with proteins, the kinetics in pure HBS was compared to those in a solution of 5.0 mg/mL bovine serum albumin (BSA) in HBS with 1.0 mM compound **2**.

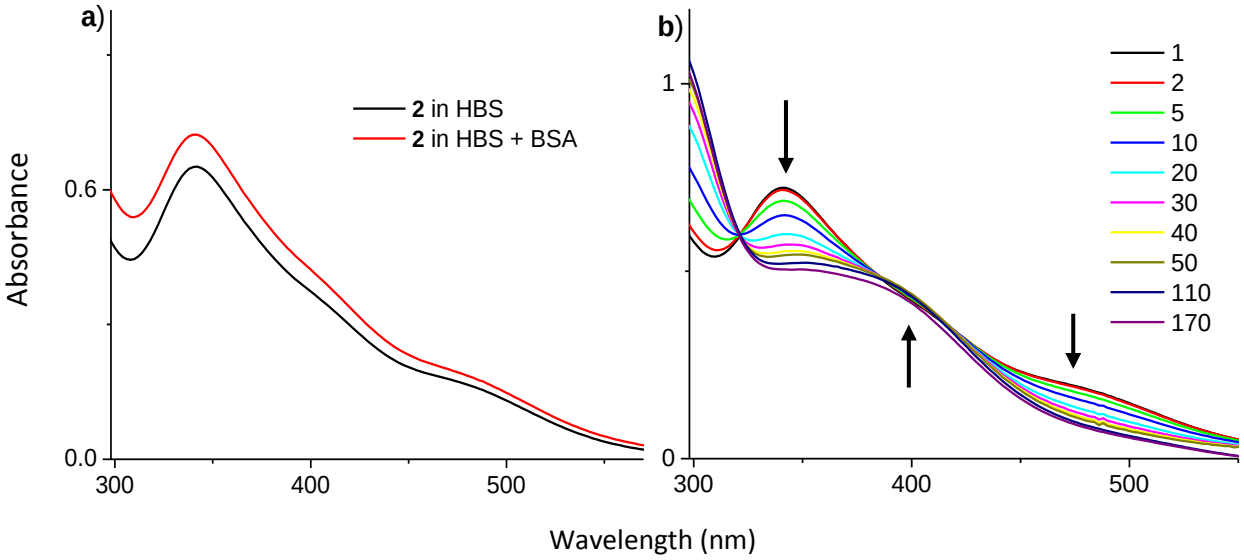

Figure 4.5: UV-Vis electronic absorption spectra for compound **2** (1.0 mM) incubated with 5.0 mg/mL BSA in HBS, pH 7.4 at 37 °C **(a)** comparison with HBS-only sample; and **(b)** time evolution for a timeframe up to 2 hr at pH 7.4. The arrows indicate the direction of changes within the spectra.

The spectra observed showed that the presence of BSA had no major effect above 300 nm **(Figure 4.5a)**. Kinetic studies showed that the intensity of the initial peak at 341 nm decreased over time, eventually flattening out at around 2 hr **(Figure 4.5b)**. Although an isosbestic point was observed at ~388 nm for the first 110 min, the last spectrum at 170 min did not pass through this isosbestic point, which shows another slower reaction occurred. This showed a more complicated set of reactions and the rate constants could only be determined if the reaction was followed for a longer period of time.

4.1.2 [(η^6-*p*-cymene)Ru(en)Cl]PF_6 (3)

4.1.2.1 Reaction of complex 3 in HBS

Arene complexes with *p*-cym as the coordinated arene and 1,2-ethanediamine (en) as a co-ligand have been reported to undergo slower aquation in comparison to compound **2**,[10] due to less pπ donation to the electron rich Ru(II) when one Cl^- ligand is lost.[11] Compound **3** showed little evidence of reactivity for at least 24 hr in HBS at pH 7.4 **(Figure 4.6a)**. There was no peak shift at 311 nm and 400 nm but a slight increase in absorbance, which might just be a slow formation of precipitate. However, the similarity of the spectrum to the final products of the reaction of **2** with BSA indicates a rapid initial loss of the Cl^- ligand, with a slow subsequent exchange reaction of the new donor group with a similar donor group.

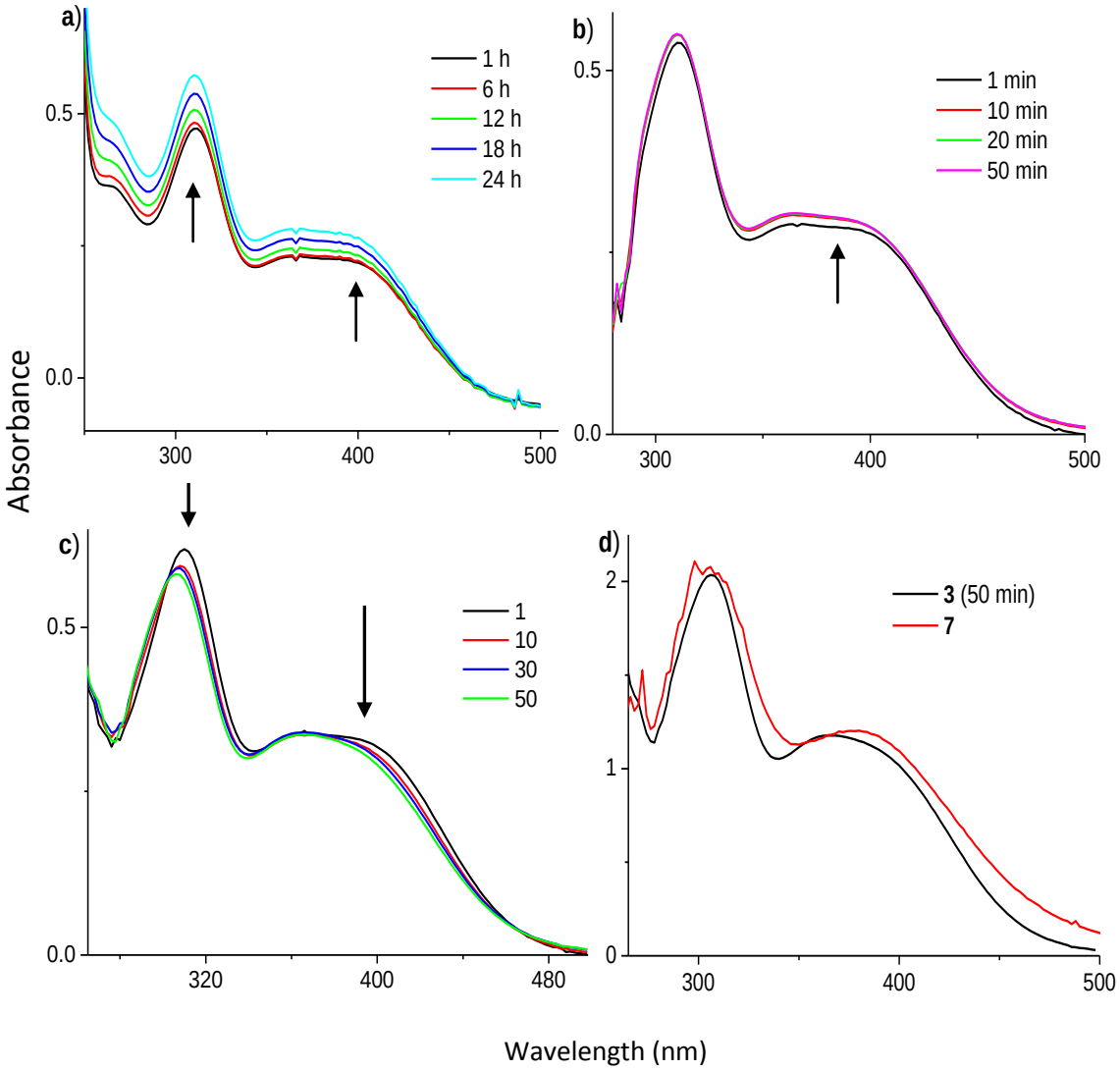

Figure 4.6: UV-Vis electronic absorption spectra for compound **3** (1.0 mM) at 37 °C **a)** in HBS (20 mM HEPES, 140 mM NaCl, pH 7.4) up to 24 hr, **b)** with BSA (5.0 mg/mL) up to 50 min, **c)** in DMEM (pH 7.4) up to 50 min, **d)** comparison with compound **7** at 50 min in DMEM. The arrows indicate the direction of the changes within the spectra.

HPLC results for the dissolution of **3** in 100 mM NaCl reported at least >90% of the parent complex remained intact within 30 min,[10] thus the complex should remain

reasonably stable in extracellular chloride concentrations (~150 mM)[12] before becoming activated in cells (~4 mM), but the experiments were not performed in the presence of BSA. Hence, further research needs to be performed in this area in the future.

4.1.2.2 Reaction of complex 3 in DMEM

Compared to its reaction in HBS, **3** displayed a more interesting reactivity in DMEM **(Figure 4.6c)**, an overall change over this timeframe resulted in a ~2 nm peak shift to lower wavelengths and a slight decrease in absorbance over time. The isosbestic point at 351 nm suggested a single-step reaction with loss of the chlorido ligand and conversion to the more reactive aqua complex $[Ru(\eta^6\text{-}p\text{-cymene})(H_2O)(en)]^{2+}$, which then undergoes rapid substitution in DMEM or in the presence of BSA. This aqua intermediate is supposed to be the dominant species at biological pH values in the absence of other ligands compared to the less active hydroxido complex, $[Ru(\eta^6\text{-}p\text{-cymene})(OH)(en)]^{+}$.[13, 14] A comparison to compound **7 (Figure 4.6d)** showed a difference in positions with a deviation of ~12 nm. Since the en ligand has not been reported to dissociate under these conditions, **3** would have reacted with the other components in DMEM to form a different species, as also observed for **2**.

The pseudo-first-order rate constant for the reaction obtained (k = 1.29 x 10^{-3} s^{-1}) **(Table 4.1)** was consistent with results for the biphenyl en complex reported in literature (range: 1.23-2.26 x 10^{-3} s^{-1}), [13] Albeit this was much slower compared to that of compound **2**, which was consistent with observations that the presence of the en ligand

slowed down the rate of loss of the chlorido leaving group.[3, 13] Another possibility for slower reactions may involve further binding of protein residues. The process reached equilibrium at about 50 min **(Figure 4.7b)**.

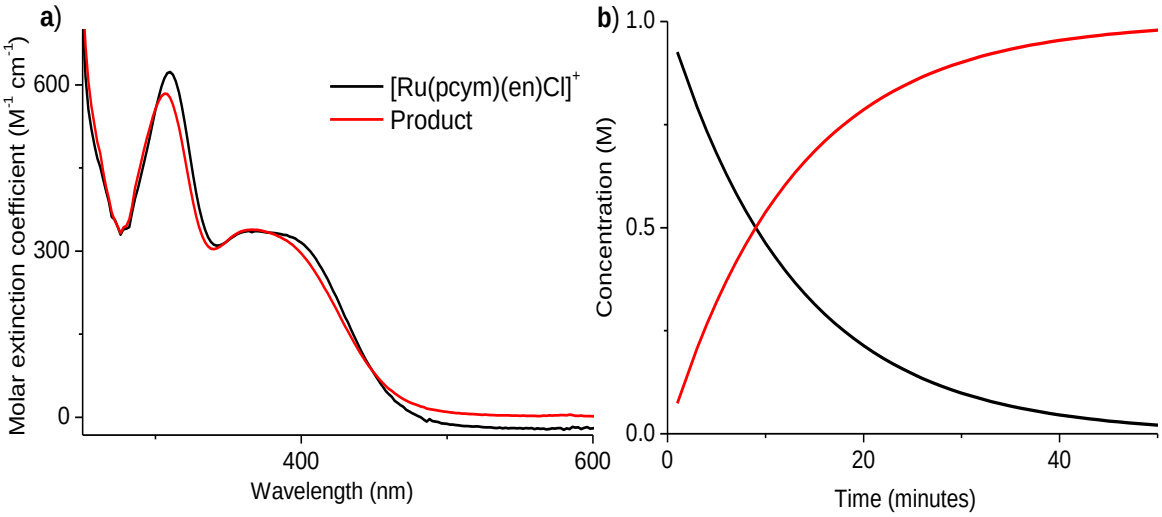

Figure 4.7: Global kinetic analysis results for: **a)** the molar extinction coefficients; and **b)** time-dependent concentration profiles upon the aquation of 1.0 mM compound **3** in DMEM (pH 7.4) at 37 °C. Product refers to the state of the solution after the reaction time (50 min)

4.1.2.3 Reaction of complex 3 with BSA

The reactivity with BSA (**Figure 4.6b)** was quite similar to that in HBS with no shifts for the peaks at 311 and 400 nm for at least 50 min. Compound **3** has been shown to bind to the histidine, methionine and the thiolate of cysteine residues on serum albumin under similar conditions (pH 7.4, 37 °C)[15] using LC-ESI-MS. Although UV-Vis spectroscopy shows how stable the compound is in aqueous buffer, the kinetics were generally too complex to follow and thus XAS studies were undertaken.

4.1.2.4 Reaction of complexes 2 and 3 in a low chloride buffer (4.0 mM NaCl)

Kinetic studies were carried out for compounds **2** and **3** in an environment that simulated the low intracellular chloride concentration (20 mM HEPES with 4.0 mM NaCl, pH 7.4).

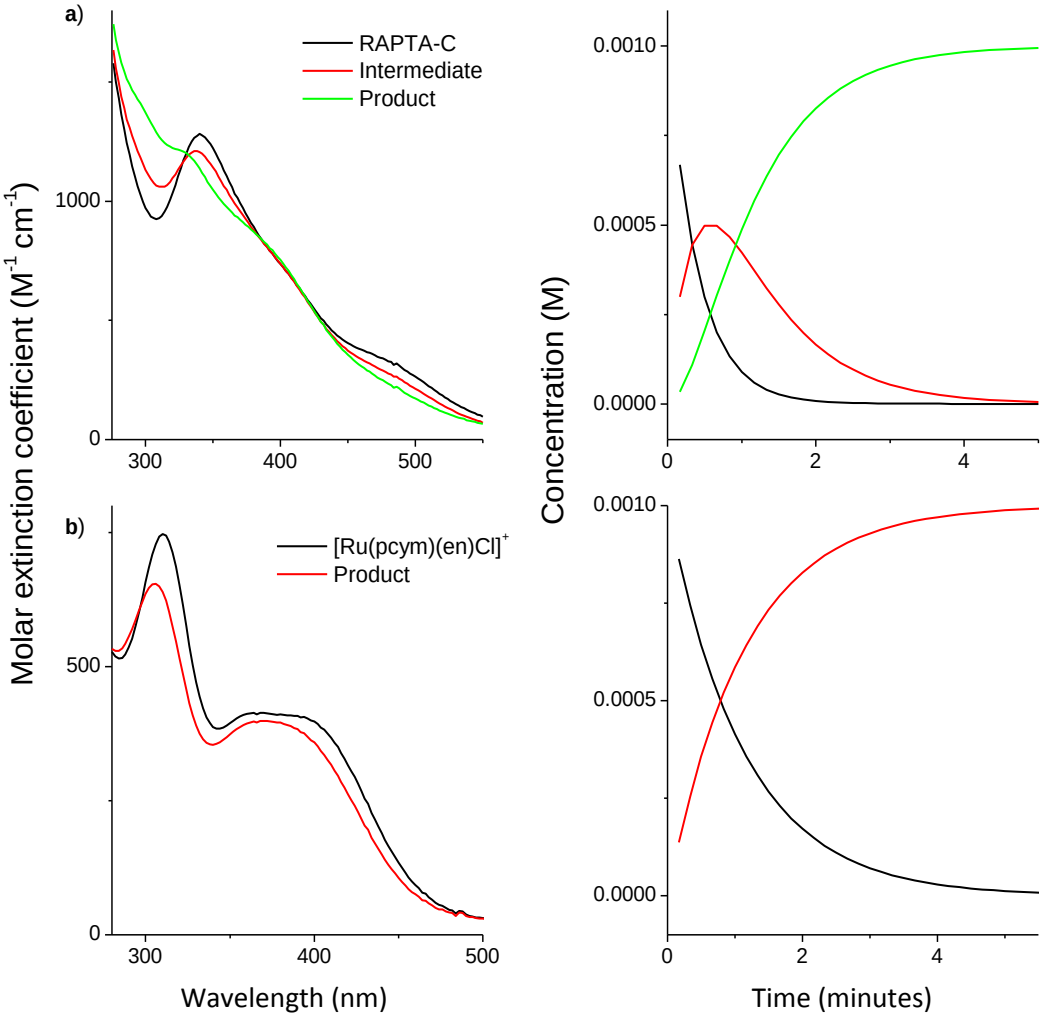

Figure 4.8: Global kinetic analysis results for the molar extinction coefficients and time dependent concentration profiles of the aquation of 1.0 mM; **a)** compound **2,** and **b)** compound **3** (20 mM HEPES, 4.0 mM NaCl, pH 7.4) at 37 °C. Product refers to the state of the solution after the reaction time.

The reactivity was about an order of a magnitude faster compared to that in the high saline environment **(Table 4.1)** and went to completion within 5 min; similar to that observed in HEPES **(Figure 4.8)**. Despite some aquation at low chloride concentrations, the reactivity of these complexes are still highly suppressed which, as postulated in literature,[16] would later form reactive aquated species once the complexes enter the cells; a behaviour that was also observed for cisplatin.[16]

4.1.3 [(η^6-*p*-cymene)Ru(acac)Cl]PF_6 (4)

4.1.3.1 Reaction of complex 4 in HBS

Apart from the en *N,N*-chelating ligand, *O,O*-chelating donor sets have been actively investigated to change the stabilities of the complexes and, hence, their anticancer activities.[1, 17, 18]

The peaks in the UV-Vis spectra for compound **4** (acac chelating ligand) decreased in intensity within 1 hr **(Figure 4.9a)**; at 24 hr the band at 443 nm was almost flat whereas the peak at 311 nm had shifted and decreased in wavelength to 300 nm. The dissolution of complexes with a chelating *O,O* donor set with a halido ligand in aqueous media has resulted in rapid aquation to form the more reactive aqua complex (dominant species),[19] though in some cases hydroxido-bridged dimers might form as a side-product, which was thought to render the complex inactive.[18] The peak at 300 nm for **4** is not solely due to the tris-hydroxido-bridged complex **7**, since the spectrum overall does not match that of **7** but it may be a component of a mixture of products.

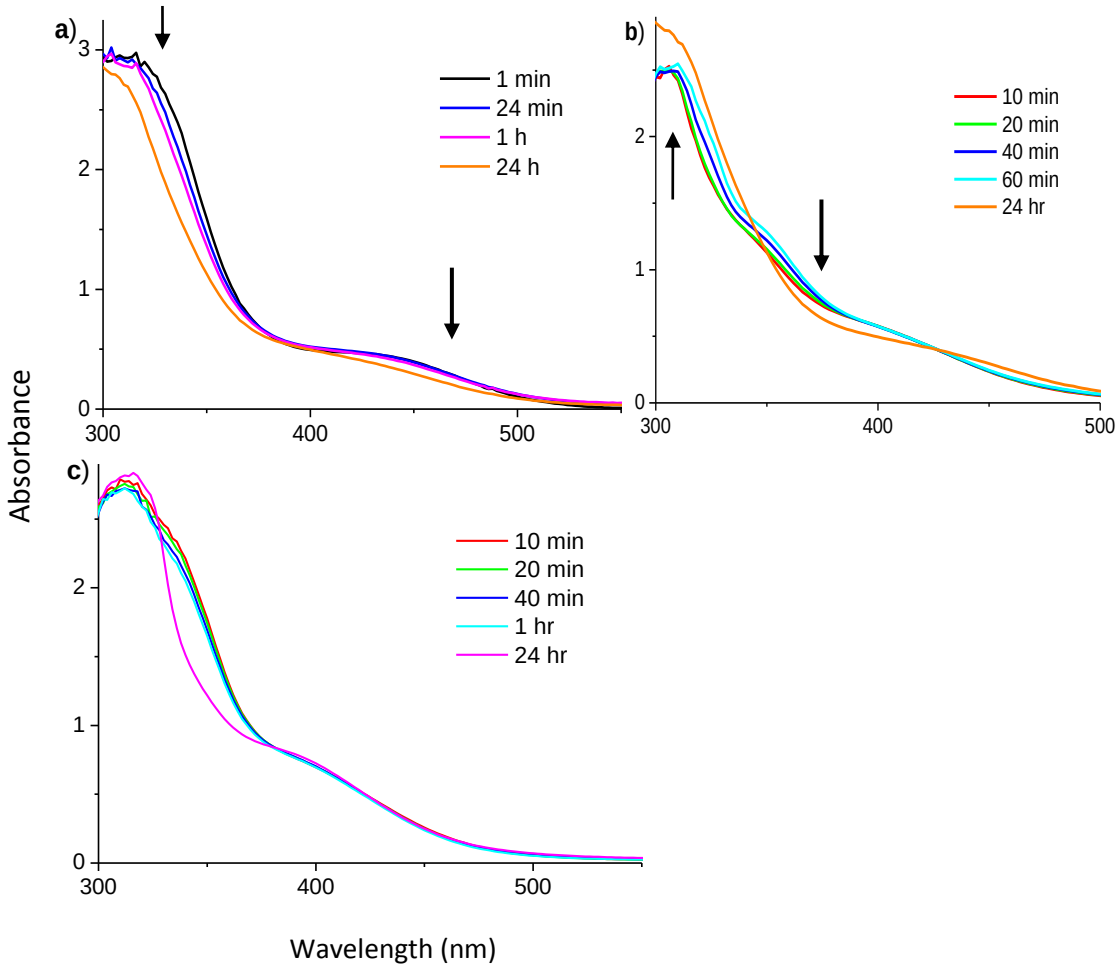

Figure 4.9: UV-Vis electronic absorption spectra for compound **4** (1.0 mM) at 37 °C **a)** in HBS (20 mM HEPES, 140 mM NaCl, pH 7.4) up to 24 hr; **b)** in DMEM (pH 7.4) up to 24 hr; and **c)** with BSA (5.0 mg/mL) up to 24 hr. The arrows indicate the direction of the changes within the spectra. Saturation occurs at absorbance values above 2.8.

4.1.3.2 Reaction of complex 4 in DMEM

The aquation in DMEM **(Figure 4.9b)** was not as straightforward as in HBS. The intensity at ~311 nm increased steadily for 1 hr, however, a totally different spectrum was observed at 24 hr which, as postulated for **2**; might be indicative of another slower

reaction happening in solution. This again points to the compound undergoing a range of reactions within 24 hr, thus leading to a mixture of adducts present in solution.

4.1.3.3 Reaction of complex 4 with BSA

The spectrum for BSA binding showed similar behaviour to its activity in HBS within 1 hr **(Figure 4.9c)**. At 24 hr, there was a change in the band at ~350 nm, which was attributed to BSA binding. These results seem to indicate that **4** is reasonably stable to aquation in biological media, as compared to **3**, but the change observed in the spectra at 24 hr is indicative of another process happening.

4.1.4 OxaloRAPTA-C (5)

4.1.4.1 Reaction of complex 5 in HBS

The aquation of an *O,O*-chelating ligand in compound **5** was also studied using both UV-Vis and NMR spectroscopies and it was reported to be more kinetically stable to aquation and hydrolysis compared to **2,**[20] with a maximum absorbance at ~302 nm. These results were comparable to the results observed for compound **5** in HBS **(Figure 4.10a)** where the initial absorbance did not change much within 1 hr, signifying a considerable amount of stability at pH levels of ~7.4.[20]

4.1.4.2 Reaction of complex 5 in DMEM

In DMEM, the compound exhibited a decrease in absorbance in the region of 300 to 330 nm in a very similar way as was observed in the spectral changes for **3**, once again

showing the reactivity of chelated complexes in the medium (**Figure 4.10b)**. There was, however, no significant change for the peak at 381 nm, which might mean that ligand-exchange reaction was happening for similar donor groups. The substitution of oxalato ligands for chlorido ligands was observed for relatively high Cl^- concentrations (150 mM).[21] From the results, it is clear that **5** was reacting with the components in DMEM due to the different changes occurring in the spectrum compared to that in HBS.

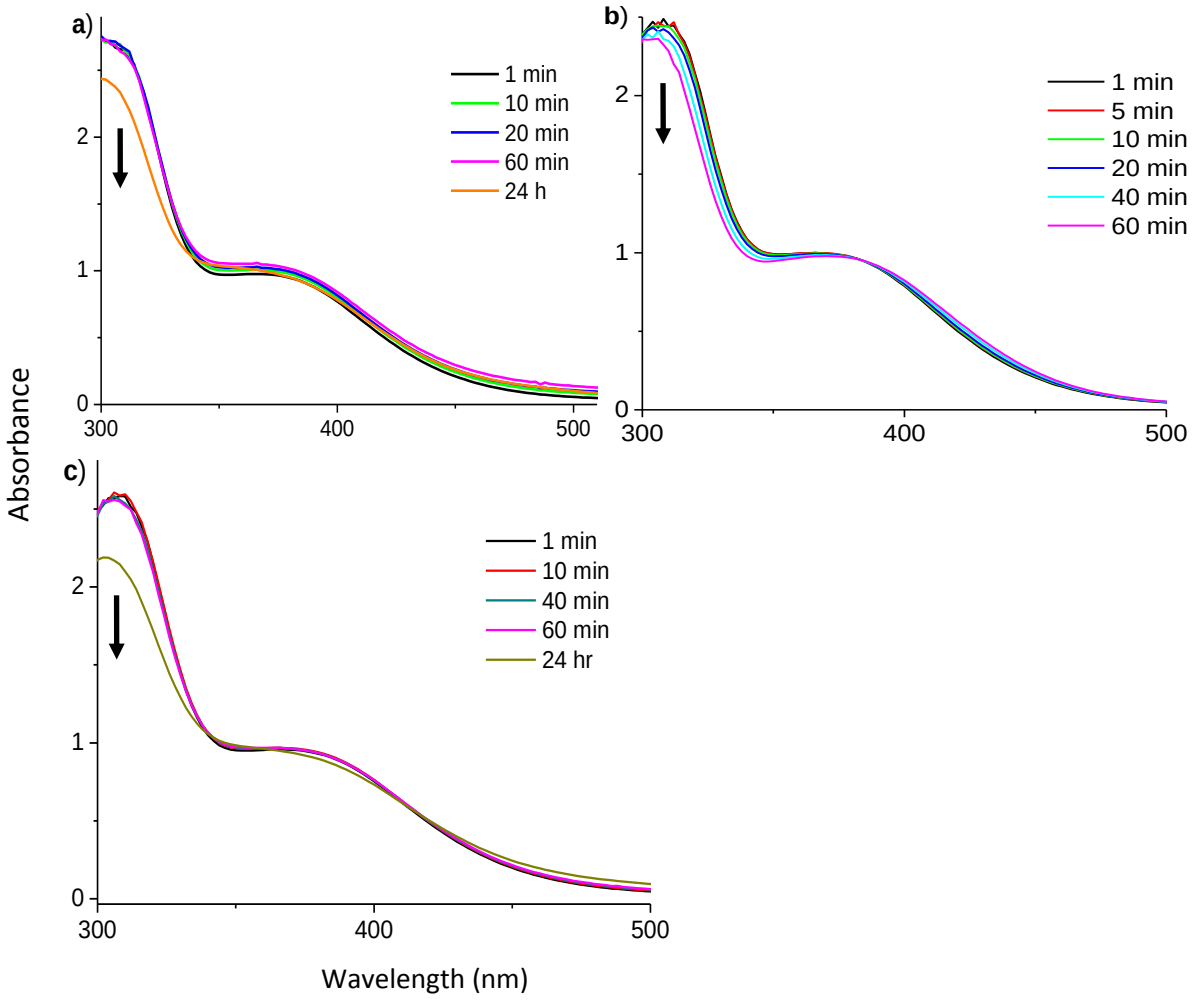

Figure 4.10: UV-Vis electronic absorption spectra for compound **5** (1.0 mM) at 37 °C; **a)** in HBS (20 mM HEPES, 140 mM NaCl, pH 7.4) up to 24 hr; **b)** in DMEM (pH 7.4) up to 60 min; and **c)** with BSA (5.0 mg/mL) up to 24 hr.

4.1.4.3 Reaction of complex 5 with BSA

The similarity of the spectrum to that of **4** was a rough indication of how the *O,O*-donors bind to proteins in aqueous media **(Figure 4.10c)**. Compound **5** remained stable for at least 1 hr before binding to BSA which is evidenced by the change in the 24 hr spectrum. The peak at 309 nm shifted and decreased to 302 nm and since this resembled its activity in DMEM, the resulting species might be the same.

4.1.5 [Ru(η^6-*p*-cymene)Cl_2(mimid)] (6)

4.1.5.1 Reaction complex of 6 in HBS

The UV-Vis spectral results indicated that compound **6** displayed ligand exchange in HBS (pH 7.4)within 1 hr but subsequent changes resulted in a shift to 387 nm within 24 hr **(Figure 4.11a)** without an isosbestic point. This showed that several reactions occurred on different timescales. The peak at 312 nm had a steady increase in absorbance throughout, which shows the formation of a new species after 24 hr. A comparison to the spectra of the product with that of compound **7 (Figure 4.11b)** suggested that compound **6** might have formed some dihydroxido-bridged species due to the similarity in peak positions. This observation also indicated that despite being a dichlorido complex, like **2**, **6** exhibited a somewhat slower substitution rate in aqueous solutions, which might be due to the electronic effects induced at the metal centre by the imidazole ligand.[18, 21]

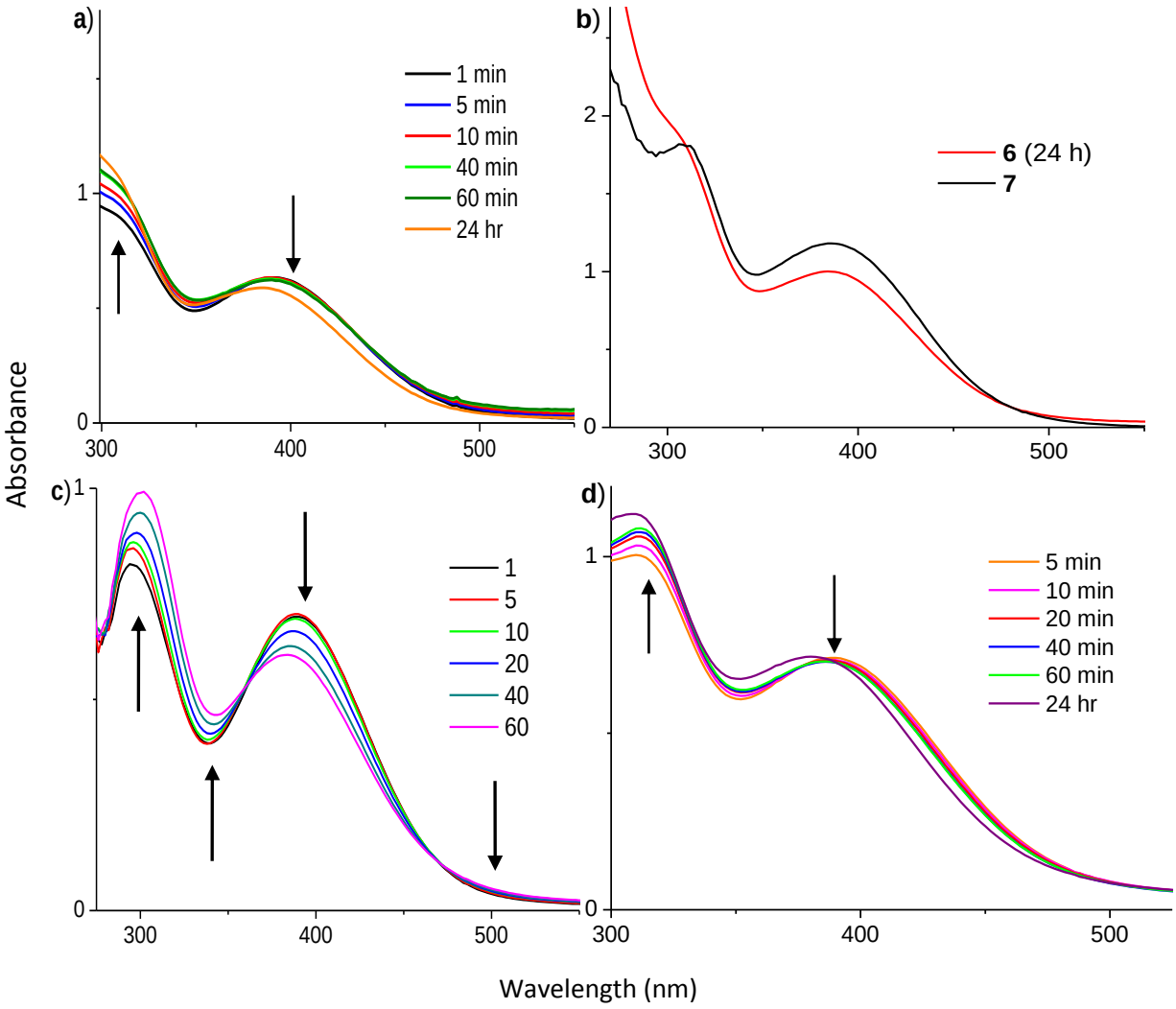

Figure 4.11: UV-Vis electronic absorption spectra for compound **6** (1.0 mM) at 37 °C; **a)** in HBS (20 mM HEPES, 140 mM NaCl, pH 7.4) up to 24 hr; **b)** comparison of the spectra in HBS with that of compound **7** at 24 hr; **c)** in DMEM (pH 7.4) up to 60 min; and **d)** with BSA (5.0 mg/mL) up to 24 hr. The arrows indicate the direction of changes within the spectra.

4.1.5.2 Reaction of complex 6 in DMEM

In contrast to HBS, the changes in the spectra of compound **6** in DMEM were quite different and were characterized by an isosbestic point at 360 nm **(Figure 4.12c)**. After 1 hr, the peak at 389 nm had shifted to 384 nm and decreased in intensity whereas another species that absorbed at 300 nm gradually formed. This was very similar to the spectral observation for compound **2** under the same conditions, which is indicative of binding to similar proteins in solution. The calculated rate constants ($4.15 \times 10^{-4}\ s^{-1}$) were an order of a magnitude lower than **2** ($4.35 \times 10^{-3}\ s^{-1}$) and **3** ($1.29 \times 10^{-3}\ s^{-1}$) in the same medium, which can be attributed to the ability of the imidazole ligand to stabilize the complex.[18, 22]

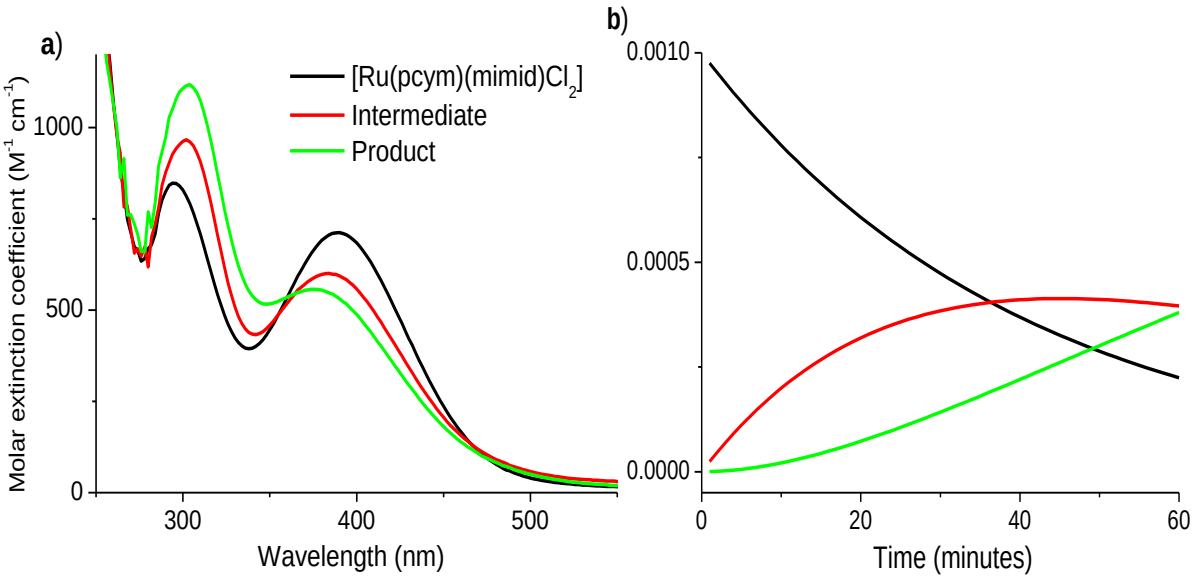

Figure 4.12: Global kinetic analysis results for: **a)** the molar extinction coefficients; and **b)** time-dependent concentration profiles upon the aquation of 1.0 mM compound **6** in DMEM at 37 °C. Product refers to the state of the solution after the reaction time.

4.1.5.3 Reaction of complex 6 with BSA

Despite the peaks being more prominent, the kinetics generally resembled the reactivity in HBS **(Figure 4.12d)**, thus the interaction with BSA did not exhibit any special characteristic features.

4.2 Discussion

Overall the Ru(II) arene compound, **2** showed the most reactivity in both cell culture medium and buffer at psychological pH values, which is likely to contribute to its anti-metastatic properties that resemble those of NAMI-A.[23] In contrast, compound **3** being more stable for longer hours in biological media then exhibits cytotoxic properties comparable to cisplatin.[24] The results reported herein show clear competition for the binding of proteins compared to the re-coordination of Cl^- ligands according to Scheme 4.2:

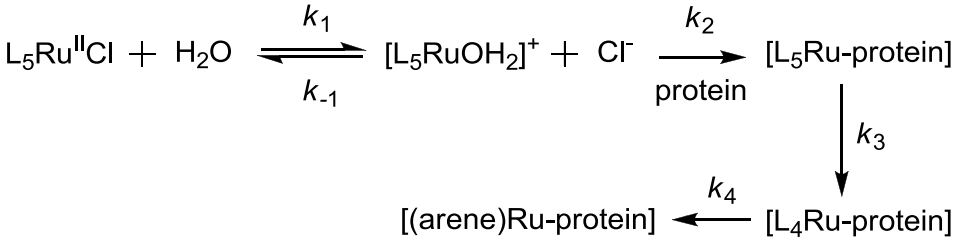

Scheme 4.2: Aquation and protein binding pathways of Ru(II) arene complexes in biological media.

In the absence of added Cl^-, the aquation goes almost to completion, but in its presence equilibrium is obtained that shifts dependent on [Cl^-]. To determine the values of k_1 and k_{-1} and the second aquation for the dichlorido species k_{-2}, detailed Cl^- dependent studies will be required. However, these have not been pursued here because Cl^- is always present in biological media and the reactions have been examined under those conditions which are biologically relevant. When proteins are present in the media (e.g. BSA or proteins in DMEM), the imidazole, carboxylato and S-donors can effectively compete with the back-reaction to rebind chlorido ligands. Therefore, studies carried out in HBS alone can give misleading results as to the reactivity in blood and the extra- , and intracellular environments of tumours. All of the studies here show that the reactions with biomolecules are fairly rapid and, hence, the nature of these reactions has been investigated in Chapter 5 using X-ray absorption spectroscopy.

4.3 References

1. Peacock, A. F. A.; Melchart, M.; Deeth, R. J.; Habtemariam, A.; Parsons, S.; Sadler, P. J., *Chem. Eur. J.* **2007,** *13*, 2601-2613.

2. Zhang, Y.; Guo, Z.; You, X.-Z., *J. Am. Chem. Soc.* **2001,** *123*, 9378-9387.

3. Scolaro, C.; Hartinger, C. G.; Allardyce, C. S.; Keppler, B. K.; Dyson, P. J., *J. Inorg. Biochem.* **2008,** *102*, 1743-1748.

4. Vargiu, A. V.; Robertazzi, A.; Magistrato, A.; Ruggerone, P.; Carloni, P., *J. Phys. Chem. B* **2008,** *112*, 4401-4409.

5. Kung, A.; Pieper, T.; Wissiack, R.; Rosenberg, E.; Keppler, B. K., *JBIC, J. Biol. Inorg. Chem.* **2001,** *6*, 292-299.

6. Futera, Z.; Klenko, J.; Sponer, J. E.; Sponer, J.; Burda, J. V., *J. Comput. Chem.* **2009,** *30*, 1758-1770.

7. Scolaro, C.; Bergamo, A.; Brescacin, L.; Delfino, R.; Cocchietto, M.; Laurenczy, G.; Geldbach, T. J.; Sava, G.; Dyson, P. J., *J Med Chem* **2005,** *48*, 4161-4171.

8. Sokolowska, M.; Bal, W., *J. Inorg. Biochem.* **2005,** *99*, 1653-1660.

9. Gossens, C.; Dorcier, A.; Dyson, P. J.; Rothlisberger, U., *Organometallics* **2007,** *26*, 3969-3975.

10. Morris, R. E.; Aird, R. E.; Murdoch, P. d. S.; Chen, H.; Cummings, J.; Hughes, N. D.; Parsons, S.; Parkin, A.; Boyd, G.; Jodrell, D. I.; Sadler, P. J., *J. Med. Chem.* **2001,** *44*, 3616-3621.

11. Peacock, A. F. A.; Habtemariam, A.; Fernandez, R.; Walland, V.; Fabbiani, F. P. A.; Parsons, S.; Aird, R. E.; Jodrell, D. I.; Sadler, P. J., *J. Am. Chem. Soc.* **2006,** *128*, 1739-1748.

12. Jennerwein, M.; Andrews, P. A., *Drug Metab. Dispos.* **1995,** *23*, 178-184.

13. Wang, F.; Chen, H.; Parsons, S.; Oswald, I. D. H.; Davidson, J. E.; Sadler, P. J., *Chem. Eur. J.* **2003,** *9*, 5810-5820.

14. Chen, H.; Parkinson, J. A.; Morris, R. E.; Sadler, P. J., *J. Am. Chem. Soc.* **2003,** *125*, 173-186.

15. Hu, W.; Luo, Q.; Ma, X.; Wu, K.; Liu, J.; Chen, Y.; Xiong, S.; Wang, J.; Sadler, P. J.; Wang, F., *Chem. Eur. J.* **2009,** *15*, 6586-6594.

16. Ang, W.-H.; Casini, A.; Sava, G.; Dyson, P. J., *J. Organomet. Chem.* **2011,** *696*, 989-998.

17. Kurzwernhart, A.; Kandioller, W.; Baechler, S.; Bartel, C.; Martic, S.; Buczkowska, M.; Muehlgassner, G.; Jakupec, M. A.; Kraatz, H.-B.; Bednarski, P. J.; Arion, V. B.; Marko, D.; Keppler, B. K.; Hartinger, C. G., *J. Med. Chem.* **2012,** *55*, 10512-10522.

18. Kandioller, W.; Hartinger, C. G.; Nazarov, A. A.; Bartel, C.; Skocic, M.; Jakupec, M. A.; Arion, V. B.; Keppler, B. K., *Chem. Eur. J.* **2009,** *15*, 12283-12291.

19. Kurzwernhart, A.; Kandioller, W.; Bartel, C.; Baechler, S.; Trondl, R.; Muehlgassner, G.; Jakupec, M. A.; Arion, V. B.; Marko, D.; Keppler, B. K.; Hartinger, C. G., *Chem. Commun.* **2012,** *48*, 4839-4841.

20. Ang , W. H.; Daldini, E.; Scolaro, C.; Scopelliti, R.; Juillerat-Jeannerat, L.; Dyson , P. J., *Inorg. Chem.* **2006,** *45*, 9006-9013.

21. Kilpin, K. J.; Cammack, S. M.; Clavel, C. M.; Dyson, P. J., *Dalton Trans.* **2013,** *42*, 2008-2014.

22. Clarke, M. J.; Bailey, V.; Doan, P.; Hiller, C.; LaChance-Galang, K. J.; Daghlian, H.; Mandal, S.; Bastos, C. M.; Lang, D., *Inorg. Chem.* **1996,** *35*, 4896-4903.

23. Bergamo, A.; Gaiddon, C.; Schellens, J. H. M.; Beijnen, J. H.; Sava, G., *J. Inorg. Biochem.* **2012,** *106*, 90-99.

24. Aird, R. E.; Cummings, J.; Ritchie, A. A.; Muir, M.; Morris, R. E.; Chen, H.; Sadler, P. J.; Jodrell, D. I., *Br. J. Cancer* **2002,** *86*, 1652-1657.

Chapter Five

Speciation Studies using XAS and XFM

5.1 Introduction

The chemical speciation of biologically active metals in living systems has always sparked considerable interest. Complexes often undergo ligand-exchange, hydrolysis (mentioned in Chapter 1), and redox reactions in biological systems, which changes the properties of the pro-drugs before reaching the targeted cells or tissue. XANES has thus emerged as a tool for obtaining important information, such as changes of the metal oxidation states and the spin-state, which might not be achievable using crystallographic experiments.[1] Spectra obtained using XANES can be used as a fingerprint for identifying speciation of metallodrugs with the help of a library of model complexes with known structures.[2] However, if an important model compound is absent from this library, the fitting obtained might be distorted from the actual speciation, which could result in some additional uncertainty in the biotransformations of the pro-drugs.[1] The studies reported here only concentrate on EXAFS values up to k = 9 Å^{-1} for linear regression analysis. Detailed EXAFS analysis at k > 9 Å^{-1} was not pursued due to noise and/or mixtures of products making MS analysis inappropriate.

5.1.1 X-ray Fluorescence Mapping

Due to the rising interest in the detection and quantification of elemental content in samples, this technique has been used in combination with XAS to determine species-specific maps.[3, 4] This enables the determination of spatial distribution of different elements by mapping the X-ray fluorescence intensity for different X-ray emission peaks.[3] Finney *et.*

al.[5, 6] have demonstrated the use of XFM in combination with 2D-gel electrophoresis to identify metalloproteins in complex biological mixtures. A typical setup of this technique is shown in **Figure 5.1**. The beam passes through a double crystal monochromator and is focused onto the sample with the help of a pinhole.[5] The sample is then raster-scanned through the focal spot and at each scan position, 10 or more elements are mapped pixel-by-pixel and quantified.[5] The emitted beam is collected at 90°.

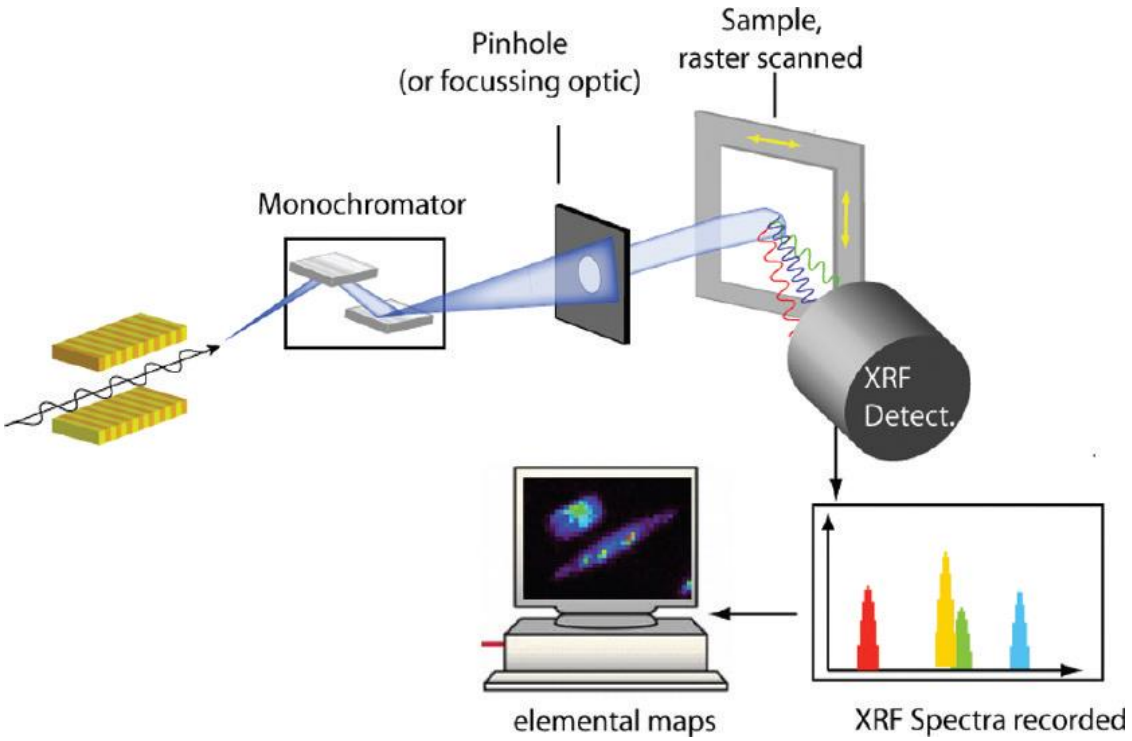

Figure 5.1: Schematic illustration of the principal components of an X-ray fluorescence microprobe beamline (not to scale).[5]

5.2 XANES results

5.2.1 Comparison of model compounds

A general comparison of the XAS spectra for the Ru(II) model compounds **1-9** (listed in **Chapter 3**, **Figure 3.5)** is displayed in **Figure 5.2**. While all EXAFS had similar general features, upon closer examination they have significantly different white-line absorbance intensities (**Figure 5.2b**) and energies as listed in **Table 5.1**. The post-edge regions were also quite different (**Chapter 3 Fig 3.6**), which serves as a good reference for predicting the coordination environment.

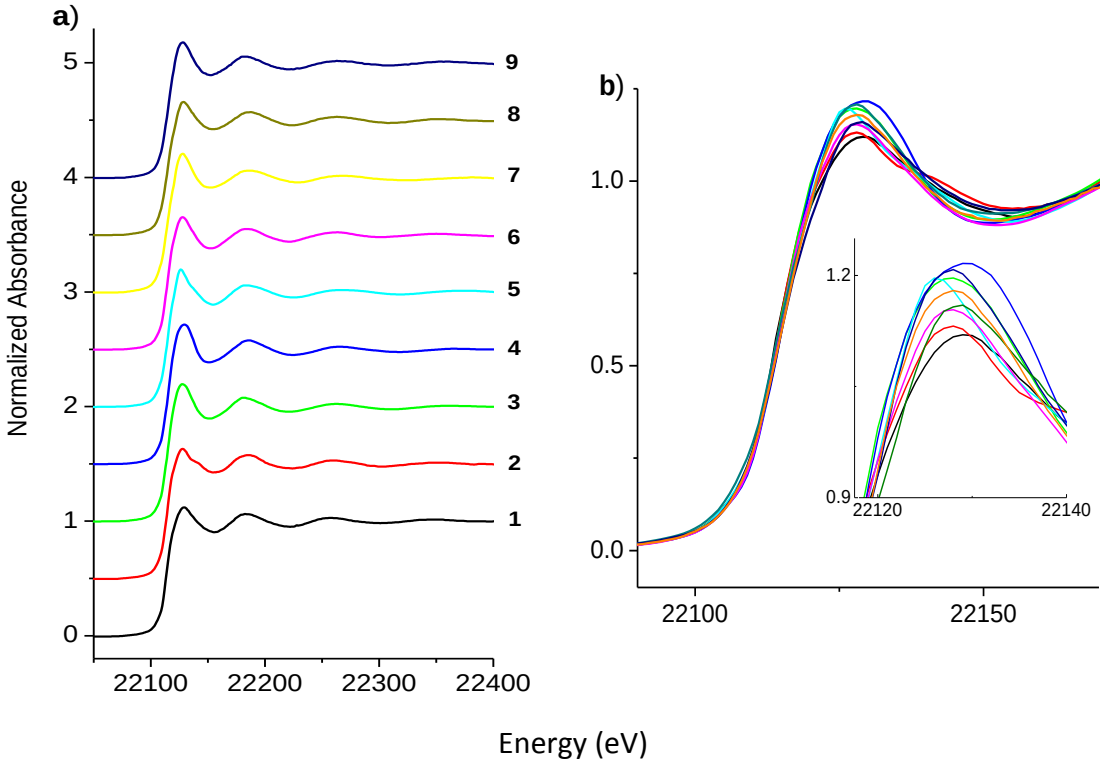

Figure 5.2.: Ru K-edge spectra of model Ru(II) compounds **1-9** (15 K, fluorescence detection mode): **a)** General XAS spectra comparison, **b)** overlay of the edge regions. Compounds were mixed at a 1:10 BN ratio.

The XANES spectral parameters of Ru(II) model complexes used in this study are listed in **Table 5.1**. For further observations of the changes in edge energy, spectra for a Ru(III) complex, $[Ru^{III}(NH_3)_6]Cl_3$ (which was found to have the closest edge compared with

the Ru(II) models) and a Ru(IV) complex, $Ru^{IV}O_2$ were obtained for oxidation state comparisons. A detailed comparison of the edge regions is shown in **Figure 5.3**, in which compound **2** was used as a reference. As already noted in literature,[7] the edge energy increased when the Ru oxidation state increased; a difference of 2.6 eV was observed between Ru(II) (**2**) and Ru(III) and a further 3.2 eV difference between Ru(III) and Ru(IV) (**Figure 5.3a)**. The position of the edge energy for this Ru(III) complex was used to determine if there was a loss of the arene ligand after reaction. The edge energies of both compounds **4** and **5** differed to that of **2** by a ~0.4 eV increase in energy, which served as a good indication for the presence of *O*-donor ligands. The XANES of the two thiol models **8** and **9**, which are representative of complexes with *S*-bound ligands, showed a significant decrease in the edge energy of 1-1.3 eV (**Figure 5.3c)**. Compound **7** with OH^- bridges showed a slight decrease in XANES edge energy by 0.4 eV, whereas the XANES of compound **3,** with *N*-donor ligands, only differed to that of **2** in intensity (**Figure 5.3d)**, as has been observed for Cr(III) complexes.[8]

XAS from three additional model complexes were obtained and introduced into the library for further references. Reactions of **2** in buffer solutions at pH 2 and pH 7 produced the aqua/chlorido and a hydroxido/aqua species, respectively after 1 hour.[9] Therefore, additional model compounds derived from **2** were obtained from reactions under these pH values, and the products were characterized by UV-Vis spectroscopy. The XAS of the resultant products **10a** (pH 2) and **10b** (pH 7) were introduced into the model library (**Figure 5.3e)**. Differences between the XANES of **2** and **10b** were very small, whereas that from the

aqua compound, **10a**, showed a ~0.8 eV decrease in the edge energy. The XAS from Na[Ru^{III}(edta)(SG)] **(11)** was used as an extra XAS reference for a Ru(III) model complex with *S*-bound ligands.[10]

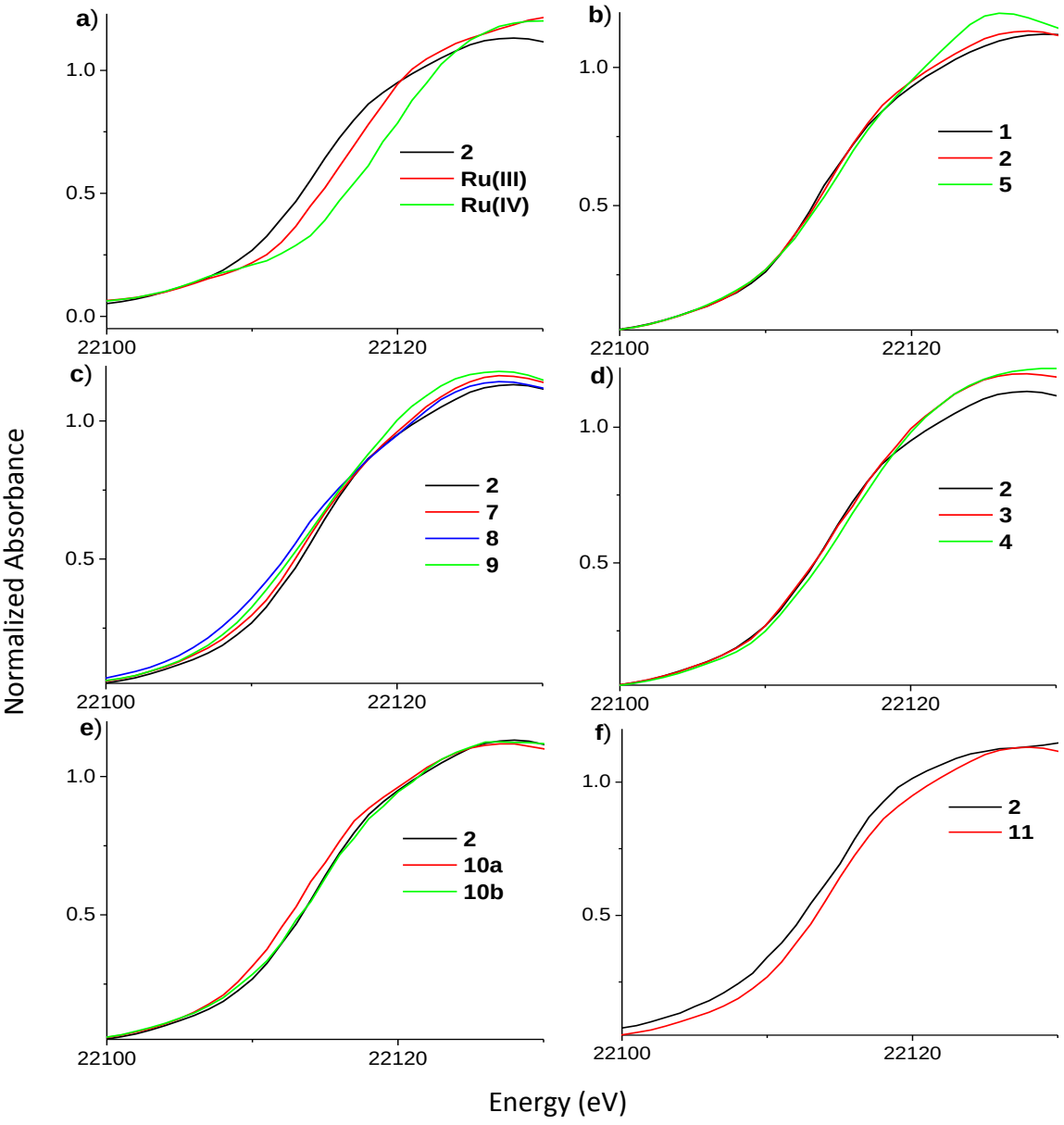

Figure 5.3: Comparison of the Ru K-edge XAS edge regions for the model Ru complexes **(Table 5.1)**: changes dependent on the **a)** oxidation state and **b-e)** different donor ligands at 15 K, fluorescence detection mode. X-axis of graphs are scaled to 22100 - 22130 eV.

Table 5.1: White line and edge energies for model compounds **1-11** (Refer to Chapter **3, Figure 3.5**).

	Model Compounds[a]	White-line Height	White-line Energy	Edge Energy (eV)	Donor ligands[b]
1	$[Ru(\eta^6\text{-}p\text{-cymene})Cl_2]_2$	1.12	22129.3	22113.2	2Cl
2	RAPTA-C	1.13	22127.6	22113.4	P, 2Cl
3	$[Ru(\eta^6\text{-}p\text{-cymene})(en)Cl]PF_6$	1.19	22127.8	22113.3	2N, Cl
4	$[Ru(\eta^6\text{-}p\text{-cymene})(acac)Cl]$	1.22	22129.5	22113.8	2O, Cl
5	OxaloRAPTA-C	1.19	22126.1	22113.7	2O, P
6	$[Ru(\eta^6\text{-}p\text{-cymene})Cl_2(mimid)]$	1.15	22127.6	22113.5	N, 2Cl
7	$[Ru_2(\eta^6\text{-}p\text{-cymene})(OH)_3]BPh_4$	1.16	22126.9	22112.9	$3OH^-$
8	$[Ru(\eta^6\text{-}p\text{-cymene})(tsal)]_2$	1.14	22126.8	22112.4	1S, 2O
9	$[Ru(\eta^6\text{-}p\text{-cymene})(en)(S\text{-}Ph)]PF_6$	1.18	22126.8	22112.6	2N, S
10a	$[Ru(\eta^6\text{-}p\text{-cymene})Cl(H_2O)(PTA)]^+$	1.12	22127.5	22112.6	H_2O,Cl^-,P
10b	$[Ru(\eta^6\text{-}p\text{-cymene})(OH)(H_2O)(PTA)]^+$	1.12	22127.6	22113.2	OH^-,H_2O,P
11	$Na[Ru^{III}(edta)(SG)]$	1.17	22134.5	22112.4	N, O, S

[a] Designations of the ligands: PTA = 1,3,5-triaza-7-phosphatricyclo-[3.3.1.1]decane; en = 1,2-ethanediamine; acac = 2,3-pentanedionato; mimid = *N*-methylimidazole; tsal = thiosalicylato acid; S-Ph = deprotonated benzenethiolato; SG = deprotonated *S*-bound glutathione (GSH); edta = *N,N,N'N'*-ethanediaminetetraacetate(4–). [b] Other than the arene carbons.

5.2.2 List of Samples

Sample preparation procedures and experimental conditions are described in Chapter 2 together with the syntheses of the model compounds **2-9**. The XAS obtained from the decomposition of compounds **2-6** in biological media, cells and blood samples were

studied under biologically relevant conditions; detailed designations are listed in **Table 5.2**. All samples were freeze-dried prior to XAS measurements to stop reactions, maximize Ru concentration and minimize Ru photoreduction in the X-ray beam.[1, 11]

Table 5.2: Sample preparation conditions for Ru(II) pro-drug interactions in biological media.

Sample[a]	Description	Incubation (h)
Reactions with Bovine Serum Albumin (A-D)		
A	0.60 mM Ru + 0.15 mM BSA in HBS, pH 7.4	1
B	0.60 mM Ru + 0.15 mM BSA in HBS, pH 7.4	24
C2a,b,c	1 mM Ru + 0.60, 0.30, 0.15 BSA in HBS, pH 7.4	15
D3-6	0.60 mM Ru + 0.30 mM BSA in HBS, pH 7.4	24
Buffer Samples at Physiological pH – E *(Ru – 0.60 mM)*		
E	Ru in HBS (pH 7.4)	24
Cell Culture Medium (DMEM, 2% v/v fetal calf serum) Samples - F *(Ru – 0.60 mM)*		
Fa,b	Ru in DMEM, pH 7.4	1,4
Serum Samples - G *(Ru – 0.60 mM)*		
Ga,b	Ru in bovine serum	1,4
HEPG2 Samples – H		
Ha, b	Ru + HEPG2 cells or cell culture medium	4
DNA Samples – I		
I2a,b,c	Ru with 10, 5, 2.5 mg/mL DNA in HBS, pH 7.4	15
Rat Blood Samples – J-K		
J2a,b	Ru in red blood cell (RBC) fraction (whole blood)	1,6
K2a,b	Ru in plasma fraction (isolated)	1,6
K2c	Ru in plasma fraction (whole blood)	1

[a] The letters indicate the treatment conditions and numbers indicate the model compounds.

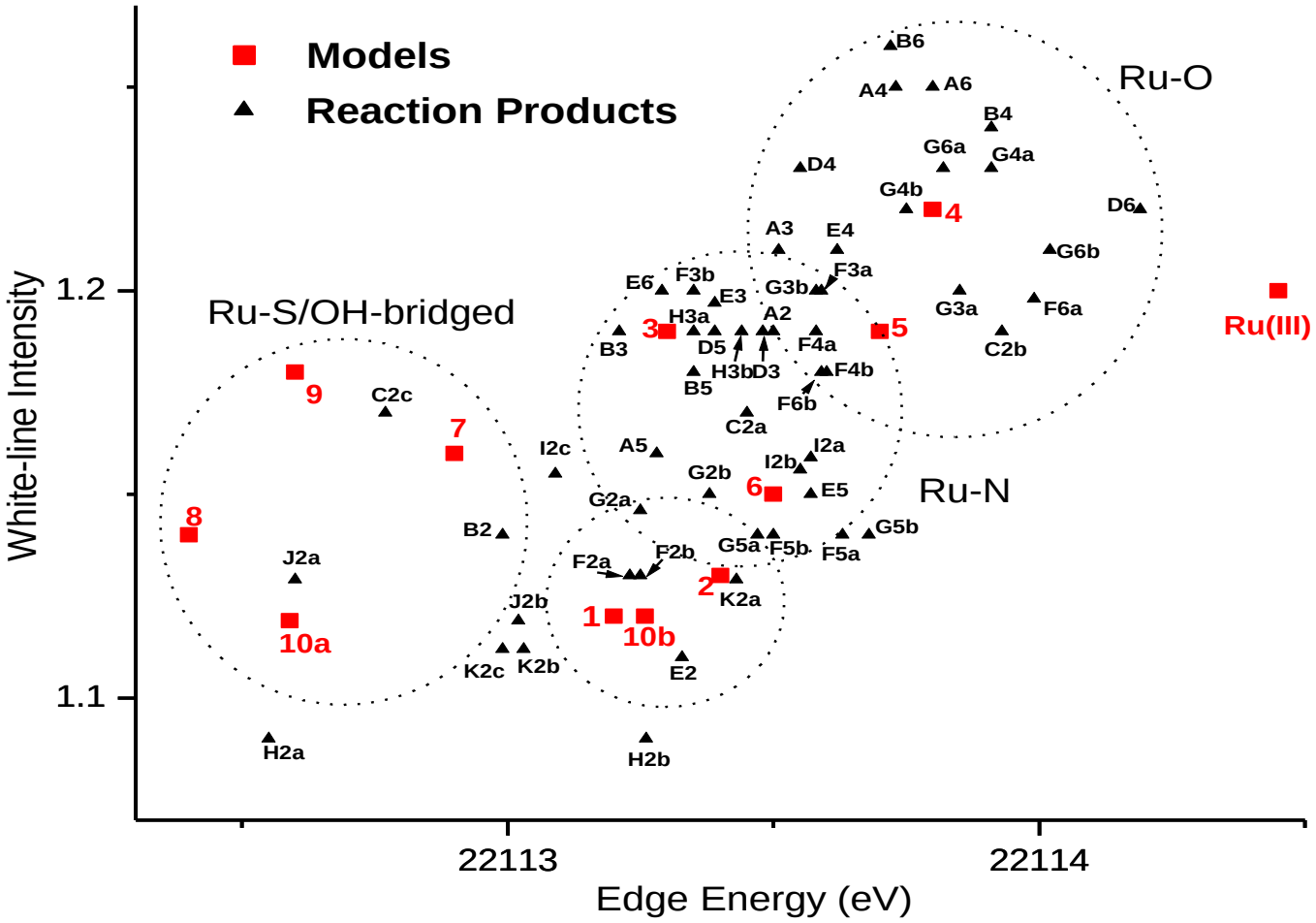

Figure 5.4: Comparison of edge energies and white-line intensities for model compounds **1-10b** and the biological samples, designations correspond to **Table 5.1** and **5.2**. Ru(III) is $[Ru^{III}(NH_3)_6]Cl_3$ shown in **Figure 5.3a** for edge energy comparisons.

The 2D and 3D plots of white-line intensities and energy comparisons for the model and biological complexes are displayed in **Figure 5.4** and **5.5**, in which the plot of the white-line intensity against the edge energy provided the best separation **(Figure 5.4)**. The XAS data from the biological samples fell at edge energy ranges below that of $[Ru^{III}(NH_3)_6]Cl_3$, which does not contain arene ligands and thus serves as an indication that the samples retained their arene ligands and were not oxidized to Ru(III). The cluster of XANES in the Ru-O and Ru-N regions indicated a mixture of Ru(II) arene species with *O* and/or *N* donors in the remaining three positions from the ligand-exchange process. A 3-D plot of white-line intensity vs. white-line energy plot that also included edge-energy **(Figure 5.5b)** did not improve the separation.

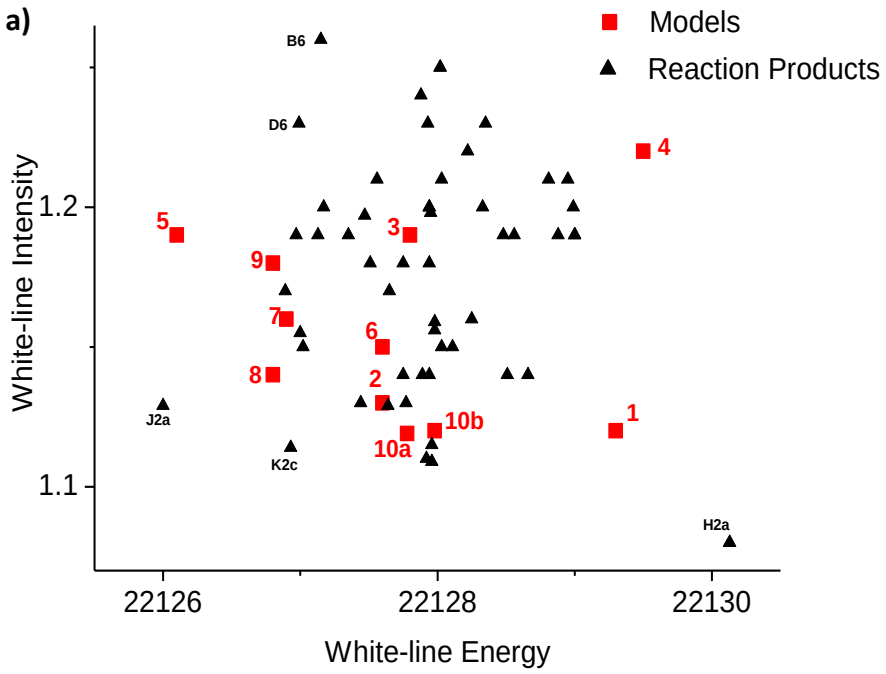

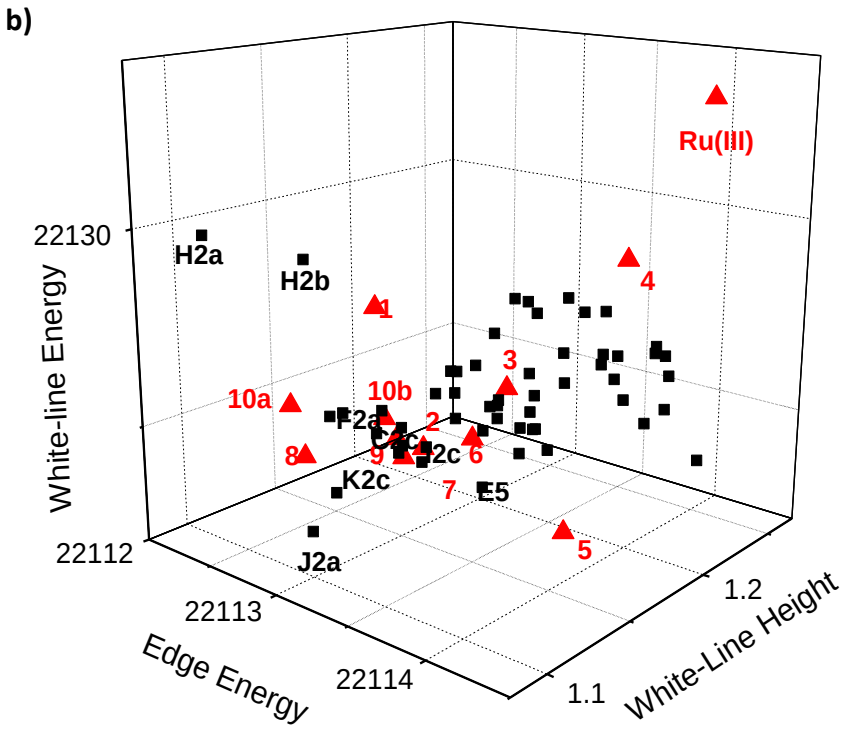

Figure 5.5: a) a 2D plot of the Ru K-edge white-line intensities vs white-line energies and **b)** a 3D plot for model compounds **1-10b** and the biological samples. These plots did not provide good enough separation for all the compounds, compared with Figure 5.4.

5.2.3 Reactions with Bovine Serum Albumin (BSA)

A comparison of XANES data for the reaction products of the Ru(II) compounds with BSA (4:1 Ru to BSA molar ratio) for 1 hr in HBS (pH 7.4) are shown in **Figure 5.6** and multiple linear regression results are given in **Table 5.3**. The spectra for compound **2** and **6** adducts

(**A2** and **A6**) were significantly different to those of their parent compounds, which indicated considerable reactivity within less than an hour. In contrast, the XANES of compounds **3**, **4** (**A3, A4**) barely differed from those of the parent complexes perhaps due to the chelating ligand providing more stability. This was consistent with UV-Vis spectroscopic results (Chapter 4). Compound **5** (**A5**) showed a slight shift of ~0.5 eV to lower energy **(Figure 5.5)**. When all adducts were compared **(Figure 5.6f)**, **A4** and **A6** converged indicating they had similar products, in which **A6** might contain *O*-donor ligands; **A2** and **A3** were very similar perhaps signifying an *N*-donor exchange for **A2**.

Next, the XANES of the Ru(II)-BSA adducts at 24 hr were compared to those from samples at 1 hr **(Figure 5.7)** and the only difference observed was a significant decrease in the edge energy by ~0.7 eV for compound **2** (**B2**). The presence of XANES from **11** (32 %) in the best fits indicated *S*-donor binding **(Table 5.3)**. Unlike that of compound **2**, the spectra for compounds **3-6** remained similar to those at 1 hr after 24 hr. A general comparison of the XANES of all adducts obtained after 24 hr of reaction (**Figure 5.7f**) showed that **B4** and **B6** still converged with linear regression results showing *O*-donor ligands as the majority contributions to the three non-arene sites **(Figure 5.8b)**. The linear regression fits to the XANES of **B3**-**B6** pointed to these Ru compounds having a higher affinity for *O*-donor ligand substitution and any Ru-S binding was probably too small to be detected. However, the fits for **B3**, which pointed to a complete change in coordination environment, were inconsistent with the XANES results and would have to be reanalysed to obtain a better fit.

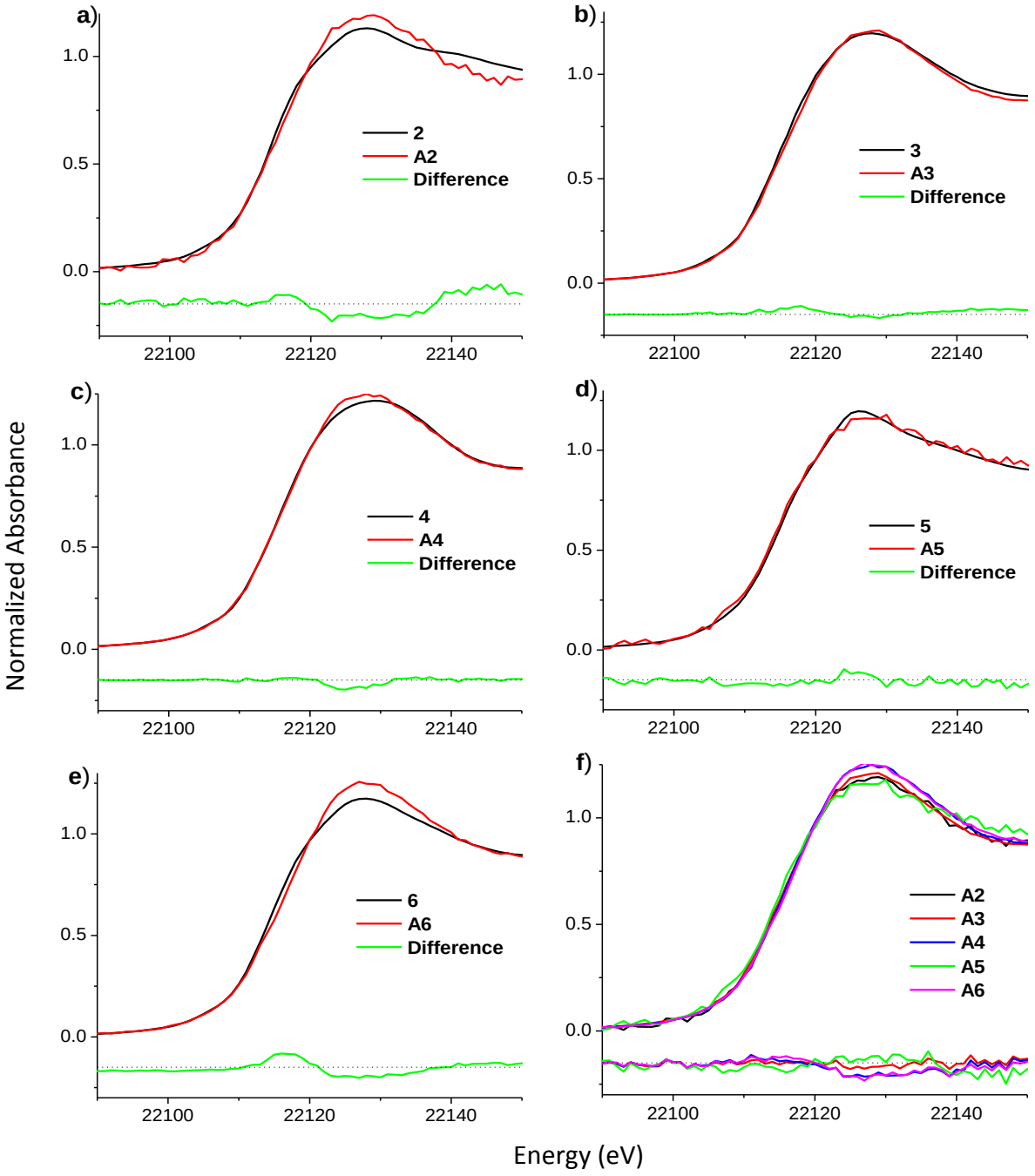

Figure 5.6.: Ru K-edge XANES (15 K, fluorescence mode) of compounds **2-6** (0.60 mM) and their reaction products with BSA (0.15 mM) in HBS (1 hr, 37 °C); and **f)** is the overlay. Designations are given in Table 5.2. All difference spectra are those of the parent compound minus those of the decomposition samples.

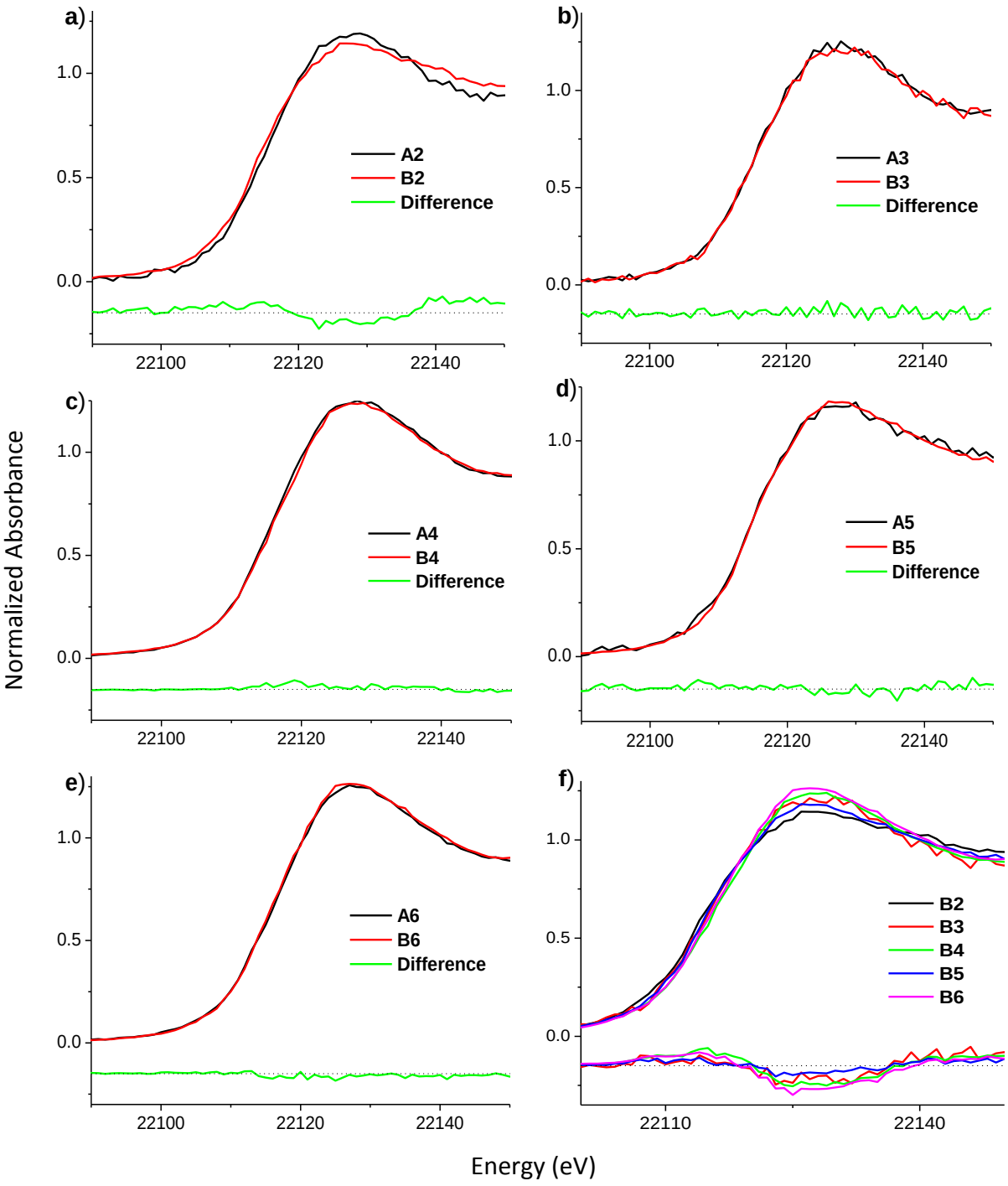

Figure 5.7.: Ru K-edge XANES (15 K, fluorescence mode) of compounds **2-6** (0.60 mM) and their reaction products with BSA (0.15 mM) in HBS for 1 h (conditions A) and 24 hr (conditions B) at 37 °C; **f)** is the overlay of the spectra of Ru-BSA adducts after 24 hr incubation. Designations are given in Table 5.2.

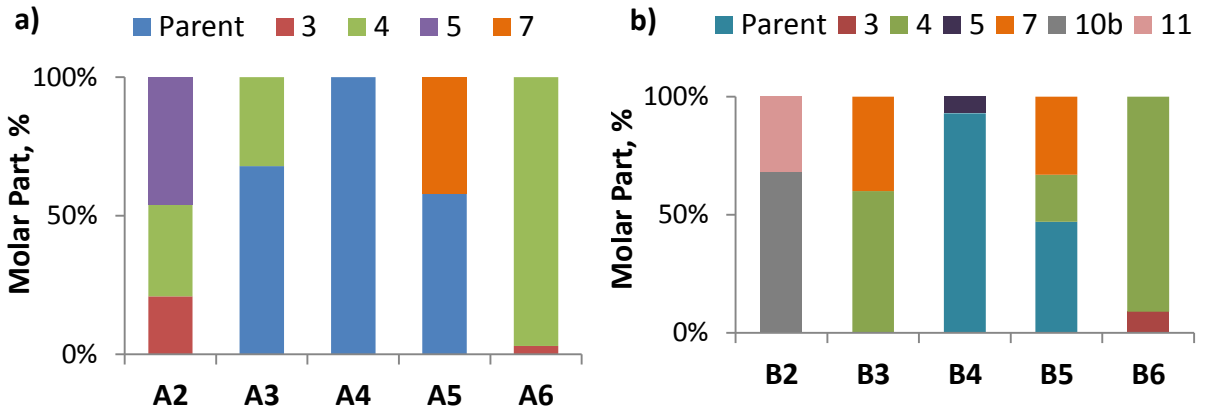

Figure 5.8.: Multiple linear regression results for the best fits of the Ru K-edge XANES for **a)** conditions A and **b)** B (designations given in Table 5.2). Details of the fits are shown in **Table 5.3.**

Table 5.3: Multiple linear regression analyses fits to the Ru K-edge XANES for conditions A and B.[a]

Sample	Parent (%)	3 (%)	4 (%)	5 (%)	7 (%)	10b (%)	11 (%)	R^2
A2	-	21(1)	33(4)	46(3)	-	-	-	0.99921
A3	68(3)	-	32(3)	-	-	-	-	0.99977
A4	100(1)	-	-	-	-	-	-	0.99967
A5	58(3)	-	-	-	42(7)	-	-	0.99844
A6	-	3(1)	97(3)	-	-	-	-	0.99948
B2	-	-	-	-	-	68(1)	32(1)	0.99962
B3	-	-	60(3)	-	40(3)	-	-	0.99845
B4	93(2)	-		7(2)	-	-	-	0.99952
B5	47(2)	-	20(2)	-	33(1)	-	-	0.99971
B6	-	9(2)	91(4)	-	-	-	-	0.99926

[a]This table shows the calculated molar percentages (%) of the XANES from the contributing model complexes with errors to the last significant figures and correlation coefficients (R^2) included. Multiple linear regression analyses were performed within the range 22100 – 22430 eV. Designations of the models and biological samples correspond to those given in Table 5.2.

Further experiments were conducted for compound **2** (1.0 mM), which was incubated with different concentrations of BSA (0.15 – 0.60 mM) for 15 hr at 37 °C, **Figure 5.9 (**conditions C in **Table 5.1)**. Post-edge regions are not shown since they were unchanged within experimental error. The XANES of all adducts differed significantly from those of the parent complex and had higher white-line intensities. For BSA concentrations lower than 0.60 mM, the edge shifted to the higher **(C2b)**, or lower energy regions **(C2c)**, depending on the conditions. The XANES of all three adducts displayed similar shapes **(Figure 5.9d)**, which indicated common reaction products were formed, mainly *O*-donor ligands **(Table 5.4)**, This also showed that 1.0 mM of **2** underwent ligand-exchange reactions with BSA regardless of the concentration within 0.15 – 0.60 mM of BSA.

A comparison of XAS for Ru(II):BSA adducts (2:1) for the pre-edge and post-edge regions for compounds **3-6** is shown in **Figure 5.11** (conditions D in **Table 5.1**)**.** Significant differences were observed in the XANES for **D6**, which had a more prominent shift to higher energy compared to that of **B6 (Figure 5.7e)** in both the pre-edge (~1.2 eV) and post-edge regions. The spectral shapes for both samples were still the same, which might mean that the same decomposition products were forming. Linear regression results of the best fits to the XANES consisted of those from model **4** (70%) and the parent complex (30%), which points to a mixture of *N/O* ligands **(Table 5.4)**. Reactions of compounds **3, 4** and **5** with BSA resulted in slight XANES spectral changes that were most apparent in the post-edge region but were overall similar to those of **B3**, **B4** and **B5 (Figure 5.7b-d)**.

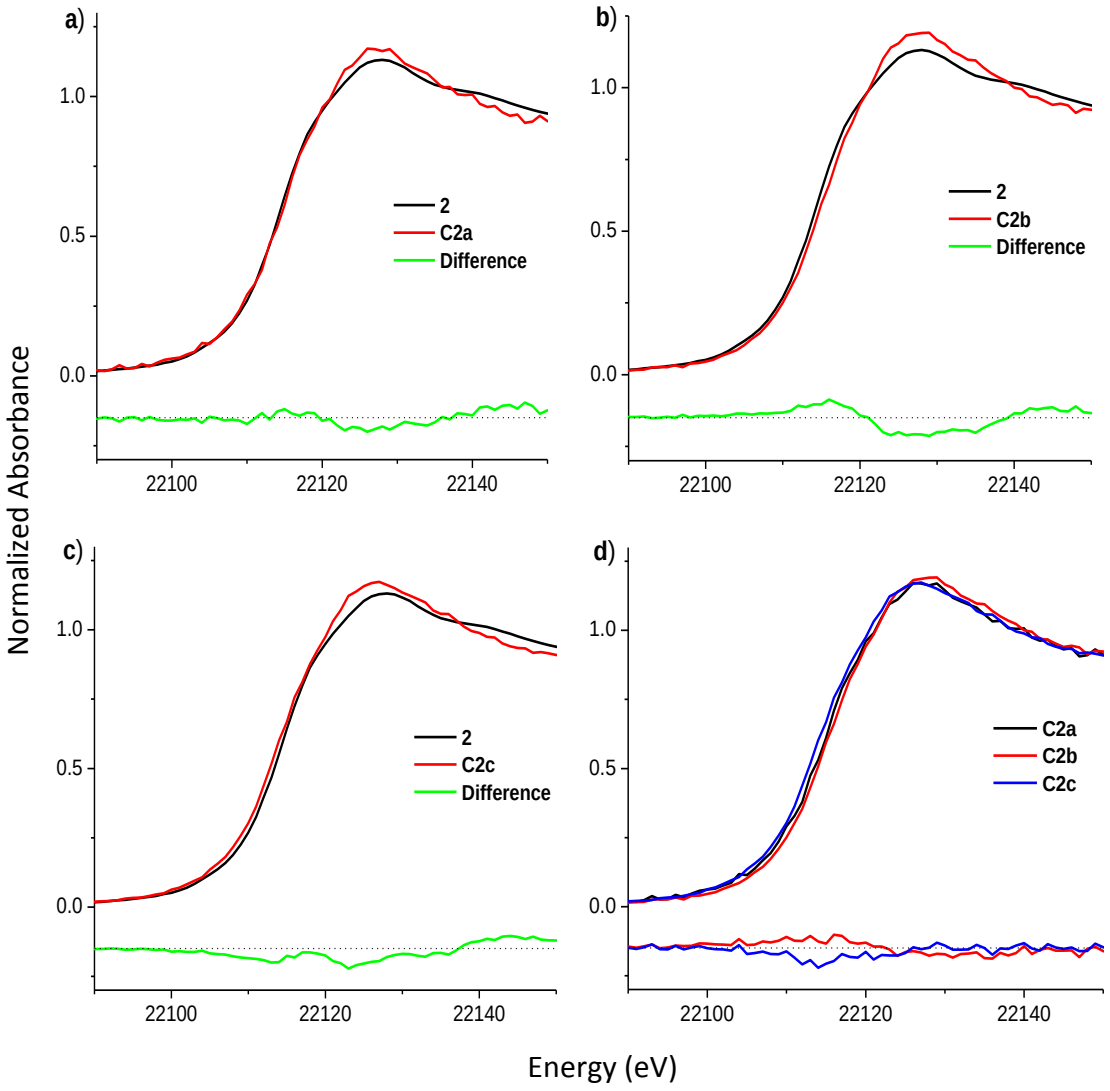

Figure 5.9: Ru K-edge XANES (15 K, fluorescence mode) comparison of compound **2** (1.0 mM) with different concentrations of BSA (conditions C): **a)** 0.60 mM, **b)** 0.30 mM, **c)** 0.15 mM in H_2O for 15 hr at 37 °C; **d)** is the overlay of the spectra of Ru-BSA adducts after 15 h incubation. Designations are given in Table 5.2.

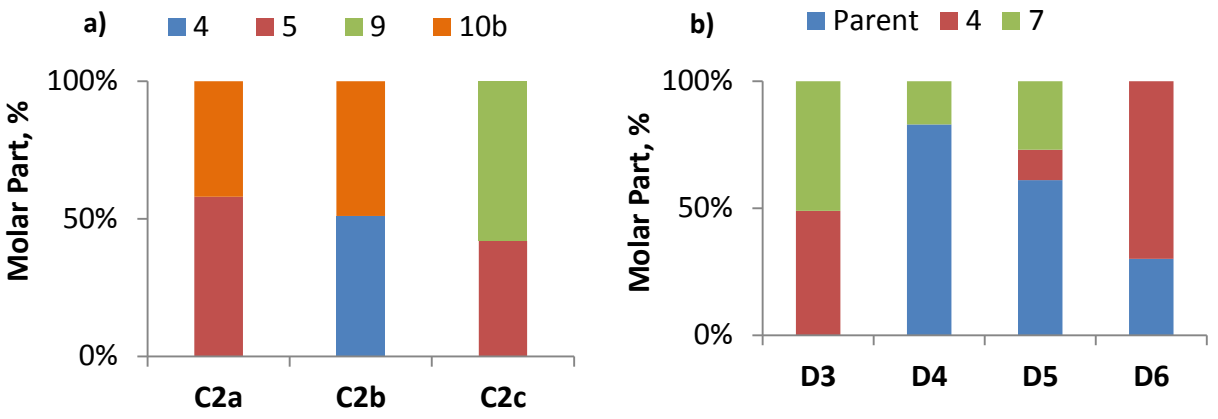

Figure 5.10.: Multiple linear regression results for the best fits of the XANES for **a)** conditions C and **b)** D (designations given in Table 5.2). Details of the fits are shown in **Table 5.4.**

Table 5.4: Multiple linear regression analyses Ru K-edge XAS fits for conditions C and D.[a]

Sample	Parent (%)	4 (%)	5 (%)	7 (%)	9 (%)	10b (%)	R^2
C2a	-	-	58(1)	-	-	42(3)	0.99972
C2b	-	51(2)	-	-	-	49(2)	0.99964
C2c	-	-	42(2)	-	58(2)	-	0.99977
D3	-	49(1)	-	51(2)	-	-	0.99972
D4	83(2)	-	-	17(1)	-	-	0.99972
D5	61(3)	12(2)	-	27(3)	-	-	0.99972
D6	30(2)	70(3)	-	-	-	-	0.99923

[a]This table shows the calculated molar percentages (%) of the XANES from contributing model complexes with errors to the last significant figures and correlation coefficients (R^2) included. Multiple linear regression analyses were performed within the range 22100 – 22430 eV. Designations of the models and biological samples correspond to those given in Table 5.2.

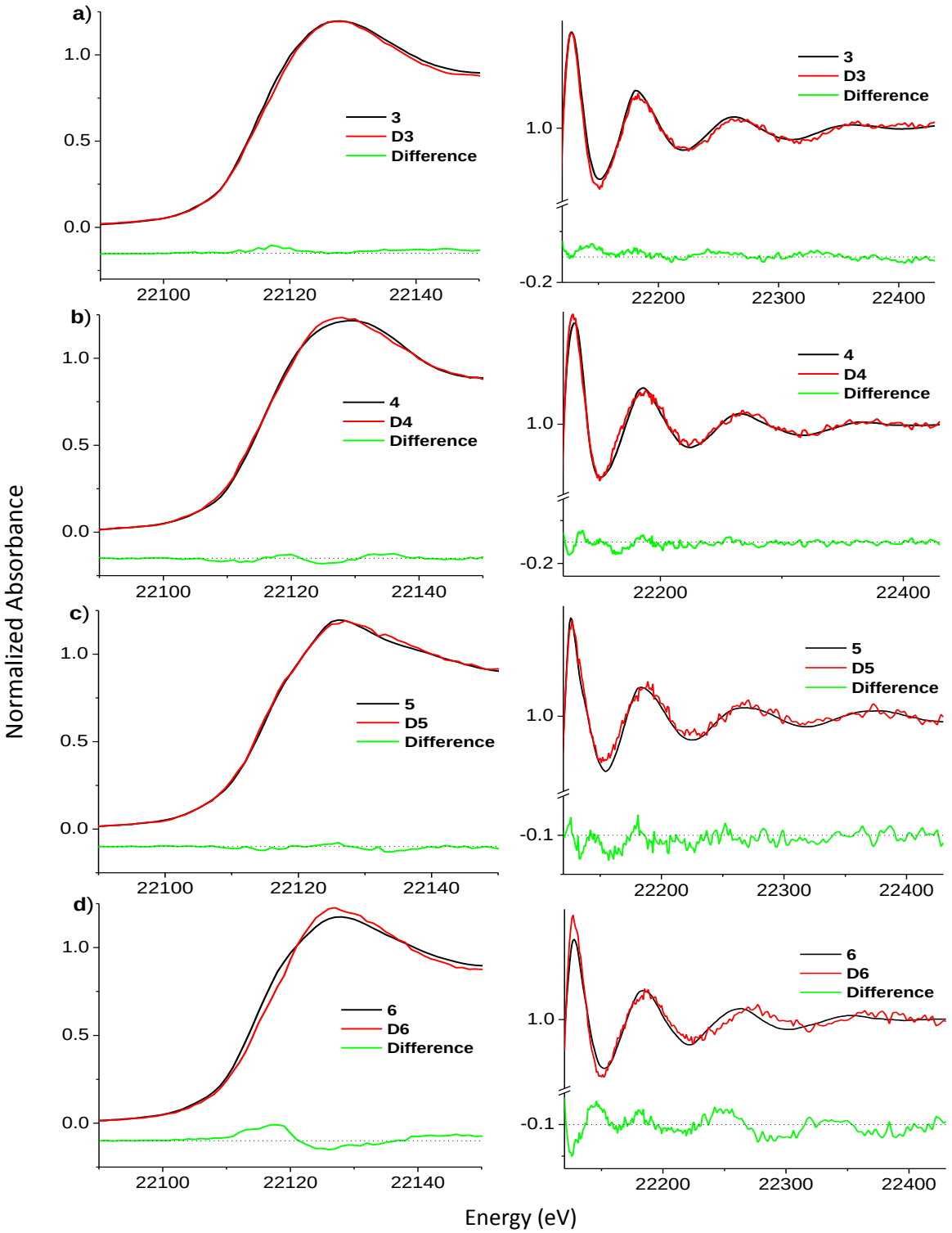

Figure 5.11.: Ru K-edge XAS (15 K, fluorescence mode) comparison of compounds **3-6** (0.60 mM) with BSA (0.30 mM) in HBS (pH 7.4) for 24 hr at 37 °C (conditions D). Designations are given in Table 5.2.

5.2.4 Reactions in aqueous buffer

The XANES spectra for all compounds incubated in HBS (pH 7.4) were compared in **Figure 5.13** (conditions **E, Table 5.2**). After 24 hr, the XANES edge of compound **5 (E5)** showed the biggest difference with a shift of 1.1 eV to a lower energy, which on linear regression fitting was indicative of complete changes in the coordination environment of the non-arene ligand sites. The best linear regression fits consisted of XAS from Model **1** (23%) and Model **7** (77%) **(Table 5.5)**, indicating that the decomposition product **E5** had undergone complete ligand exchange in the non-arene positions and probably lost its PTA ligand. In contrast to compound **2 (E2)**, which only showed slight changes in the XANES over 24 hr, the changes observed for compound **5** were not consistent with the literature claims that this compound was kinetically more stable than **2** in aqueous media.[12]

Over 24 hr, the XANES from the reactions of compounds **2, 4** and **6** exhibited slight changes in their intensities compared to the parent complexes, whereas the XANES of compound **3** remained largely unchanged, retaining 85% of the parent complex over 24 hr in the best fit to the XANES **(Table 5.5)**. This suggests that the *N*-*N* chelating ligand is comparatively more tightly bound in an aqueous buffer environment at pH 7.4. An overlay of the spectra showed that the XANES of the decomposition products of compounds **3 (E6)** and **6 (E6)** converged with linear regression results pointing to a mixture of *N/O*-donor ligands, possibly forming common products.

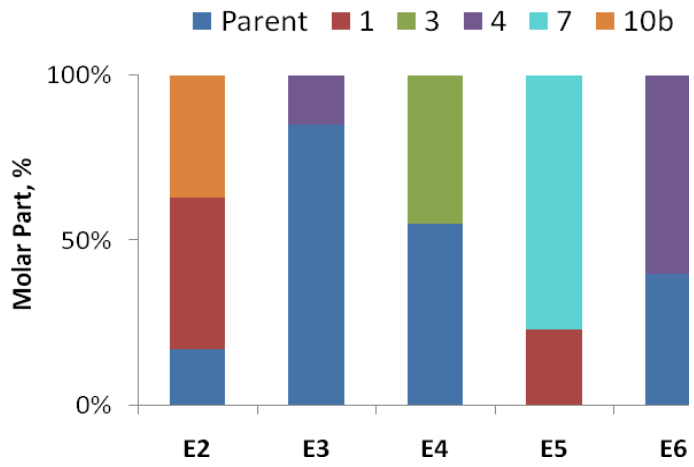

Figure 5.12.: Multiple linear regression results for fits to the Ru K-edge XAS under conditions **E** (designations are given in Table 5.2). Details of the fits are shown in **Table 5.4.**

Table 5.5: Multiple linear regression analyses fits to the Ru K-edge XAS for conditions **E**.[a]

Sample	Parent (%)	1 (%)	3 (%)	4 (%)	7 (%)	10b (%)	R^2
E2	17(2)	46(3)	-	-	-	37(2)	0.99990
E3	85(2)	-	-	15(2)	-	-	0.99987
E4	55(2)	-	45(2)	-	-	-	0.99983
E5	-	23(3)	-	-	77(3)	-	0.99952
E6	41(2)	-	-	59(2)	-	-	0.99961

[a]This table shows the calculated molar percentages (%) of the XANES from the contributing model complexes with errors to the last significant figures and correlation coefficients (R^2) included. Multiple linear regression analyses were performed within the range 22100 – 22430 eV. Designations of the models and biological samples correspond to those given in Table 5.2.

.

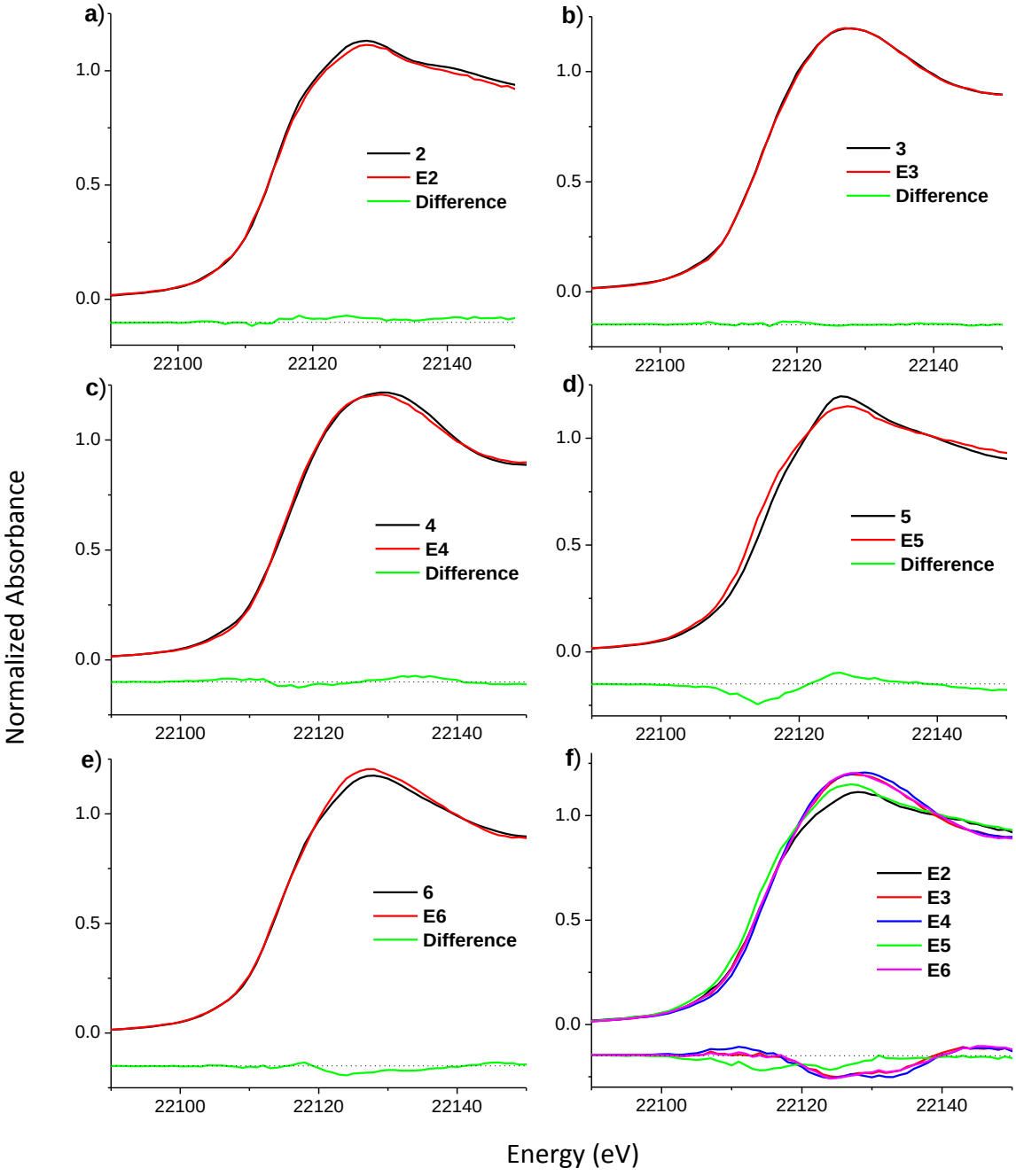

Figure 5.13: Ru K-edge XANES (15 K, fluorescence mode) from the decomposition products of compounds **2-6** (0.60 mM) in HBS (pH 7.4) for 24 hr at 37 °C (conditions **E**), **f)** overlay of the compounds at 24 h. Designations are given in Table 5.2. All difference spectra are those of **E2** minus **E3 – E5**.

5.2.5 Reactions of Ru complexes in cell culture medium and serum

Compounds **2-6** were incubated in cell culture medium (DMEM, containing 2% v/v fetal calf serum) (**Figure 5.15**) (conditions **F, Table 5.2**) or newborn calf serum (**Figure 5.17**) (conditions **G, Table 5.2**) for 1 or 4 hr at 37 °C, and the resultant spectra were compared (**Figures 5.14 – 5.17**). The XAS spectra for the decomposition products of compound **4** in DMEM were the same for both the 1- and 4-hr treatments **(Figure 5.15c)**. There was a decrease in white-line intensity but negligible changes in edge energy compared to those of the parent complex and linear regression results suggested partial aquation and *N*-donor ligand exchange **(Table 5.5)**. There were subtle differences between the 1 and 4 hr XAS for the reaction of compound **3**, which indicated slow ligand-exchange reactions **(Figure 5.15b)**. The XANES edge energy of compound **3** showed a gradual shift to higher energy, which might be due to an increase in the average number of *O*-donors **(Table 5.5)**.

The XANES edge energy for compound **5** slightly shifted to the lower values, which may indicate partial binding to *S*-donor ligands **(Figure 5.15d)**. This is supported by the results for the best fit in linear regression of the XANES: ~22-25% fit to model **11**. Larger changes in the XAS were observed for both compounds **2** and **6**, which had edge shifts to lower and higher energies, respectively. Compound **6** displayed similar spectral changes to **3**, in which the edge shifted ~0.35 eV to a higher energy with a concomitant increase in white-line peak intensity, which once again suggested an exchange to *O*-donor ligands **(Figure 5.15e)**.

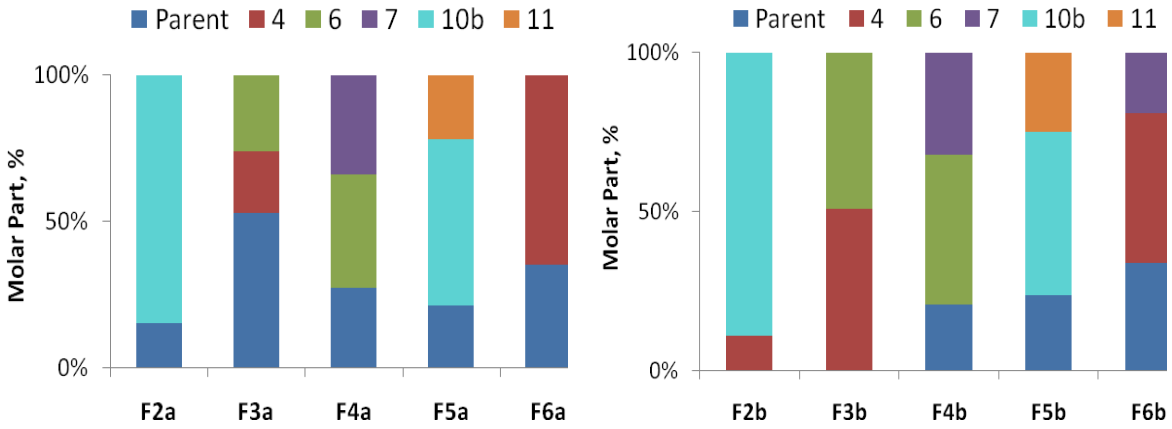

Figure 5.14.: Multiple linear regression results for the best fits to the XANES from conditions **F** (designations given in Table 5.2). Details of the fits are shown in **Table 5.5.**

Table 5.5: Multiple linear regression analyses fits to the Ru K-edge XANES for conditions **F**.[a]

Sample	Parent (%)	4 (%)	6 (%)	7 (%)	10b (%)	11 (%)	R^2
F2a	15(3)	-	-	-	85(3)	-	0.99973
F3a	53(3)	21(3)	26(3)	-	-	-	0.99974
F4a	27(2)	-	39(1)	34(2)	-	-	0.99982
F5a	21(3)	-	-	-	57(3)	22(1)	0.99970
F6a	35(2)	65(2)	-	-	-	-	0.99962
F2b	-	11(2)	-	-	89(2)	-	0.99962
F3b	-	51(2)	49(2)	-	-	-	0.99970
F4b	21(2)	-	47(1)	32(2)	-	-	0.99980
F5b	24(2)	-	-	-	51(3)	25(1)	0.99976
F6b	34(3)	47(2)	-	19(3)	-	-	0.99974

[a]This table shows the calculated molar percentages (%) of the XANES from contributing model complexes with errors to the last significant figures and correlation coefficients (R^2) included. Multiple linear regression analyses were performed within the range 22100 – 22430 eV. Designations of the models and biological samples correspond to those given in Table 5.2.

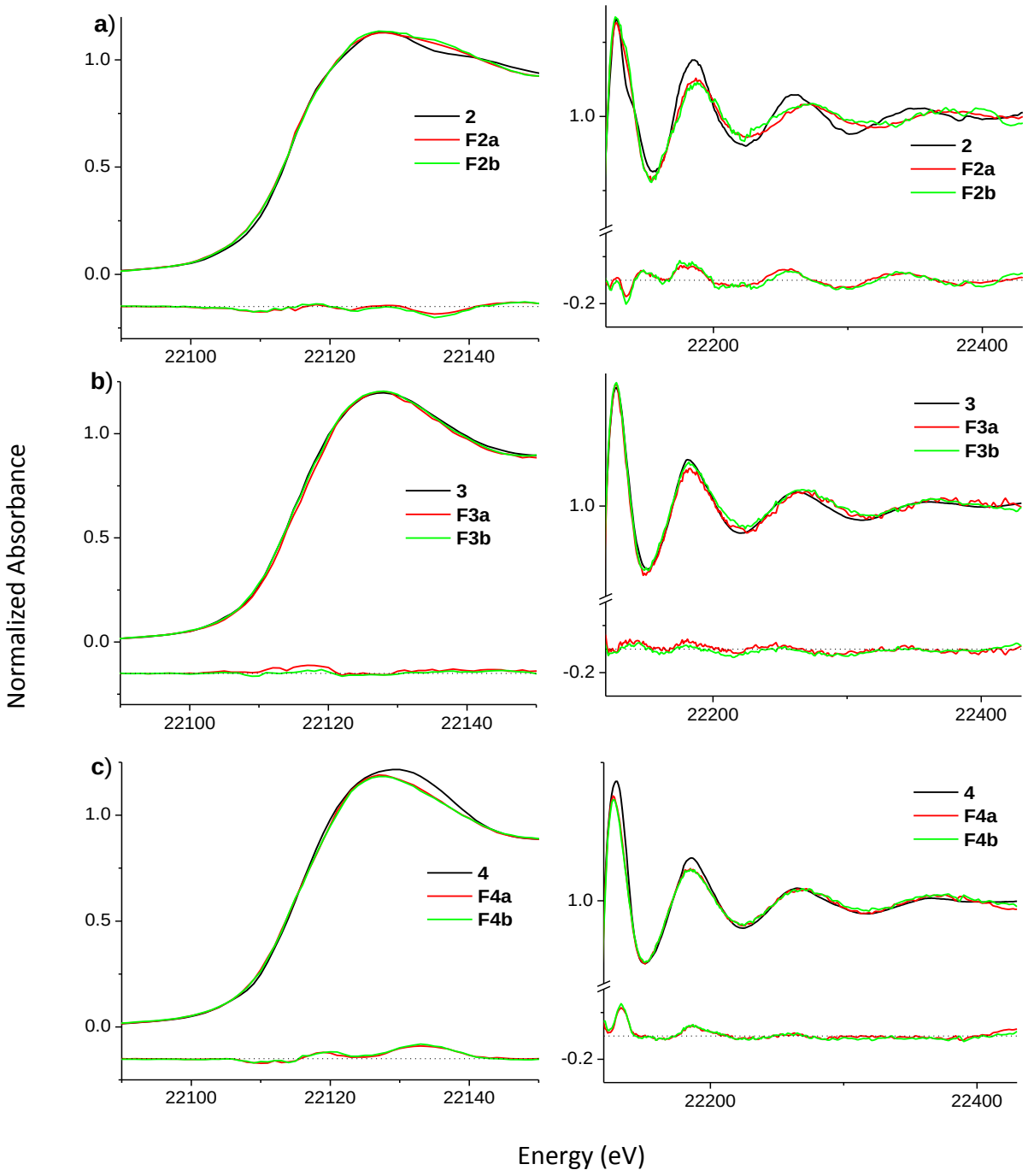

Figure 5.15: Ru K-edge XAS (15 K, fluorescence mode) XAS comparison of the decomposition of compounds **2-6** (0.60 mM) in DMEM for 1 and 4 hr at 37 °C (conditions F); **f)** is the overlay of the compounds in DMEM after 4 hr. Descriptions and designations are listed in **Table 5.2**.

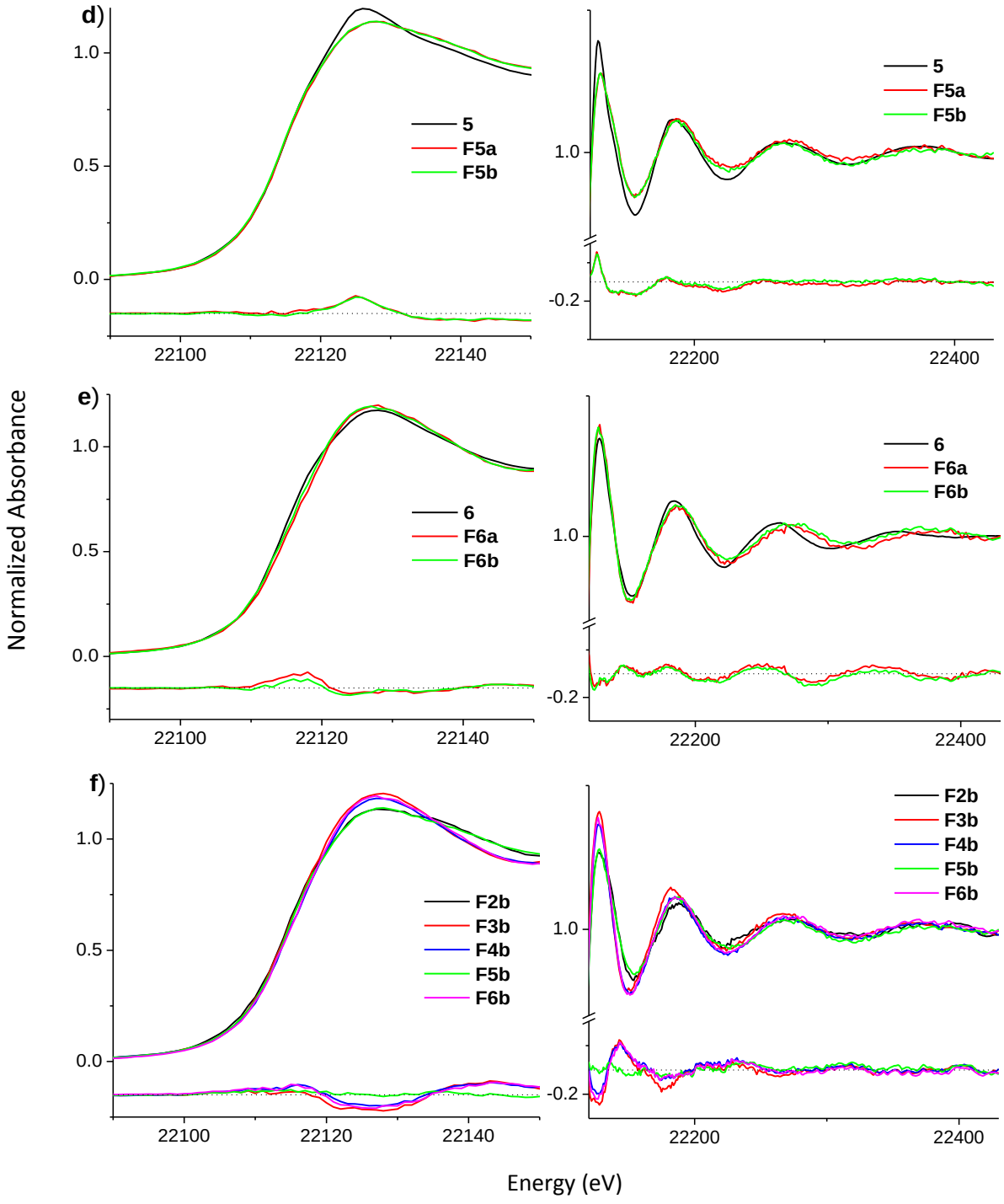

Figure 5.15 (cont.)

From the overlay of all spectra at 4 hr, the XAS of compounds **4** and **6** converged in both the edge and post-edge regions, implying a common mixture of *N/O*-ligands in the decomposition products **(Figure 5.15f)**. The XAS of **3** showed a similar XANES region to both **4** and **6** but a significantly different post-edge region, which may be due to retaining around ~50% of its parent compound after 4 hr, as indicated from the best fits from the linear regression results; thus, a different coordination environment. The XAS of compounds **2** and **5** were similar and showed good fits to *O/*H_2O ligands. It is also worth noting that the XAS of **F2b** was similar to the reaction with BSA **(B2)** (**Figure 5.7a**), which supports the evidence that **2** has a high binding affinity to serum proteins (BSA) during decomposition in serum-containing media due to the abundance of albumin.[10, 13]

The Ru K-edge XAS results for the decomposition in undiluted serum are shown in **Figure 5.17** (conditions **G, Table 5.2**), and the results of multiple linear regression analyses are given in **Table 5.6**. The edge for compounds **3** and **6** shifted to higher energies, which indicated substitution of some of the ligands with *O*-donors **(Table 5.6)** though the changes seemed to occur faster for compound **6** (**G6b)** with only ~30% of the parent XANES contributing to the best fit after 4 hr. The XAS of compounds **2, 4** and **5** had slight decrease in their intensities compared to their parent complexes, but overall, their XAS did not show changes as significant as in DMEM; especially for the post-edge part of the spectra. This indicated that the compounds were either reasonably stable in serum up to 4 hr, or, more

likely, underwent ligand exchange with similar donor groups that were different in the presence of serum proteins.

An increase in the white-line intensity of the XANES was observed for compound **2** between the 1 **(G2a)** and 4 hr **(G2b)** reactions **(Figure 5.17a)**. Linear regression gave good fits to the XANES using models **1** (53%), **4** (17%) and **5** (30%), which pointed to *O*-donor exchanges over time. Comparatively, differences between the XAS of the samples at 1 and 4 hr for the other compounds were not prominent, which showed that most decomposition had happened within 1 hr. Compound **4** even appeared to be relatively inert throughout this time period **(Figure 5.17c, Table 5.6)**. The overlay of all spectra showed that compounds **3** and **6**, compounds **2** and **5** shared similar decomposition products **(Table 5.6, Figure 5.17f)**. Since BSA is the most abundant serum protein,[14] not surprisingly the XAS spectra of the decomposition products had similar shapes to the Ru-BSA adducts (**Figure 5.6**, Conditions **A** and **B**).

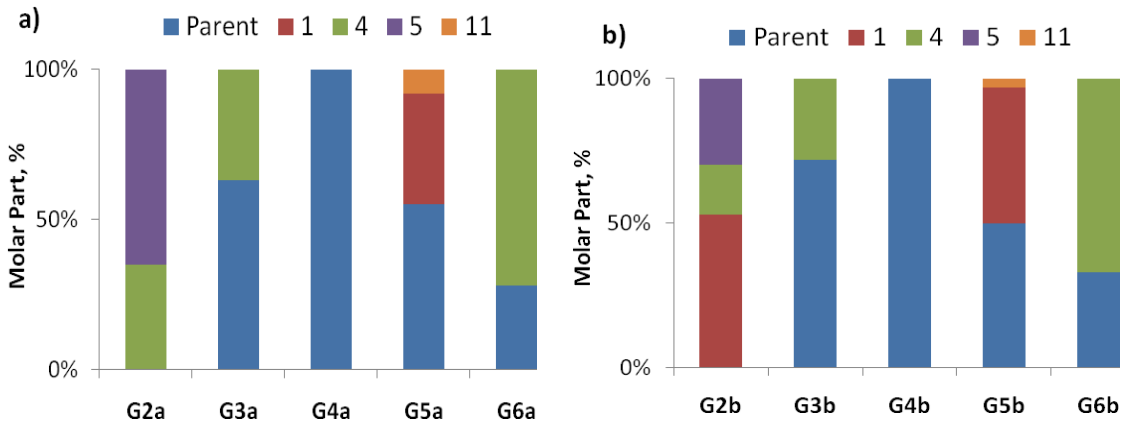

Figure 5.16.: Multiple linear regression results for fits to the Ru K-edge XAS for conditions **G** (designations given in Table 5.2). Details of the fits are shown in **Table 5.6.**

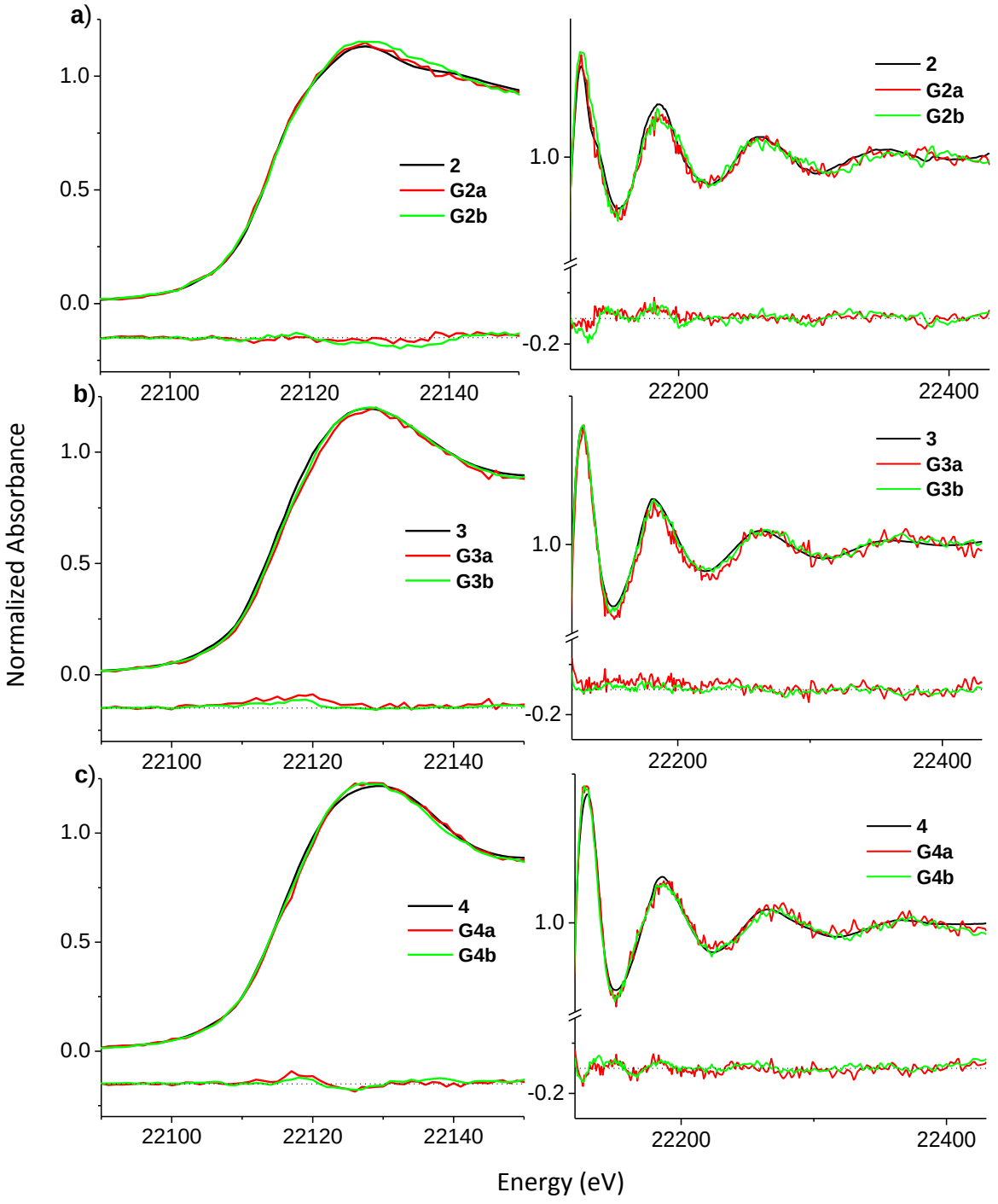

Figure 5.17: Ru K-edge XAS (15 K, fluorescence mode) from the decomposition of compounds **2-6** (0.60 mM) in serum for 1 and 4 hr at 37 °C (conditions G); **f)** is the overlay in serum after 4 h. Designations are given in Table 5.2.

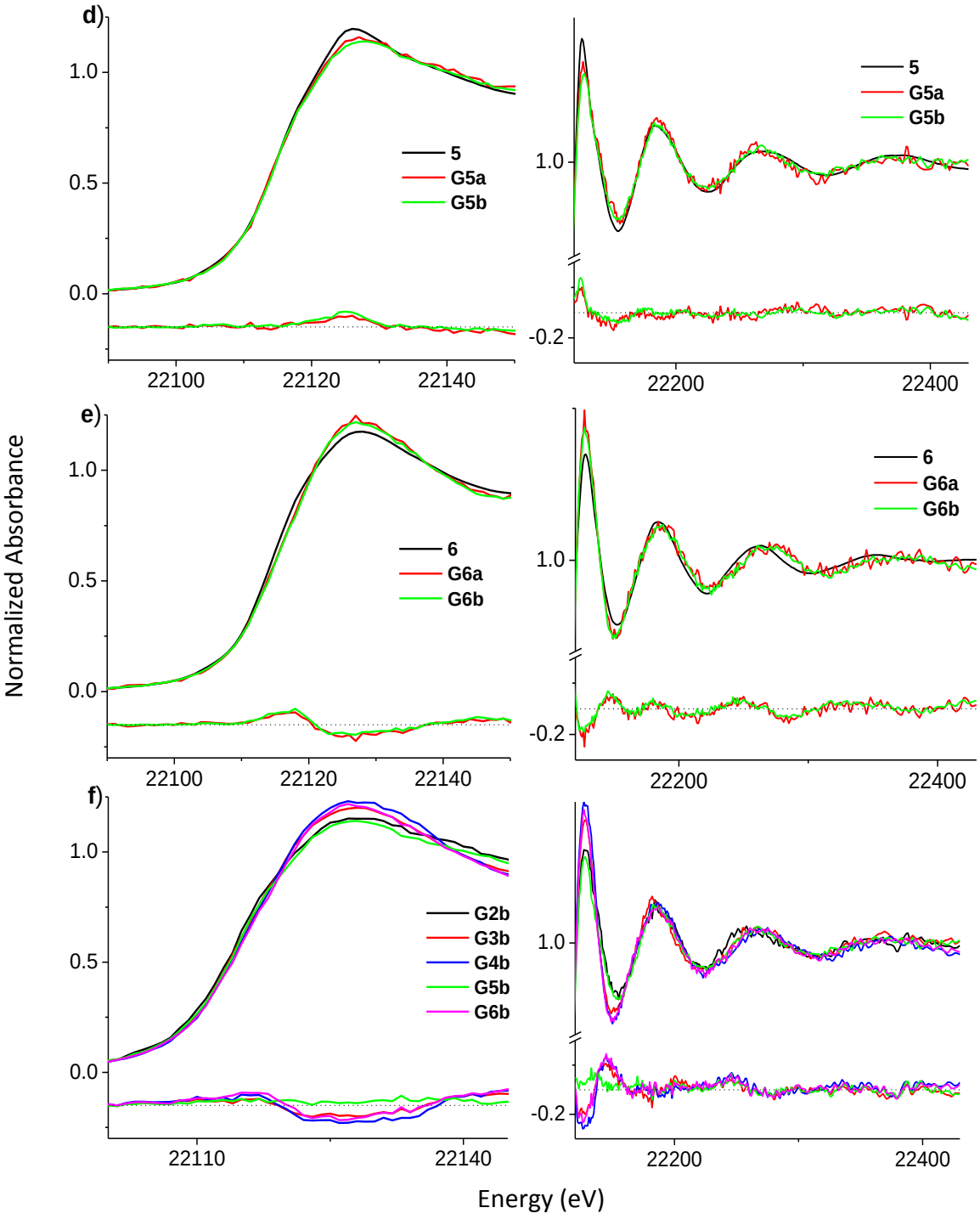

Figure 5.17 (cont.)

Table 5.6: Multiple linear regression analyses of Ru K-edge XANES fits for conditions **G**.[a]

Sample	Parent (%)	1 (%)	4 (%)	5 (%)	11 (%)	R^2
G2a	-	-	35(2)	65(2)	-	0.99981
G3a	63(4)	-	37(4)	-	-	0.99929
G4a	100(1)	-	-	-	-	0.99953
G5a	55(2)	37(2)	-	-	8(1)	0.99970
G6a	28(2)	-	72(2)	-	-	0.99950
G2b	-	53(4)	17(1)	30(2)	-	0.99967
G3b	72(2)	-	28(2)	-	-	0.99982
G4b	100(1)	-	-	-	-	0.99972
G5b	50(2)	47(2)	-	-	3(1)	0.99979
G6b	33(2)	-	67(2)	-	-	0.99963

[a]This table shows the calculated molar percentages (%) of the XANES from contributing model complexes with errors to the last significant figures and correlation coefficients (R^2) included. Multiple linear regression analyses were performed within the range 22100 – 22430 eV. Designations of the models and biological samples correspond to those given in Table 5.2.

5.2.6 Reactions with HEPG2 cells

Compounds **2** and **3** (0.60 mM) were incubated with HepG2 liver carcinoma cells for 4 hr, the medium was then separated to enable analysis of both the freeze-dried cells and medium. All results are shown in **Figure 5.19** (conditions **H, Table 5.2**) and the results of multiple linear regression analyses are given in **Table 5.7**. Significant changes in the Ru K-

edge XAS were observed for compound **2** in both the cells and the cell medium, the edge shift for **2** in cells **(H2a)** was larger than in the medium **(H2b)**, which showed that it underwent a higher degree of substitution in the cells, or at the cell surface, compared to reactions in the medium. The decrease in the white-line intensity (~0.04 units) in the XANES for **H2b (Figure 5.19b)** and the large changes in the period and intensities of the EXAFS oscillations showed that **2** was already undergoing substitution in the extracellular media before cellular uptake. The linear regression fits to the XAS for both **H2a** and **H2b** pointed to similar reaction products; represented by the models **10b** and **11**. The noisy spectra for **H2a** resulted in a relatively poor fit (R^2 = 0.99703) compared to other fits, however the spectra for both reaction products look the same within the experimental error of the noise.

The spectral difference between the reaction products of **3** in HEPG2 cells **(H3a)** and in medium **(H3b)** were minimal **(Figure 5.19c,d)**; however, shifts in the oscillations to higher energies were observed in the EXAFS region though not as much as in **2**. The shape of the spectra was very similar to the XAS of **3** in DMEM **(F3b, Figure 5.14b)**, which indicated similar reactivity in cell culture media. The best regression fits to the XANES pointed to large proportions of *O* (52%) and *S*-donor (~48%) ligands in the product **(Table 5.7)**.

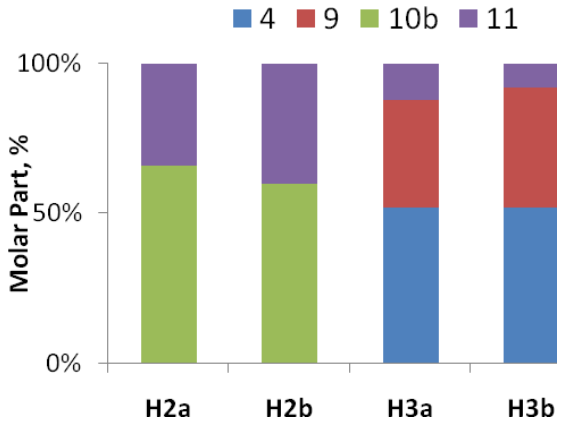

Figure 5.18.: Multiple linear regression results for fits to the Ru K-edge XAS for conditions **H** (designations given in Table 5.2). Details of the fits are shown in **Table 5.7.**

Table 5.7: Multiple linear regression analyses for Ru K-edge XANES fits for conditions **H**.[a]

Sample	4 (%)	9 (%)	10b (%)	11 (%)	R^2
H2a	-	-	66(5)	34(4)	0.99703
H2b	-	-	60(2)	40(2)	0.99917
H3a	52(2)	36(2)	-	12(1)	0.99955
H3b	52(1)	40(1)	-	8(1)	0.99976

[a]This table shows the calculated molar percentages (%) of the XANES from the contributing model complexes with errors to the last significant figures and correlation coefficients (R^2) included. Multiple linear regression analyses were performed within the range 22100 – 22430 eV. Designations of the models and biological samples correspond to those given in Table 5.2.

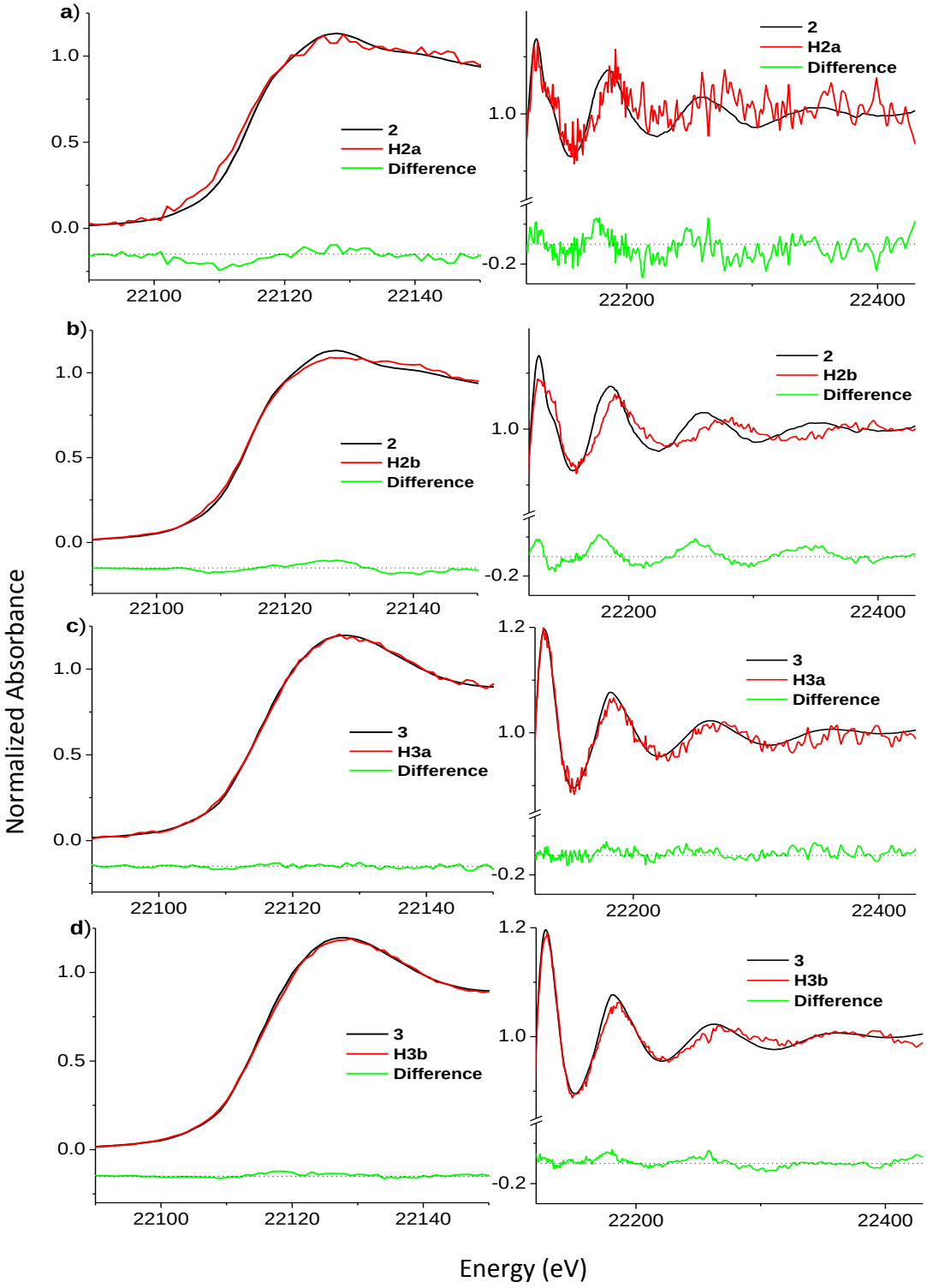

Figure 5.19: Ru K-edge XAS (15 K, fluorescence mode) spectra for compounds **2** and **3** (0.60 mM) incubated with **a, c)** HEPG2 cells and **b, d)** the separated medium for 4 hr at 37 ^{o}C (conditions **H**). Designations are given in Table 5.2.

5.2.7 Reactions with DNA

Additional experiments were conducted to examine the reactivity of compound **2** (1.0 mM) with different concentrations of DNA-Na at 10, 5 and 2.5 mg/mL for up to 15 hr **(Figure 5.21)** (conditions **I, Table 5.2**). The resulting XAS for all adducts were significantly different from those of the parent compounds, which was consistent with previous studies, which showed that this compound lost its chlorido ligands before binding to DNA.[15, 16] The XANES from the lowest DNA concentration at 2.5 mg/mL (**I2c);** however, showed a different edge energy from the others with a 0.5 eV shift to lower energy **(Figure 5.21d)**. This indicated the presence of different adducts at different Ru:DNA ratios, thus showing the versatility of **2** to bind to different sites.

Multiple linear regression results for **I2a** and **I2b** displayed good fits to models **4** (11-17%), **5** (19%) and **10b** (65-70%), which pointed to aqua/hydroxido and other *O*-donor ligand substitution reactions **(Table 5.8)**. The results for **I2c** differed to the others with a significant proportion of the best fit to the XANES being attributed to model **7 (Figure 5.20)**, which may point to the formation of OH^- bridges at lower DNA concentrations and, thus, another possible mode of DNA interaction. The presence of model **10b** in all fits is a sign that aquation may be a pre-requisite for DNA-binding, which is consistent with literature results.[17]

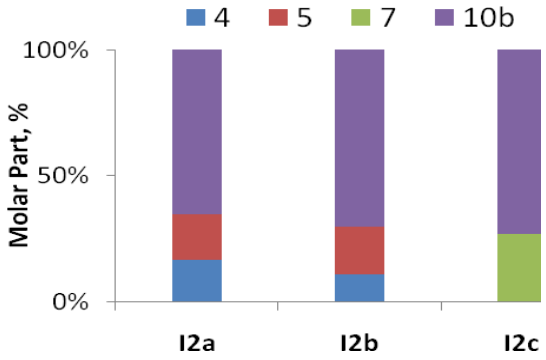

Figure 5.20.: Multiple linear regression results for fits to the Ru K-edge XANES for conditions **I** (designations given in Table 5.2). Details of the fits are shown in **Table 5.7.**

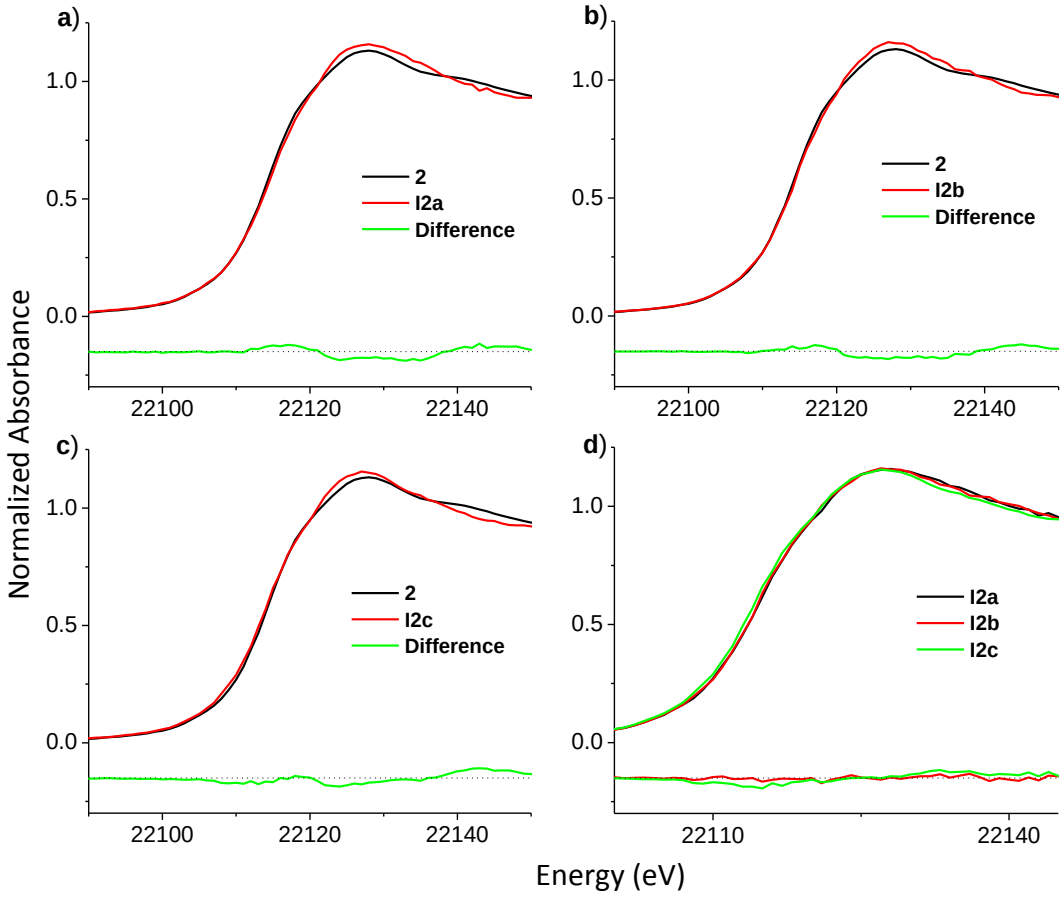

Figure 5.21: Ru K-edge XANES (15 K, fluorescence mode) spectra for compound **2** (1.0 mM) reacted with different concentrations of DNA: **a)** 10 mg/mL, **b)** 5 mg/mL, **c)** 2.5 mg/mL in HBS for 15 hr; (pH 7.1, 22 °C, conditions **I**); **d)** is the overlay of XANES from all reactions after 15 hr. Designations are given in Table 5.2.

Table 5.8: Multiple linear regression analyses of Ru K-edge XANES fits for conditions **I**.[a]

Sample	4 (%)	5 (%)	7 (%)	10b (%)	R^2
I2a	17(2)	18(4)	-	65(3)	0.99975
I2b	11(2)	19(3)	-	70(2)	0.99981
I2c	-	-	27(1)	73(1)	0.99987

[a]This table shows the calculated molar percentages (%) of the XANES from the contributing model complexes with errors to the last significant figures and correlation coefficients (R^2) included. Multiple linear regression analyses were performed within the range 22100 – 22430 eV. Designations of the models and biological samples correspond to those given in Table 5.2.

5.2.8 Reactions with Rat Blood

The K-edge Ru XANES of compound **2** showed profound changes in both cell culture medium and serum (**Figures 5.15a and 5.17a**). Further studies were carried out to examine its decomposition in rat blood; red blood cells (RBC), and plasma after 1 or 6 hr (**Figure 5.23** conditions **J** and **K, Table 5.2**). Two types of plasma samples were prepared for comparisons: the plasma fraction isolated from the whole blood sample before the addition of Ru (**K2a, K2b)**, and the plasma fraction isolated after Ru had reacted with the whole blood sample **(K2c)**. Prominent shifts in the edges (-0.7 eV) for the RBC fractions **(J2)** compared with the parent compound were observed, the XANES for 1 hr **(J2a)** had a lower edge energy (~0.4 eV) than the XANES for 6 hr **(J2b)** indicating different decomposition products.

The reaction of **2** in isolated plasma **(K2a)** displayed a slight increase (~0.4 eV) in the XANES edge energies **(Figure 5.23b)**. The whole blood plasma, **K2c** had a slightly lower edge energy value compared to the isolated plasma, **K2a (Figure 5.23c)**, and was similar to that of the RBC fraction **(J2a) (Figure 5.23d and Table 5.9)**. This observation showed that RBC played a crucial role in Ru metabolism in the whole blood, which has not been discussed in literature and would be interesting to conduct further studies. Multiple linear regression fits to the XAS for **J2a and J2b (Table 5.10)** suggested that the products in RBC mainly consisted of *S*-donor ligands; models **8** (70-77%) and **11** (23-30%); although these results were not definitive for **J2a** due to the somewhat poorer fit obtained (R^2 = 0.99748) compared to the other fits. XAS of the isolated plasma samples displayed good fits to model **10b**, which indicated that **2** was prone to aquation in blood plasma.

Table 5.9: XANES edge energy values for conditions J and K

Sample	Edge Energy (eV)
Parent	22113.40
J2a	22112.60
J2b	22113.02
K2a	22113.43
K2b	22113.03
K2c	22112.90

Table 5.10: Multiple linear regression analyses of Ru K-edge XANES fits for conditions **J** and **K**[a].

Sample	8 (%)	10b (%)	11 (%)	R^2
J2a	77(4)	-	23(4)	0.99748
J2b	70(2)	-	30(2)	0.99942
K2a	-	100(1)	-	0.99962
K2b	21(2)	66(2)	13(1)	0.99977
K2c	87(2)	-	13(2)	0.99940

[a]This table shows the calculated molar percentages (%)of the XANES from the contributing model complexes with errors to the last significant figures and correlation coefficients (R^2) included. Designations of the models and biological samples correspond to those given in Table 5.2.

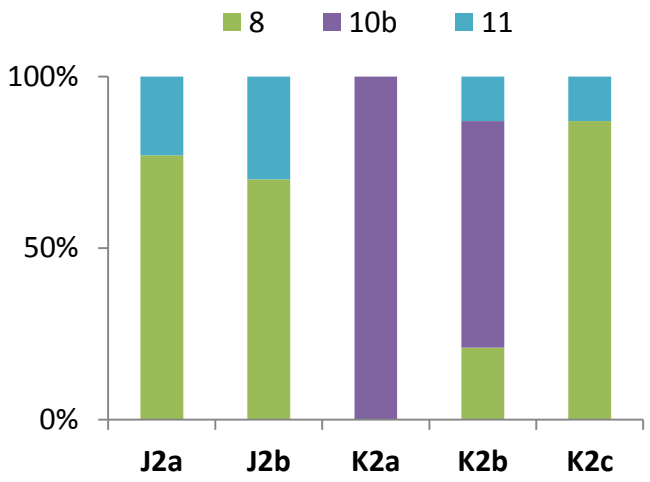

Figure 5.22.: Multiple linear regression results from the best fits to the Ru K-edge XAS for conditions **J** and **K** (designations given in Table 5.2). Details of the fits are shown in **Table 5.9.**

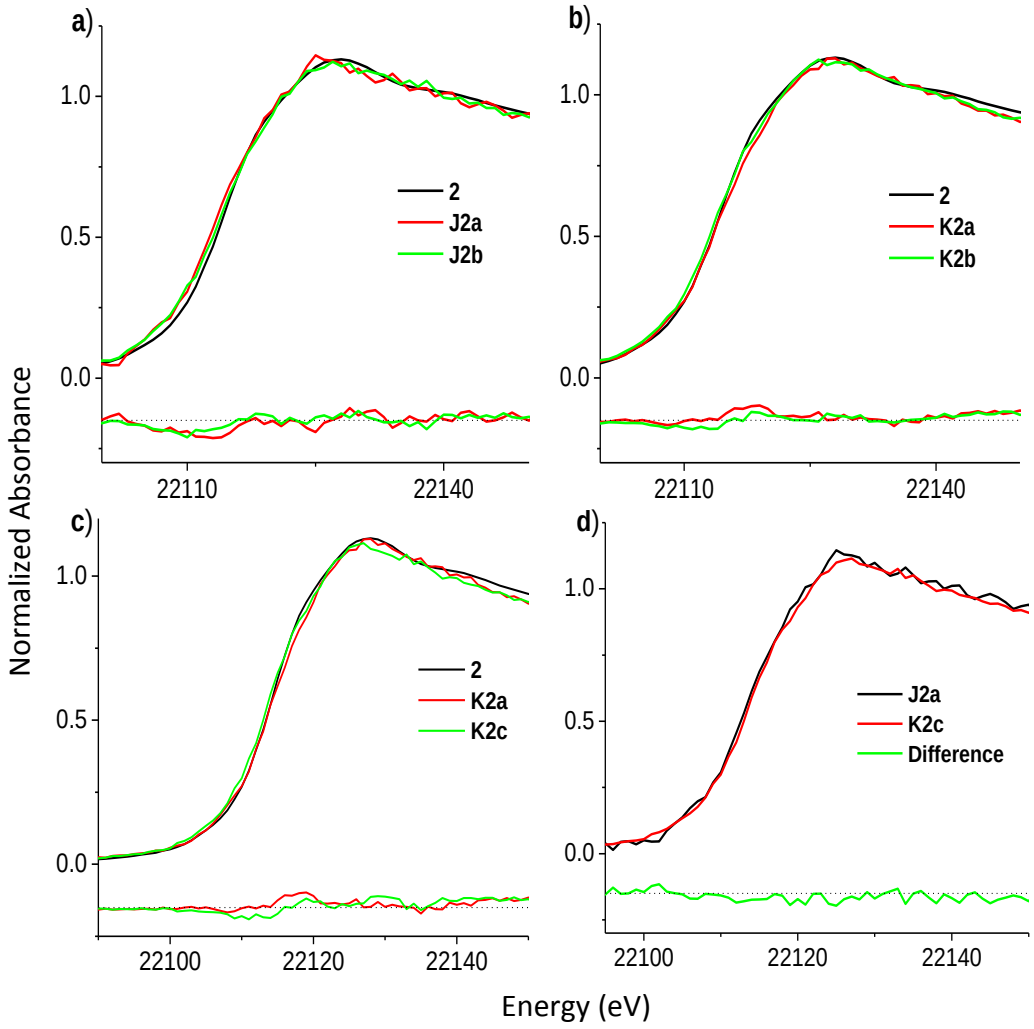

Figure 5.23: Ru K-edge XANES (15 K, fluorescence mode) from compound **2** (0.60 mM) in rat blood incubated for 1 or 6 hr at 37 °C, (conditions **J** and **K**). Designations are given in **Table 5.2**.

5.3 Speciation of Ru-Protein Reactions with Protein Gels

5.3.1 Reactions with Albumin and Transferrin

Initial studies combining XFM with gel-electrophoresis were carried out for the Ru compounds NAMI-A (**1**), KP1019 (**2**) and RAPTA-C (**3**) with BSA (1.0 mg/mL) and bovine apo-transferrin (BTf) (1.0 mg/mL) (For the XFM experiments, compounds were renumbered once again for convenience). The compounds were reacted with these proteins in HBS for 4 hr at 37 °C. The upper section of the SDS-PAGE gel that contained high-MW proteins were not scanned in XFM and only the lower section which contained the monomers for BSA (~65 kDa) and BTf (~80 kDa) **(Figure 5.24a)** was focused on. It was possible to view the strong binding interactions between these Ru compounds and the proteins through XFM **(Figure 5.24b, c)**. The strong signals at more than 80 kDa in the raw scan were evidence for the extensive cross-linking interactions between KP1019 and the serum proteins; in agreement with the literature.[18, 19] Both NAMI-A and RAPTA-C showed comparatively weaker binding, which might be a factor for their anti-metastatic properties.

XANES scans were conducted for the Ru-BTf monomers (labelled A, B, C in **Figure 5.24c**) and the noisy spectra obtained made it hard for accurate linear regression analysis. However, the Tf adducts of these three compounds had significantly different edge energies (NAMI-A being the lowest at 22112.5 eV and RAPTA-C the highest at 22113.3 eV) to each other, which shows a different coordination environment. This showed that some of the original ligands from each of the parent complexes were bound in the adduct, at least for RAPTA-C **(Figure 5.24d)**.[10]

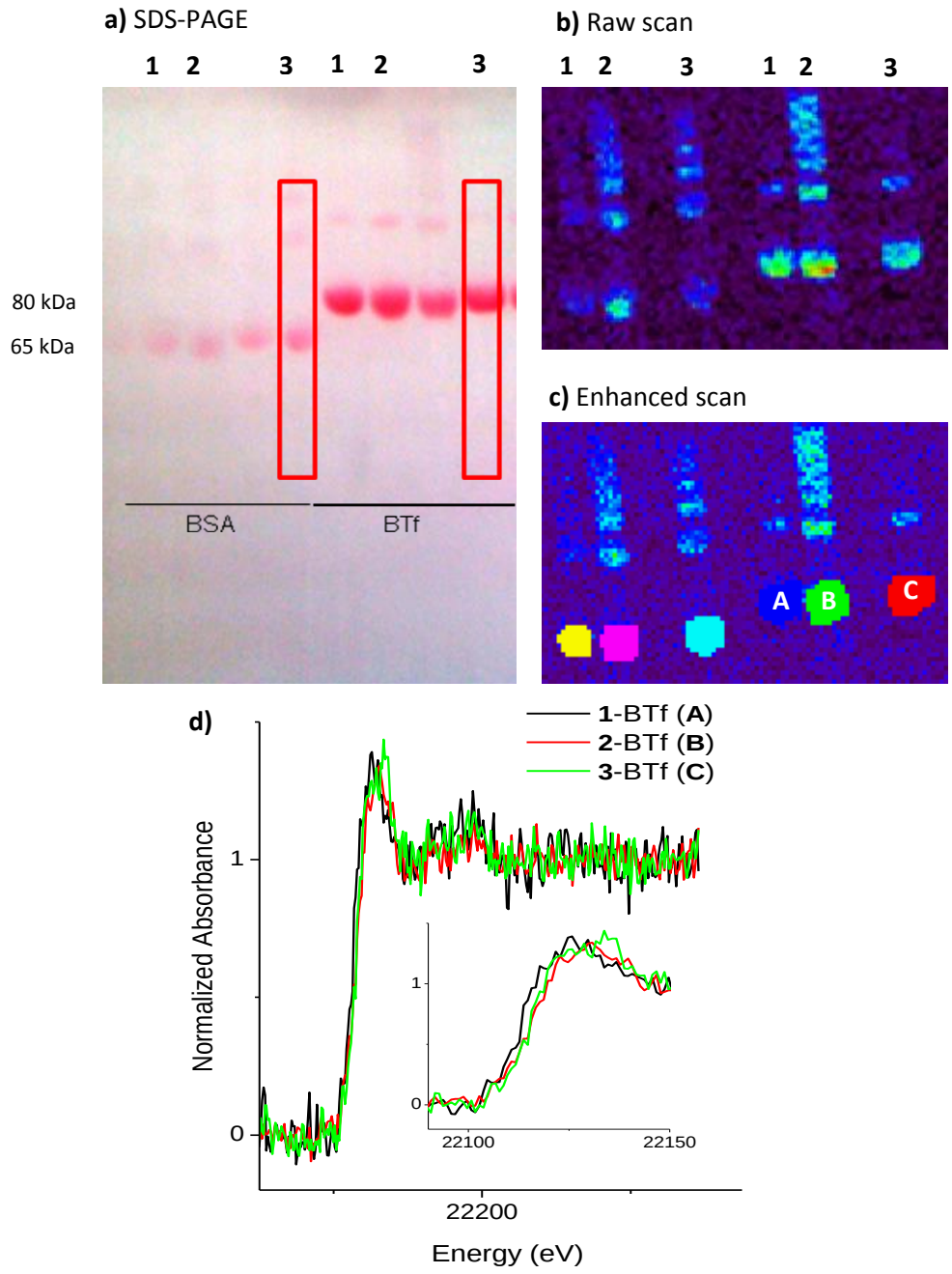

Figure 5.24: **a)** Protein stain of gels **b)** Raw XFM scan and **c)** enhanced XFM scan for the reaction products of Ru compounds NAMI-A **(1)**, KP1019 **(2)**, RAPTA-C **(3)** (0.20 mM each) with BSA (1.0 mg/mL) and BTf (1.0 mg/mL) in HBS (4 hr, 37 °C), separated by gel electrophoresis. Protein bands at 65 and 80 kDa correspond to monomeric forms of BSA and BTf, respectively; **d)** XANES for the compounds with monomeric BTf, scanned at spots **A, B, C** in **c)**. The lane that is not investigated here corresponds to the $[Ru^{II}((CH_2)_6S_3)(dmso)Cl_2]$ studied separately by Ms. Hannah O'Riley. Graph for the XANES spectra prepared by Dr. Aviva Levina. Maps displayed are quantified with threshold values in $\mu g/cm^2$. Experiment performed at the Australian Synchrotron.

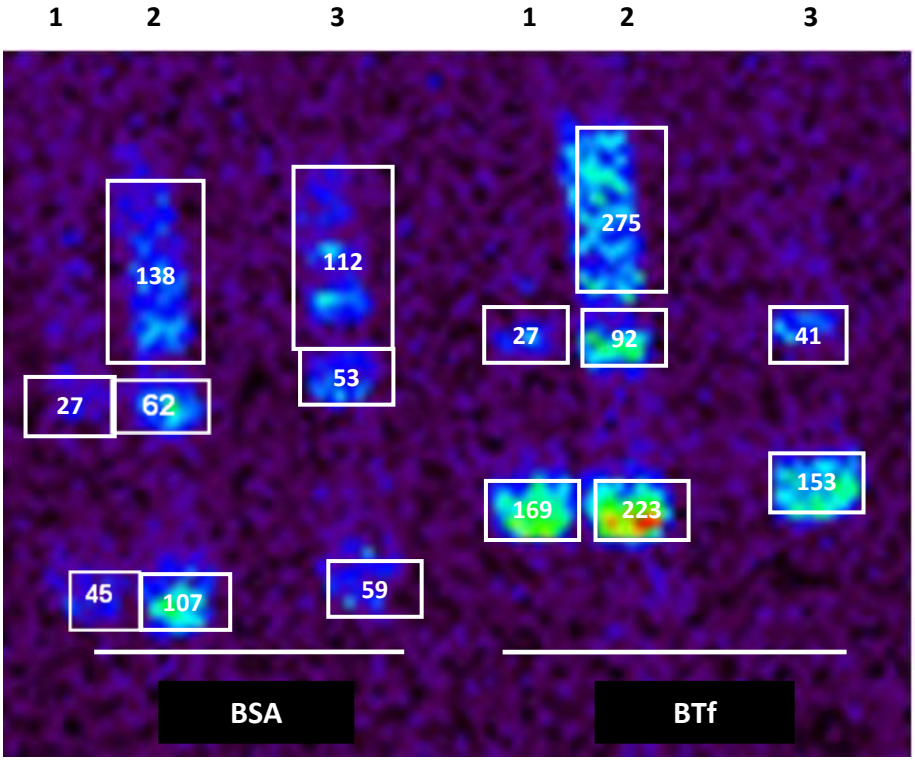

Figure 5.25: The calculated Ru content for the reactions of Ru compounds NAMI-A **(1)**, KP1019 **(2)**, RAPTA-C **(3)** with BSA and BTf. Total expected amount in each lane was ~200 ng per rectangular area, which was close to most of the values obtained except for **2** with BTf. Maps displayed are quantified with threshold values in µg/cm^2.

The calculated Ru content for each lane showed that there was protein content in the samples with values close to the expected amount (~200 ng) **(Figure 5.25)** for complete Ru binding to proteins. The results for KP1019 **(2)** to BTf displayed a huge deviation from the other compounds with a total of 590 ng, which could be due to the small volumes of Ru (1.0 µL stock) used in the sample preparation process, thus causing an error. This needs to be investigated further. NAMI-A **(1)** appeared to have weaker signals, showing a lower degree of binding compared to KP1019. This was consistent with the reports from phase I clinical

trials that KP1019 was bound to serum proteins to a higher extent.[20] It could be observed that RAPTA-C **(3)** also displayed lots of BSA crosslinking interactions, comparable to KP1019.

Figure 5.26 shows maps of the interactions of NAMI-A (black box) and RAPTA-C (red box) with various proteins, or with albumin-depleted bovine serum. The interactions of NAMI-A with actin[21] and hemoglobin (Hb)[22] have been reported and thus served as a good comparison. The monomeric and dimeric Hb (~16 kDa and 32 kDa respectively) could be easily observed for both complexes; RAPTA-C however, showed more crosslinking with Hb. In collagen, RAPTA-C showed stronger binding at 24 hr (red spot) compared to NAMI-A, which seemed to contradict the results in lung metastases in which RAPTA-C was found to exit the lung faster than NAMI-A with an assumption that it was due to weaker collagen binding.[15]

Blood serum differs from plasma by having no blood-clotting proteins.[20] The commercial bovine serum and fresh rat plasma, used in this experiment, were albumin-depleted, to allow for the studies of Ru binding to less abundant protein. Binding was still observed for both NAMI-A and RAPTA-C, but it was much weaker although it still resembled the binding patterns with BSA (**Figure 5.26** lower left).

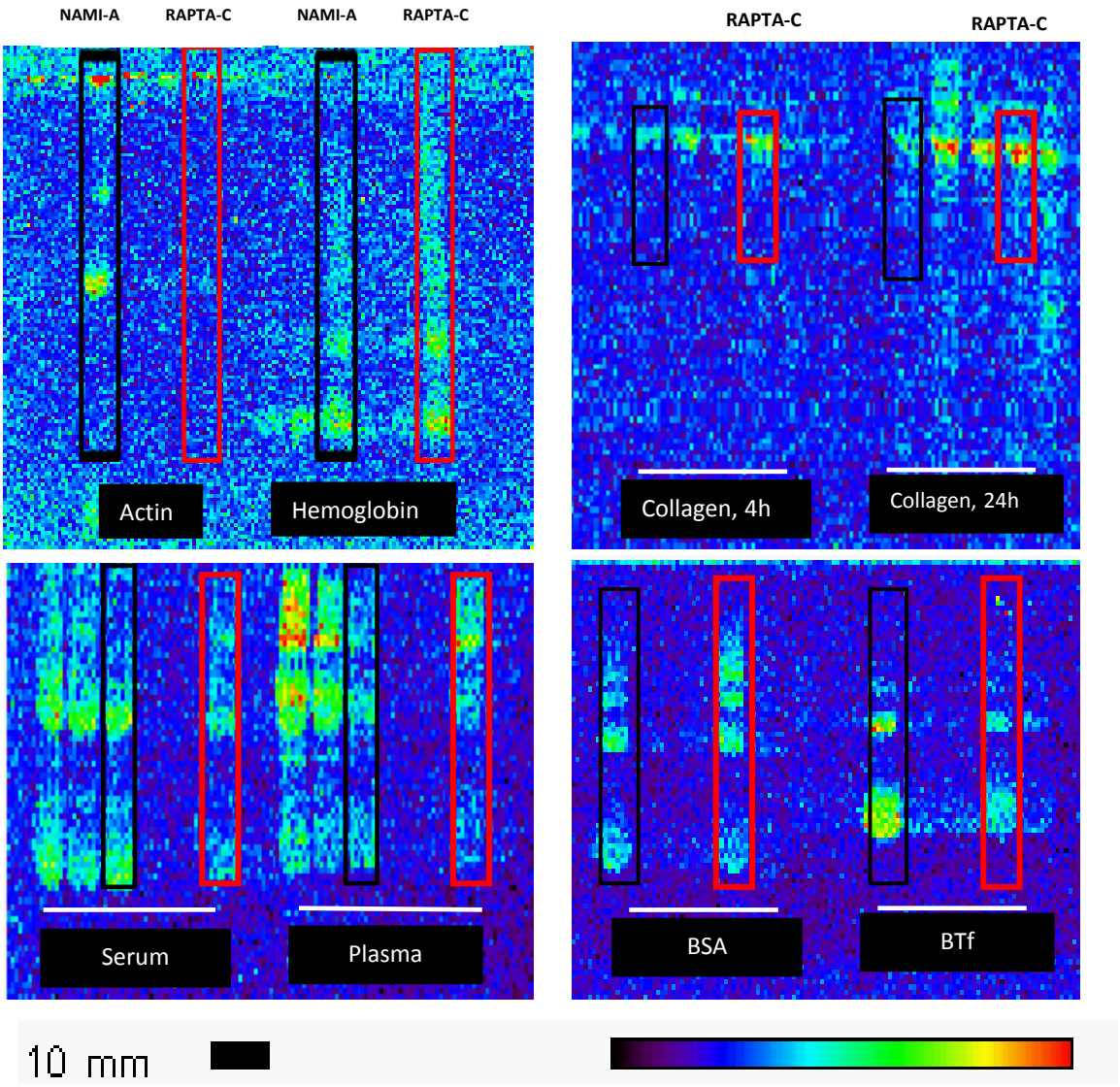

Figure 5.26: XFM maps of the interactions of the reaction products of 0.50 mM Ru compounds: NAMI-A (Black box) and RAPTA-C (Red box) with various proteins in HBS at 37 °C. separated by gel electrophoresis. (Upper left) Actin and Hemoglobin (1 mg/mL) at 8 hr. (Upper right) Collagen (1 mg/mL) at 4 and 24 hr. (Lower left) Albumin-depleted bovine serum and rat plasma at 8 hr. (Lower right) BSA and BTf (2 mg/mL) at 8 hr. Maps displayed are quantified with threshold values in µg/cm^2. Additional lanes observed here that are not mentioned in this study correspond to the $[Ru^{II}Cl_2([9]aneS_3)dmso]$, $[Ru^{II}Br_2([9]aneS_3)dmso]$, $[Ru^{II}Cl(S_2COC(CH_3)_2)(dmso)_3]$, and $[Ru_3Br_6(Me_2tacn)_2]Br$ that will be reported by Ms Hannah O'Riley. Experiment was performed at the APS.

For reactions in rat plasma, more interactions were found in the higher MW fraction, which might be representative of the blood-clotting proteins. The yellow spots observed for RAPTA-C indicated much stronger binding with the blood proteins. The binding of NAMI-A to BTf was also observed to be stronger than RAPTA-C with higher intensity spots for Ru-BTf monomers and dimers (**Figure 5.26** lower right).

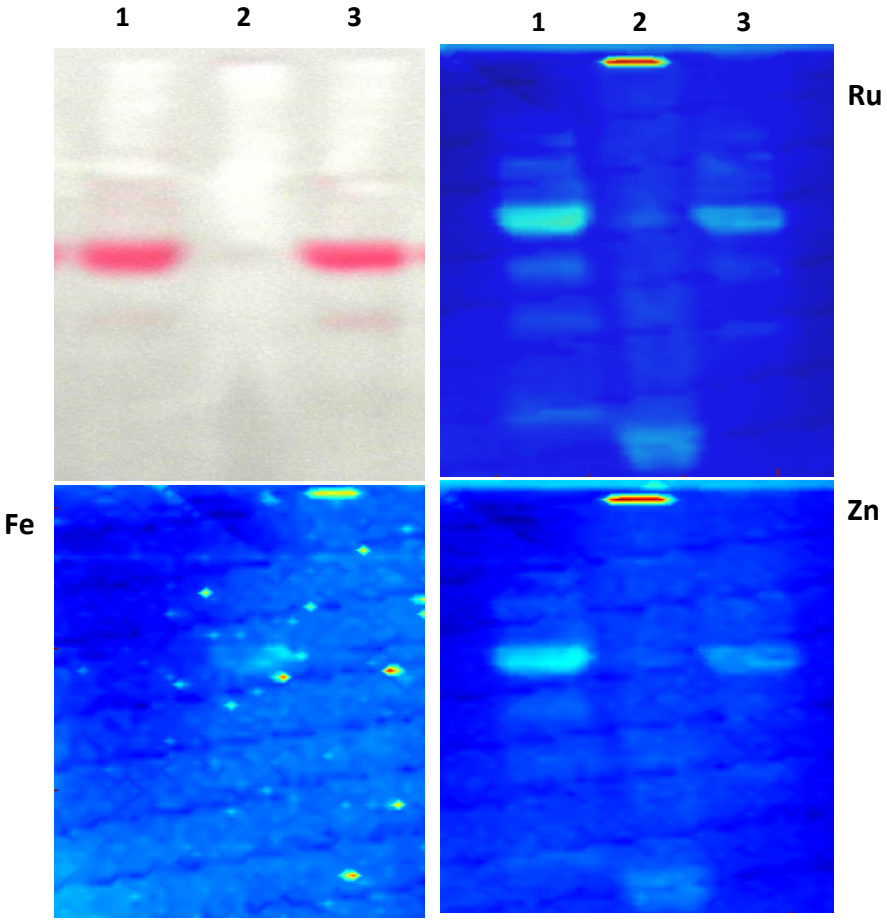

Figure 5.27: XFM maps of NAMI-A **(1)**, KP1019 **(2)** and RAPTA-C **(3)** (1.0 mM) reaction products with BSA (1.0 mg/mL) at 4 hr, 37 °C, separated by gel electrophoresis. (Upper left) Photograph of blot. Maps displayed are quantified with threshold values in μg/cm^2. Results obtained from the Australian Synchrotron.

Figure 5.27 shows the mapping for the BSA interactions (obtained from the Australian Synchrotron) with NAMI-A **(1)**, KP1019 **(2)** and RAPTA-C **(3)** in HBS at 4 hr. The map here, however, displayed less resolution but clearly showed protein-bound Ru. The intense band for **1** showed strong BSA monomer bindings whereas **2** concentrated on the high MW region. A good resolution for the iron content was not achieved to determine its distribution, although the green and yellow spots did indicate its presence. The Zn map showed similar densities to the Ru map, which is due to albumin being a major zinc carrier in the bloodstream (~80% of plasma zinc bound)[23]

The results for the interactions in a BSA collagen mixture are illustrated in **Figure 5.28** with increased clarity, which resemble the previous observations for BSA studies **(Figure 5.27)**. Once again, the results emphasize bindings to the BSA monomers. A large amount of Ru and Zn were observed to be concentrated on the monomeric region for **1**-BSA whereas **2** showed a stronger interaction with collagen in the high MW region, which has an implication for their different anticancer properties. Data could not be extracted for the Fe content beyond the noise level.

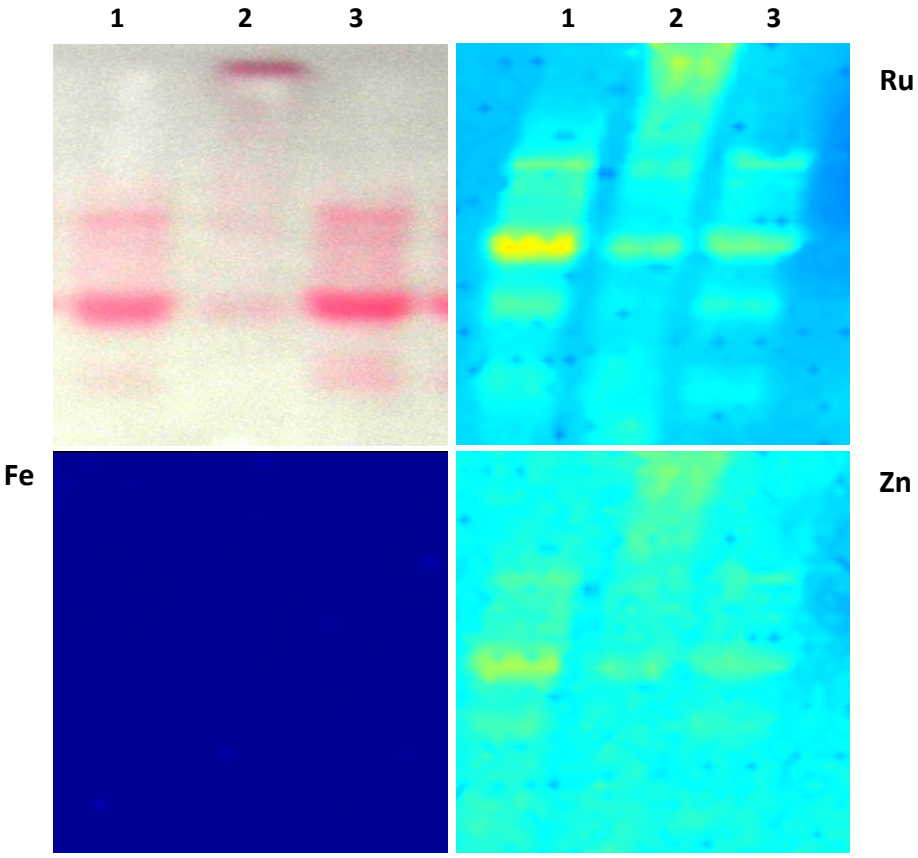

Figure 5.28: XFM maps of the reaction products NAMI-A **(1)**, KP1019 **(2)**, RAPTA-C **(3)** (1.0 mM) with a mixture of BSA and collagen (1.0 mg/mL each) in HBS (pH 7.4) for 4 hr at 37 °C, separated by gel electrophoresis. (Upper left) Photograph of blot. Maps displayed are quantified with threshold values in µg/cm^2. Results obtained from the Australian Synchrotron.

5.4 References

1. Gunter, K. K.; Miller, L. M.; Aschner, M.; Eliseev, R.; Depuis, D.; Gavin, C. E.; Gunter, T. E., *Neurotoxicology* **2002,** *23*, 127-146.

2. Penner-Hahn, J. E., *Coord. Chem. Rev.* **1999,** *190-192*, 1101-1123.

3. Penner-Hahn, J. E.; Peariso, K., *Synch. Rad. News.* **2000,** *13*, 22-30.

4. Aitken, J. B.; Antony, S.; Weekley, C. M.; Lai, B.; Spiccia, L.; Harris, H. H., *Metallomics* **2012,** *4*, 1051-1056.

5. Finney, L.; Chishti, Y.; Khare, T.; Giometti, C.; Levina, A.; Lay, P. A.; Vogt, S., *ACS Chem. Biol.* **2010,** *5*, 577-587.

6. Raimunda, D.; Khare, T.; Giometti, C.; Vogt, S.; Argueello, J. M.; Finney, L., *Metallomics* **2012,** *4*, 921-927.

7. Milsmann, C.; Bill, E.; Weyhermuller, T.; DeBeer George, S.; Wieghardt, K., *Inorg. Chem.* **2009,** *48*, 9754-9766.

8. Milsmann, C.; Levina, A.; Harris, H. H.; Foran, G. J.; Turner, P.; Lay, P. A., *Inorg. Chem.* **2006,** *45*, 4743-4754.

9. Scolaro, C.; Hartinger, C. G.; Allardyce, C. S.; Keppler, B. K.; Dyson, P. J., *J. Inorg. Biochem.* **2008,** *102*, 1743-1748.

10. Levina, A.; Aitken, J. B.; Gwee, Y. Y.; Lim, Z. J.; Liu, M.; Singharay, A. M.; Wong, P. F.; Lay, P. A., *Chem. Eur. J.* **2013,** *19*, 3609-3619.

11. George, G. N.; Pickering, I. J.; Pushie, M. J.; Nienaber, K.; Hackett, M. J.; Ascone, I.; Hedman, B.; Hodgson, K. O.; Aitken, J. B.; Levina, A.; Glover, C.; Lay, P. A., *J. Synchrotron Radiat.* **2012,** *19*, 875-886.

12. Ang , W. H.; Daldini, E.; Scolaro, C.; Scopelliti, R.; Juillerat-Jeannerat, L.; Dyson , P. J., *Inorg. Chem.* **2006,** *45*, 9006-9013.

13. Groessl, M.; Terenghi, M.; Casini, A.; Elviri, L.; Lobinski, R.; Dyson, P. J., *J. Anal. At. Spectrom.* **2010,** *25*, 305-313.

14. Kratz, F., In *Metal Complexes in Cancer Chemotherapy*, Keppler Bernhard, K., Ed. VCH: Weinheim, Germany, 1993; p 391.

15. Scolaro, C.; Bergamo, A.; Brescacin, L.; Delfino, R.; Cocchietto, M.; Laurenczy, G.; Geldbach, T. J.; Sava, G.; Dyson, P. J., *J Med Chem* **2005,** *48*, 4161-4171.

16. Dorcier, A.; Dyson, P. J.; Gossens, C.; Rothlisberger, U.; Scopelliti, R.; Tavernelli, I., *Organometallics* **2005,** *24*, 2114-2123.

17. Ratanaphan, A.; Temboot, P.; Dyson, P. J., *Chem. Biodiversity* **2010,** *7*, 1290-1302.

18. Hartinger, C. G.; Zorbas-Seifried, S.; Jakupec, M. A.; Kynast, B.; Zorbas, H.; Keppler, B. K., *J. Inorg. Biochem.* **2006,** *100*, 891-904.

19. Pongratz, M.; Schluga, P.; Jakupec, M. A.; Arion, V. B.; Hartinger, C. G.; Allmaier, G.; Keppler, B. K., *J. Anal. At. Spectrom.* **2004,** *19*, 46-51.

20. Timerbaev, A. R.; Hartinger, C. G.; Aleksenko, S. S.; Keppler, B. K., *Chem. Rev.* **2006,** *106*, 2224-2248.

21. Gava, B.; Zorzet, S.; Spessotto, P.; Cocchietto, M.; Sava, G., *J. Pharmacol. Exp. Ther.* **2006,** *317*, 284-291.

22. Pacor, S.; Zorzet, S.; Cocchietto, M.; Bacac, M.; Vadori, M.; Turrin, C.; Gava, B.; Castellarin, A.; Sava, G., *J. Pharmacol. Exp. Ther.* **2004,** *310*, 737-744.

23. Lu, J.; Stewart, A. J.; Sadler, P. J.; Pinheiro, T. J. T.; Blindauer, C. A., *Biochem. Soc. Trans.* **2008,** *36*, 1317-1321.

Chapter Six

Discussion and Conclusion of Results

6.1 Summary of Results

In the rapidly expanding field of Ru anti-cancer drugs, Ru(II) arene complexes are among the most prominent classes of compounds, due to their structural versatility and the ability to combine cytotoxic and anti-metastatic properties (Chapter 1). In this work, a library of model Ru(II) arene complexes with biologically relevant donor groups has been synthesized (Chapter 2) and characterized using a range of experimental techniques, including multiple-scattering EXAFS analysis (Chapter 3). Preliminary studies of the reactivities of Ru(II) arene complexes under biologically relevant conditions were performed by UV-Vis spectroscopy (Chapter 4), and more detailed studies were performed by empirical analysis of XANES spectra (Chapter 5) to identify the speciation products formed during ligand exchange reactions in biological media.

The reaction pathways of Ru complexes with biomolecules (discussed in detail in Chapter 1) are shown in **Scheme 6.1**. In general, both UV-Vis and XAS results showed that compounds which were prone to ligand substitution (RAPTA-C, **2**) exhibited anti-metastatic properties,[1, 2] whereas compounds that remained stable for longer periods in biological media ([Ru(η^6-arene)(en)(Cl]PF_6, **3**) were cytotoxic.[3, 4] All of the Ru(II) complexes studied formed Ru-BSA adducts in which halido and some other ligands exchanged to bind *N*-, *O*-donor ligands of the protein within 24 hr. The linear regression fits for **2** indicated a stepwise exchange of chlorido-ligands with *N/O*-donors, proceeding on to form reaction products with *S*-donor ligands after 1 hr, which can be attributed to BSA-binding.[5, 6] The crystal structure of a Ru-protein adduct obtained by soaking a model protein (human

carbonic anhydrase) in an aqueous buffer of NAMI-A showed binding to the His64 residue, thus supporting the observation of *N*-binding.[7]

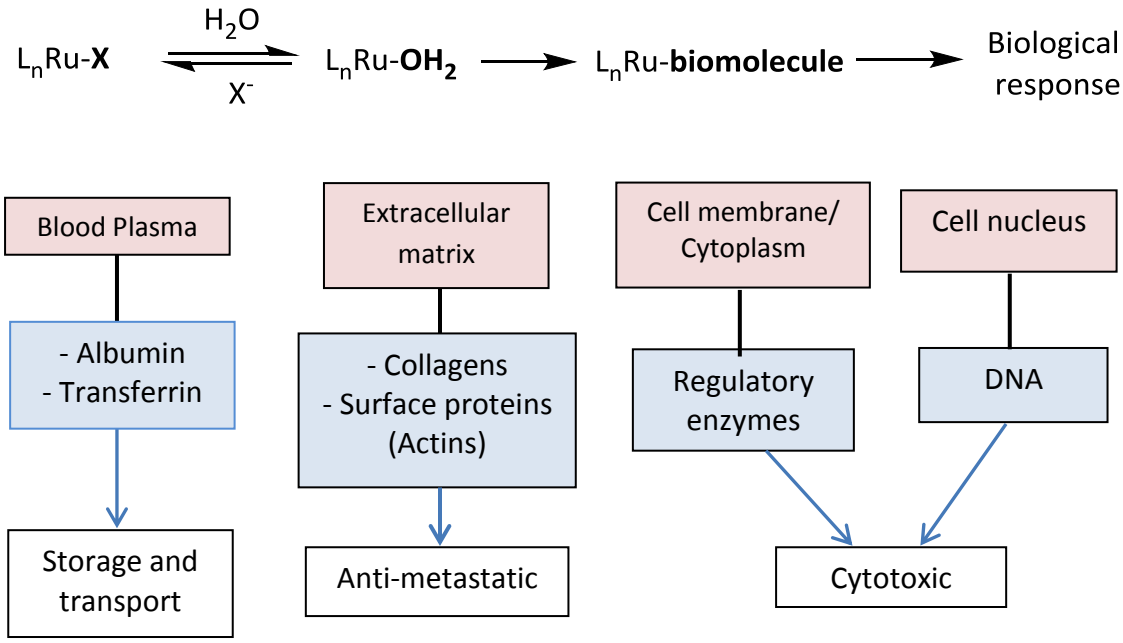

Scheme 6.1: General reaction pathways of Ru anti-cancer complexes where L are the bound ligands and X is the leaving group. The biomolecules are indicated in blue boxes, specific binding locations in red boxes and the proposed mode of action in white boxes.[8]

It was surprising to find that the XAS results for OxaloRAPTA-C **(5)** showed more prominent ligand-exchange reactions in HBS (pH 7.4) compared to **2**, especially since the chelating ligand was supposed to provide more stability to aquation (also observed for the UV-Vis results in Chapter 4). This might be due to the lack of other components in the buffer solution to compete with the reversed of re-coordination of chlorido ligands, unlike in biological media and cells where other donors can compete with this back-reaction. Also, although aquation is generally thought to be suppressed under the high saline environment

([Cl^-] ~150 mM) of the blood,[2] the change in the edges from the XANES results and peak shifts in the UV-Vis spectra clearly show that this suppression is not complete. Even in the absence of competing ligands, the equilibrium of the products shows some chloride loss.

It was obvious from the linear regression fits that the speciation of the Ru(II) compounds in cell culture media were complicated and the kinetics could not be resolved easily using UV-Vis spectroscopy alone. On the other hand, in undiluted bovine serum, the XAS spectra for Ru(II) complexes displayed less prominent changes, although another possibility would be ligand-exchange reactions occurring within similar donor groups. The fits for the complexes in undiluted serum (Chapter 5**, Table 5.6**) showed different speciation products from their reactions in cell culture media (Chapter 5**, Table 5.5**) and, therefore, indicated other binding processes taking place in the presence of serum proteins.

Studies of **2** in cell culture media (with 2% v/v fetal calf serum) and undiluted serum revealed similar XAS spectra to those of the Ru-BSA adducts, which pointed to preferential binding to albumin due to its abundance in the bloodstream. This has contributed to passive tumour targeting by tethering albumin to Ru in an attempt to improve drug efficacy,[9] and suggests that in protein-rich systems, serum albumin acts as a suitable carrier for transporting the complexes to the tumour cells.[10] The presence of model **10b** in the spectral fit for the reaction products of **2** in cell culture media **(F2)** indicated the replacement of the chlorido ligand by a hydroxido or aqua ligand, which subsequently led to the binding of *O*-donor groups (model **4**) of the protein sites. This was consistent with the similarity of the UV-Vis spectra for **2** in cell culture media after 1 hr and the hydroxido-bridged model **7**

(Chapter 4, **Figure 4.3**). Furthermore, the absence of model **5** in the fit pointed to the dissociation of the PTA ligand upon aquation before adduct formation; consistent with the ESI-MS results reported in the literature.[10] The loss of the PTA ligand however, might lower the solubility of the complex and thus hinder diffusion through biological membranes. In contrast to **2**, compound **3** had slower ligand-exchange reactions with 53% of the parent drug being retained after 1 hr, only to bind to *O,N*-donors over 24 hr. This is in agreement with the observations from the UV-Vis spectroscopic studies of the kinetics in cell culture media (Chapter 4, **Figure 4.6**). The higher stability of this complex to aquation would then allow its diffusion into the cytoplasm, thus exhibiting cytotoxicity (Scheme 1).[3]

The coordination environments for **2** and **3** in the HEPG2 cells were observed to be similar to those in the HEPG2 cell medium within experimental error (Chapter 5, **Figure 5.19**), yielding similar reaction products (Chapter 5, **Table 5.7**). However, the noisy XANES spectra might give inaccurate regression fits, especially for the cell samples in which poor R^2 values were obtained. Compound **2** showed large changes in the EXAFS region for the HEPG2 cell medium (**H2b**), implying reactivity in the extracellular medium before cellular uptake. This might be the reason why **2** is only weakly cytotoxic compared to the platinum anticancer complexes. Unlike its activity in cell culture media **(F2)**, the presence of model **11** in the linear regression fits indicated the formation of an *S*-bound adduct, possibly from the binding of **2** to cathepsin B or other thiol-containing enzymes.[11] The large proportion of model **10b**, present in the spectral fits for both **2** in HEPG2 cell medium and in cell medium (2% v/v serum) (**F2**) suggests similar coordination environments, and that the reaction products for **2** in DMEM may be responsible for cell interactions.[2] Compound **3** displayed

minimal reactivity in the XANES region for the HEPG2 cell samples (**H3**), although the presence of *S*-donors in the spectral fits might indicate binding to Cys residues of cytoplasmic proteins.[6, 12] Apart from the presence of model **4**, the reaction products for **3** in HEPG2 cell medium were found to be different to the fits for cell culture medium **(F3)**, indicating that the cellular decomposition occurred through different pathways.

Although initial interest to DNA-binding for compound **2** has waned due to **2** favouring serum protein binding over DNA interactions (postulated to be due to the hydrophobic arene moiety),[13] XAS studies were still carried out for different DNA concentrations and found to have different regression fits (Chapter 5, **Table 5.8**). The aqua/hydroxido (model **10b**) present in all fits is evidence for chlorido loss before DNA-binding.[14] For higher concentrations of DNA (5-10 mg/mL), *N/O*-donor substitutions (model 4,5) were observed that is indicative of purine site binding right after losing its chlorido ligand.[15] At lower concentrations (2.5 mg/mL), the presence of OH^- bridges (model **7**) might be attributed to preferential binding to the adenine site.[14, 16] These results show that there is a lack of specific adduct formation at the DNA sites for **2**, which may not desirable for targeted drug delivery; as opposed to the selectivity shown with proteins.[11, 17-19]

For reactions in rat blood, the XANES of **2** in whole blood plasma **(K2c)** showed similar spectral fits to that of the RBC fractions **(J2a)** (Chapter 5, **Figure 5.23d**), and largely differed to the isolated plasma and serum samples. Therefore, RBC can be postulated to play an important part for the metabolism of Ru in whole blood and may potentially serve as a transport mechanism for tumour targeted drug delivery.[20] The linear regression fits for

the RBC samples pointed to a large proportion of *S*-donor ligands in the product (modelled by **8** and **11**). The isolated plasma samples demonstrated different speciation, with the exchange of the chlorido ligand for aqua/hydroxo species (modelled by **10b**) being dominant. To my knowledge, these results have not yet been discussed in detail in literature, and together, they suggest the various possible binding modes of compound **2** to the components in the bloodstream which can account for its anti-metastatic properties. This has been described for NAMI-A, KP1019,[2] and for anti-diabetic Vanadium complexes (Levina, A., "to be submitted"). It is also important to mention that the arene ligands for all the Ru(II) complexes studied remained bound and under biologically relevant conditions, there was no oxidation to Ru(III) as a consequence of the ligand-exchange processes (Chapter 5, **Figure 5.4**), which then should not affect the hydrophobic properties of the complexes.

Preliminary results for the XFM elemental studies of Ru-protein adduct speciation using protein gels showed the power of this technique to understand interactions of Ru with various proteins. We attempted to ascertain the extent of transferrin binding in mixtures by a co-localization of Ru and Fe but we were not able to obtain sufficient sensitivity for the Fe maps using excitation at the Ru K-edge to examine the resolution. KP1019 showed extensive cross-linking interactions with BSA and BTf, whereas both **2** and NAMI-A showed comparatively weaker binding, thus, a possible factor for their anti-metastatic properties as discussed in previous studies.[2, 17] The difference in edge energy for the three Ru-BTf adducts suggested that some of the original ligands from the parent complexes were still bound in the adduct. Another reason would be the difference in ligand-exchange mechanisms for the Ru complexes with BTf, as reported for NAMI-A and KP1019.[6]

The XFM maps for the interactions of **2** and NAMI-A with various proteins (Chapter 5, **Figure 5.26**), clearly displayed their different binding abilities. The strong signals observed for **2**-Hb (~15 kDa) might be evidence for the binding of Hb contributing to the large spectral changes in the XAS of red blood cells (Chapter 5, **Figure 5.23**). The signals in the high MW fraction of plasma suggested binding to blood-clotting proteins; once again supporting the XAS results of the different speciation products between plasma and RBC. The signals in collagen increased between 4 and 24 hr reactions, showing that **2** binds more strongly to collagen compared to NAMI-A; contradicting the literature results.[1] To summarize with reference to the XAS results, **2** had been observed to display a large amount of reactivity in the blood plasma and the extracellular matrix, which largely contributes to its anti-metastatic properties (Scheme 1). With such knowledge, Ru drugs can be designed to target specific cellular signalling pathways to improve selectivity.

6.2 Future Work

The reactions of Ru(II) complexes with isolated proteins and in biological media led to changes in the coordination environment, as shown by the spectral differences in UV-Vis spectroscopic studies of reactive bonds and verified by multiple linear regression analysis of the time-dependent XAS. This was achievable using an XAS database of Ru(II) arene model compounds although the uncertainty of some of the results (especially for cell and blood samples), indicated a larger variety of ligand coordinations for Ru would be needed to improve the fits. Some samples produced weak XAS spectra with moderate noise levels and future analysis would benefit by the use of more intense beamlines and/or more scans. As

of now, the current library synthesized would serve as a good starting point for future Ru(II) arene studies.

More research is required to cor-relate the UV-Vis spectroscopic studies of the reactions in biological media with the XAS results for the serum and blood samples. As the field of the binding of serum proteins to RAPTA is still being explored, the preliminary XFM results shown here, although not yet conclusive, are useful in identifying the speciation with reference to KP1019 and NAMI-A.[2] These interactions will most likely provide further explanation for their different anticancer activities and it will be worthy carrying out detailed studies for their reactivity with serum proteins and the activities of the Ru-arene adducts with proteins on the cytotoxicities and anti-metastatic properties of Ru-arene pathways. Future studies will also include obtaining Fe maps with higher sensitivity before drawing anymore conclusions of their overall distribution.

6.3 References

1. Scolaro, C.; Bergamo, A.; Brescacin, L.; Delfino, R.; Cocchietto, M.; Laurenczy, G.; Geldbach, T. J.; Sava, G.; Dyson, P. J., *J. Med. Chem.* 2005, *48*, 4161-4171.

2. Scolaro, C.; Hartinger, C. G.; Allardyce, C. S.; Keppler, B. K.; Dyson, P. J., *J. Inorg. Biochem.* 2008, *102*, 1743-1748.

3. Morris, R. E.; Aird, R. E.; Murdoch, P. d. S.; Chen, H.; Cummings, J.; Hughes, N. D.; Parsons, S.; Parkin, A.; Boyd, G.; Jodrell, D. I.; Sadler, P. J., *J. Med. Chem.* 2001, *44*, 3616-3621.

4. Wang, F.; Chen, H.; Parsons, S.; Oswald, I. D. H.; Davidson, J. E.; Sadler, P. J., *Chem. Eur. J.* 2003, *9*, 5810-5820.

5. Liu, M.; Lim, Z. J.; Gwee, Y. Y.; Levina, A.; Lay, P. A., *Angew. Chem., Int. Ed.* 2010, *49*, 1661-1664.

6. Levina, A.; Aitken, J. B.; Gwee, Y. Y.; Lim, Z. J.; Liu, M.; Singharay, A. M.; Wong, P. F.; Lay, P. A., *Chem. Eur. J.* 2013, *19*, 3609-3619.

7. Casini, A.; Temperini, C.; Gabbiani, C.; Supuran, C. T.; Messori, L., *ChemMedChem* 2010, *5*, 1989-1994.

8. Levina, A. M., A.; Lay, P.A., *Metallomics* 2009, *1*, 458-470.

9. Ang, W. H.; Daldini, E.; Juillerat-Jeanneret, L.; Dyson, P. J., *Inorg. Chem.* 2007, *46*, 9048-9050.

10. Groessl, M.; Terenghi, M.; Casini, A.; Elviri, L.; Lobinski, R.; Dyson, P. J., *J. Anal. At. Spectrom.* 2010, *25*, 305-313.

11. Casini, A.; Gabbiani, C.; Sorrentino, F.; Rigobello, M. P.; Bindoli, A.; Geldbach, T. J.; Marrone, A.; Re, N.; Hartinger, C. G.; Dyson, P. J.; Messori, L., *J. Med. Chem.* 2008, *51*, 6773-6781.

12. Hu, W.; Luo, Q.; Ma, X.; Wu, K.; Liu, J.; Chen, Y.; Xiong, S.; Wang, J.; Sadler, P. J.; Wang, F., *Chem. Eur. J.* 2009, *15*, 6586-6594.

13. Ang, W.-H.; Casini, A.; Sava, G.; Dyson, P. J., *J. Organomet. Chem.* 2011, *696*, 989-998.

14. Dorcier, A.; Hartinger, C. G.; Scopelliti, R.; Fish, R. H.; Keppler, B. K.; Dyson, P. J., *J. Inorg. Biochem.* 2008, *102*, 1066-1076.

15. Ratanaphan, A.; Temboot, P.; Dyson, P. J., *Chem. Biodiversity* 2010, *7*, 1290-1302.

16. Fish, R. H., *Coord. Chem. Rev.* 1999, *185-186*, 569-584.

17. Casini, A.; Gabbiani, C.; Michelucci, E.; Pieraccini, G.; Moneti, G.; Dyson, P. J.; Messori, L*., J. Biol. Inorg. Chem.* 2009, *14*, 761-770.

18. Hartinger, C. G.; Casini, A.; Duhot, C.; Tsybin, Y. O.; Messori, L.; Dyson, P. J., *J. Inorg. Biochem.* 2008, *102*, 2136-2141.

19. Wu, B.; Ong, M. S.; Groessl, M.; Adhireksan, Z.; Hartinger, C. G.; Dyson, P. J.; Davey, C. A., *Chem. Eur. J.* 2011, *17*, 3562-3566.

20. Muzykantov, V. R., *Expert Opin. Drug Delivery* 2010, *7*, 403-427.

Appendix

a)

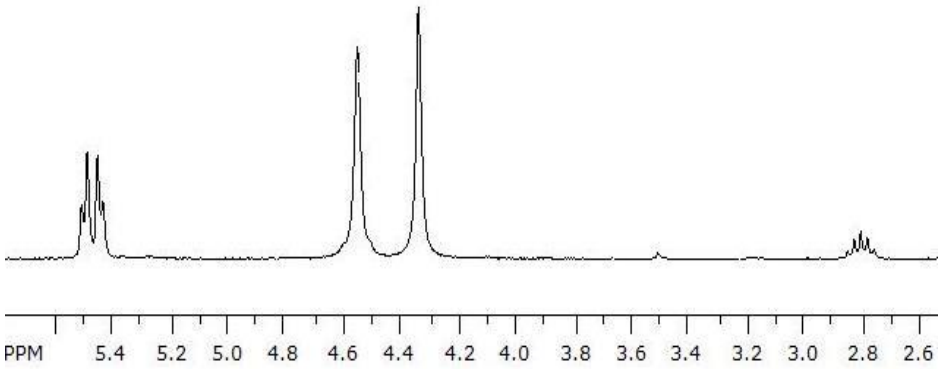

b)

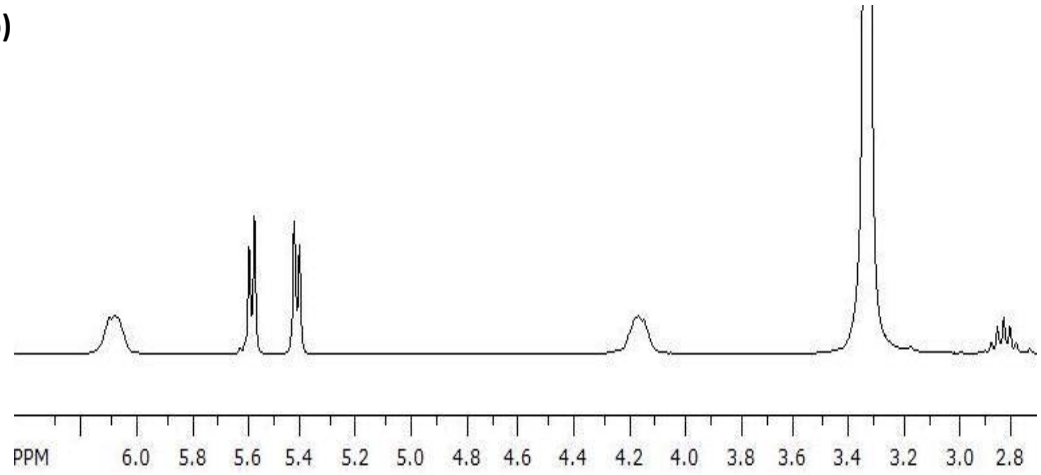

Figure S1: Main peaks for 300 MHz ^{1}H NMR spectra of **a)** compound **2** in $CDCl_3$ and **b)** compound **3** in DMSO-d_6, huge peak at 3.3 ppm is attributed to the water peak in the solvent. All peak assignments are listed in Chapter 2.

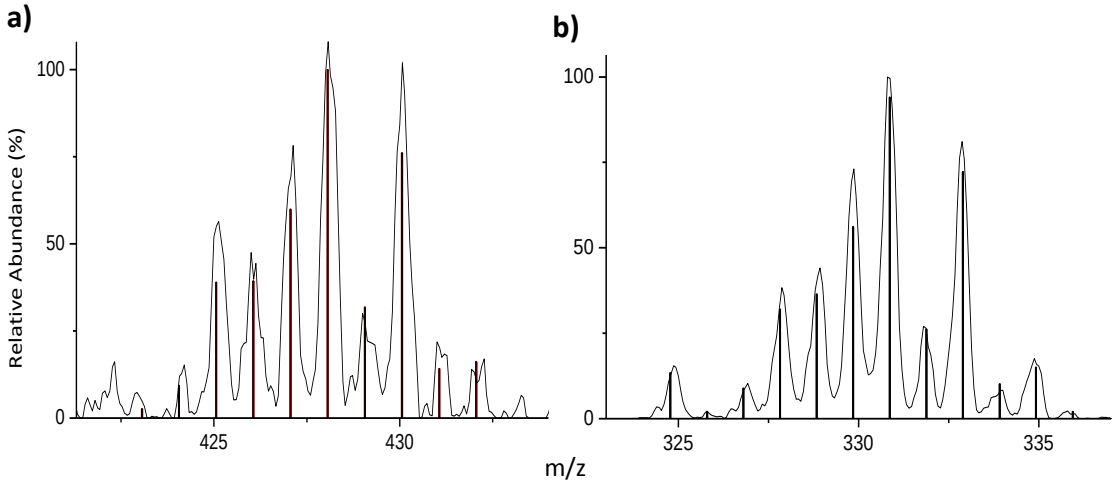

Figure S2: Experimental (lines) and simulated isotope distributions (columns) for major ESMS spectra for **a)** compound **2** and **b)** compound **3** in MeOH. Simulation was performed using the IsoPro 3.01 software (M.Senko, Sunnyvale, CA, 1998).

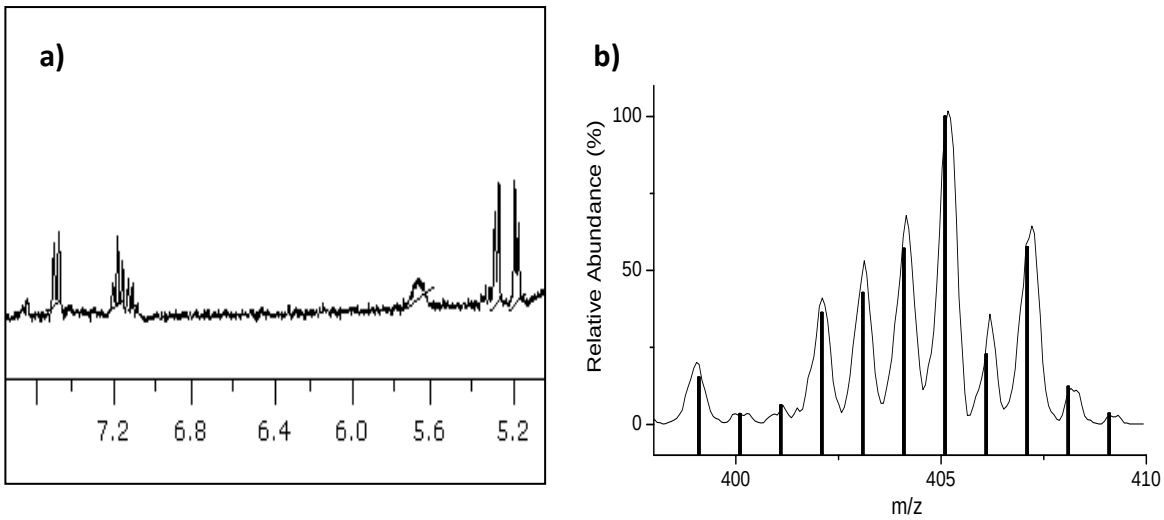

Figure S3: Main spectra for Complex **9**: **a)** ^{1}H NMR spectra in MeOD-d_4, detailed peak assignments are listed in Chapter 2 and **b)** ESMS spectra in MeOH, experimental (lines) and simulated isotope distributions (columns) are shown.

Table A.2 Conditions, restraints, and constraints used in MS XAFS fitting for RAPTA-C[a]

Conditions

K range, $Å^{-1}$: 0-13 [b]
FT range, Å : 1-5[b]
Determinancy (N_i/p):[c] 2.1
Maximal effective path length of a photoelectron: 5.0 Å
Maximum number of legs: 4
Plane-wave path filter threshold: 0%
Curved-wave path filter threshold: 0%
Scale factor: 0.9 ± 0.1

Bond length restraints (Å):[d]

Ru^0-$Cl^1 \approx 2.42$ {0.02}
Ru^0-$Cl^2 \approx 2.42$ {0.02}
Ru^0-$P^3 \approx 2.42$ {0.02}
Ru^0-$C^{13} \approx 2.18$ {0.02}
Ru^0-$C^{16} \approx 2.18$ {0.02}
P^3-$C^7 \approx 1.83$ {0.01}
N^4-$C^7 \approx 1.47$ {0.01}
N^5-$C^8 \approx 1.47$ {0.01}
N^6-$C^9 \approx 1.47$ {0.01}
C^{13}-$C^{14} \approx 1.41$ {0.02}
C^{16}-$C^{17} \approx 1.41$ {0.02}
C^{20}-$C^{21} \approx 1.53$ {0.02}
C^{15}-$C^{19} \approx 1.51$ {0.02}

Ru^0-$C^{13} \approx Ru^0$-$C^{14} \approx Ru^0$-C^{15} {0.02}
Ru^0-$C^{16} \approx Ru^0$-$C^{17} \approx Ru^0$-C^{18} {0.02}
P^3-$C^7 \approx P^3$-$C^8 \approx P^3$-C^9 {0.01}
N^5-$C^8 \approx N^5$-$C^{10} \approx N^5$-C^{12} {0.02}
N^4-$C^7 \approx N^4$-$C^{10} \approx N^4$-C^{11} {0.02}
N^6-$C^9 \approx N^6$-$C^{11} \approx N^6$-C^{12} {0.02}
C^{14}-$C^{15} \approx C^{15}$-$C^{16} \approx C^{16}$-C^{17} {0.02}
C^{16}-$C^{17} \approx C^{17}$-C^{18} {0.02}
C^{15}-$C^{19} \approx C^{18}$-C^{20} {0.02}
C^{20}-$C^{21} \approx C^{20}$-C^{22} {0.02}

Bond angle restraints (°):[d]

C^{18}-C^{13}-C^{14} = 120 {2}
C^{18}-C^{20}-C^{21} = 110 {2}
Cl^2-Ru^0-Cl^1 = 88 {5}
Cl^2-Ru^0-P^3 = 82 {5}
Cl^1-Ru^0-P^3 = 89 {5}
C^{13}-C^{12}-C^{11} = 120 {3}
C^{12}-C^{11}-C^{10} = 120 {3}
C^{11}-C^{10}-N^7 = 119 {3}

C^{18}-C^{13}-C^{14} = C^{17}-C^{16}-C^{15} {2}
C^{18}-C^{20}-C^{21} = C^{20}-C^{21}-C^{22} = C^{22}-C^{20}-C^{18} {2}

Debye-Waller factor restraints ($Å^2$):[d]

$0.001\{0.0005\} < \sigma_i^2 < 0.02$ {0.001}, i= 1-22
σ_i^2 (Ru^0) > (σ_i^2 ($C1^3$) + 0.001) {0.0005}

Continued on the next page

Debye-Waller factor constraints:[d]

σ_i^2 (Cl^1) = σ_i^2 (Cl^2)
σ_i^2 (C^7) = σ_i^2 (C^8) = σ_i^2 (C^9)
σ_i^2 (N^5) = σ_i^2 (N^5) = σ_i^2 (N^6)
σ_i^2 (C^{10}) = σ_i^2 (C^{11}) = σ_i^2 (C^{12})
σ_i^2 (C^{13}) = σ_i^2 (C^{14}) = σ_i^2 (C^{15})
σ_i^2 (C^{16}) = σ_i^2 (C^{17}) = σ_i^2 (C^{18})
σ_i^2 (C^{21}) = σ_i^2 (C^{22})

Atoms restrained to be approximately coplanar

(C^{18} – C^{17}) x (C^{16} – C^{17})^ . (C^{14} - C^{17}) ≈ 0 {0.1}
(C^{13} – C^{14}) x (C^{15} – C^{14})^ . (C^{17} - C^{14}) ≈ 0 {0.1}

[a]Experimental and calculated spectra are shown in **Figure 3.7** (Chapter 3).. [b]The applied window functions are shown in Figure 3.7. [c]The number of independent observations (N_i) and the number of varied parameters (p) were calculated taking into account the applied restraints and constraints [ref. 27 in Chapter 3]. [d] The atom numbering used in the MS XAFS calculation are shown in Figure 3.8 (Chapter 3).

Table A.3 Results of MS XAFS Analysis Fitting for RAPTA-C[a]

Parameter[b]	
-E0	15.38
S_0^2	0.92
σ^2 (Cl^1), Å$^{2\,c}$	0.0065(1)
σ^2 (P^3), Å$^{2\,c}$	0.0005(1)
σ^2 (N^4), Å$^{2\,c}$	0.0005(1)
σ^2 (C^{10}), Å$^{2\,c}$	0.0070(5)
σ^2 (C^{13}), Å$^{2\,c}$	0.0011(3)
σ^2 (C^{16}), Å$^{2\,c}$	0.0029(1)
σ^2 (C^{19}), Å$^{2\,c}$	0.0005(1)
σ^2 (C^{20}), Å$^{2\,c}$	0.0043(2)
σ^2 (C^{21}), Å$^{2\,c}$	0.0010(2)

[a]Experimental and calculated spectra are shown in Figure 3.9 (Chapter 3).

[b]Designations of parameters: $-E_0$ is the threshold energy; S_0^2 is the scale factor; σ^2 (Å^2) is the Debye-Waller factor; and N is the number of scatterers in a shell. [c]Atom numbering corresponds to Figure 3.8 with the resulting fit parameters listed in Table 3.1 (Chapter 3).

Appendix A.4

Most significant Photoelectron Scattering Paths in the Calculated XAFS spectrum of *RAPTA-C*					
Path	Legs	Dege-neracy	σ_i^2, Å^2	Length, Å	Contribution, %
Ru(0)–Cl(7)	2	1	0.00286	2.189	100.00
Ru(0)–C(14)	3	1	0.00116	2.191	100.00
Ru(0)–C(13)	1	1	0.00116	2.184	53.90
Ru(0)–P(3)	1	1	0.00050	2.425	37.59
Ru(0)–Cl(1)	1	1	0.00651	2.427	24.85
Ru(0)–Cl(2)	1	1	0.00651	2.427	24.85
Ru(0)–C(16)– C(15)	4	1	0.00266	2.887	12.99
Ru(0)–C(18)–C(17)	4	1	0.00379	2.891	12.36
Ru(0)–C(19)	1	1	0.00050	3.201	11.82
Ru(0)–C(7)	1	1	0.00050	3.592	7.89
Ru(0)–C(8)	1	1	0.00050	3.625	7.89
Ru(0)–C(13)–Ru(0)	2	1	0.00166	4.609	7.79
Ru(0)–C(20)-C(18)	2	1	0.00461	3.524	7.54
Ru(0)–C(9)	1	1	0.00050	3.426	7.26
Ru(0)–C(20)	1	1	0.00439	3.354	7.24
Ru(0)–C(14)–C(13)	2	1	0.00153	2.893	6.59
Ru(0)–N(6)–C(9)	2	1	0.00051	4.867	6.39
Ru(0)–C(19)–C(15)	2	1	0.00075	3.446	6.26
Ru(0)–C(18)–C(13)	2	1	0.00268	2.912	5.72
Ru(0)–N(5)–P(3)	2	1	0.00052	4.862	5.52
Ru(0)–C(9)–P(3)	2	1	0.00061	3.841	4.92
Ru(0)–N(4)–P(3)	2	1	0.00053	4.883	4.89
Ru(0)–C(22)–C(18)	2	1	0.00114	4.630	4.79
Ru(0)–C(15)-Ru(0)	2	1	0.00767	4.608	4.77
Ru(0)–C(14)-Ru(0)	2	1	0.00166	4.616	4.47
Ru(0)–C(18)-Ru(0)	2	1	0.00938	4.610	4.34
Ru(0)–C(21)	1	1	0.00104	4.001	4.32
Ru(0)–C(16)-Ru(0)	2	1	0.00938	4.610	4.29
Ru(0)–C(17)-Ru(0)	2	1	0.00938	4.616	4.26
Ru(0)–C(13)-P(3)	2	1	0.00165	4.598	3.53
Ru(0)–N(4)-C(7)	2	1	0.00053	4.927	3.46
Ru(0)–C(7)-P(3)	2	1	0.00059	3.924	3.44
Ru(0)-C(22)	2	1	0.00059	3.940	3.19
Ru(0)-N(5)	1	1	0.00050	4.785	3.11

Continued on the next page

Path	Legs	Dege-neracy	σ_i^2, Å^2	Length, Å	Contri-bution, %
Ru(0)-C(5)-C(8)	2	1	0.00053	4.940	3.08
Ru(0)-N(4)	1	1	0.00050	4.792	3.07
Ru(0)-C(14)-P(3)	2	1	0.00163	4.549	2.99
Ru(0)-N(6)	1	1	0.00050	4.838	2.79
Ru(0)-C(18)-Ru(0)	3	1	0.01146	4.366	2.78
Ru(0)-C(8)-Cl(1)	2	1	0.00355	4.319	2.70
Ru(0)–C(20)–C(22)	2	1	0.00165	4.779	2.68
Ru(0)–C(22)–C(20)	2	1	0.00157	4.736	2.48
Ru(18)–C(22)–C(18)	1	1	0.00146	4.673	2.46
Ru(0)–C(9)–N(6)-C(9)	1	1	0.00056	4.896	2.45
Ru(0)–C(15)–C(16)-C(15)	3	1	0.00592	3.591	2.44
Ru(0)–P(3)–C(18)	2	1	0.00320	4.402	2.16
Ru(0)–C(13)–C(15)	2	1	0.00180	3.399	2.13
Ru(0)–C(15)–Cl(1)	2	1	0.00762	4.579	2.09
Ru(0)–C(17)–C(15)	2	1	0.00314	3.407	1.97
Ru(0)–C(16)–Cl(1)	2	1	0.00931	4.576	1.94
Ru(0)–C(18)–Cl(2)	2	1	0.00931	4.577	1.94
Ru(0)–C(17)–Cl(2)	2	1	0.00931	4.581	1.93
Ru(0)–C(18)–C(16)	2	1	0.00447	3.405	1.92
Ru(0)–C(18)–C(20)-C(18)	1	1	0.00646	3.693	1.91
Ru(0)–C(16)–C(14)	2	1	0.00314	3.417	1.88
Ru(0)–C(17)–C(13)	2	1	0.00315	3.425	1.79
Ru(0)–C(17)–Ru(0)-C(17)	2	1	0.01146	4.378	1.79
Ru(0)–C(18)–C(14)	2	1	0.00315	3.428	1.76
Ru(0)–C(16)–C(15)-C(17)	4	1	0.00521	4.114	1.71
Ru(0)–C(15)–C(16)-C(14)	4	1	0.00435	4.121	1.71
Ru(0)–C(16)–C(15)-C(16)	2	1	0.00875	3.594	1.51
Ru(0)–C(18)–C(17)-C(18)	2	1	0.01042	3.593	1.41
Ru(0)–C(21)–C(18)	2	1	0.00174	4.337	1.40
Ru(0)–C(14)–C(15)-C(14)-C(15)	4	1	0.00690	4.301	1.17
Ru(0)–C1(1)–C(14)	2	1	0.00730	4.378	1.05
Ru(0)–C(16)–C(17)-C(16)-C(17)	4	1	0.01709	4.301	0.92

Appendix A.5

Table A.5 Conditions, restraints, and constraints used in MS XAFS fitting for $[(\eta^6\text{-}p\text{-cymene})Ru(en)Cl]^{+}$ [a]

Condition

K range: 2-13 $Å^{-1}$ [b]
FT range : 1-4.5 Å [b]
Determinancy (N_i/p): [c] 1.1
Maximal effective path length of a photoelectron: 5.0 Å
Maximum number of legs: 2
Plane-wave path filter threshold: 0%
Curved-wave path filter threshold: 0%
Scale factor: 0.9 ± 0.1

Bond length restraints (Å)

$Ru^0–Cl^1 \approx 2.42$ {0.04}
$Ru^0–N^{12} \approx 2.12$ {0.04}
$Ru^0–C^3 \approx 2.19$ {0.03}
$Ru^0–C^6 \approx 2.19$ {0.03}
$C^6–C^9 \approx 1.52$ {0.03}
$C^9–C^{10} \approx 1.52$ {0.03}
$N^{12}–C^{13} \approx 1.30$ {0.05}
$C^{13}–C^{14} \approx 1.49$ {0.05}
$C^3–C^4 \approx 1.41$ {0.03}
$C^6–C^7 \approx 1.41$ {0.03}

$Ru^0\text{-}C^3 \approx Ru^0\text{-}C^4 \approx Ru^0\text{-}C^5$ {0.03}
$Ru^0\text{-}C^6 \approx Ru^0\text{-}C^7 \approx Ru^0\text{-}C^8$ {0.03}
$Ru^0–N^{12} \approx Ru^0–N^{15}$ {0.04}
$C^6–C^9 \approx C^2–C^3$ {0.03}
$C^9–C^{10} \approx C^9–C^{11}$ {0.03}

$N^{12}–C^{13} \approx N^{15}–C^{14}$ {0.05}
$C^3–C^4 \approx C^4–C^5 \approx C^5–C^6$ {0.03}
$C^6–C^7 \approx C^7–C^8 \approx C^8–C^3$ {0.03}

Bond angle restraints (°):

$C^5–C^4–C^3 \approx 120$ {10}
$C^7–C^6–C^5 \approx 120$ {10}
$C^{13}–C^{14}–N^{15} \approx 110$ {10}
$N^{12}–Ru^0–N^{15} \approx 78$ {10}
$Cl^1–Ru^0–N^{15} \approx 83$ {10}
$Cl^1–Ru^0–N^{12} \approx 84$ {10}
$Ru^0–N^{15}–C^{14} \approx 123$ {10}

$C^5\text{-}C^4\text{-}C^3 = C^8\text{-}C^3\text{-}C^4 = C^7\text{-}C^8\text{-}C^3$ {10}
$C^7–C^6–C^5 = C^6–C^5–C^4 = C^8–C^7–C^6$ {10}
$Ru^0–N^{15}–C^{14} = Ru^0–N^{12}–C^{13}$ {10}

Debye-Waller factor restraints ($Å^2$):

$0.001\{0.0005\} < \sigma_i^2 < 0.02$ {0.001}, i= 1-15
$\sigma_i^2 (Ru^0) > (\sigma_i^2 (C1^1) + 0.001)$ {0.0005}

Continued on the next page

Debye-Waller factor constraints:
σ_i^2 (C^2) = σ_i^2 (C^9)
σ_i^2 (C^{10}) = σ_i^2 (C^{11})
σ_i^2 (C^3) = σ_i^2 (C^4) = σ_i^2 (C^5) = σ_i^2 (C^6)
σ_i^2 (N^{12}) = σ_i^2 (N^{15})

Atoms restrained to be approximately coplanar
($C^3 - C^4$) x ($C^5 - C^4$)^.($C^7 - C^4$) ≈ 0 {0.2}
($C^8 - C^7$) x ($C^6 - C^7$)^.($C^4 - C^7$) ≈ 0 {0.2}

[a]Experimental and calculated spectra are shown in Figure 3.9 (Chapter 3).

[b]The applied window functions are shown in Figure 3.9. [c]The number of independent observations (N_i) and the number of varied parameters (p) were calculated taking into account the applied restraints and constraints [ref. 27 in Chapter 3]. [d] The atom numbering used in the MS XAFS calculation are shown in Figure 3.10 (Chapter 3).

Table A.6 Results of MS XAFS Analysis Fitting for [(η^6-*p*-cymene)Ru(en)Cl]$^{+a}$

Parameter[b]	
-E0	20.34
S_0^2	0.95
σ_i^2 (Cl^1), Å^2 [c]	0.0004(1)
σ_i^2 (C^2), Å^2 [c]	0.0005(1)
σ_i^2 (C^8), Å^2 [c]	0.0008(1)
σ_i^2 (C^9), Å^2 [c]	0.0005(1)
σ_i^2 (C^{10}), Å^2 [c]	0.0005(1)
σ_i^2 (N^{12}), Å^2 [c]	0.0005(1)
σ_i^2 (C^{13}), Å^2 [c]	0.0005(1)
σ_i^2 (N^{15}), Å^2 [c]	0.0005(1)

[a]Experimental and calculated spectra are shown in Figure 3.9 (Chapter 3). [b]Designations of parameters: -E_0 is the threshold energy; S_0^2 is the scale factor; σ^2 (Å^2) is the Debye-Waller factor; and *N* is the number of scatterers in a shell. The values in the parentheses are the errors in the last significant figures, obtained from the Monte-Carlo analysis. [c]Atom numbering corresponds to Figure 3.10 with the resulting fit parameters listed in Table 3.2 (Chapter 3).

Appendix A.7

Most significant Photoelectron Scattering Paths in the Calculated XAFS spectrum of $[(\eta^6\text{-}p\text{-cymene})Ru(en)Cl]^+$

Path	Legs	Dege-neracy	σ_i^2, Å^2	Length, Å	Contribution, %
Ru0-N15	1	1	0.00044	2.10963	100.00%
Ru0-C7	2	1	0.00101	2.17213	100.00%
Ru0-N12	1	1	0.00044	2.10976	99.97%
Ru0-C8	1	1	0.00101	2.1931	75.69%
Ru0-C4	1	1	0.00101	2.19885	74.44%
Ru0-C3	1	1	0.00101	2.1989	74.43%
Ru0-C5	1	1	0.00101	2.19955	74.28%
Ru0-Cl1	1	1	0.00048	2.40602	53.81%
N15-Ru0-C4	2	1	0.00145	4.30848	18.58%
Ru0-N12-Ru0-C6	2	1	0.00145	4.33035	16.51%
Ru0-C14	1	1	0.00482	2.96428	15.04%
Ru0-C13	1	1	0.00482	2.96376	15.02%
Ru0-C2-C3	2	1	0.00163	3.61045	11.82%
Ru0-C8-Ru0-Cl1	2	1	0.00149	4.59912	11.52%
Ru0-C10	1	1	0.0005	3.65207	11.37%
Ru0-C2	1	1	0.00158	3.50214	10.91%
Ru0-C9	1	1	0.00158	3.3769	10.56%
Ru0-C5-Ru0-N12	2	1	0.00145	4.30931	10.35%
Ru0-C9-C6	2	1	0.00166	3.55875	9.00%
Ru0-C7-C8	2	1	0.00133	2.88872	8.67%
Ru0-N15-C4	2	1	0.00145	4.2977	8.34%
Ru0-C8-C3	2	1	0.00133	2.90156	8.32%
Ru0-C7-C6	2	1	0.00133	2.90226	8.28%
Ru0-C3-C4	2	1	0.00133	2.90469	8.24%
Ru0-C5-C4	2	1	0.00133	2.90497	8.23%
Ru0-C11	1	1	0.0005	3.82942	8.15%
Ru0-C6-C5	2	1	0.00133	2.91518	8.02%
Ru0-C14-N15	2	1	0.0044	3.19183	7.93%
Ru0-C13-N12	2	1	0.0044	3.19159	7.92%
Ru0-N12-C6	2	1	0.00144	4.31065	7.92%
Ru0-C5-N12	2	1	0.00142	4.23213	7.72%
Ru0-C3-N15	2	1	0.0014	4.15919	6.41%
Ru0-C5-N15	2	1	0.0014	4.15729	6.36%
Ru0-C3-Ru0-N15	2	1	0.00145	4.30853	5.02%
Ru0-C5-Ru0-N15	2	1	0.00145	4.30918	4.88%

Continued on the next page

Path	Legs	Dege-neracy	σ_i^2, Å^2	Length, Å	Contribution, %
Ru0-C3-C2-C3	1	1	0.00205	3.71877	4.73%
Ru0-C8-Cl1	2	1	0.00149	4.59567	4.47%
Ru0-C7-N12	2	1	0.00137	4.05829	4.23%
Ru0-Cl1-Ru0-C7	2	1	0.00149	4.57816	3.90%
Ru0-C13-C14	2	1	0.00604	3.71761	3.76%
Ru0-Cl1-C7	2	1	0.00145	4.4665	3.30%
Ru0-C7-Ru0-C7	2	1	0.00403	4.34427	3.14%
Ru0-C4-N12	2	1	0.00133	3.95398	3.09%
Ru0-N12-N15	2	1	0.00071	3.37768	2.96%
Ru0-C13-N15	2	1	0.00436	3.70109	2.83%
Ru0-C14-N12	2	1	0.00436	3.7014	2.83%
Ru0-Cl1-C3	2	1	0.00143	4.44202	2.77%
Ru0-C7-C5	2	1	0.00157	3.39765	2.76%
Ru0-C7-C3	2	1	0.00157	3.39958	2.73%
Ru0-C8-N15	2	1	0.0013	3.8385	2.61%
Ru0-C8-C4	2	1	0.00157	3.41763	2.57%
Ru0-C6-N15	2	1	0.0013	3.86445	2.52%
Ru0-C5-C3	2	1	0.00157	3.42576	2.50%

Table A.8 Conditions, restraints, and constraints used in MS XAFS fitting for (η^6-*p*-cymene)Ru(acac)Cl [a]

Conditions

K range, $Å^{-1}$: 0-16 [b]

FT range, Å : 1-4.5[b]

Determinancy (N_i/p):[c] 1.1

Maximal effective path length of a photoelectron: 5.0 Å

Maximum number of legs: 2

Plane-wave path filter threshold: 0%

Curved-wave path filter threshold: 0%

Scale factor: 0.9 ± 0.1

Bond length restraints (Å):[d]

Ru^0-$Cl^1 \approx 2.41$ {0.03}

Ru^0-$O^3 \approx 2.06$ {0.03}

Ru^0-$C^{10} \approx 2.145$ {0.04}

Ru^0-$C^{13} \approx 2.145$ {0.04}

C^{10}-$C^9 \approx 1.57$ {0.03}

C^{13}-$C^{16} \approx 1.52$ {0.03}

O^7-$C^6 \approx 1.27$ {0.05}

C^5-$C^6 \approx 1.43$ {0.05}

C^6-$C^8 \approx 1.45$ {0.05}

C^{10}-$C^{11} \approx 1.41$ {0.05}

C^{13}-$C^{14} \approx 1.41$ {0.05}

Ru^0-$C^{10} \approx Ru^0$-$C^{11} \approx Ru^0$-C^{12} {0.04}

Ru^0-$C^{13} \approx Ru^0$-$C^{14} \approx Ru^0$-C^{15} {0.04}

Ru^0-$O^3 \approx Ru^0$-O^7 {0.03}

C^{13}-$C^{16} \approx C^{16}$-$C^{17} \approx C^{16}$-C^{18} {0.03}

O^7-$C^6 \approx O^3$-C^2 {0.05}

C^5-$C^6 \approx C^2$-C^5 {0.05}

C^6-$C^8 \approx C^2$-C^4 {0.05}

C^{10}-$C^{11} \approx C^{11}$-$C^{12} \approx C^{12}$-C^{13} {0.05}

C^{13}-$C^{14} \approx C^{14}$-$C^{15} \approx C^{15}$-C^{10} {0.05}

C^{20}-$C^{21} \approx C^{20}$-C^{22} {0.02}

Bond angle restraints (º):[d]

C^{10}-C^{11}-$C^{12} = 120$ {5}

C^{15}-C^{14}-$C^{13} = 120$ {5}

O^7-C^6-$C^5 = 120$ {10}

Ru^0-O^7- $C^6 = 125$ {10}

O^3- Ru^0- $Cl^1 = 86$ {5}

O^3- Ru^0- $O^7 = 87$ {5}

O^7- Ru^0- $Cl^1 = 84$ {5}

C^{10}-C^{11}-$C^{12} = C^{11}$-C^{12}-$C^{13} = C^{14}$-C^{13}-C^{12} {5}

C^{15}-C^{14}-$C^{13} = C^{10}$-C^{15}-$C^{14} = C^{11}$-C^{10}-C^{15} {5}

O^7-C^6-$C^5 = O^3$-C^2-$C^5 = C^6$-C^5-C^2 {10}

Ru^0-O^7-$C^6 = Ru^0$-O^3-C^2

Debye-Waller factor restraints ($Å^2$):[d]

$0.001\{0.0005\} < \sigma_i^2 < 0.02$ {0.001}, i= 18

$\sigma_i^2 (Cl^1) > (\sigma_i^2 (O^3) + 0.001)$ {0.0005}

Continued on the next page

Debye-Waller factor constraints:[d]

$\sigma_i^2 (O^3) = \sigma_i^2 (O^7)$
$\sigma_i^2 (C^8) = \sigma_i^2 (C^4)$
$\sigma_i^2 (C^{17}) = \sigma_i^2 (C^{18})$
$\sigma_i^2 (C^{10}) = \sigma_i^2 (C^{11}) = \sigma_i^2 (C^{12})$
$\sigma_i^2 (C^{13}) = \sigma_i^2 (C^{14}) = \sigma_i^2 (C^{15})$
$\sigma_i^2 (C^6) = \sigma_i^2 (C^2)$

Atoms restrained to be approximately coplanar

$(C^{10} – C^{15}) \times (C^{14} – C^{15})^{\wedge} . (C^{12} - C^{15}) \approx 0$ {0.05}
$(C^{13} – C^{12}) \times (C^{11} – C^{12})^{\wedge} . (C^{15} - C^{12}) \approx 0$ {0.05}

[a]Experimental and calculated spectra are shown in **Figure 3.11** (Chapter 3).. [b]The applied window functions are shown in Figure 3.11. [c]The number of independent observations (N_i) and the number of varied parameters (p) were calculated taking into account the applied restraints and constraints [ref. 27 in Chapter 3]. [d] The atom numbering used in the MS XAFS calculation are shown in Figure 3.14 (Chapter 3).

Table A.9 Results of MS XAFS Analysis Fitting for (η^6-*p*-cymene)Ru(acac)Cl [a]

Parameter[b]	
-E0	18.69
S_0^2	0.90
σ^2 (Cl^1), Å^2 [c]	0.0041(1)
σ^2 (O^3), Å^2 [c]	0.0009(1)
σ^2 (O^7), Å^2 [c]	0.0009(1)
σ^2 (C^{10}), Å^2 [c]	0.0020(1)
σ^2 (C^{16}), Å^2 [c]	0.0005(1)
σ^2 (C^{17}), Å^2 [c]	0.0005(9)
σ^2 (C^2), Å^2 [c]	0.0200(1)
σ^2 (C^4), Å^2 [c]	0.0005(1)
σ^2 (C^5), Å^2 [c]	0.0200(1)

[a]Experimental and calculated spectra are shown in Figure 3.11 (Chapter 3). [b]Designations of parameters: -E_0 is the threshold energy; S_0^2 is the scale factor; σ^2 (Å^2) is the Debye-Waller factor; and *N* is the number of scatterers in a shell. The values in the parentheses are the errors in the last significant figures, obtained from the Monte-Carlo analysis. [c]Atom numbering corresponds to Figure 3.12 with the resulting fit parameters listed in Table 3.3 (Chapter 3).

Appendix A.10

Most significant Photoelectron Scattering Paths in the Calculated XAFS spectrum of (η^6-*p*-cymene)Ru(acac)Cl					
Path	Legs	Dege-neracy	σ_i^2, Å^2	Length, Å	Contribution, %
Ru0-O3	1	1	0.00096	2.04723	100.00%
Ru0-C14	2	1	0.00205	2.1706	100.00%
Ru0-O7	1	1	0.00096	2.04958	99.32%
Ru0-C13	1	1	0.00205	2.15423	66.28%
Ru0-C10	1	1	0.00205	2.15577	65.94%
Ru0-C15	1	1	0.00205	2.16109	64.79%
Ru0-Cl1	1	1	0.00408	2.4096	56.40%
Ru0-C11	1	1	0.00205	2.15994	51.87%
Ru0-O7-Ru0-C11	2	1	0.003	4.20952	23.18%
Ru0-C14-C13	4	1	0.00271	2.86543	18.31%
Ru0-C6-O7	2	1	0.01877	3.18195	16.26%
Ru0-C2-O3	2	1	0.01877	3.17955	16.25%
Ru0-C16	1	1	0.0005	3.33677	14.78%
Ru0-C2	1	1	0.02	3.03731	13.72%
Ru0-C6	1	1	0.02	3.03983	13.68%
Ru0-C9	1	1	0.00106	3.29121	13.58%
Ru0-C8-O7	2	1	0.00051	4.30933	13.50%
Ru0-C4-O3	2	1	0.00051	4.3095	13.48%
Ru0-C15-Ru0-O3	2	1	0.003	4.20832	11.26%
Ru0-C16-C13	2	1	0.00083	3.50501	10.70%
Ru0-C18	1	1	0.0005	3.70527	10.52%
Ru0-C14-Ru0-Cl1	2	1	0.00613	4.5802	10.43%
Ru0-C13-Ru0-Cl1	2	1	0.00613	4.56383	9.75%
Ru0-C12-Ru0-O7	2	1	0.003	4.19704	9.48%
Ru0-C11-C12	2	1	0.00271	2.85818	9.19%
Ru0-C11-C10	2	1	0.00271	2.86148	9.17%
Ru0-C10-C15	2	1	0.00271	2.86288	9.15%
Ru0-C14-C15	2	1	0.00271	2.8705	9.13%
Ru0-C12-C7	2	1	0.00293	4.09889	8.93%
Ru0-C15-O3	2	1	0.00295	4.1299	8.78%
Ru0-O7-C11	2	1	0.003	4.20753	8.63%
Ru0-C10-O3	2	1	0.0029	4.06038	8.38%
Ru0-C2-C4-O3	2	1	0.00247	4.41008	8.36%
Ru0-C6-C8-O7	2	1	0.00249	4.41114	8.31%

Continued on the next page

Path	Legs	Dege-neracy	σ_i^2, Å^2	Length, Å	Contribution, %
Ru0-C10-O7	2	1	0.0029	4.05893	8.30%
Ru0-C5	1	1	0.02	3.38479	8.04%
Ru0-C17	1	1	0.0005	4.13994	7.92%
Ru0-C9-C10	2	1	0.00143	3.50807	7.79%
Ru0-C4-C2	2	1	0.00247	4.39651	7.36%
Ru0-O7-C8-O7	1	1	0.00054	4.32258	7.30%
Ru0-C8-C6	2	1	0.00249	4.39789	7.29%
Ru0-O3-C4-O3	1	1	0.00054	4.32307	7.28%
Ru0-C4	1	1	0.0005	4.29593	6.25%
Ru0-C8	1	1	0.0005	4.29608	6.25%
Ru0-C10-Ru0-O3	2	1	0.003	4.20301	5.78%
Ru0-C10-Ru0-O7	2	1	0.003	4.20535	5.51%
Ru0-O7-C6-O7	1	1	0.02066	3.32407	5.13%
Ru0-O3-C2-O3	1	1	0.02066	3.3218	5.12%
Ru0-C14-Cl1	2	1	0.00608	4.54688	5.01%
Ru0-C10-O7	2	1	0.0029	4.05893	8.30%
Ru0-C5	1	1	0.02	3.38479	8.04%
Ru0-C17	1	1	0.0005	4.13994	7.92%
Ru0-C9-C10	2	1	0.00143	3.50807	7.79%
Ru0-C4-C2	2	1	0.00247	4.39651	7.36%
Ru0-O7-C8-O7	1	1	0.00054	4.32258	7.30%
Ru0-C8-C6	2	1	0.00249	4.39789	7.29%
Ru0-O3-C4-O3	1	1	0.00054	4.32307	7.28%
Ru0-C4	1	1	0.0005	4.29593	6.25%
Ru0-C8	1	1	0.0005	4.29608	6.25%
Ru0-C10-Ru0-O3	2	1	0.003	4.20301	5.78%
Ru0-C10-Ru0-O7	2	1	0.003	4.20535	5.51%
Ru0-O7-C6-O7	1	1	0.02066	3.32407	5.13%
Ru0-O3-C2-O3	1	1	0.02066	3.3218	5.12%
Ru0-C14-Cl1	2	1	0.00608	4.54688	5.01%

Appendix A.11

Table A.11 Conditions, restraints, and constraints used in MS XAFS fitting for OxaloRAPTA-C [a]

Condition

K range: 0-15 Å^{-1} [b]
FT range : 1-4.5 Å [b]
Determinancy (N_i/p): [c] 1
Maximal effective path length of a photoelectron: 5.0 Å
Maximum number of legs: 2
Plane-wave path filter threshold: 0%
Curved-wave path filter threshold: 0%
Scale factor: 0.9 ± 0.1

Bond length restraints (Å)

Ru^0–P^1 ≈ 2.31 {0.02}
Ru^0–O^2 ≈ 2.09 {0.02}
Ru^0–C^9 ≈ 2.19 {0.02}
Ru^0–C^{12} ≈ 2.19 {0.02}
P^1–C^{19} ≈ 1.84 {0.04}
N^6–C^{21} ≈ 1.47 {0.04}
N^7–C^{19} ≈ 1.47 {0.04}
N^8–C^{20} ≈ 1.47 {0.04}
C^9–C^{10} ≈ 1.41 {0.03}
C^{12}–C^{13} ≈ 1.41 {0.03}
C^9–C^{15} ≈ 1.52 {0.05}
O^3–C^{26} ≈ 1.25 {0.04}
C^{25}–C^{26} ≈ 1.56 {0.05}
O^5–C^{26} ≈ 1.23 {0.02}

Ru^0–O^2 ≈ Ru^0–O^3 {0.02}
Ru^0-C^9 ≈ Ru^0-C^{10} ≈ Ru^0-C^{11} {0.02}
Ru^0–C^{12} ≈ Ru^0–C^{13}≈ Ru^0–C^{14} {0.02}
P^1–C^{19} ≈ P^1–C^{20}≈ P^1–C^{21} {0.04}
N^6–C^{21} ≈ N^6–C^{22} ≈ N^6–C^{23} {0.04}

N^7–C^{19} ≈ N^7–C^{23} ≈ N^7–C^{24} {0.04}
N^8–C^{20} ≈ N^8–C^{22} ≈ N^8–C^{24} {0.04}
C^9–C^{10} ≈ C^{10}–C^{11} ≈ C^{11}–C^{12} {0.03}
C^{12}–C^{13} ≈ C^{13}–C^{14} ≈ C^{14}–C^9 {0.03}
C^9–C^{15}≈ C^{12}–C^{18} ≈ C^{15}–C^{16} ≈ C^{15}–C^{17} {0.05}
O^3–C^{26} ≈ O^2–C^{25} {0.05}

O^5–C^{26} ≈ O^4–C^{25} {0.02}

Bond angle restraints (°):

C^{14}–C^{13}–C^{12} ≈ 120 {5}
C^9–C^{10}–C^{11} ≈ 120 {10}
O^3–C^{26}–C^{25} ≈ 108 {10}
C^{21}–P^1–C^{19} ≈ 120{10}
P^1–C^{19}–N^7 ≈ 109 {10}
C^{20}–N^8–C^{24} ≈ 109 {10}
C^{24}–N^8–C^{22} ≈ 120 {10}
N^8–C^{22}–N^6 ≈ 120 {10}
C^{21}–N^6–C^{22} ≈ 109 {10}
O^3–Ru^0–O^2 ≈ 78 {5}
P^1–Ru^0–O^3 ≈ 84 {5}
P^1–Ru^0–O^2 ≈ 87 {5}

C^{14}-C^{13}-C^{12} = C^{11}-C^{12}-C^{13}= C^{10}-C^{11}-C^{12} {5}
C^9–C^{10}–C^{11} = C^{10}–C^9–C^{14}= C^9–C^{14}–C^{13} {5}
O^3–C^{26}–C^{25} = O^2–C^{25}–C^{26} {10}
C^{21}–P^1–C^{19} = C^{20}–P^1–C^{21} = C^{19}–P^1–C^{20} {10}
P^1–C^{19}–N^7 = P^1–C^{21}–N^6 = P^1–C^{20}–N^8 {10}
C^{20}–N^8–C^{24} = C^{20}–N^8–C^{22} = C^{19}–N^7–C^{24} {10}
C^{24}–N^8–C^{22} = C^{24}–N^7–C^{23} {10}
N^8–C^{22}–N^6 = N^8–C^{24}–N^7 = N^7–C^{23}–N^6 {10}
C^{21}–N^6–C^{22} = C^{21}–N^6–C^{23} = C^{22}–N^6–C^{23} {10}

Continued on the next page

Debye-Waller factor restraints (Å^2):
$0.001\{0.0005\} < \sigma_i^2 < 0.02\ \{0.001\}$, i= 1-26

Debye-Waller factor constraints:
$\sigma_i^2 (C^2) = \sigma_i^2 (C^3)$
$\sigma_i^2 (C^{21}) = \sigma_i^2 (C^{20}) = \sigma_i^2 (C^{19})$
$\sigma_i^2 (C^9) = \sigma_i^2 (C^{10}) = \sigma_i^2 (C^{11}) = \sigma_i^2 (C^{12}) = \sigma_i^2 (C^{13}) = \sigma_i^2 (C^{14})$
$\sigma_i^2 (N^6) = \sigma_i^2 (N^7) = \sigma_i^2 (N^8)$
$\sigma_i^2 (C^{23}) = \sigma_i^2 (C^{22}) = \sigma_i^2 (C^{24})$
$\sigma_i^2 (C^{16}) = \sigma_i^2 (C^{17})$
$\sigma_i^2 (C^{25}) = \sigma_i^2 (C^{26})$
$\sigma_i^2 (O^4) = \sigma_i^2 (O^5)$

Atoms restrained to be approximately coplanar
$(C^{10} – C^{11}) \times (C^{12} – C^{11})\text{^}.(C^{14} – C^{11}) \approx 0\ \{0.1\}$
$(C^{13} – C^{14}) \times (C^9 – C^{14})\text{^}.(C^{11} – C^{14}) \approx 0\ \{0.1\}$

[a]Experimental and calculated spectra are shown in Figure 3.13 (Chapter 3). [b]The applied window functions are shown in Figure 3.13. [c]The number of independent observations (N_i) and the number of varied parameters (p) were calculated taking into account the applied restraints and constraints [ref. 27 in Chapter 3]. [d] The atom numbering used in the MS XAFS calculation are shown in Figure 3.14 (Chapter 3).

Table A.12 Results of MS XAFS Analysis Fitting for OxaloRAPTA-C[a]

Parameter[b]	
-E0	15.11
S_0^2	0.97
σ_i^2 (P^1), Å$^{2\,c}$	0.0001(1)
σ_i^2 (O^2), Å$^{2\,c}$	0.0004(1)
σ_i^2 (O^4), Å$^{2\,c}$	0.0005(1)
σ_i^2 (N^6), Å$^{2\,c}$	0.0005(1)
σ_i^2 (C^9), Å$^{2\,c}$	0.0005(1)
σ_i^2 (C^{15}), Å$^{2\,c}$	0.0005(1)
σ_i^2 (C^{16}), Å$^{2\,c}$	0.0005(1)
σ_i^2 (C^{25}), Å$^{2\,c}$	0.0005(1)

[a]Experimental and calculated spectra are shown in Figure 3.13 (Chapter 3). [b]Designations of parameters: $-E_0$ is the threshold energy; S_0^2 is the scale factor; σ^2 (Å^2) is the Debye-Waller factor; and *N* is the number of scatterers in a shell. The values in the parentheses are the errors in the last significant figures, obtained from the Monte-Carlo analysis [ref. 27 in Chapter 3]. [c]The atom numbering correspond to Figure 3.14 and the corresponding goodness-of-fit parameters are listed in Table 3.4 (Chapter 3).

Appendix A.13

Most significant Photoelectron Scattering Paths in the Calculated XAFS spectrum of OxaloRAPTA-C					
Path	Legs	Dege-neracy	σ_i^2, Å^2	Length, Å	Contribution, %
Ru0-O2	1	1	0.0015	2.11218	100.00%
Ru0-O3	1	1	0.0015	2.0966	100.00%
Ru0-P1	1	1	0.00045	2.32921	100.00%
Ru0-C14	1	1	0.00821	2.06186	80.64%
Ru0-C13	1	1	0.00821	2.08738	74.93%
Ru0-C9	1	1	0.00821	2.10493	70.86%
Ru0-C26	1	1	0.00047	2.93276	34.08%
Ru0-C10	1	1	0.02025	2.20864	31.77%
Ru0-C12	1	1	0.02025	2.20968	31.65%
Ru0-O4-C25	2	1	0.0015	4.05239	29.22%
Ru0-C25	1	1	0.00047	2.78688	28.93%
Ru0-C11	1	1	0.02025	2.24975	27.73%
Ru0-O-C26	2	1	0.0015	4.14683	22.64%
Ru0-C15	1	1	0.00049	3.40879	21.00%
Ru0-C26-O3	2	1	0.0008	3.14923	20.40%
Ru0-C15-C9	2	1	0.00154	3.52929	20.03%
Ru0-C18	1	1	0.00048	3.18836	19.34%
Ru0-O2-Ru0-C13	2	1	0.0097	4.19956	18.38%
Ru0-C19	1	1	0.00064	3.53617	16.76%
Ru0-O3-Ru0-C9	2	1	0.0097	4.20153	15.58%
Ru0-C21	1	1	0.00064	3.60924	14.04%
Ru0-C25-O4-C25	1	1	0.00151	4.05458	13.84%
Ru0-N7	2	1	0.00261	4.78301	13.64%
Ru0-C20	1	1	0.00064	3.63468	13.22%
Ru0-C16	1	1	0.0005	3.78661	13.18%
Ru0-C26-N5-O3	2	1	0.00159	4.26026	13.09%
Ru0-C26-O5-C26	1	1	0.00154	4.16348	13.07%
Ru0-C17-C9	2	1	0.00084	4.64465	11.19%
Ru0-O3-Ru0-C14	2	1	0.0097	4.15846	11.10%
Ru0-O5	1	1	0.0015	4.13018	10.80%
Ru0-O4	1	1	0.0015	4.0502	10.64%
Ru0-O5-O3	2	1	0.00162	4.24361	10.15%
Ru0-C25-O4-O2	2	1	0.00169	4.24924	9.89%
Ru0-C11-Ru0-P1	2	1	0.0207	4.57896	9.81%
Ru0-C25-O2	2	1	0.00092	3.09662	9.15%

Continued on the next page

Path	Legs	Dege-neracy	σ_i^2, Å^2	Length, Å	Contribution, %
Ru0-C14-C13	2	1	0.01097	2.77398	9.10%
Ru0-C9-C14	2	1	0.01096	2.78334	8.71%
Ru0-O3-C14	2	1	0.00952	4.08284	8.24%
Ru0-N6-P1	2	1	0.00261	4.92715	7.96%
Ru0-C14-O2	2	1	0.00933	4.01561	7.68%
Ru0-N8-C20	2	1	0.00256	5.03565	7.62%
Ru0-N8-P1	2	1	0.00261	5.04675	7.44%
Ru0-O2-C13	2	1	0.0097	4.19599	7.28%
Ru0-C10-Ru0-P1	2	1	0.0207	4.53784	7.22%
Ru0-O3-C9	2	1	0.00965	4.17907	7.14%
Ru0-C19-P1	2	1	0.00071	3.86467	6.96%
Ru0-C21-P1	2	1	0.00071	3.90249	6.89%
Ru0-N7-C19	2	1	0.00254	4.89023	6.87%
Ru0-N6-C21	2	1	0.00253	4.95675	6.83%
Ru0-C20-P1	2	1	0.0007	3.915	6.72%
Ru0-O4-O2	2	1	0.0017	4.24706	6.63%
Ru0-O5-C26-O3	2	1	0.00196	4.36329	6.40%
Ru0-N6	1	1	0.00261	4.84044	6.34%
Ru0-N7-P1	2	1	0.0026	4.88979	6.27%
Ru0-C26-O5-C26-O3	2	1	0.00203	4.37994	6.15%
Ru0-C17	1	1	0.0005	4.59515	6.10%
Ru0-C10-C11	2	1	0.02665	2.93435	5.94%
Ru0-C10-C9	2	1	0.01925	2.8619	5.79%
Ru0-C12-C13	2	1	0.01933	2.85348	5.59%
Ru0-C17-C15	2	1	0.00054	4.75953	5.41%
Ru0-O4-C25-O2	2	1	0.00211	4.36213	5.35%
Ru0-C18-C12	2	1	0.00614	3.46319	5.33%
Ru0-C26-C25	2	1	0.0006	3.636	5.01%

Appendix A.14

Table A.14 Conditions, restraints, and constraints used in MS XAFS fitting for [Ru(η^6-*p*-cymene)Cl_2(mimid)] [a]

Conditions

K range, $Å^{-1}$: 0-15 [b]
FT range, Å : 1-4.5[b]
Determinancy (N_i/p):[c] 1.1
Maximal effective path length of a photoelectron: 5.0 Å
Maximum number of legs: 2
Plane-wave path filter threshold: 0%
Curved-wave path filter threshold: 0%
Scale factor: 0.9 ± 0.1

Bond length restraints (Å):[d]

Ru^0-Cl^1 ≈ 2.42 {0.05}
Ru^0-Cl^2 ≈ 2.42 {0.05}
Ru^0-C^5 ≈ 2.19 {0.04}
Ru^0-C^8 ≈ 2.19 {0.04}
Ru^0-N^3 ≈ 2.13 {0.05}
C^5-C^{11} ≈ 1.5 {0.05}
C^{12}-C^{13} ≈ 1.45 {0.05}
N^3-C^{15} ≈ 1.35 {0.04}
N^4-C^{15} ≈ 1.35 {0.03}
C^5-C^6 ≈ 1.41 {0.03}
C^8-C^9 ≈ 1.41 {0.03}

Ru^0-C^5 ≈ Ru^0-C^6 ≈ Ru^0-C^7 {0.04}
Ru^0-C^8 ≈ Ru^0-C^9 ≈ Ru^0-C^{10} {0.02}
C^5-C^{11}≈ C^8-C^{12} {0.05}
C^{12}-C^{13} ≈ C^{12}-C^{14} {0.05}
N^3-C^{15} ≈ N^3-C^{16} {0.02}
N^4-C^{15} ≈ N^4-C^{17} ≈ N^4-C^{18} {0.02}
C^5-C^6≈ C^6-C^7 ≈ C^7-C^8 {0.03}
C^8-C^9 ≈ C^9-C^{10} ≈ C^{10}-C^5 {0.03}

Bond angle restraints (°):[d]

C^6-C^5-C^{10} = 120 {10}
C^9-C^8-C^7 = 120 {10}
C^{15}-N^3-C^{16} = 108 {10}
C^{15}-N^4-C^{17} = 108 {10}
Cl^1-N^3-Cl^2 = 88 {10}
Cl^2-Ru^0-N^3 = 85 {3}
N^3-Ru^0-Cl^1 = 85 {3}

C^6-C^5-C^{10} = C^5-C^{10}-C^9 = C^{10}-C^9-C^8 {10}
C^9-C^8-C^7 = C^8-C^7-C^6 = C^5-C^6-C^7 {10}
C^{15}-N^3-C^{16} = N^3-C^{16}-C^{17} = N^4-C^{17}-C^{16}
C^{15}-N^4-C^{17} = N^3-C^{15}-N^4

Debye-Waller factor restraints ($Å^2$):[d]

0.001{0.0005} < σ_i^2 < 0.02 {0.001}, i= 1-18

Continued on the next page

Debye-Waller factor constraints:[d]
σ_i^2 (Cl^1) = σ_i^2 (Cl^2)
σ_i^2 (N^4) = σ_i^2 (N^3)
σ_i^2 (C^5) = σ_i^2 (C^6) = σ_i^2 (C^7)
σ_i^2 (C^8) = σ_i^2 (C^9) = σ_i^2 (C^{10})
σ_i^2 (C^{13}) = σ_i^2 (C^{14})

Atoms restrained to be approximately coplanar
(C^5 – C^{10}) x (C^9 – C^{10})^ . (C^7 - C^{10}) ≈ 0 {0.1}
(C^6 – C^7) x (C^8 – C^7)^ . (C^{10} – C^7) ≈ 0 {0.1}

[a]Experimental and calculated spectra are shown in **Figure 3.15** (Chapter 3). [b]The applied window functions are shown in Figure 3.15. [c]The number of independent observations (N_i) and the number of varied parameters (p) were calculated taking into account the applied restraints and constraints [ref. 27 in Chapter 3]. [d] The atom numbering used in the MS XAFS calculation are shown in Figure 3.16 (Chapter 3).

Table A.15 Results of MS XAFS Analysis Fitting for [Ru(η^6-*p*-cymene)Cl_2(mimid)] [a]

Parameter[b]	
-E0	15.09
S_0^2	0.97
σ^2 (Cl^1), Å^2 [c]	0.0022(6)
σ^2 (Cl^2), Å^2 [c]	0.0022(6)
σ^2 (N^3), Å^2 [c]	0.0005(1)
σ^2 (C^5), Å^2 [c]	0.0032(1)
σ^2 (C^{11}), Å^2 [c]	0.0005(1)
σ^2 (C^{12}), Å^2 [c]	0.0200(1)
σ^2 (C^{13}), Å^2 [c]	0.0005(1)
σ^2 (C^{15}), Å^2 [c]	0.0005(1)
σ^2 (C^{16}), Å^2 [c]	0.0112(5)
σ^2 (C^{17}), Å^2 [c]	0.0005(1)

[a]Experimental and calculated spectra are shown in Figure 3.15 (Chapter 3).

[b]Designations of parameters: E_0 is the threshold energy; S_0^2 is the scale factor; σ^2 (Å^2) is the Debye-Waller factor; and *N* is the number of scatterers in a shell. The values in the parentheses are the errors in the last significant figures, obtained from the Monte-Carlo analysis. [c]The atom numbering correspond to Figure 3.16 and the corresponding goodness-of-fit parameters are listed in Table 3.5 (Chapter 3).

Appendix A.16

Most significant Photoelectron Scattering Paths in the Calculated XAFS spectrum of [Ru(η^6-*p*-cymene)Cl_2(mimid)]					
Path	Legs	Dege-neracy	σ_i^2, Å^2	Length, Å	Contribution, %
Ru0-N3	1	1	0.0005	2.08738	100.00%
Ru0-C5	1	1	0.00324	2.18977	68.65%
Ru0-Cl2	1	1	0.00215	2.43541	68.27%
Ru0-Cl1	1	1	0.00215	2.43626	68.19%
Ru0-C10	1	1	0.00324	2.19433	67.79%
Ru0-C8	1	1	0.00324	2.19475	67.70%
Ru0-C7	1	1	0.00324	2.19488	67.68%
Ru0-C6	1	1	0.00324	2.195	67.65%
Ru0-C9	1	1	0.00324	2.19567	67.52%
Ru0-N3-Ru0-C6	2	1	0.00374	4.28237	31.32%
Ru0-C15	1	1	0.0005	3.06561	29.83%
Ru0-C11	1	1	0.0005	3.2586	23.40%
Ru0-C15-N3	2	1	0.00057	3.26645	19.89%
Ru0-C16	1	1	0.01121	3.02149	19.80%
Ru0-C14-C8	2	1	0.0005	4.46432	18.13%
Ru0-N4-N3	2	1	0.00053	4.20549	17.30%
Ru0-C11-C5	2	1	0.00119	3.47166	15.78%
Ru0-C17-N3	2	1	0.00052	4.19735	14.48%
Ru0-N3-C6	2	1	0.00374	4.28187	13.43%
Ru0-N4	1	1	0.0005	4.12937	12.85%
Ru0-C16-N3	2	1	0.01025	3.2302	12.64%
Ru0-C10-C5	2	1	0.00428	2.89668	12.35%
Ru0-C6-C5	2	1	0.00428	2.89696	12.34%
Ru0-C8-C7	2	1	0.00428	2.89947	12.24%
Ru0-N4-C15	2	1	0.00053	4.27217	12.24%
Ru0-C6-C7	2	1	0.00428	2.89956	12.23%
Ru0-C10-C9	2	1	0.00428	2.89962	12.23%
Ru0-C9-C8	2	1	0.00428	2.89987	12.22%
Ru0-C17-C16	2	1	0.00172	4.23886	11.90%
Ru0-C17	1	1	0.0005	4.13395	11.75%
Ru0-C13	1	1	0.0005	4.09106	11.42%
Ru0-C12-C8	2	1	0.01959	3.656	10.65%
Ru0-C5-Ru0-N3	2	1	0.00374	4.27715	10.31%
Ru0-C7-Ru0-N3	2	1	0.00374	4.28225	10.23%

Continued on the next page

Path	Legs	Dege-neracy	σ_i^2, Å^2	Length, Å	Contribution, %
Ru0-C7-N3	2	1	0.00364	4.1622	10.10%
Ru0-C5-N3	2	1	0.00364	4.15761	10.09%
Ru0-C12	1	1	0.02	3.5566	9.84%
Ru0-C16-C17-N3	2	1	0.00173	4.30226	9.57%
Ru0-C8-Ru0-Cl2	2	1	0.00539	4.63016	9.54%
Ru0-C8-C14-C8	1	1	0.0005	4.46445	8.09%
Ru0-C15-N4-N3	2	1	0.00056	4.3483	6.97%
Ru0-C14	1	1	0.0005	4.46418	6.88%
Ru0-C10-Ru0-Cl1	2	1	0.00539	4.63059	6.58%
Ru0-N3-C17-N3	1	1	0.00062	4.26075	6.41%
Ru0-N3-N4-N3	1	1	0.00064	4.28161	5.57%
Ru0-C10-N3	2	1	0.00342	3.89907	4.86%
Ru0-C8-N3	2	1	0.00342	3.89931	4.86%
Ru0-C8-Cl2	2	1	0.00534	4.58158	4.83%
Ru0-C8-C12-C8	1	1	0.02138	3.75539	4.62%
Ru0-C11-Cl2	2	1	0.00174	4.23632	4.54%
Ru0-N3-C15-N3	1	1	0.00095	3.4673	4.51%
Ru0-N3-C17-C16-N3	2	1	0.00451	4.51097	4.44%
Ru0-C10-Cl1	2	1	0.00529	4.54514	4.36%
Ru0-C15-N3-C15-N3	2	1	0.0027	4.64637	4.26%
Ru0-N3-Ru0-N3	1	1	0.002	4.17476	4.14%
Ru0-C17-C16-N3	2	1	0.0044	4.44758	4.01%

Appendix A.17

Table A.17 Conditions, restraints, and constraints used in MS XAFS fitting for $Ru_2(OH)_3$[a]

Condition	
K range: 0-16 $Å^{-1}$ [b]	
FT range : 1-4.5 Å [b]	
Determinancy (N_i/p):[c] 1	
Maximal effective path length of a photoelectron: 5.0 Å	
Maximum number of legs: 8	
Plane-wave path filter threshold: 0%	
Curved-wave path filter threshold: 0%	
Scale factor: 0.9 ± 0.1	
Bond length restraints (Å)	
$Ru^0 - Ru^1 \approx 2.95$ {0.05}	
$Ru^0–O^2 \approx 2.09$ {0.05}	$Ru^0 - O^2 \approx Ru^0 - O^3 \approx Ru^0 - O^4$ {0.05}
$Ru^1–O^2 \approx 2.09$ {0.03}	$Ru^1 - O^2 \approx Ru^1–O^3 \approx Ru^1–O^4$ {0.05}
$Ru^0–C^5 \approx 2.18$ {0.03}	$Ru^0–C^5 \approx Ru^0–C^6 \approx Ru^0–C^7$ {0.03}
$Ru^0–C^8 \approx 2.18$ {0.03}	$Ru^0–C^8 \approx Ru^0–C^9 \approx Ru^0–C^{10}$ {0.03}
$Ru^1–C^{15} \approx 2.18$ {0.03}	$Ru^1–C^{15} \approx Ru^1–C^{16} \approx Ru^1–C^{17}$ {0.03}
$Ru^1–C^{18} \approx 2.18$ {0.03}	$Ru^1–C^{18} \approx Ru^1–C^{19} \approx Ru^1–C^{20}$ {0.03}
$C^7–C^{11} \approx 1.52$ {0.05}	$C^7–C^{11} \approx C^{10}–C^{14} \approx C^{14}–C^{12} \approx C^{14}–C^{13}$ {0.05}
$C^{17}–C^{21} \approx 1.52$ {0.05}	$C^{17}–C^{21} \approx C^{20}–C^{24} \approx C^{24}–C^{23} \approx C^{24}–C^{22}$ {0.05}
$C^5–C^6 \approx 1.41$ {0.02}	$C^5–C^6 \approx C^6–C^7 \approx C^7–C^8$ {0.01}
$C^8–C^9 \approx 1.41$ {0.02}	$C^8–C^9 \approx C^9–C^{10} \approx C^{10}–C^5$ {0.01}
$C^{15}–C^{16} \approx 1.41$ {0.02}	$C^{15}–C^{16} \approx C^{16}–C^{17} \approx C^{17}–C^{18}$ {0.01}
$C^{18}–C^{19} \approx 1.41$ {0.02}	$C^{18}–C^{19} \approx C^{19}–C^{20} \approx C^{20}–C^{15}$ {0.01}
x6 ≈ 0 {0.2}	
x9 ≈ 0 {0.2}	
Bond angle restraints (°):	
$C^{16}–C^{15}–C^{20} \approx 120$ {5}	$C^{16}-C^{15}-C^{20} = C^{17}-C^{16}-C^{15} = C^{18}-C^{17}-C^{16}$ {5}
$C^{19}–C^{18}–C^{17} \approx 120$ {5}	$C^{19}–C^{18}–C^{17} = C^{20}–C^{19}–C^{18} = C^{15}–C^{20}–C^{19}$ {5}
$C^6–C^5–C^{10} \approx 120$ {5}	$C^6-C^5-C^{10} = C^7-C^6-C^5 = C^8-C^7-C^6$ {5}
$C^9–C^8–C^7 \approx 120$ {5}	$C^9–C^8–C^7 = C^{10}–C^9–C^8 = C^5–C^{10}–C^9$ {5}
$C^8–C^7–C^{11} \approx 120$ {10}	$C^8–C^7–C^{11} = C^6–C^7–C^{11} = C^5–C^{10}–C^{14}$ {10}
$C^{14}–C^{10}–C^9 \approx 120$ {10}	$C^{14}–C^{10}–C^9 = C^{18}–C^{17}–C^{21} = C^{16}–C^{17}–C^{21}$ {10}
$C^{15}–C^{20}–C^{24} \approx 120$ {10}	$C^{15}–C^{20}–C^{24} = C^{24}–C^{20}–C^{19}$ {10}
$C^{12}–C^{14}–C^{13} \approx 110$ {10}	$C^{10}–C^{14}–C^{12} = C^{10}–C^{14}–C^{13}$ {10}
$C^{22}–C^{24}–C^{23} \approx 110$ {10}	$C^{22}–C^{24}–C^{23} = C^{20}–C^{24}–C^{22} = C^{20}–C^{24}–C^{23}$ {10}
$O^3–Ru^0–O^2 \approx 78$ {3}	$O^3–Ru^0–O^2 = O^2–Ru^0–O^4 = O^4–Ru^0–O^3$ {3}

Continued on the next page

$O^3–Ru^1–O^2 \approx 78$ {3}	$O^3–Ru^1–O^2 = O^2–Ru^1–O^4 = O^4–Ru^1–O^3$ {3}
$Ru^1–O^4–Ru^0 \approx 90$ {6}	$Ru^1–O^4–Ru^0 = Ru^1–O^3–Ru^0 = Ru^1–O^2–Ru^0$ {6}

Debye-Waller factor restraints (Å^2):

$0.001\{0.0005\} < \sigma_i^2 < 0.02\ \{0.001\}$, i= 1-24

Debye-Waller factor constraints:

$\sigma_i^2 (C^{15}) = \sigma_i^2 (C^{16}) = \sigma_i^2 (C^{17})$

$\sigma_i^2 (C^{18}) = \sigma_i^2 (C^{19}) = \sigma_i^2 (C^{20})$

$\sigma_i^2 (C^5) = \sigma_i^2 (C^6) = \sigma_i^2 (C^7) = \sigma_i^2 (C^8) = \sigma_i^2 (C^9) = \sigma_i^2 (C^{10})$

Atoms restrained to be approximately coplanar

$(C^{17} – C^{16}) \times (C^{15} – C^{16})\text{^}.(C^{19} – C^{16}) \approx 0$ {0.1}

$(C^{18} – C^{19}) \times (C^{20} – C^{19})\text{^}.(C^{16} – C^{19}) \approx 0$ {0.1}

$(C^5 – C^6) \times (C^7 – C^6)\text{^}.(C^9 – C^6) \approx 0$ {0.1}

$(C^{10} – C^9) \times (C^8 – C^9)\text{^}.(C^6 – C^9) \approx 0$ {0.1}

$(C^7 – C^8) \times (C^9 – C^8)\text{^}.(C^{11} – C^8) \approx 0$ {0.1}

$(C^{17} – C^{18}) \times (C^{19} – C^{18})\text{^}.(C^{21} – C^{18}) \approx 0$ {0.1}

[a]Experimental and calculated spectra are shown in Figure 3.17 (Chapter 3). [b]The applied window functions are shown in Figure 3.17. [c]The number of independent observations (N_i) and the number of varied parameters (p) were calculated taking into account the applied restraints and constraints [ref. 27 in Chapter 3]. [d] The atom numbering used in the MS XAFS calculation are shown in Figure 3.18 (Chapter 3).

Appendix A.18

Table A.18 Results of MS XAFS Analysis Fitting for $Ru_2(OH)_3$ [a]

Parameter[b]	
-E0	18.44
S_0^2	0.97
σ_i^2 (Ru^1), Å^2 [c]	0.0105(2)
σ_i^2 (O^2), Å^2 [c]	0.0029(3)
σ_i^2 (O^3), Å^2 [c]	0.0015(1)
σ_i^2 (O^4), Å^2 [c]	0.0073(8)
σ_i^2 (C^5), Å^2 [c]	0.0053(2)
σ_i^2 (C^{11}), Å^2 [c]	0.0200(1)
σ_i^2 (C^{15}), Å^2 [c]	0.0200(4)
σ_i^2 (C^{14}), Å^2 [c]	0.0005(1)

[a]Experimental and calculated spectra are shown in Figure 3.17 (Chapter 3). [b]Designations of parameters: E_0 is the threshold energy; S_0^2 is the scale factor; σ^2 (Å^2) is the Debye-Waller factor; and N is the number of scatterers in a shell. The values in the parentheses are the errors in the last significant figures, obtained from the Monte-Carlo analysis. [c]The atom numbering corresponds to Figure 3.18 and the corresponding goodness-of-fit parameters are listed in Table 3.6 (Chapter 3).

Appendix A.19

Most significant Photoelectron Scattering Paths in the Calculated XAFS spectrum of $Ru_2(OH)_3$

Path	Legs	Dege-neracy	σ_i^2, Å^2	Length, Å	Contribution, %
Ru0-C5	4	1	0.0005	2.09429	100.00%
Ru0-O3	2	1	0.00051	2.15933	44.57%
Ru0-C9	2	1	0.0005	2.1764	39.38%
Ru0-O2	1	1	0.00049	2.03193	32.25%
Ru0-C6-C5	8	1	0.00066	2.84099	15.28%
Ru0-Ru1	1	1	0.0016	2.98443	11.92%
Ru0-O2-Ru0-C8	4	1	0.00099	4.19198	11.03%
Ru0-C17-Ru1	8	1	0.00104	5.03202	10.77%
Ru0-C5-Ru0-O4	4	1	0.0205	4.21857	10.09%
Ru0-C11	2	1	0.00049	3.34406	9.79%
Ru0-O2-Ru0-C9	2	1	0.00099	4.20833	8.90%
Ru0-C6-Ru0-O3	4	1	0.00101	4.33574	7.69%
Ru0-C14-C10	4	1	0.00056	3.48712	7.59%
Ru0-O2-C8	4	1	0.00097	4.12573	7.49%
Ru0-C8-C7	4	1	0.00066	2.87923	7.22%
Ru0-C15	4	1	0.00091	4.88647	6.78%
Ru0-C6-C8	8	1	0.00078	3.39504	4.39%
Ru0-C5-O4	4	1	0.02044	4.20463	4.23%
Ru0-C12	1	1	0.00511	3.59909	4.20%
Ru0-O2-C9	2	1	0.00099	4.19533	3.69%
Ru0-O3-O2	4	1	0.00081	3.40304	3.60%
Ru0-Ru1-C8	8	1	0.00205	4.98994	3.53%
Ru0-O4-C10	4	1	0.02018	4.22385	3.47%
Ru0-C5-Ru0-C5	4	1	0.002	4.18859	3.42%
Ru0-C16	2	1	0.00091	4.92418	3.40%
Ru0-C13-C10	2	1	0.0005	4.52519	3.37%
Ru0-C19-Ru1	4	1	0.0011	4.97512	3.25%
Ru0-C6-O4	4	1	0.01947	4.08848	2.98%
Ru0-O2-C7	4	1	0.00092	3.89956	2.73%
Ru0-C13	1	1	0.0005	4.50229	2.42%
Ru0-C10-C5-C10	4	1	0.00187	3.5788	2.32%
Ru0-C9-C10-C9-C10	8	1	0.00299	4.2905	2.27%

Continued on the next page

Path	Legs	Dege-neracy	σ_i^2, Å^2	Length, Å	Contribution, %
Ru0-C7-C8-C6	8	1	0.00119	4.11422	2.21%
Ru0-C7-C5	4	1	0.00078	3.35098	2.14%
Ru0-C9-C8-C9	4	1	0.00183	3.58872	2.09%
Ru0-C13-C14	2	1	0.00053	4.65536	2.00%
Ru0-C8-C5	4	1	0.00083	3.52658	1.99%
Ru0-C9-C8-C10	8	1	0.00119	4.08938	1.99%
Ru0-C10-C9-C10	4	1	0.00182	3.57903	1.96%
Ru0-C7-C5-C8	8	1	0.00128	4.78326	1.96%
Ru0-C10-C9-C5	8	1	0.00118	4.06318	1.90%
Ru0-C6-C5-C10	8	1	0.00081	3.58324	1.87%
Ru0-C5-C9-C6	8	1	0.00127	4.79234	1.83%
Ru0-C6-C7-Ru0-O3	4	1	0.00117	5.0468	1.80%
Ru0-C9-C7-C10	8	1	0.00126	4.80107	1.78%
Ru0-C6-Ru0-C8	8	1	0.001	4.33645	1.77%
Ru0-O3-Ru0-C8	4	1	0.00101	4.31938	1.70%
Ru0-Ru1-C9	4	1	0.00205	5.00085	1.70%
Ru0-C9-Ru0-C9	2	1	0.002	4.3528	1.67%
Ru0-C14-C9	4	1	0.0007	4.01522	1.66%
Ru0-C14-C13-C10	2	1	0.00052	4.67827	1.63%
Ru0-Ru1-C4	4	1	0.01149	3.61618	1.40%
Ru0-C10-C14-C10	2	1	0.0009	3.6773	1.34%
Ru0-C10-C9-Ru0-O2	4	1	0.00115	4.90965	1.29%
Ru0-O3-O4	2	1	0.01643	3.44922	1.15%
Ru0-C8-C7-C8-C7	4	1	0.00298	4.28938	1.13%
Ru0-C7-C6-C8-C7	8	1	0.00189	4.82528	1.13%
Ru0-O4-C7	4	1	0.01812	3.82733	1.11%
Ru0-C5-C7-C5	4	1	0.00204	4.5137	1.10%
Ru0-C6-C10-C6	4	1	0.00207	4.63329	1.05%

Appendix A.20

Table A.20 Conditions, restrains, and constrains used in MS XAFS fitting for $[Ru(\eta^6\text{-}p\text{-cymene})(tsal)]_2$ [a]

Condition

K range: 0-16 $Å^{-1}$ [b]
FT range : 1-4.5 Å[b]
Determinancy (N_i/p):[c] 1.2
Maximal effective path length of a photoelectron: 5.0 Å
Maximum number of legs: 6
Plane-wave path filter threshold: 0%
Curved-wave path filter threshold: 0%
Scale factor: 0.9 ± 0.1

Bond length restraints (Å)

$Ru^0– S^1 \approx 2.39$ {0.02}	$Ru^0– S^1 \approx Ru^{21}- S^{22}$ {0.02}
$Ru^0–O^2 \approx 2.09$ {0.02}	$Ru^0–O^2 \approx Ru^{21}–O^{23}$ {0.02}
$Ru^0–S^{22} \approx 2.42$ {0.02}	$Ru^0–S^{22} \approx Ru^1–S^{21}$ {0.02}
$O^3–C^4 \approx 1.25$ {0.02}	$O^3- C^4 \approx O^2- C^4$ {0.02}
$S^1–C^6 \approx 1.78$ {0.04}	$S^1–C^6 \approx S^{22}–C^{27}$ {0.02}
$C^4–C^5 \approx 1.51$ {0.04}	$C^4–C^5 \approx C^{25}–C^{26}$ {0.04}
$Ru^0–C^{12} \approx 2.18$ {0.02}	$Ru^0– C^{12} \approx Ru^0–C^{13} \approx Ru^0–C^{14} \approx Ru^0–C^{16} \approx Ru^0–C^{17}$ {0.02}
$C^5–C^6 \approx 1.41$ {0.02}	$C^5–C^6 \approx C^6–C^7 \approx C^7–C^8 \approx C^8–C^9$ {0.01}
$C^9–C^{10} \approx 1.41$ {0.02}	$C^9–C^{10} \approx C^{10}–C^5$ {0.01}
$C^{12}–C^{13} \approx 1.41$ {0.02}	$C^{12}–C^{13} \approx C^{13}–C^{14} \approx C^{14}–C^{15}$ {0.01}
$C^{15}–C^{18} \approx 1.52$ {0.02}	$C^{15}–C^{18} \approx C^{18}–C^{19} \approx C^{18}–C^{20} \approx C^{12}–C^{11}$ {0.02}
$C^{18}–C^{19} \approx 1.41$ {0.02}	$C^{18}–C^{19} \approx C^{19}–C^{20} \approx C^{20}–C^{15}$ {0.01}
$Ru^{21}–C^{33} \approx 2.18$ {0.02}	$Ru^{21}– C^{33} \approx Ru^{21}–C^{34} \approx Ru^{21}–C^{35}$ {0.02}
$Ru^{21}–C^{36} \approx 2.18$ {0.02}	$Ru^{21}– C^{36} \approx Ru^{21}–C^{37} \approx Ru^{21}–C^{38}$ {0.02}
$C^{26}–C^{27} \approx 1.41$ {0.02}	$C^{26}–C^{27} \approx C^{27}–C^{28} \approx C^{28}–C^{29} \approx C^{29}–C^{30}$ {0.01}
$C^{30}–C^{31} \approx 1.41$ {0.02}	$C^{30}–C^{31} \approx C^{31}–C^{26}$ {0.01}
$C^{33}–C^{34} \approx 1.41$ {0.02}	$C^{33}–C^{34} \approx C^{34}–C^{35} \approx C^{35}–C^{36} \approx C^{36}–C^{37}$ {0.01}
$C^{37}–C^{38} \approx 1.41$ {0.02}	$C^{37}–C^{38} \approx C^{38}–C^{23}$ {0.01}
$C^{32}–C^{33} \approx 1.52$ {0.05}	$C^{32}–C^{33} \approx C^{36}–C^{39} \approx C^{39}–C^{40} \approx C^{39}–C^{41}$ {0.05}

Bond angle restraints (°):

$C^{12}–C^{13}–C^{14} \approx 120$ {2}	$C^{12}\text{-}C^{13}\text{-}C^{14} = C^{17}\text{-}C^{12}\text{-}C^{13} = C^{12}\text{-}C^{17}\text{-}C^{16}$ {2}
$C^{17}–C^{16}–C^{15} \approx 120$ {2}	$C^{17}–C^{16}–C^{15} = C^{16}–C^{15}–C^{14} = C^{13}–C^{14}–C^{15}$ {2}
$C^{18}–C^{15}–C^{14} \approx 120$ {3}	$C^{18}\text{-}C^{15}\text{-}C^{14} = C^{18}\text{-}C^{15}\text{-}C^{16}$ {3}
$O^2–Ru^0–S^1 \approx 88$ {5}	$O^2–Ru^0–S^1 = O^{22}–Ru^{21}–S^1$ {5}
$O^2–Ru^0–S^{22} \approx 78$ {5}	$O^2–Ru^0–S^{22} = O^{23}–Ru^{21}–S^1$ {5}
$S^1–Ru^0–S^{22} \approx 81$ {5}	$S^1–Ru^0–S^{22} = S^1–Ru^{21}–S^{22}$ {5}

Continued on the next page

$C^6–S^1–Ru^0 \approx 105$ {5}	$C^6–S^1–Ru^0 = C^{27}–S^{22}–Ru^{21}$ {5}
$C^6–S^1–Ru^{21} \approx 112$ {5}	$C^6–S^1–Ru^{21} = C^{27}–S^{22}–Ru^0$ {5}
$Ru^0–S^1–Ru^{21} \approx 99$ {5}	$Ru^0–S^1–Ru^{21} = Ru^0–S^{22}–Ru^{21}$ {5}
$C^4–C^5–C^6 \approx 124$ {5}	$C^4–C^5–C^6 = C^{25}–C^{26}–C^{27}$ {5}
$C^4–O^2–Ru^0 \approx 134$ {5}	$C^4–O^2–Ru^0 = C^{25}–O^{23}–Ru^{21}$ {5}
$C^{10}–C^5–C^4 \approx 117$ {5}	$C^{10}–C^5–C^4 = C^{26}–C^{25}–C^{24}$ {5}
$O^3–C^4–O^2 \approx 122$ {5}	$O^3–C^4–O^2 = O^{24}–C^{25}–O^{23}$ {5}
$C^5–C^6–S^1 \approx 124$ {5}	$C^5–C^6–S^1 = C^{25}–C^{26}–S^{27}$ {5}
$O^3–C^4–C^5 \approx 118$ {5}	$O^3–C^4–C^5 = O^{24}–C^{25}–C^{26}$ {5}
$C^7–C^6–S^1 \approx 116$ {5}	$C^7–C^6–S^1 = C^{28}–C^{27}–S^{22}$ {5}
$C^{10}–C^5–C^6 \approx 120$ {2}	$C^{10}–C^5–C^6 = C^7–C^6–C^5 = C^8–C^7–C^6 = C^9–C^8–C^7$ {2}
$C^{37}–C^{36}–C^{35} \approx 120$ {2}	$C^{37}–C^{36}–C^{35} = C^{34}–C^{35}–C^{36} = C^{33}–C^{34}–C^{35}$ $= C^{38}–C^{33}–C^{34}$ {2}
$C^{37}–C^{36}–C^{35} \approx 120$ {3}	$C^{37}–C^{36}–C^{35} = C^{35}–C^{36}–C^{39}$ {3}
$C^{26}–C^{27}–C^{28} \approx 120$ {2}	$C^{26}–C^{27}–C^{28} = C^{27}–C^{28}–C^{29} = C^{30}–C^{29}–C^{28} = C^{30}–C^{29}–C^{28}$ $= C^{31}–C^{30}–C^{29} = C^{26}–C^{31}–C^{30} = C^{27}–C^{26}–C^{31}$ {2}
$C^{40}–C^{39}–C^{41} \approx 110$ {5}	

Debye-Waller factor restraints (Å^2):

$0.001\{0.0005\} < \sigma_i^2 < 0.02\ \{0.001\}$, i= 1-41

Debye-Waller factor constraints:

$\sigma_i^2 (C^{19}) = \sigma_i^2 (C^{20})$
$\sigma_i^2 (C^{40}) = \sigma_i^2 (C^{41})$
$\sigma_i^2 (C^5) = \sigma_i^2 (C^6) = \sigma_i^2 (C^{10}) = \sigma_i^2 (C^9) = \sigma_i^2 (C^8)$
$\sigma_i^2 (C^{15}) = \sigma_i^2 (C^{16}) = \sigma_i^2 (C^{14}) = \sigma_i^2 (C^{12}) = \sigma_i^2 (C^{13})$
$\sigma_i^2 (C^{38}) = \sigma_i^2 (C^{37}) = \sigma_i^2 (C^{33}) = \sigma_i^2 (C^{34}) = \sigma_i^2 (C^{35})$
$\sigma_i^2 (C^{26}) = \sigma_i^2 (C^{27}) = \sigma_i^2 (C^{28})$
$\sigma_i^2 (C^{30}) = \sigma_i^2 (C^{31}) = \sigma_i^2 (C^{29})$
$\sigma_i^2 (O^3) = \sigma_i^2 (O^{24})$

Atoms restrained to be approximately coplanar

$(C^{16} – C^{15})$ x $(C^{14} – C^{15})$^.$(C^{12} – C^{15}) \approx 0$ {0.1}	$(C^{27} – C^{26})$ x $(C^{31} – C^{26})$^.$(C^{29} – C^{26}) \approx 0$ {0.1}
$(C^{13} – C^{12})$ x $(C^{17} – C^{12})$^.$(C^{15} – C^{12}) \approx 0$ {0.1}	$(C^{28} – C^{29})$ x $(C^{30} – C^{29})$^.$(C^{26} – C^{29}) \approx 0$ {0.1}
$(C^{38} – C^{33})$ x $(C^{34} – C^{33})$^.$(C^{36} – C^{33}) \approx 0$ {0.1}	$(C^5 – C^6)$ x $(C^7 – C^6)$^.$(C^9 – C^6) \approx 0$ {0.1}
$(C^{35} – C^{36})$ x $(C^{37} – C^{36})$^.$(C^{33} – C^{36}) \approx 0$ {0.1}	$(C^{10} – C^9)$ x $(C^8 – C^9)$^.$(C^6 – C^9) \approx 0$ {0.1}

[a]Experimental and calculated spectra are shown in Figure 3.19 (Chapter 3). [b]The applied window functions are shown in Figure 3.19. [c]The number of independent observations (N_i) and the number of varied parameters (p) were calculated taking into account the applied restraints and constraints [ref. 27 in Chapter 3]. [d] The atom numbering used in the MS XAFS calculation are shown in Figure 3.20 (Chapter 3).

Appendix A.21

Table A.21 Results of MS XAFS Analysis Fitting for [Ru(η^6-*p*-cymene)(tsal)]$_2$[a]

Parameter[b]	
-E0	17.10
S_0^2	0.97
σ_i^2 (S^1), Å^2 [c]	0.0011(2)
σ_i^2 (O^2), Å^2 [c]	0.0051(3)
σ_i^2 (O^3), Å^2 [c]	0.0005(1)
σ_i^2 (C^4), Å^2 [c]	0.0200(1)
σ_i^2 (C^5), Å^2 [c]	0.0005(4)
σ_i^2 (C^{12}), Å^2 [c]	0.0083(3)
σ_i^2 (C^{14}), Å^2 [c]	0.0017(4)
σ_i^2 (C^{17}), Å^2 [c]	0.0083(3)
σ_i^2 (Ru^{21}), Å^2 [c]	0.0037(4)
σ_i^2 (S^{22}), Å^2 [c]	0.0019(3)
σ_i^2 (O^{23}), Å^2 [c]	0.0033(10)
σ_i^2 (O^{24}), Å^2 [c]	0.0005(1)
σ_i^2 (C^{25}), Å^2 [c]	0.0005(5)

[a]Experimental and calculated spectra are shown in Figure 3.19 (Chapter 3). [b]Designations of parameters: E_0 is the threshold energy; S_0^2 is the scale factor; σ^2 (Å^2) is the Debye-Waller factor; and *N* is the number of scatterers in a shell. The values in the parentheses are the errors in the last significant figures, obtained from the Monte-Carlo analysis. [c]The atom numbering correspond to Figure 3.20 and the corresponding goodness-of-fit parameters are listed in Table 3.7 (Chapter 3).

Appendix A.22

Most significant Photoelectron Scattering Paths in the Calculated XAFS spectrum of $[Ru(\eta^6\text{-}p\text{-cymene})(tsal)]_2$

Path	Legs	Dege-neracy	σ_i^2, Å^2	Length, Å	Contribution, %
Ru0-O2	1	1	0.0051	2.09454	100.00%
Ru0-C13	3	1	0.00828	2.18353	100.00%
Ru0-C16	3	1	0.00174	2.18727	100.00%
Ru0-S1	1	1	0.00114	2.37646	44.32%
Ru0-S22	1	1	0.00193	2.41089	40.79%
Ru0-C4-O2	2	1	0.01952	3.22682	10.66%
Ru0-C27	1	1	0.0005	3.48983	10.36%
Ru0-C5	1	1	0.0005	3.55062	9.85%
Ru0-C11	1	1	0.0005	3.41044	9.40%
Ru0-C6	1	1	0.0005	3.30233	9.18%
Ru0-C18	1	1	0.00104	3.30126	9.07%
Ru0-Ru21	1	1	0.00374	3.63717	9.01%
Ru0-O3-O2	2	1	0.00082	4.21889	8.89%
Ru0-C17-C12	4	1	0.01095	2.88526	8.32%
Ru0-C15-Ru0-S22	2	1	0.00366	4.59305	8.30%
Ru0-C4	1	1	0.02	3.10166	8.06%
Ru0-O2-Ru0-C14	2	1	0.00684	4.27509	7.92%
Ru0-O23	1	1	0.0033	3.87207	7.52%
Ru0-C11-C12	2	1	0.00176	3.55608	7.30%
Ru0-O3-C4	2	1	0.00269	4.2508	7.04%
Ru0-C26	1	1	0.0005	3.96622	6.80%
Ru0-O2-Ru0-C13	2	1	0.01338	4.27807	6.57%
Ru0-C19	1	1	0.0005	3.95957	6.53%
Ru0-C20-C15	2	1	0.00053	4.49197	6.33%
Ru0-C18-C15	2	1	0.00132	3.50156	6.26%
Ru0-C17-Ru0-S1	2	1	0.00942	4.55763	6.06%
Ru0-C16-Ru-S22	2	1	0.00366	4.59816	6.04%
Ru0-C25	1	1	0.0005	3.81965	6.03%
Ru0-C15-C14	2	1	0.0023	2.88512	5.65%
Ru0-C16-C15	2	1	0.0023	2.88849	5.62%
Ru0-O3	1	1	0.0005	4.14979	5.62%
Ru0-C6-S1	2	1	0.00086	3.72996	5.58%
Ru0-C4-O3-O2	2	1	0.00301	4.3199	5.51%

Path	Legs	Dege-neracy	σ_i^2, Å^2	Length, Å	Contribution, %
Ru0-O24	1	1	0.0005	4.49107	5.07%
Ru0-C12-Ru0-S1	2	1	0.00942	4.55832	5.06%
Ru0-C7-C6	2	1	0.00052	4.6164	5.04%
Ru0-C14-C13	2	1	0.00663	2.88578	4.82%
Ru0-C16-C17	2	1	0.00661	2.88797	4.80%
Ru0-C10-C5	2	1	0.00051	4.92431	4.79%
Ru0-O2-C14	2	1	0.00675	4.22377	4.72%
Ru0-C20	1	1	0.0005	4.47337	4.46%
Ru0-C7	1	1	0.0005	4.52167	4.43%
Ru0-C28	1	1	0.0005	4.54894	4.29%
Ru0-C15-S22	2	1	0.00365	4.57161	4.03%
Ru0-O2-C13	2	1	0.01322	4.2266	3.91%
Ru0-C15-C20-C15	1	1	0.00061	4.51057	3.67%
Ru0-C16-S22	2	1	0.00362	4.54183	3.63%
Ru0-O2-O3-O2	1	1	0.00179	4.28799	3.61%
Ru0-O2-C4-O2	1	1	0.02313	3.35198	3.59%
Ru0-C27-S22	2	1	0.00105	3.84141	3.59%
Ru0-C28-C27	2	1	0.00054	4.72414	3.44%
Ru0-C16-Ru0-C16	3	1	0.00695	4.37455	3.32%
Ru0-O3-C4-O2	2	1	0.00595	4.37596	3.32%
Ru0-C17-S1	2	1	0.00933	4.51859	3.24%
Ru0-C34	1	1	0.0005	4.93414	3.23%
Ru0-C35	1	1	0.0005	4.93441	3.23%
Ru0-C10	1	1	0.0005	4.8895	3.12%
Ru0-C15-C13	4	1	0.0078	3.40162	3.02%
Ru0-C12-S1	2	1	0.00929	4.49945	3.02%
Ru0-C20-C18	2	1	0.00063	4.6475	2.98%
Ru0-C18-C20-C15	2	1	0.00064	4.66611	2.71%
Ru0-C5-C10-C5	1	1	0.00057	4.95912	2.68%
Ru0-C18-C14	4	1	0.0018	4.0079	2.66%
Ru0-C15-O2	2	1	0.00633	3.96402	2.31%
Ru0-C4-O3-C4	1	1	0.00936	4.3518	2.29%
Ru0-O2-O3-C4-O2	2	1	0.00706	4.44506	2.17%
Ru0-C12-O2	2	1	0.01241	3.96363	1.90%

Table A.23 Conditions, restrains, and constrains used in MS XAFS fitting for $[(\eta^6\text{-}p\text{-cymene})Ru(en)SPh]^{+}$ [a]

Condition	
K range: 0-15 $Å^{-1}$ [b]	
FT range : 1-4.5 Å [b]	
Determinancy (N_i/p): [c] 1.1	
Maximal effective path length of a photoelectron: 5.0 Å	
Maximum number of legs: 2	
Plane-wave path filter threshold: 0%	
Curved-wave path filter threshold: 0%	
Scale factor: 0.9 ± 0.1	
Bond length restraints (Å)	
$Ru^0 – N^1 \approx 2.13$ {0.03}	$Ru^0 – N^1 \approx Ru^0 - N^2$ {0.03}
$Ru^0 – S^3 \approx 2.39$ {0.05}	
$N^1 – C^4 \approx 1.45$ {0.05}	$N^1 – C^4 \approx N^2 – C^5$ {0.05}
$C^4 – C^5 \approx 1.41$ {0.05}	
$C^{12} – C^{13} \approx 1.50$ {0.04}	$C^{12} – C^{13} \approx C^{12} – C^{14}$ {0.04}
$C^9 – C^{12} \approx 1.51$ {0.05}	$C^9 – C^{12} \approx C^6 – C^{15}$ {0.05}
$Ru^0 – C^6 \approx 2.10$ {0.03}	$Ru^0 – C^6 \approx Ru^0 – C^7 \approx Ru^0 – C^8$ {0.03}
$Ru^0 – C^9 \approx 2.10$ {0.03}	$Ru^0 – C^9 \approx Ru^0 – C^{10} \approx Ru^0 – C^{11}$ {0.03}
$S^3 – C^{21} \approx 1.77$ {0.05}	
$C^6 – C^7 \approx 1.41$ {0.02}	$C^6 – C^7 \approx C^7 – C^8 \approx C^8 – C^9 \approx C^9 – C^{10} \approx C^{10} – C^{11} \approx C^{11} – C^6$ {0.01}
$C^{21} – C^{16} \approx 1.41$ {0.02}	$C^{21} – C^{16} \approx C^{16} – C^{17} \approx C^{17} – C^{18} \approx C^{18} – C^{19} \approx C^{19} – C^{20} \approx C^{20} – C^{21}$ {0.01}
Bond angle restraints (°):	
$C^7 – C^6 – C^{11} \approx 120$ {2}	$C^7\text{-}C^6\text{-}C^{11} = C^6\text{-}C^7\text{-}C^8 = C^7\text{-}C^8\text{-}C^9 = C^8 – C^9 – C^{10} = C^9 – C^{10} – C^{11} = C^{10} – C^{11} – C^6$ {2}
$C^8 – C^9 – C^{12} \approx 120$ {5}	$C^8\text{-}C^9\text{-}C^{12} = C^{10}\text{-}C^9\text{-}C^{12} = C^7\text{-}C^6\text{-}C^{15} = C^{11}\text{-}C^6\text{-}C^{15}$ {5}
$C^{13} – C^{12} – C^9 \approx 110$ {5}	$C^{13} – C^{12} – C^9 = C^{14} – C^{12} – C^9$ {5}
$C^{16} – C^{21} – C^{20} \approx 120$ {2}	$C^{16}\text{-}C^{21}\text{-}C^{20} = C^{21}\text{-}C^{16}\text{-}C^{17} = C^{18}\text{-}C^{17}\text{-}C^{16} = C^{19} – C^{18} – C^{17} = C^{20} – C^{19} – C^{18} = C^{19} – C^{20} – C^{21}$ {2}
$N^1 – Ru^0 – N^2 \approx 79$ {8}	
$S^3 – Ru^0 – N^2 \approx 83$ {6}	
$S^3 – Ru^0 – N^1 \approx 84$ {6}	
$Ru^0 – N^1 – C^4 \approx 123$ {10}	$Ru^0 – N^1 – C^4 = Ru^0 – N^2 – C^5$ {10}
$N^1 – C^4 – C^5 \approx 110$ {10}	$N^1 – C^4 – C^5 = C^4 – C^5 – N^2$ {10}

Continued on the next page

Debye-Waller factor restraints (Å^2):
0.001{0.0005} < σ_i^2 < 0.02 {0.001}, i= 1-21

Debye-Waller factor constraints:
σ_i^2 (C^{13}) = σ_i^2 (C^{14})
σ_i^2 (C^{10}) = σ_i^2 (C^{11}) = σ_i^2 (C^6)
σ_i^2 (C^6) = σ_i^2 (C^7) = σ_i^2 (C^8) = σ_i^2 (C^9) = σ_i^2 (C^{10})
σ_i^2 (C^{21}) = σ_i^2 (C^{16}) = σ_i^2 (C^{17}) = σ_i^2 (C^{18}) = σ_i^2 (C^{19})
σ_i^2 (C^{19}) = σ_i^2 (C^{20}) = σ_i^2 (C^{21})

Atoms restrained to be approximately coplanar
(C^9 – C^{10}) x (C^{11} – C^{10})^.(C^7 – C^{10}) ≈ 0 {0.1}
(C^8 – C^7) x (C^6 – C^7)^.(C^{10} – C^7) ≈ 0 {0.1}
(C^{16} – C^{21}) x (C^{20} – C^{21})^.(C^{18} – C^{21}) ≈ 0 {0.1}
(C^{17} – C^{18}) x (C^{19} – C^{18})^.(C^{21} – C^{18}) ≈ 0 {0.1}

[a]Experimental and calculated spectra are shown in Figure 3.21 (Chapter 3). [b]The applied window functions are shown in Figure 3.21. [c]The number of independent observations (N_i) and the number of varied parameters (p) were calculated taking into account the applied restraints and constraints [ref. 27 in Chapter 3]. [d] The atom numbering used in the MS XAFS calculation are shown in Figure 3.22 (Chapter 3).

Table A.24 Results of MS XAFS Analysis Fitting for [(η^6-*p*-cymene)Ru(en)SPh]$^{+}$ [a]

Parameter[b]	
-E0	15.72
S_0^2	0.94
σ_i^2 (N^1), Å^2 [c]	0.0001(4)
σ_i^2 (N^2), Å^2 [c]	0.0001(4)
σ_i^2 (S^3), Å^2 [c]	0.0002(1)
σ_i^2 (C^6), Å^2 [c]	0.0035(2)
σ_i^2 (C^{12}), Å^2 [c]	0.0005(1)
σ_i^2 (C^{13}), Å^2 [c]	0.0005(1)
σ_i^2 (C^{15}), Å^2 [c]	0.0005(1)
σ_i^2 (C^{21}), Å^2 [c]	0.0005(1)

[a]Experimental and calculated spectra are shown in Figure 3.21 (Chapter 3). [b]Designations of parameters: E_0 is the threshold energy; S_0^2 is the scale factor; σ^2 (Å^2) is the Debye-Waller factor; and *N* is the number of scatterers in a shell. The values in the parentheses are the errors in the last significant figures, obtained from the Monte-Carlo analysis. [c]The atom numbering correspond to Figure 3.22 and the corresponding goodness-of-fit parameters are listed in Table 3.8 (Chapter 3).

Appendix A.25

Most significant Photoelectron Scattering Paths in the Calculated XAFS spectrum of $[(\eta^6\text{-}p\text{-cymene})Ru(en)SPh]^+$

Path	Legs	Dege-neracy	σ_i^2, Å^2	Length, Å	Contribution, %
Ru0-C11	2	1	0.0047	2.10564	100.00%
Ru0-S3	1	1	0.00063	2.33274	100.00%
Ru0-C9	2	1	0.0047	2.10804	99.69%
Ru0-N2	1	1	0.0005	2.14351	89.70%
Ru0-N1	1	1	0.00313	2.1227	73.77%
Ru0-C8	1	1	0.0047	2.10557	50.00%
Ru0-C7	1	1	0.0047	2.10678	49.92%
Ru0-C21	1	1	0.0005	2.58807	33.09%
Ru0-C5	1	1	0.0005	3.21741	22.54%
Ru0-C20	1	1	0.0005	3.01409	20.43%
Ru0-C12-C9	2	1	0.00103	3.50434	19.84%
Ru0-C15-C6	2	1	0.00105	3.50612	19.28%
Ru0-C6-Ru0-N1	2	1	0.00783	4.23014	19.07%
Ru0-C16	1	1	0.0005	3.52852	15.79%
Ru0-C10-Ru0-S3	2	1	0.00532	4.43732	15.23%
Ru0-C15	1	1	0.0005	3.3952	14.47%
Ru0-C5-N2	2	1	0.00056	3.41192	14.41%
Ru0-C12	1	1	0.0005	3.39857	14.24%
Ru0-C8-Ru0-N2	2	1	0.00519	4.24908	13.62%
Ru0-C7-Ru0-N2	2	1	0.00519	4.25029	13.11%
Ru0-C14	1	1	0.0005	3.7311	12.78%
Ru0-C11-C10	2	1	0.00628	2.81377	12.19%
Ru0-C7-C8	2	1	0.00628	2.81481	12.19%
Ru0-C9-C10	2	1	0.00628	2.81495	12.18%
Ru0-C6-C11	2	1	0.00627	2.81519	12.18%
Ru0-C9-C8	2	1	0.00627	2.81543	12.18%
Ru0-C6-C7	2	1	0.00627	2.81561	12.18%
Ru0-C13-C9	2	1	0.0005	4.53688	11.02%
Ru0-C4	1	1	0.02001	3.16709	10.96%
Ru0-C21-S3	2	1	0.00075	3.34167	10.24%
Ru0-C19	1	1	0.0005	4.11114	9.87%
Ru0-C9-Ru0-S3	2	1	0.00532	4.44078	9.47%
Ru0-C19-C20	2	1	0.00054	4.26664	8.43%

Path	Legs	Dege-neracy	σ_i^2, Å^2	Length, Å	Contribution, %
Ru0-C8-N2	2	1	0.00513	4.1992	7.91%
Ru0-C7-N2	2	1	0.00513	4.19684	7.87%
Ru0-C10-S3	2	1	0.0053	4.42266	7.63%
Ru0-C6-N1	2	1	0.00781	4.22052	7.61%
Ru0-C4-N1	2	1	0.01899	3.37438	7.08%
Ru0-C16-C21	2	1	0.00056	3.76235	7.05%
Ru0-C13	1	1	0.0005	4.53531	7.04%
Ru0-C9-C13-C9	1	1	0.00052	4.53846	6.73%
Ru0-C9-C12-C9	1	1	0.0027	3.61011	6.64%
Ru0-C17	1	1	0.0005	4.57393	6.52%
Ru0-C6-C15-C6	1	1	0.0028	3.61705	6.14%
Ru0-C9-S3	2	1	0.00524	4.38232	6.05%
Ru0-N1-C7	2	1	0.00754	4.07251	5.66%
Ru0-N1-C11	2	1	0.00753	4.06966	5.60%
Ru0-C18	1	1	0.0005	4.79633	5.25%
Ru0-C13-C12	2	1	0.00054	4.71465	5.01%
Ru0-S3-C11	2	1	0.00507	4.24874	4.91%
Ru0-C17-C16	2	1	0.00054	4.75529	4.81%
Ru0-C20-S3	2	1	0.00079	3.90608	4.64%
Ru0-C21-C10	2	1	0.00503	4.56687	4.09%
Ru0-S3-C8	2	1	0.00495	4.1522	3.93%
Ru0-C12-C13-C9	2	1	0.00054	4.71623	3.61%
Ru0-C21-Ru0-C10	2	1	0.00519	4.69265	3.56%
Ru0-N1-Ru0-C7	2	1	0.00783	4.22947	3.53%
Ru0-N1-Ru0-C11	2	1	0.00783	4.22834	3.45%
Ru0-N2-C6	2	1	0.00478	3.91855	3.42%
Ru0-C20-C21	2	1	0.00061	3.50513	3.40%
Ru0-N2-C9	2	1	0.00479	3.92721	3.40%
Ru0-C17-C21	2	1	0.00056	4.79902	3.37%
Ru0-N2-Ru0-N2	1	1	0.00199	4.28702	3.26%
Ru0-C20-N2	2	1	0.00096	4.96157	2.96%
Ru0-N2-N1	2	1	0.00285	3.35636	2.86%
Ru0-C8-C10	2	1	0.00743	3.33217	2.76%
Ru0-C6-C10	2	1	0.00743	3.33315	2.76%
Ru0-C7-C11	2	1	0.00743	3.33344	2.75%
Ru0-C6-C8	2	1	0.00743	3.33407	2.75%
Ru0-C9-C7	2	1	0.00743	3.33471	2.75%
Ru0-C9-C11	2	1	0.00743	3.33469	2.74%
Ru0-C11-C6-C11	2	1	0.01723	3.52294	2.63%